Characterization, Measurement and Prediction of the Turbulent Flow in Stirred Tanks.

By

SUZANNE MARIE KRESTA, M.Sc.

A Thesis

Submitted to the School of Graduate Studies

in Partial Fulfilment of the Requirements

for the Degree of

Doctor of Philosophy

McMaster University

TURBULENT FLOW IN STIRRED TANKS

DOCTOR OF PHILOSOPHY (1991)
(Chemical Engineering)

McMASTER UNIVERSITY
Hamilton, Ontario, Canada

TITLE: Characterization, Measurement and Prediction of the Turbulent Flow in Stirred Tanks

AUTHOR: Suzanne Marie Kresta,
B.Sc.Eng. (University of New Brunswick)
M.Sc. (University of Leeds, UK)

ADVISOR: Professor Philip Eric Wood

NUMBER OF PAGES: 321

Abstract

Characterization of the Rushton turbine (RT) and pitched blade turbine (PBT) impellers was undertaken with two objectives: 1) development of impeller boundary conditions which can be generally applied to CFD simulations of stirred tank flows for predictive purposes, and 2) accurate characterization of the turbulence quantities k and ε for use in model development and verification. Since the flow field for the RT is well characterized in the literature, work on this impeller proceeded directly to a fundamental model of the discharge flow. Using this swirling radial jet (SRJ) model, it was possible to accurately predict the impeller boundary condition, including k and ε. The predicted boundary condition was used in a three dimensional CFD simulation of the entire flow field. The results of this simulation accurately reproduce mean velocity profiles, the decay of k and ε in the bulk of the tank, and details of the flow behind the baffles. Characterization of the PBT commenced with mean velocity and flow visualization studies of the impeller discharge zone for various geometries. It was found that there is a definite transition of the entire time averaged flow field from a single circulation loop, to two circulation loops, which occurs at a specific off bottom clearance. It was also shown that the boundary condition is affected by feedback from this transition in the flow field. The time varying characteristics of the flow field were examined in some detail. Various proposed methods of estimating ε were applied, and the results compared. It was found that autocorrelation function methods revealed useful physical information about the flow, particularly the existence of not only the dominant blade passage frequency (BPF), but also a second, low frequency component in the flow. The effects of these frequencies on the calculated value of ε were examined. It has been

possible to characterize the boundary conditions for both the RT and the PBT impellers, using both theoretical and experimental methods; and to show that mathematical modelling and CFD simulations based on the k-ε model can yield accurate and useful information about the flow field.

Acknowledgements

There is a whole host of people who I would like to thank for their guidance and support over the last four years. They range from good friends, who have been around through the best and the worst, to many people who made a single appearance at a critical moment, and kept things rolling. To name them all individually would miss the point, and not do justice to their contributions. I think that you all know who you are, and how important you have been. Thanks!

I would also like to thank the Natural Sciences and Engineering Research Council of Canada, the Ontario Graduate Scholars program, the McMaster Department of Chemical Engineering, Prof. P.E. Wood, my husband, and my parents, for their financial support of this enterprise.

Hamilton, September 1991

To my Mom and Dad, who taught me how to ask hard questions...

To my students, who will never know how much they gave back, and how many times they patched a bruised ego...

To Jim, who always remembered how much I wanted Fluid Mechanics, even when I forgot...

To Michel, who convinced me that modelling was important...

To Phil, who began it all with, "Do an energy balance on a differential slice - what's the area? - what's the volume? - now, take the limit as dx goes to zero. There's the DE you were looking for." I said, "Oh!" and wondered what all the fuss had been about.

To Phil who teaches us how to <u>think</u> about things - not just how to do them; and who accepted the hardest questions I could ask with a smile...

WHY?

Table of Contents

Chapter 1. Introduction

In this thesis, the turbulent flow field produced by an impeller rotating in a fully baffled cylindrical tank is examined. This "stirred tank" flow field is of substantial practical interest, since it is widely used in the chemical process industries for mixing of single and multi-phase fluids, solids suspension, gas dispersion, and chemical reactions. The physical and chemical processes taking place in these stirred tanks are complex, and are closely coupled to the underlying transport processes; in particular, the flow field. At present, design of these tanks is based on rules of thumb, on integrated dimensionless quantities such as N_p, the power number, and N_q, the flow number, and on the advice of experts with years of practical experience. Progress towards rational design methods will require a better understanding of the flow field, and the effect of this flow field on the dominant physical mechanisms in a given process. Fully predictive design will require the ability to predict the flow field generated by a given impeller in new geometric configurations.

In this thesis, two impellers are studied in some detail. The first, a Rushton turbine (RT), has been widely studied in the literature, and produces a flow field which is relatively well understood. The focus of the work for this impeller is on modelling and prediction. The second impeller, a pitched blade turbine (PBT), has only recently begun to attract attention, although it has seen widespread industrial use as a "general purpose" impeller for some time. The focus of the work for the PBT is on characterization of the flow field, particularly in terms of a) instabilities in the impeller discharge condition, and b) the turbulent aspects of the flow.

The principal contributions of this work to the body of knowledge surrounding turbulent flow in stirred tanks are:

1) characterization of the impeller discharge stream produced by a pitched blade turbine (PBT), using a combination of flow visualization and laser Doppler anemometry measurement techniques. This has revealed two distinct circulation patterns, depending on the impeller size and location, which are shown to have a substantial impact on the discharge stream. These effects are significant even very close to the edge of the impeller blades, resulting in a shift in the impeller discharge condition. This instability, or change in the impeller discharge condition, has substantial implications for future modelling of stirred tanks.

2) the first experimental comparison of the various proposed methods for measuring the rate of dissipation of turbulence kinetic energy (ε) at the edge of the impeller. The results show a surprisingly good level of agreement among the methods, even at the tip of the impeller blades, where trailing vortices disrupt the flow. One of the methods examined, which relies on determination of the integral time scale from the autocorrelation coefficient function, was investigated in some detail. Several developments related to this method of data analysis have proven successful. These are the first reported measurements of ε for the PBT, and the lessons learned from this comparison will make future measurements much more reliable, as well as providing a rational means of comparison between reported results.

3) successful prediction of the turbulence quantities k (the turbulence kinetic energy per unit mass) and ε (its rate of dissipation) at the edge of the Rushton

turbine (RT) using the swirling radial jet model, which is derived from the Navier Stokes equations and the standard k-ε model. This predicted boundary condition was used in three dimensional simulations of the flow field in the bulk of the tank; which successfully replicated all reported features of the flow field at a quantitative level.

The physical mechanisms underlying industrial processes which are carried out in stirred tanks remain one of the least understood areas in chemical engineering. The turbulent fluid mechanics of the complex flow field underlies many of these processes, and not until it can be successfully characterized and predicted for various impeller and tank geometries will reliable, predictive design of these processes be possible. The insights gained on the path toward full predictive ability are quickly put to use as design heuristics, and thus prove useful long before the final objective is met.

1.1 Definition of a stirred tank

The stirred tank as defined for this work is shown in figure 1. The tank diameter, T equals the height of liquid in the tank, H. This is known as the "square" configuration. There are four baffles of width T/10 spaced at equal intervals around the tank, and placed flush with the tank wall. A lid is placed on the top to eliminate the free surface. The impeller diameter D is defined as a fraction of the tank diameter; both D=T/2 and D=T/3 were used. The impeller off-bottom clearance, C, was varied over a wide range from C=T/2 to C=T/20. For all of the experimental work, a single tank with diameter T=152.4 mm =6 in. was used.

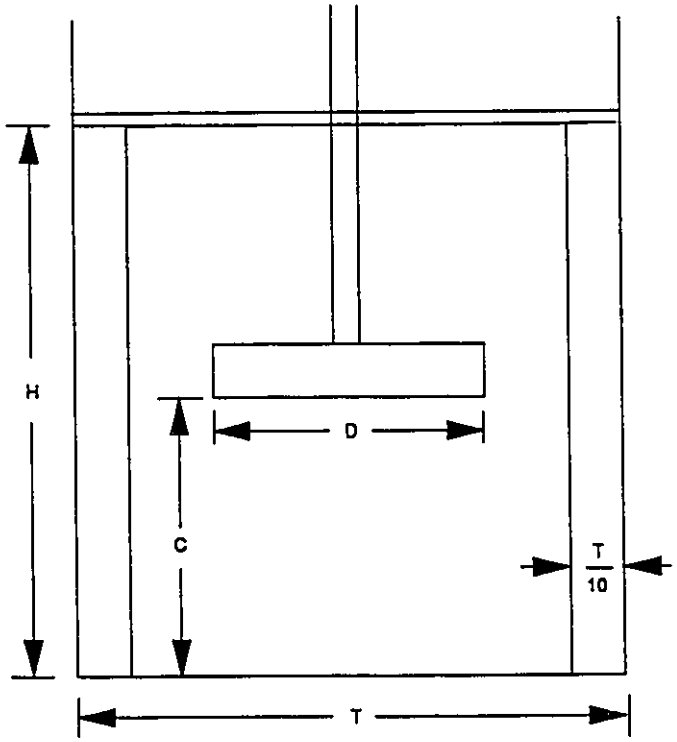

Figure 1. Geometry of the stirred tank as defined for this work.

The two impellers studied are shown in figure 2. On the left is the Rushton turbine (RT), which has 6 vertical blades of width W=D/5 and length L=D/4. The blades are mounted on a disc of diameter 2D/3. On the right is the pitched blade impeller (PBT), with 4 blades inclined at 45° to the horizontal. The width of these blades is W=D/5. The stock used for construction of all impellers was brass with a thickness of 0.8 mm. The hubs have an outer diameter of 12.7 mm = 0.5 in., and an inner diameter of 6.35 mm = 0.25 in..

Two mixers were used over the course of the experimental work. The first is a Canlab variable speed mixer with a 6.3 mm diameter shaft, the second is a Labmaster TS2010 mixer with a 9.5 mm diameter shaft. The larger diameter shaft

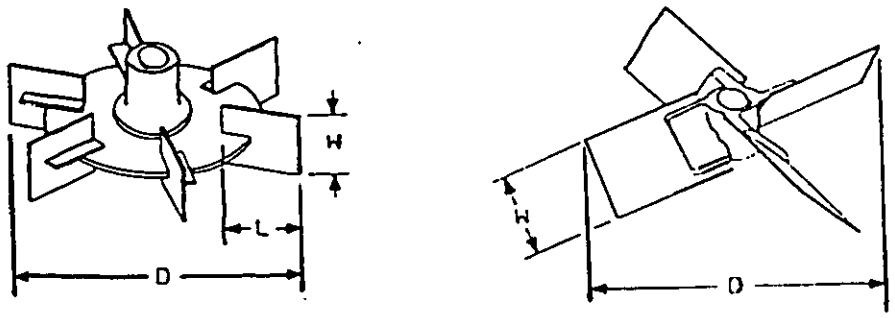

Rushton Turbine (RT) Pitched Blade Impeller (PBI)

Figure 2. Dimensions of the Rushton turbine and the pitched blade impeller (from Oldshue (1983)).

was much less prone to run-out (or "wobble") at the end of the shaft, which is partly due to the increased diameter, and partly due to the superior shaft mount. In all cases, run-out was less than 1 mm.

1.2 Variables of interest for characterization of the flow

The first variable of interest for characterization of the flow is the set of mean velocity vectors which defines the overall circulation pattern in the stirred tank. Since this system is closed, the fluid recirculates through the impeller, and will normally form one or two well defined circulation loops. In a three dimensional sense, these can be described as "a rolling donut," or as "a fixed torus, the surface of which revolves about the circular axis." The shape and orientation of the circulation loops depends on the type of impeller in use. The RT is a radial impeller, which discharges the fluid at the tips of the impeller blades, directing it radially towards the tank walls. A radial impeller produces two circulation loops, one above,

and one below the plane of the impeller. A purely axial impeller discharges the fluid through the lower surface of the blades, directing it towards the bottom of the tank. The fluid then turns at the bottom of the tank, travels up the tank walls, radially inward across the top of the tank, and back down to the impeller in a single circulation loop. The PBT produces a combined axial-radial flow, discharging the fluid mainly through the lower surface of the blades, at some angle to the horizontal. Current literature reports that the PBT produces a single circulation loop, like that of the axial impeller. It will be shown that this is not always the case.

Circulation patterns determine tank turnover times, the location of dead zones, optimal locations for feed points, required impeller spacing and baffling arrangements.

Quantitative experimental determination of circulation patterns is time consuming, and there are always parts of the tank which are difficult or impossible to reach with a probe. The results are limited to the geometry of the original experiment, and thus have limited usefulness for general applications. Flow visualization (FV) experiments offer a faster experimental alternative to measurements of the mean velocity vectors. Within minutes, a whole range of configurations can be examined and recorded. In addition, it is possible to observe the dynamic nature of the flow, so that the observer is left with some impression of the relative stabilities of various configurations. This overall impression does not, however, provide any quantitative information. Given appropriate boundary conditions, and an adequate turbulence closure model, computational fluid mechanics (CFD) can be used to perform numerical experiments on the flow field. The numerical experiments obtain solutions to discretized versions of the differential equations which describe the

momentum transfer, and which are bounded by the conditions at the boundaries of the system. These experiments combine the visual appeal of the FV experiments with the quantitative appeal of detailed measurements of the velocity vectors. The difficulty with this approach is that the boundary condition to be used to define the impeller is both critical to the success of the experiment, and extremely difficult to determine. Not only mean velocities are needed, but also turbulent quantities such as k, the turbulence kinetic energy per unit mass, and ε, its dissipation rate. Nonetheless, given an accurate boundary condition, numerical experiments are reasonably fast, are flexible, and provide an easy way to link the flow field with related scalar fields (eg. temperature, concentration) via addition of another partial differential equation to the finite difference calculations. Because of these advantages, and the inherent importance of the impeller discharge stream, determination of appropriate impeller boundary conditions for use in CFD experiments has been the major focus of this work.

Given the overall circulation patterns in the tank, it is possible to define the dimensionless flow number, N_q, which quantifies the amount of flow produced by an impeller.

$$N_q = \frac{Q}{ND^3} \qquad (1)$$

where Q is the primary volumetric flow (ie. the flow generated by the impeller), and N is the rotational speed of the impeller. For the Rushton turbine, this is defined as the integral of the radial component of velocity, V_r, across the tip of the impeller blades

$$Q = \int_{z=-W/2}^{z=+W/2} \pi D V_r dz \qquad (2)$$

The appropriate definition of Q for the PBT will be discussed in chapter 4. The power number, which reflects the power requirements of a given impeller, is defined

$$N_p = \frac{P}{\rho N^3 D^5} \qquad (3)$$

where P is the power input. The flow number and the power number provide the two principal means of comparison of various impellers. They represent a simple quantitative picture of the amount of flow produced, and the amount of power needed to produce it. The amount of power used in the tank will be closely related to the turbulence levels in the tank, and can be related to the rate of dissipation of turbulence kinetic energy per unit mass through an overall energy balance

$$\frac{P}{m} = \int_{V_{tank}} \varepsilon dV \qquad (4)$$

Characterization of the turbulent aspects of the flow field is conceptually more difficult than that of the mean velocity field and its overall circulation patterns. Direct experimental measurement of the relevant quantities is at best difficult, and at worst impossible. The quantities of interest stem from the time averaged Navier Stokes equations of the instantaneous flow field; the turbulence kinetic energy per unit mass, $k = \frac{1}{2}\overline{u_i'^2}$; the rate of dissipation of k, $\varepsilon = \nu\overline{\left(\frac{\partial u_i'}{\partial x_j}\right)^2}$; the Reynolds stresses $\overline{u_i' u_j'}$; the RMS velocity $\sqrt{\overline{u_i'^2}}$; and the turbulence intensity $\frac{\sqrt{\overline{u_i'^2}}}{U_i}$. The development, definition, and measurement of these terms will be considered in some detail in later chapters, but in a general sense, it can be said that they are all used to describe the

statistical properties of the fluctuating flow field. Single point statistics, which are measured at a single point in the flow field, represent the mean and the distribution of events over time. These include the quantities k, $\overline{u_i'u_j'}$, the turbulence intensity, and the RMS velocity. Two point statistics give a measure of the spatial structure in the flow, its statistical mean and distribution. While ε is not itself a two point statistic; it is closely related to various length and time scales, all of which are defined by two point statistical auto- and cross-correlations. Since no two-point statistics are directly measured here, ε is used to define the structure of the turbulent flow through the length and time scales. This information is often the determining factor for modelling of the related physical and chemical processes: it will determine length scales of drops, flocs, bubbles, and striation thicknesses. These length scales determine the area available for mass transfer and chemical reaction, and the final product size distribution. It is for this reason that characterization of the turbulent flow field assumes great importance, in spite of the difficulty of the problem.

1.3 Current state of knowledge

Research into the flow in stirred tanks began in the 1950's with work by Rushton et al. (1950) and by Bates et al. (1963) on the characterization of dimensionless numbers for various impellers, and various tank geometries. Of the impellers studied in this thesis, the RT received the most attention through the 1960's and 1970's since it was the most commonly used industrial impeller at the time. With the rise of energy costs in the 1970's, industry shifted to use of the more efficient PBT. However, with the exception of an extensive series of articles by Fort and other authors (Studies on Mixing, Coll. Czech. Chem. Comm., Part I, 1958, Part

LXXVIII, 1989), academic research has only recently begun to shift its focus to reflect this industrial trend. By the early 1970's, the circulation patterns for the RT were well established, and progress made in the understanding of the flow field since then has focussed on two things: resolution of the trailing vortices behind individual impeller blades, and development of CFD simulations of the flow. In contrast to the attention devoted to measurements of the mean and ensemble averaged velocities, measurement of the turbulence quantities has been limited to those quantities which are easy to measure, and has thus consistently been incomplete. Examination of the quantitative impact of the various assumptions which are imposed in the course of analysis has been almost non-existant.

Several technical developments in the 1970's have had a significant impact on the way in which all flow fields are studied. The first is the advent of computers and their continually increasing speed, which allows not only CFD experiments, but faster and more extensive data collection and analysis in the wet laboratory. The second is the development of the laser Doppler anemometer (LDA), an optical technique which allows *non-intrusive* measurement of the fluid velocity. LDA provides the additional advantages of an almost instantaneous response to velocity fluctuations, and unambiguous separation of the three directional components of velocity. Progress in the understanding of the flow field in a stirred tank has gone hand in hand with these developments.

The discharge stream at the tip of the RT impeller has been characterized from two perspectives. The first considers the mean velocity profile across the tip of the impeller blades, and its decay as one moves radially outward in the tank (Cooper and Wolf (1968), Nouri et al. (1987)). The profile is jet-like; its shape is

roughly parabolic, with the edges spreading and the maximum decreasing as more fluid is entrained in the flow, as shown in figure 3. The tangential, or swirl component of velocity adds a third dimension to the behavior, and this swirling radial jet concept is used in chapter 6 to develop a rigorous model of the impeller boundary condition, beginning from first principles. The second perspective on the impeller discharge stream considers the flow behind a single blade, and builds up a picture of the trailing vortices using ensemble averaged velocity measurements. Van't Riet and Smith (1975) were the first to examine the flow from this perspective, showing that a pair of vortices exists, one above and one below the impeller disc plane as shown in figure 4. The most definitive measurements reported to date are probably those of Yianneskis et al. (1987) who show cross sections of the vortex as it moves out and away from the impeller. More recent work, as yet unpublished, has been done by Stoots and Calabrese (1989).

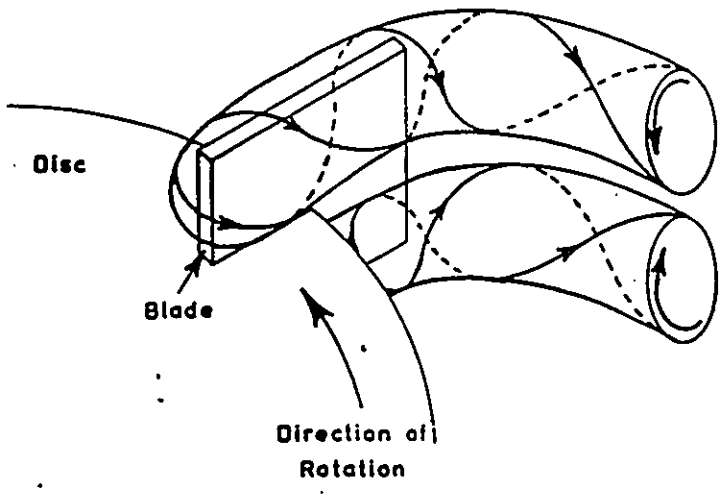

Figure 4. Trailing vortices shed from a Rushton turbine blade as given by Van't Riet and Smith (1975).

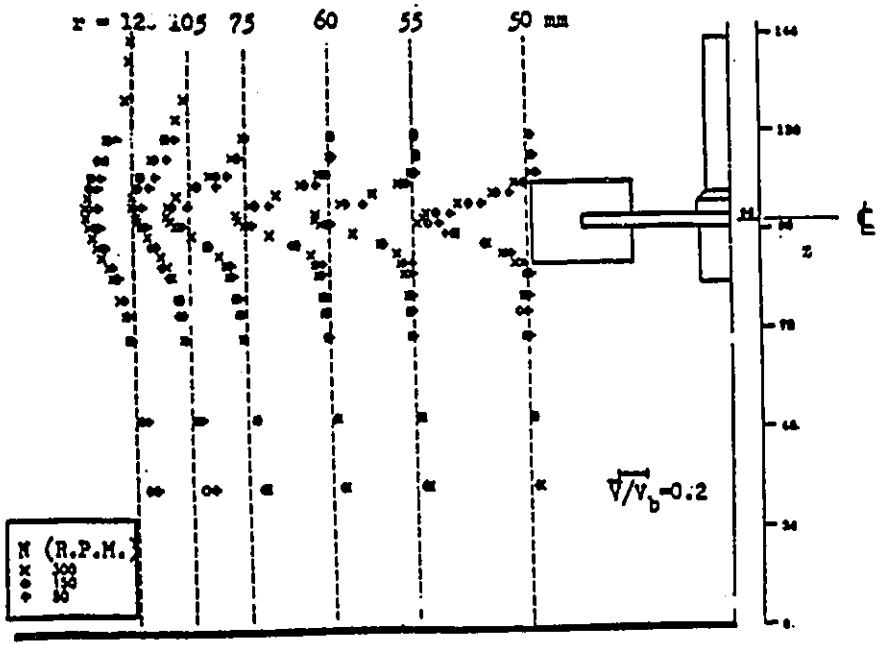

Figure 3. Decay of the jet in the discharge stream of the RT impeller (from Nouri et al. (1987)).

Turbulence studies for this impeller have often focussed on the effect of the "pseudo-turbulence," or regular fluctuations, which arise from the blade passages and the trailing vortices. There has also been some concern about the levels of anisotropy in the immediate vicinity of the impeller blades (Rao and Brodkey (1972)). Authors have frequently taken the position that either a) these factors can be ignored (Laufhutte and Mersmann (1987), Cutter (1966)) and proceeded with analysis, or that b) all analysis must be based on removal of these factors (Okamoto (1981), Placek et al. (1986), Van't Riet et al. (1976)). Wu and Patterson (1989) and Wu et al. (1989) have attempted to compare the two approaches. These papers are discussed in some detail in chapter 5, where the various methods available for the examination of turbulence in stirred tanks are laid out.

The various attempts at modelling and CFD simulations are discussed in some detail in chapter 6, as part of the assessment of the swirling radial jet (SRJ) model developed in this work. Until the development of the SRJ model, boundary conditions available for CFD simulations did not include accurate evaluations of the turbulence quantities. While some successes had been achieved with simulations of the mean velocity field, results for the turbulent aspects of the flow had never been successfully compared with quantitative experimental results.

Another area of research which is worthy of note is a small set of flow visualization studies which examine various impellers, and various aspects of the flow. These studies often give an excellent qualitative picture of the more complex aspects of the flow, which are difficult to reproduce in a time averaged quantitative experiment. Tatterson et al. (1980) examined the flow around the impeller blades for a PBT, and considered the shedding and decay of the trailing vortices as the impeller rotates, and the vortices move down through the tank. They concluded that the flow produced by a PBT is a combination of "high-speed jets," or streaming flow, and trailing vortices; and that the dominant flow depends on the number of blades, and/or the scale of the experiment. A later paper from the same group (Ali et al. (1981)) considers the mechanisms of drop break-up at the tip of the impeller. They observe both ligament stretching (due to the trailing vortices), and turbulent fragmentation. Winardi and co-authors (1988, 1991) concentrate on variations of the flow field over time. They first consider a 90 degree pitched blade impeller, which produces mean circulation patterns similar to those produced by a Rushton turbine. If the flow field is observed over time, however, several dominant flow fields with distinct circulation patterns emerge. The later paper shows the same kind of unstable

behaviour for the marine propeller, which produces an axial flow field on the mean. Winardi et al. report properties such as lifetime distributions and probability density functions for the various flow patterns.

Information specific to the PBT is notably lacking in the literature. Fort's work was mentioned earlier, and is best summarized in his 1986 review. Recent papers by Ranade and co-authors (1989a,b, 1991) and by Rewatkar and co-authors (1990, 1991) of the same group report LDA measurements of the mean velocity, and some simulations using simplified boundary conditions. None of these authors examine the stability of the flow field, or a detailed characterization of the turbulent aspect of the flow.

1.4 Approach used in this work

The ultimate objective of this work is to gain sufficient understanding of the flow field produced by an impeller to allow

1) prediction of the flow field produced by the same impeller in a different tank geometry, and
2) characterization of the important features of the fluid mechanics, in all parts of the tank, for use in modelling of phenomena such as mixing, chemical reaction, and particle size distributions.

Since the current state of knowledge is clearly far removed from these ultimate objectives, an intermediate approach was developed to focus the research in the context of what is already known. This is depicted in figure 5. The first section of the figure focusses on gaining an overall understanding of the flow produced by the impeller. Aspects of this include circulation patterns, definition and measurement

of dimensionless numbers, and characterization of the impeller discharge stream. Depending on the ultimate objective of the work, different aspects of the impeller discharge stream will be emphasized in this step. For detailed examination of mechanisms which lead to drop break-up and mixing processes, resolution of the trailing vortices and the time varying characteristics of the flow may be emphasized. For modelling of the time averaged characteristics of the flow, the mean velocity profiles and turbulence quantities are more important. Once a basic understanding of the characteristics of the flow is attained, more detailed studies leading to either a) a model of the impeller boundary condition suitable for use in a CFD simulation, or b) mechanistic models relating the time varying details of the flow field to the physical processes we wish to describe can be undertaken.

For the Rushton turbine, the focus of the work was on branch (a). The SRJ model of the boundary condition was developed from first principles, verified using data at the impeller tip, and simulations were performed for two different geometries. The results were verified with the available data, and used to define appropriate zones for use in models of related processes which require ε as an input parameter. The majority of the work on the PBT focussed on the first section of the figure; gaining a basic understanding of the circulation patterns and the impeller discharge stream. The first experiments involved flow visualization of the overall patterns, which are presented in the next chapter. This information was quantified using LDA, with a particular focus on the mean velocity impeller boundary condition and its stability with respect to the system variables. The experimental method, its verification, and the mean velocity results are discussed in chapters 3 and 4.

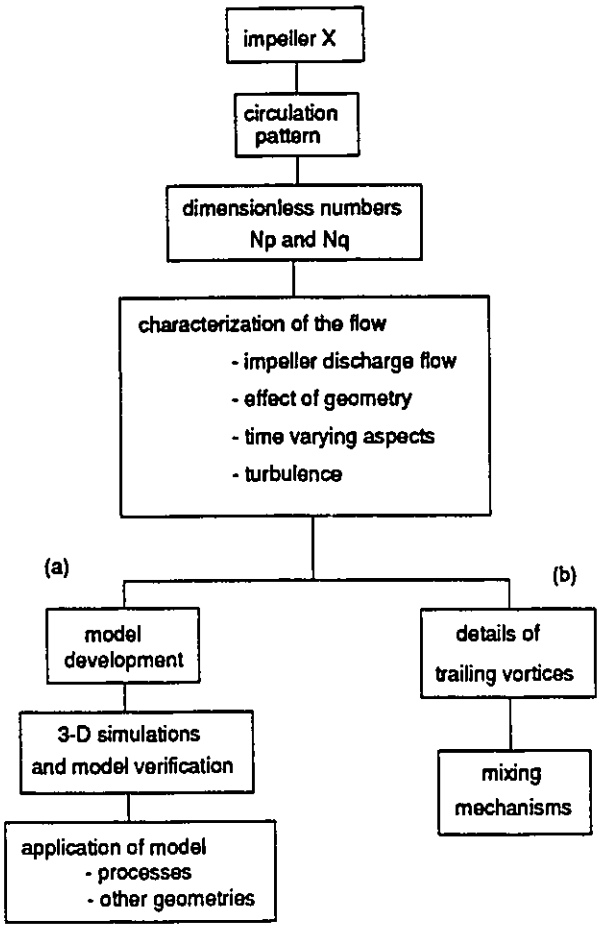

Figure 5. The overall research strategy.

One of the key perspectives of this work is the accurate characterization of the turbulence, and examination of the various assumptions used to do this. In chapter 5, the examination begins with the definition of turbulence, from both conceptual and mathematical perspectives. The development of the various equations used to estimate, model, predict, and/or characterize ε are reviewed, with an eye to examining the accumulated assumptions. Five methods are chosen for further evaluation; four of which are experimental. The fifth is the k-ε closure model, which is successfully used in the SRJ model of the RT in chapter 6. Chapter 7 is devoted to measurement

of ε for the PBT, and examination of the experimental implications of the assumptions laid out in chapter 5. This work provides a strong basis both for modelling of the PBT boundary condition, and for further studies into the relationship between the time varying aspects of the flow field and the process mechanisms we wish to understand.

1.5 References

Ali, A. M., H. H. S. Yuan, D. S. Dickey, G. B. Tatterson, "Liquid dispersion mechanisms in stirred tanks: Part 1, pitched blade turbine," Chem. Eng. Comm., v. 10, pp. 205-213, 1981.

Bates, Robert L., Philip L. Fondy, and Robert R. Corpstein, "An examination of some geometric parameters of impeller power," I. and E. C. Process Des. and Dev., v. 2, pp. 311-314, 1963.

Cooper, R. G. and D. Wolf, "Velocity profiles and pumping capacities for turbine type impellers," Can. J. Chem. Eng., v. 46, pp. 94-100, 1968.

Cutter, Louis A., "Flow and turbulence in a stirred tank," AIChE Journal, v. 12, pp. 35-45, 1966.

Fort, I. and co-authors, Studies on Mixing, Coll. Czech. Chem. Comm., Part I, 1958, Part LXXVIII, 1989.

Fort, Ivan, "Flow and turbulence in vessels with axial impellers," in Mixing: Theory and Practice v. 3, V.W. Uhl and J.B. Gray, eds., Academic Press, Toronto, 1986.

Laufhutte, Hans Deitrich, and Alfons Mersmann, "Local energy dissipation in agitated turbulent fluids and its significance for the design of stirring equipment," Chem. Eng. Technol., v. 10, pp. 56-63, 1987.

Nouri, J. M., J. H. Whitelaw and M. Yianneskis, "The scaling of the flow field with impeller size and rotational speed in a stirred reactor," Second International Conference on Laser Anemometry - Advances and Applications, Strathclyde, UK, Sept. 1987.

Okamoto, Y., N. Nishikawa, K. Hashimoto, "Energy dissipation rate distribution in mixing vessels and its effects on liquid-liquid dispersion and solid-liquid mass transfer," International Chemical Engineering, v. 21, pp. 88-94, 1981.

Oldshue, J. Y., Fluid Mixing Technology, McGraw Hill, New York, 1983.

Placek, J., L. L. Tavlarides, G. W. Smith and I. Fort, "Turbulent flow in stirred tanks, Part II: a two scale model of turbulence," AIChE Journal, v. 32, pp. 1771-1786, 1986.

Ranade, V. V. and J. B. Joshi, "Flow generated by pitched blade turbines I: Measurements using laser Doppler anemometer," Chem. Eng. Comm., v. 81, pp. 197-224, 1989.

Ranade, V. V., J. B. Joshi, and A. G. Marathe, "Flow generated by pitched blade turbines II: Simulation using $k-\varepsilon$ model," Chem. Eng. Comm., v. 81, pp. 225-248, 1989.

Ranade, V. V., J.R. Bourne, J.B. Joshi, "Fluid mechanics and blending in agitated tanks," Chem. Eng. Sci., v. 46, pp. 1881-1893, 1991.

Rao, M. A. and R. S. Brodkey, "Continuous flow stirred tank turbulence parameters in the impeller stream," Chem. Eng. Sci., v. 27, p. 137-156, 1972.

Rewatkar, V. B., K.S.M.S. Raghava Rao, J. B. Joshi, "Power consumption in mechanically agitated contactors using pitched bladed turbine impellers," Chem. Eng. Comm., v. 88, pp. 69-90, 1990.

Rewatkar, V. B. and J. B. Joshi, "Effect of impeller design on liquid phase mixing in mechanically agitated reactors," Chem. Eng. Comm., v. 102, pp. 1-33, 1991.

Rushton, J. H., E.W. Costich, and H.J. Everett, "Power characteristics of mixing impellers," Parts I and II, Chem. Eng. Prog., v. 46, pg. 395, 1950.

Stoots, Carl M., and Richard V. Calabrese, "The trailing vortex system behind a Rushton turbine blade," Mixing XIII - Engineering Foundation Conference on Mixing, 1989.

Tatterson, Gary B., H. S. Yuan, and R.B. Brodkey, "Stereoscopic visualization of the flows for pitched blade turbines," Chem. Eng. Sci., v. 35, pp. 1369-1375, 1980.

Van't Riet, K. and J. M. Smith, "The trailing vortex system produced by Rushton turbine agitators," Chem. Eng. Sci., v. 30, pp. 1093-1105, 1975.

Van't Riet, K., W. Bruijn, and J. M. Smith, "Real and pseudo-turbulence in the discharge stream from a Rushtom turbine," Chem. Eng. Sci., v. 31, pg. 407, 1976.

Winardi, S., S. Nakao, and Y. Nagase, "Pattern recognition in flow visualization around a paddle impeller," J. Chem. Eng. Japan, v. 21, pg. 503, 1988.

Winardi, Sugeng, and Yoichi Nagase, "Unstable phenomenon of flow in a mixing vessel with a marine propeller," J. Chem. Eng. Japan, v. 24, pp.243-249, 1991.

Wu, H. and G. K. Patterson, "Laser Doppler measurements of turbulent flow parameters in a stirred mixer," Chem. Eng. Sci., v. 44, pp. 2207-2221, 1989.

Wu, H., G. K. Patterson and M. Van Doorn, "Distribution of turbulence energy dissipation rates in a Rushton turbine stirred mixer," Expts. in Fluids, v. 8, pp. 153-160, 1989.

Yianneskis, M., Z. Popiolek and J. H. Whitelaw, "An experimental study of the steady and unsteady flow characteristics of stirred reactors," J. Fluid Mech., v. 175, pp. 537-555, 1987.

Chapter 2. Flow visualization

In this chapter, the flow field produced by a 4-bladed, 45°pitched blade impeller is introduced via the results of flow visualization experiments. This provides a qualitative picture of the major flow patterns in the flow field. In later chapters, these results will be combined with LDA studies to confirm the observed flow patterns, which have not previously been reported; and which are somewhat more complex than the conventional "textbook" picture.

The flow visualization techniques used to illustrate the flow have been chosen from the many explained in the text by Merzkirch (1987), and from those used for similar flow fields. Flow visualization in stirred tanks has historically concentrated on particle seeding methods (Winardi et al. (1988), Nouri and Whitelaw (1990), Winardi and Nagase (1991)) and liquid tracers (Ali et al. (1981), Tatterson et al (1980)). Shen and Baird (1991) have recently used a short tuft method to examine the flow close to the surface of the delta impeller blade. In this study, longer streamers are used to examine the flow as it comes off the impeller blades. To examine the overall circulation patterns, the flow is seeded with particles, and a single plane is illuminated with a sheet of light.

Classic fluid mixing texts (eg. Oldshue (1983), Uhl and Gray (1986)) illustrate the overall circulation pattern for the PBT as a single circulation loop which fills the entire tank for all geometric configurations. Rewatkar and Joshi (1991) have reported similar results from current experimental work, which are reproduced in figure 6.

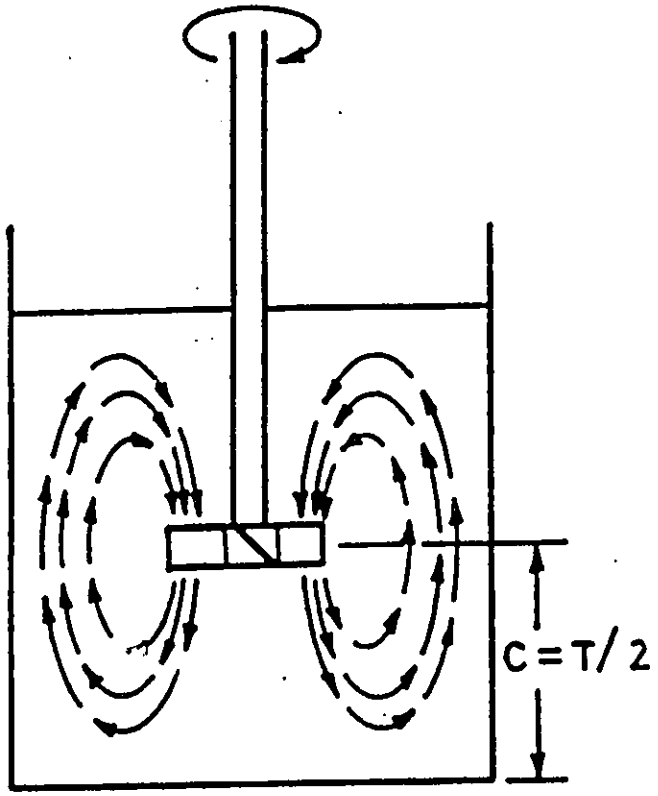

Figure 6. Conventional circulation pattern for the PBT as reported by Rewatkar and Joshi (1991).

In contrast to this simple picture, our results show that the primary circulation loop is much smaller than previously reported. Above the impeller, in the upper third of the tank, there is very little circulation and many of the weaker circulation patterns are unstable. For some geometric configurations, the primary circulation loop is accompanied by a weak secondary circulation loop which forms in the lower corners of the tank. Where the circulation is strong (D=T/2), the impeller discharge flow is actually deflected toward the horizontal by this secondary circulation loop.

Moving to a Lagrangian frame of reference, the flow coming off the impeller blades is a combination of rotational streaming flow which extends over the inner 80% of the blades, and trailing vortices at the outer tips. These flow patterns are illustrated using the long tuft, or streamer method, and agree well with the results obtained by Tatterson et al. (1980) and Ali et al. (1981), who used liquid tracers.

2.1 Seeding method

Visualization of the overall circulation patterns was carried out using the particle tracer method. The flow was seeded with polystyrene beads in the size range $180-250\mu m$. The particle time scale (defined by Buchave (1979) and given in equation 11, chapter 3) of 4 msec, allowed the particles to track fluctuations of the order of 200 Hz (much larger than the blade passage frequency). The flow was illuminated with a sheet of light produced by a 1000 W filament light source, contained by a funnelling system as shown in figure 7. The filament was oriented in the same direction as the desired sheet of light. The thickness of the spacers in the funnelling system was varied, and it was found that 2 mm gave the optimum balance of spatial resolution with sufficient lighting for photography. On entry to the tank, the light sheet was 2 mm thick; this had dispersed to 5 mm on exit at the other side. Because of the heat generated by the light source, it was necessary to cool the light and funnelling system using a fan.

The photographic settings were optimized for each experimental set up, and are individually reported in the figure captions. 400 ASA color slide film was used throughout. Two impeller diameters (D=T/2 and D=T/3), and two off bottom clearances (D=T/2 and D=T/3) were considered. All of the rotational speeds put the flow at the impeller discharge in the fully turbulent region.

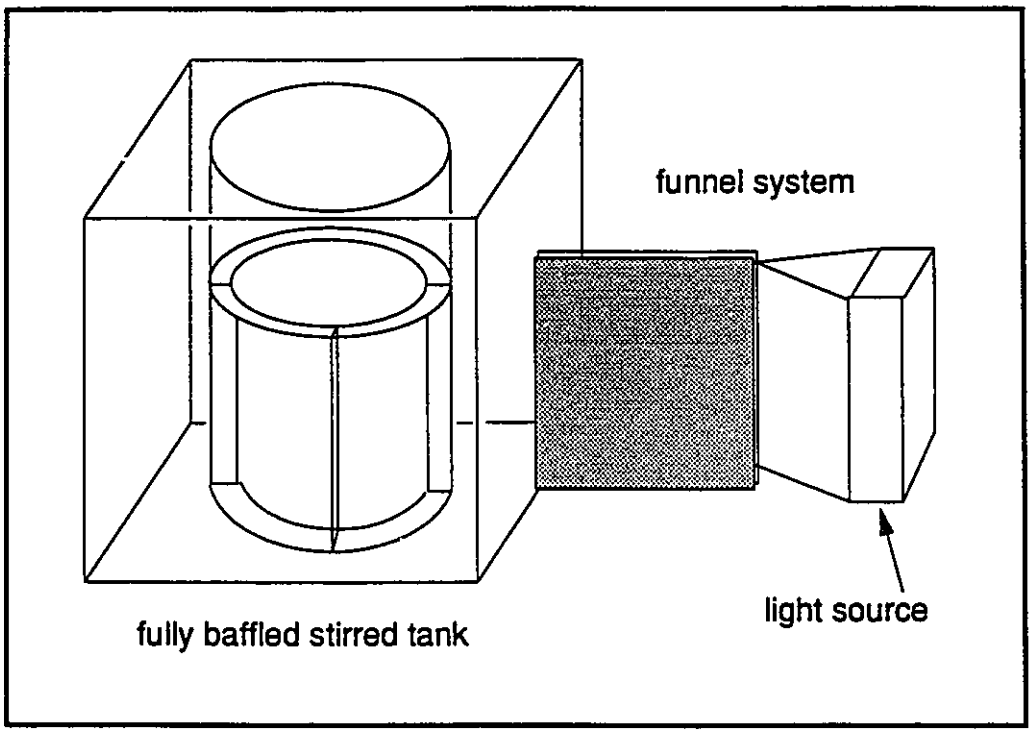

Figure 7. Funnel system used to produce light sheet for flow visualization by particle seeding.

2.2 Seeding results

The figures showing the experimental results (which are grouped together at the end of this chapter) have been traced directly from prints of the flow visualization records. In order to reproduce as much detail as possible, the individual particle paths have been reported, rather than the combined, overall trend. In order to clarify the flow patterns, arrows have been added to the experimental image; these arrows are not to be interpreted as velocity vectors. This method of reporting the flow visualization results provides more detail and is less interpretive than that of sketching the overall flow patterns.

The figures examine vertical (r-z) planes at two radii; across the axis of the tank (r=1/4 in.), and close to the tank wall (r=2.75 in.); and horizontal (r-θ) planes at various positions below the impeller. These views are combined to verify several distinct flow patterns. The results must be interpreted with some caution, for two reasons; first, particles with a large tangential (θ) velocity will spend very little time in the plane, thus tending to disappear; second, particles which remain in the plane but move very quickly relative to the other particles will leave a dimmer impression on the film. This means that in the impeller discharge stream, the particles tend to disappear. The side of the tank closest to the light source (the RHS) is better illuminated; this is apparent in most of the figures.

2.2.1 Conventional axial flow

The conventional circulation pattern for an axial flow impeller is a single circulation loop which proceeds from the bottom surface of the impeller, to the bottom of the tank, up the side walls to the top of the tank, and back to the impeller through the core of the tank (see figure 6). In our experiments this was only observed for the T/3 clearances, as shown in figures 8 and 9, and the main circulation did not extend to the top of the tank. Figure 10 gives a more detailed view of the flow in the region of the impeller, clearly showing the shape of the circulation loop. Note that on the RHS of the picture, the light sheet is just in front of a baffle, and on the LHS, it is just behind a baffle. The impeller is rotating in the clockwise direction.

The view at the wall of the tank, shown in figure 11, corroborates this result. The main circulation flow up the tank wall is strong, but there is very little flow in the top third of the tank. The asymmetry at the bottom left hand corner is due to the effect of the baffle, which is just beyond the edge of the lit area.

A third perspective on the flow is available from consideration of r-θ cross sections. At the bottom of the tank (figure 12), the impingement is vigorous (see especially the RHS impingement point), although the outward flow is somewhat more random than expected. Moving upward in the tank toward the impeller, figure 13 shows a cross section of the circulation loop. In this figure, the flow appears almost completely axisymmetric, and the outward flow is well defined. Figure 14 is at a position immediately below the impeller. Four distinct streams (or jets) appear, one for each impeller blade; note that one of these streams is much stronger than the others (bottom RHS), and appears to have borrowed from its neighbor (bottom LHS). Combination of the discharge from adjacent blades into a single "jet" was also observed by Tatterson et al. (1980).

2.2.2 Secondary circulation loop

When the impeller clearance is increased to T/2, a secondary circulation loop forms in the bottom of the tank, as shown in figures 15 and 16 (bottom RHS). The secondary circulation loop circulates in the opposite sense to the primary loop. It is not as strong as the primary loop, but it has been observed many times, is relatively stable, and has a profound impact on the whole flow field.

Concentrating on the flow in the impeller region, figures 10 and 17 reveal virtually no change in the impeller discharge flow as the clearance is increased from C=T/3 to C=T/2 for the T/3 impeller. As the off-bottom clearance is increased for the T/2 impeller, however, there is a distinct deflection in the angle of the flow discharge from the axial toward the horizontal (figures 8 and 15). This is due to the strength of the secondary circulation loop for the T/2 impeller. The LDA results

reported in chapter 4 confirm these observations.

Figure 18 shows the view at the wall, with the primary loop flowing upwards in the top two thirds of the tank, and the secondary loop flowing downwards and to the left in the bottom third of the tank. Impeller rotation in this figure is from right to left.

At the bottom of the tank, the flow patterns have completely changed from the T/3 clearance case. In figure 19, the impeller rotation is counter-clockwise, producing high velocity flow behind the baffles, which then streams *inward* at the bottom of the tank. Again, one quadrant (bottom LHS) appears stronger than the other three, with a corresponding weaker neighbor (bottom RHS).

Nouri and Whitelaw (1990) have reported very similar flow patterns for this impeller at very low Reynolds numbers (< 650) in high viscosity fluids.

2.2.3 Flow instabilities

While the circulation patterns discussed above are the dominant ones for the T/2 and T/3 clearances, the flow field is not stable, and other patterns have been observed. Figure 20 shows the T/3 impeller at a T/2 clearance. Note that the exposure time for this is 1/4 sec, making the slow flow in the top of the tank appear much stronger than in some of the earlier figures with shorter exposure times. The secondary circulation loop is not apparent in this figure; the flow in the bottom of the tank is more or less random. Figure 21 shows the T/3 impeller at a T/3 clearance with a 1/8 second exposure time. Note the weak circulation up the LHS of the tank, across the top, and back down to rejoin the main circulation. Winardi and Nagase

(1991) observe similar time varying asymmetric flows across the top of the tank for a marine propeller. They report that stable flow patterns such as this appear and disappear over a distribution of "lifetimes."

Figure 22 shows an r-θ view just below the main circulation loop for a T/2 clearance. The upper right half of the figure shows the remains of the outward radial flow, while in the lower left half of the figure, a weak vortex appears. This is some of the first reported evidence of the "precessing vortex" often mentioned by workers in this field. The precessing vortex is believed to form in the bottom of the tank, having the appearance of an inverted tornado. It precesses about the tank axis, and once again seems to appear and disappear at random. This figure is the only evidence of the precessing vortex observed in this study.

2.3 Tuft method

In order to examine the flow coming off the impeller blades, streamers of one half a strand of cotton embroidery floss in various colors were attached to the impeller blades at 2 and 3 mm intervals. The streamer length was limited by the distance between blades. The ability of this method to capture trailing vortices was tested using a Rushton turbine; it was found that two streamers, one placed on either side of the corner of the blade, are needed to capture the flow. This configuration is shown in figure 23. Flood lighting using the 1000W filament light allowed very fast exposures of 1/2000 sec, which freeze the rotation of the impeller. This method is not intended to show anything other than the existence and positioning of the trailing vortices.

2.4 Tuft results; trailing vortices

Figures 24, 25, and 26 show the bottom edge of the blade, and a trailing vortex at the tip which extends over approximately 20% of the blade. The inner part of the blade shows no vortex action; this combination of inner streaming with a tip vortex is similar to the flow coming off the wing of an airplane (Nakayama et al. (1988)). Figure 27 shows a similar, smaller vortex on the top corner of the blade.

2.5 Conclusions

The characteristics of the PBT flow field illustrated in this chapter are substantially more complex than the conventional patterns reported in classic texts, and in current literature. Instead of a single circulation loop which extends over the whole tank for all geometries, the primary circulation loop reaches the bottom of the tank only for the T/3 clearance; and is accompanied by a secondary circulation loop when the clearance is increased to T/2. This change in circulation pattern affects the angle of impeller discharge for the strong circulation flows induced by the T/2 impeller, deflecting the discharge angle toward the horizontal. For the T/3 impeller, the secondary circulation loop is not as strong, and does not affect the impeller discharge. The top third of the tank exhibits various weak, unstable flow patterns. Instabilities have also been observed in the lower portion of the tank, including the often cited "precessing vortex"; the circulation loops, however, can be considered dominant.

A streamer method was developed to reveal the existence of trailing vortices for a single impeller blade. Consideration of the discharge flow using this method revealed a streaming flow over the inner 80% of the blade, with a trailing vortex extending over the outer 20%.

The methods used in this chapter should be considered qualitative at best, and must be compared with results from other methods before final conclusions about the general trends are drawn. Quantitative results obtained from laser Doppler anemometry (to be discussed in chapters 4 and 7) will verify the initial insights gained from these illustrations.

2.6 Figures

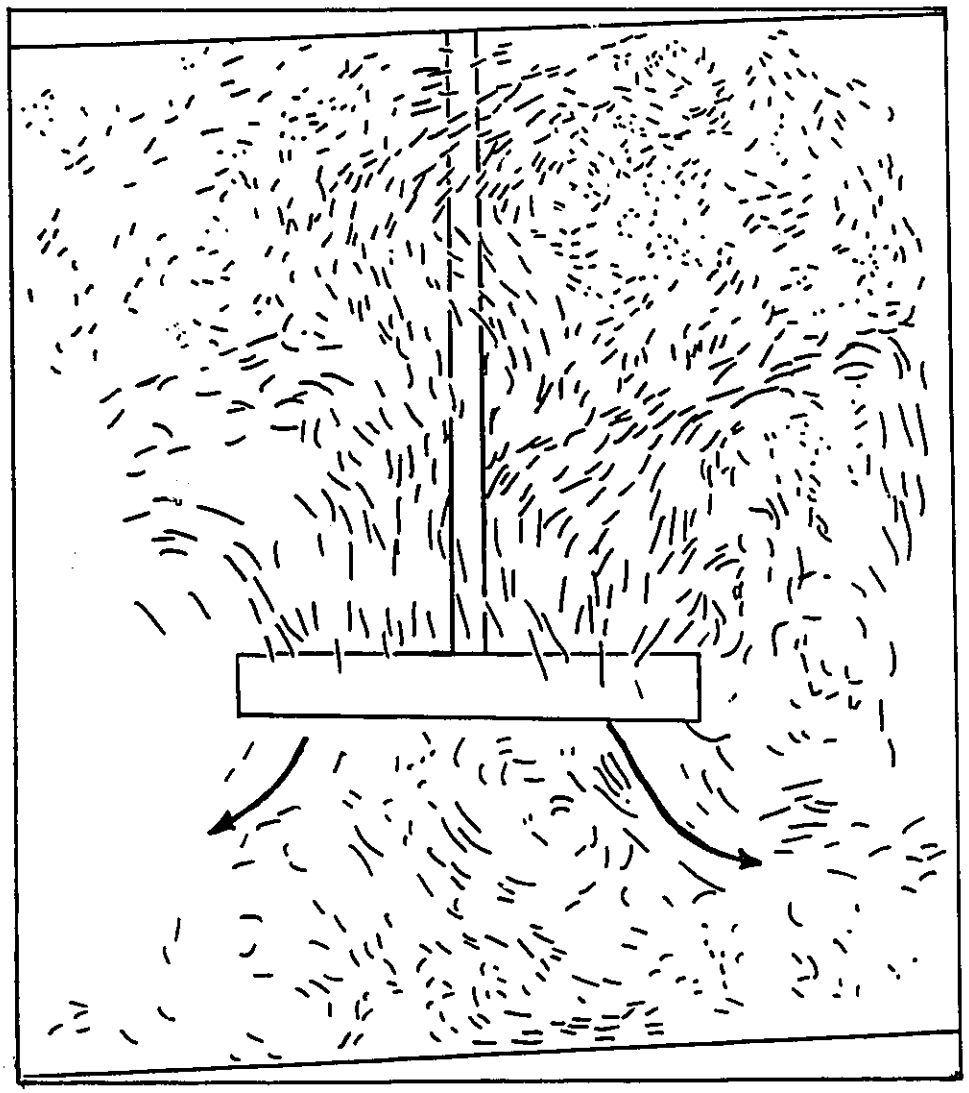

Figure 8. Classic circulation pattern; D=T/2 impeller at C=T/3.
Radius of 1/4in, f2, 1/60 sec.

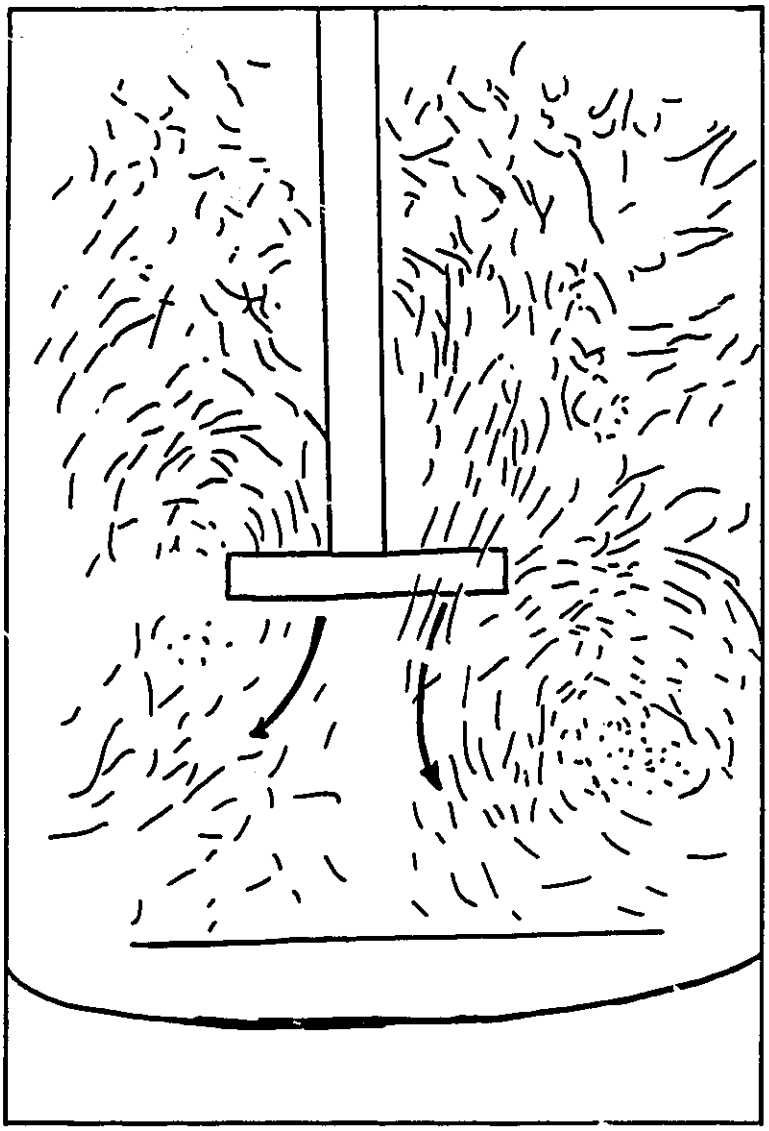

Figure 9. Classic circulation pattern; D=T/3 impeller at C=T/3. Radius of 1/4in, f2.8, 1/2 sec.

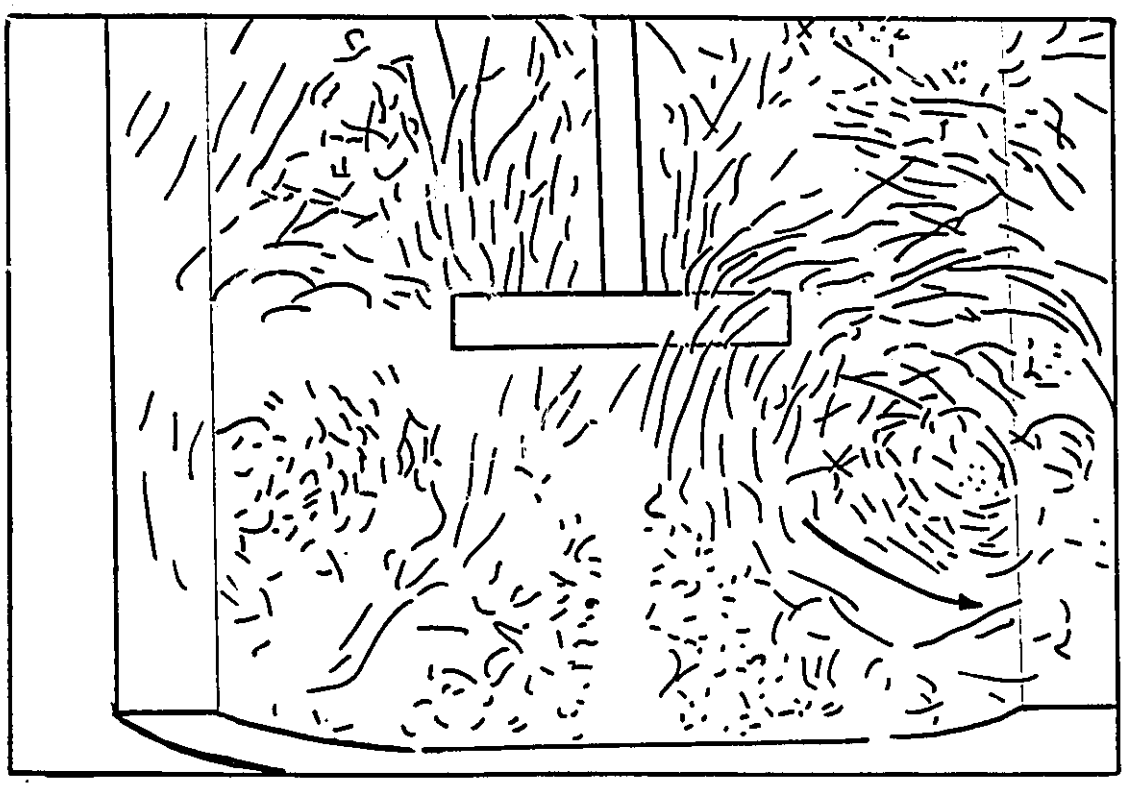

Figure 10. Close up of impeller region for the classic circulation pattern; D=T/3 impeller at C=T/3.
Radius of 1/4in, f2.8, 1/2 sec.

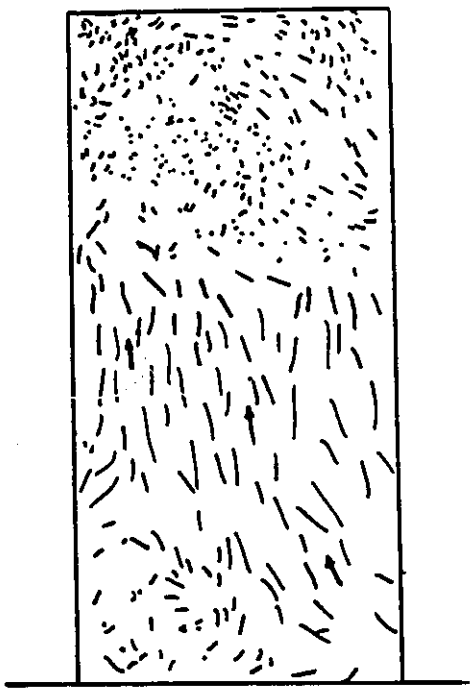

Figure 11. Flow at the tank wall for the classic circulation pattern;
D=T/2 impeller at C=T/3.
Radius of 2.75 in, f2, 1/60 sec.

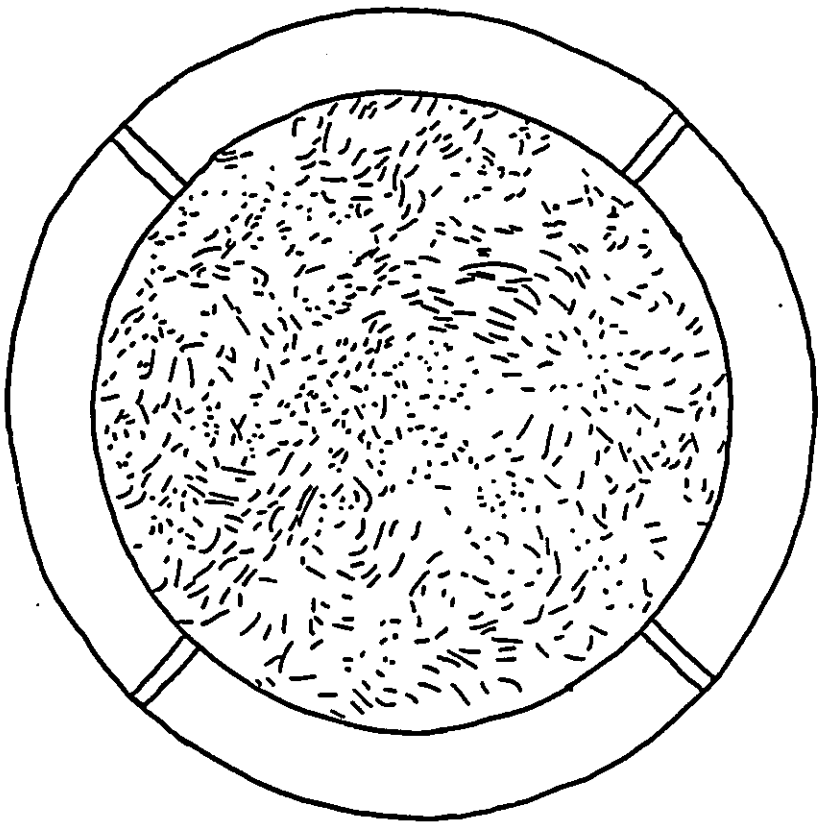

Figure 12. Impingement at the bottom of the tank for the classic circulation pattern; D=T/2 impeller at C=T/3.
N=480rpm, f2, 1/60 sec.

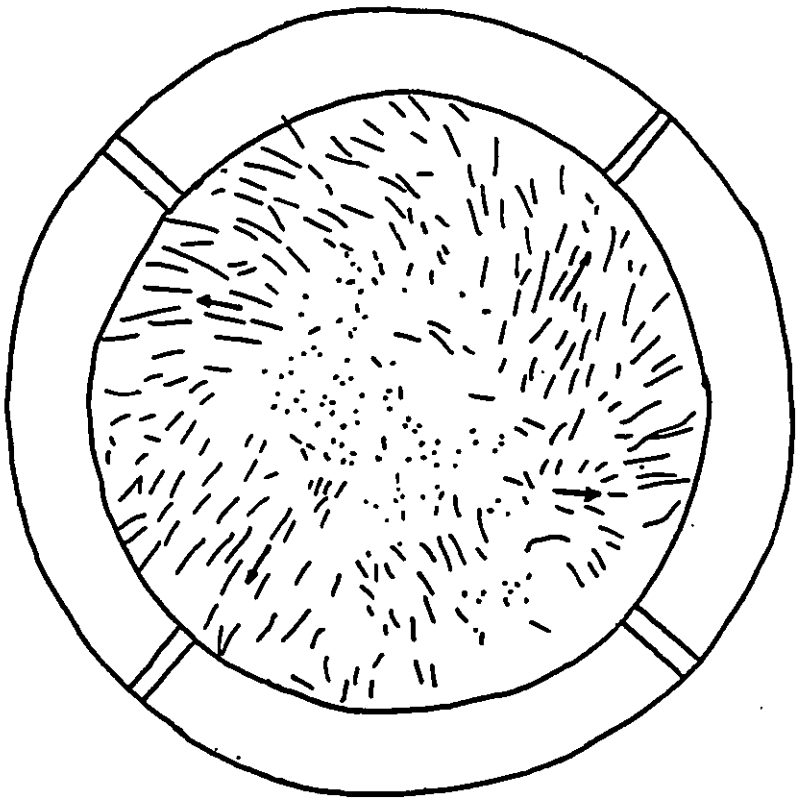

Figure 13. Cross section of the primary circulation loop; D=T/2 impeller at C=T/2. Light positioned at 2/3 of the way from the bottom to the impeller. N=480rpm, f2, 1/60 sec.

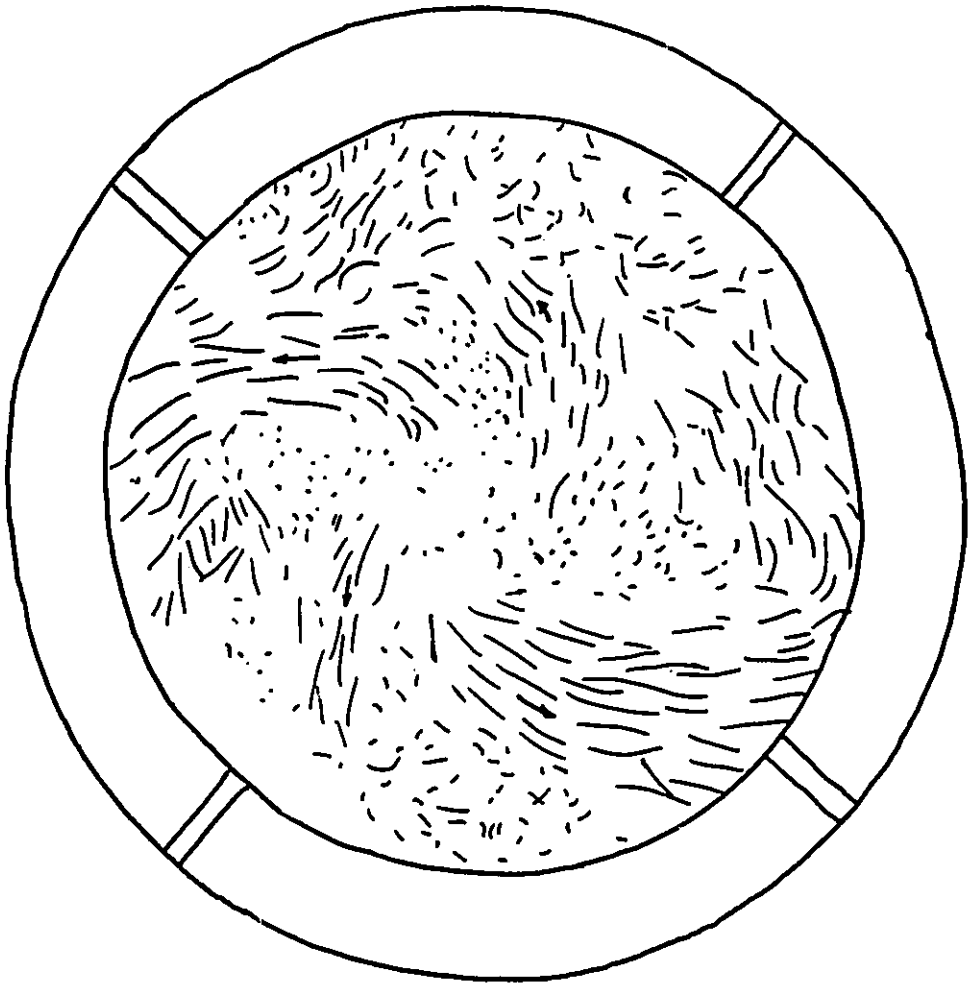

Figure 14. Flow just below the impeller blades; D=T/2 impeller at C=T/3. N=480rpm, f2, 1/60 sec.

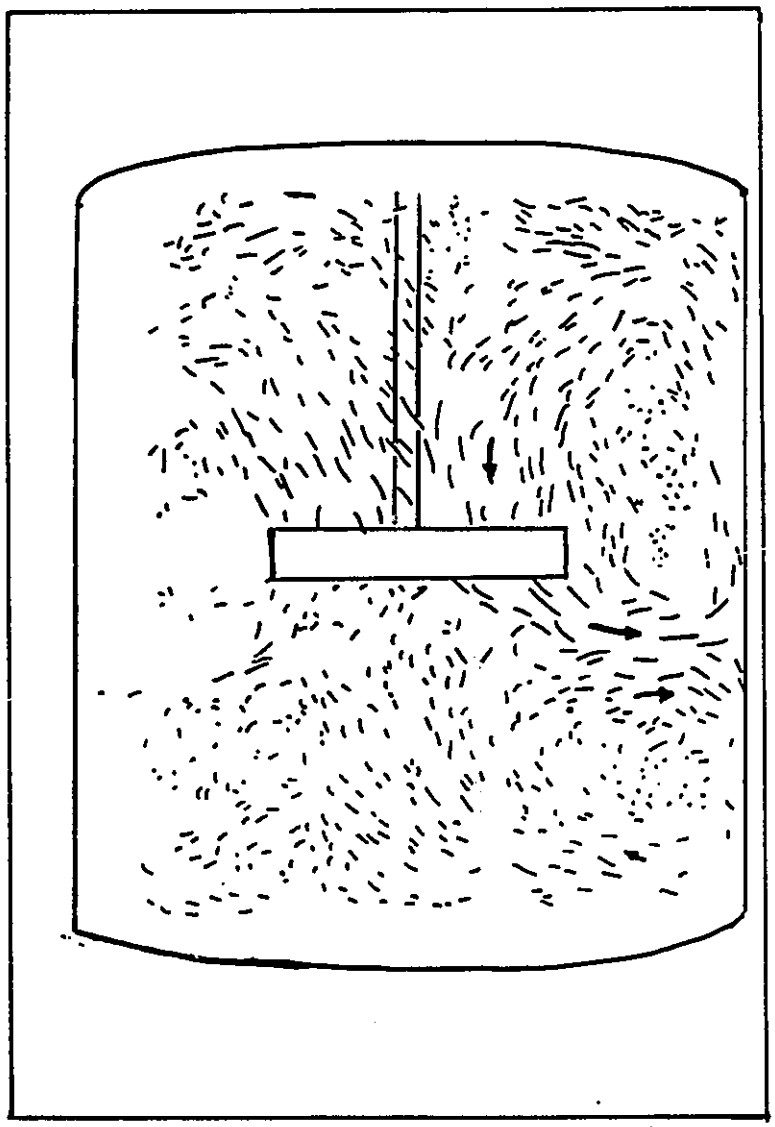

Figure 15. Axial flow showing secondary circulation loop; D=T/2 impeller at C=T/2. Radius of 1/4in., f2, 1/60 sec.

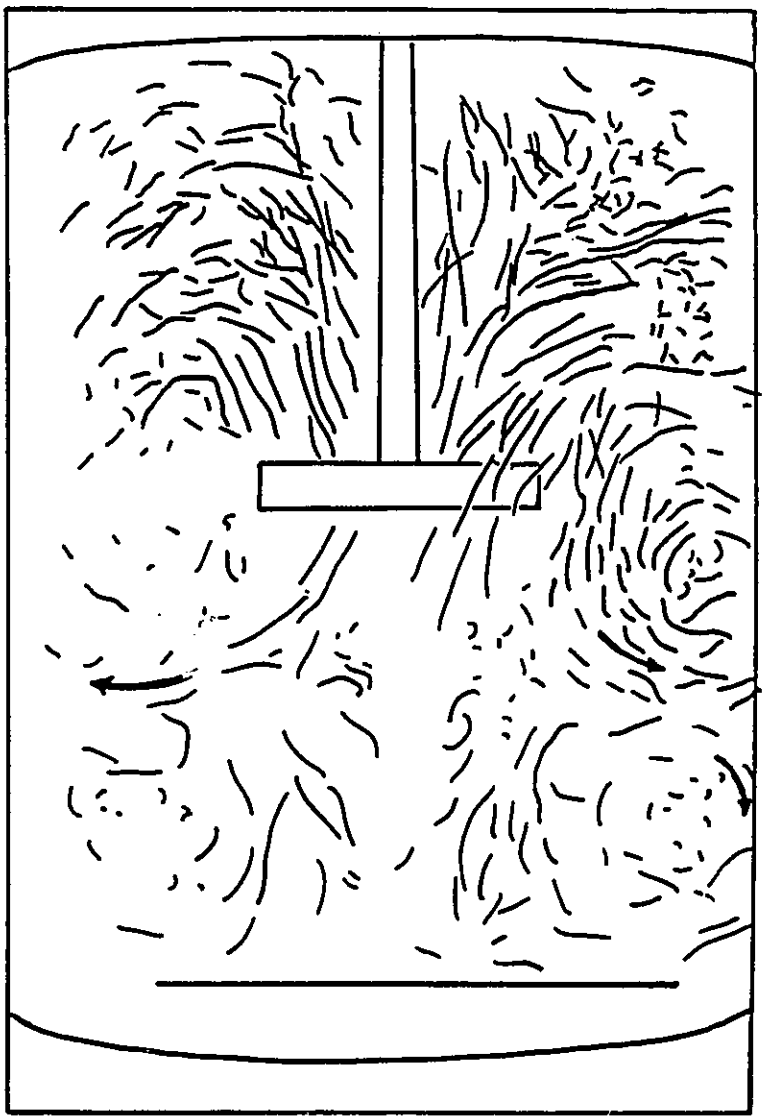

Figure 16. Axial flow showing secondary circulation loop; D=T/3 impeller at C=T/2. f2.8, 1/2 sec.

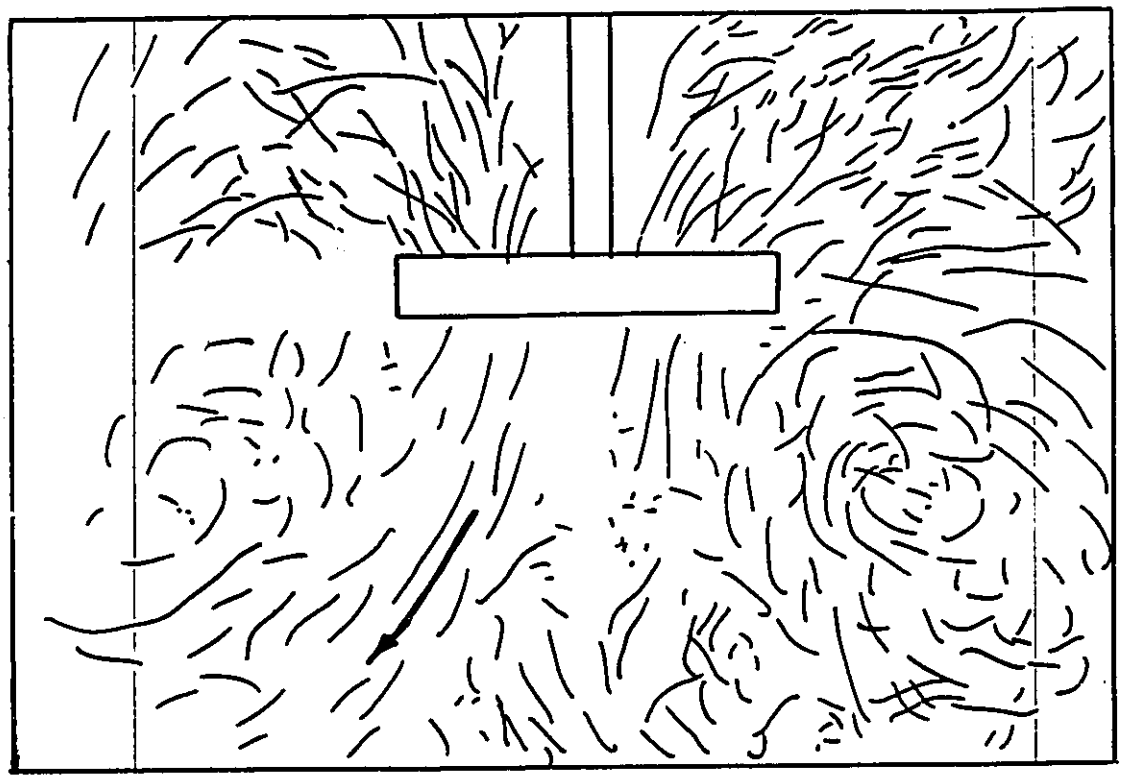

Figure 17. Close up of impeller region for axial flow with a secondary circulation loop below the region shown; D=T/3 impeller at C=T/2.
Radius of 1/4in, f2.8, 1/2 sec.

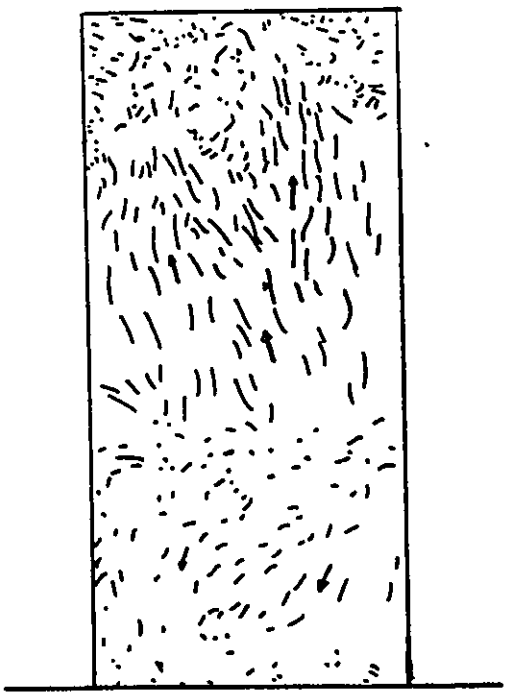

Figure 18. View at the wall showing secondary circulation loop; D=T/2 impeller at C=T/2. f2, 1/60 sec.

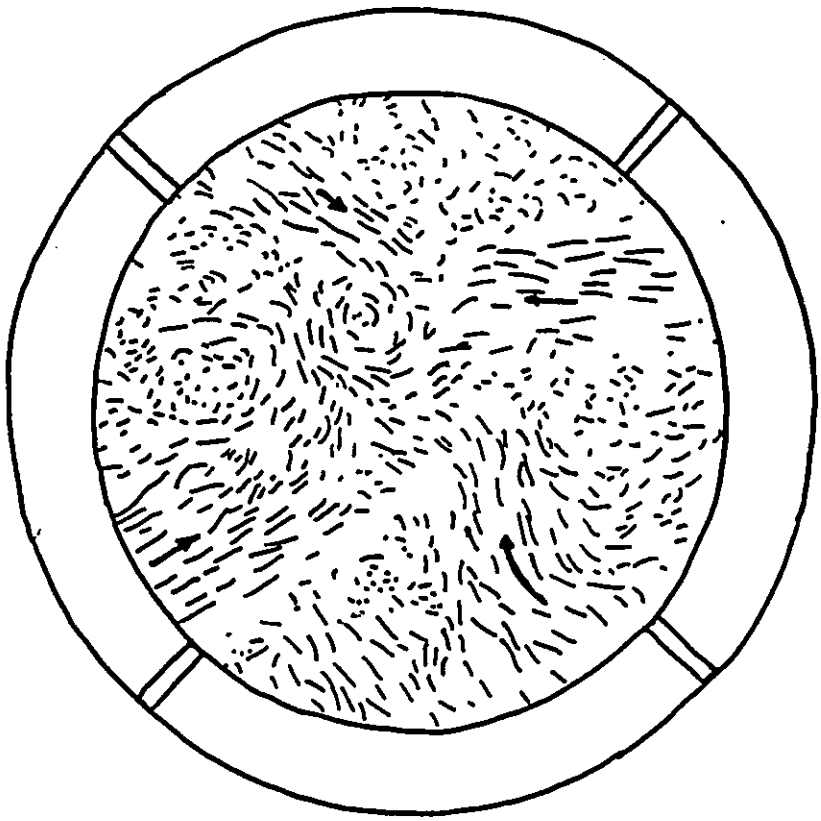

Figure 19. Flow at the bottom of the tank with secondary circulation loop; D=T/2 impeller at C=T/2. N=480rpm, f2, 1/60 sec.

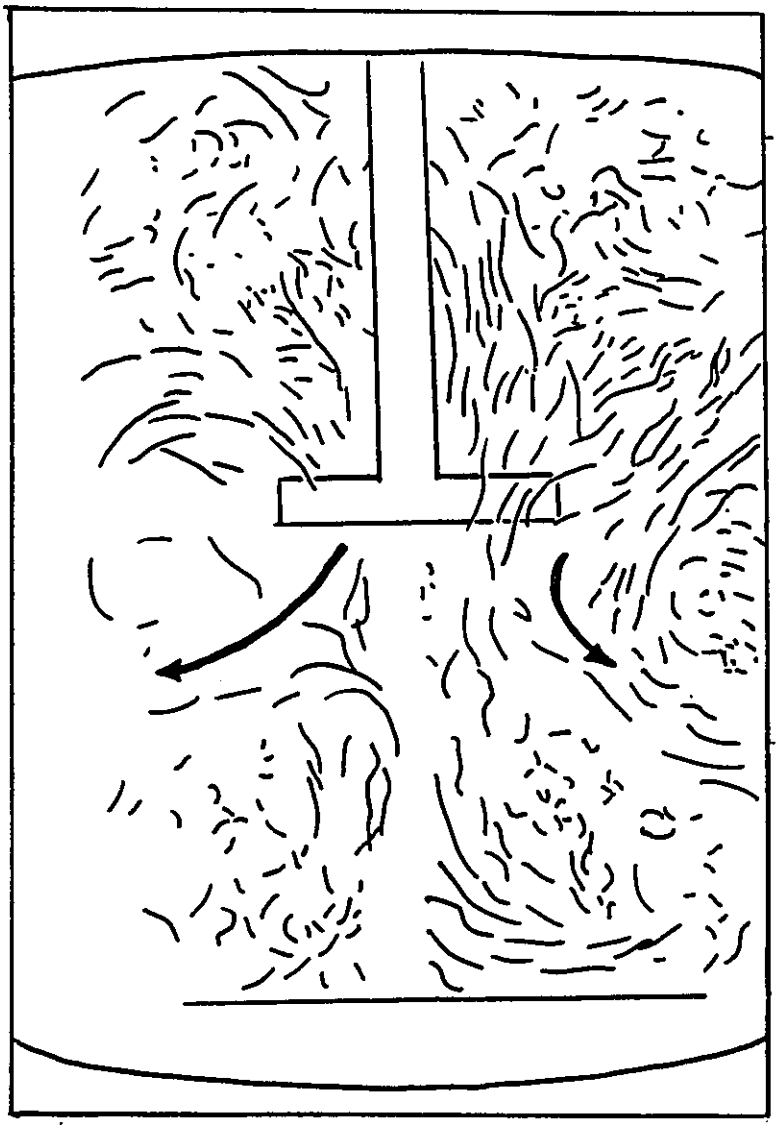

Figure 20. Unstable pattern #1, random flow in bottom portion;
D=T/3 impeller at C=T/2.
Radius of 1/4in, f2.8, 1/4 sec.

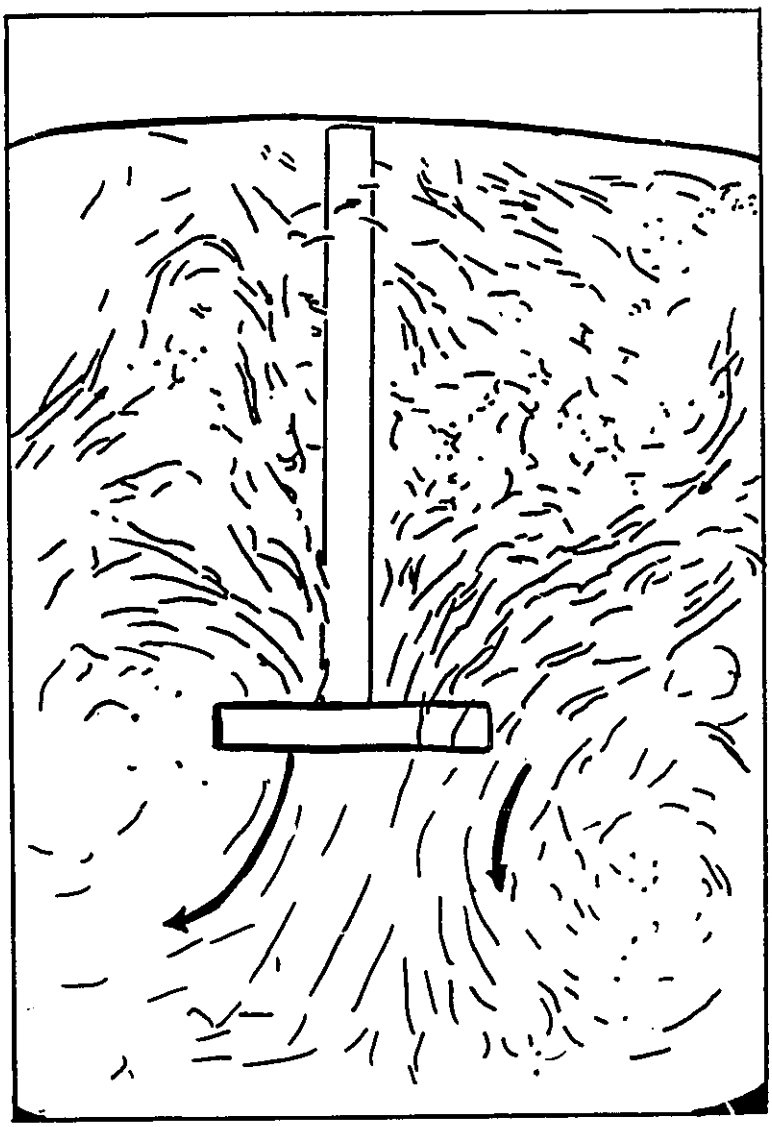

Figure 21. Unstable pattern #2, flow across the top of the tank;
D=T/3 impeller at C=T/3.
Radius of 1/4in, f2.8, 1/8 sec.

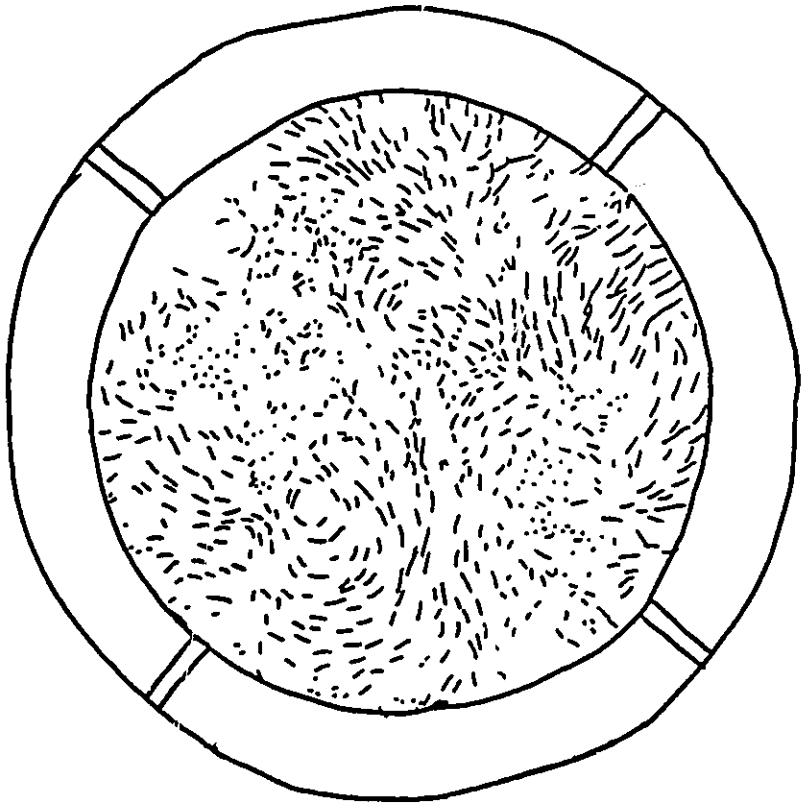

Figure 22. Unstable pattern #3, precessing vortex; D=T/2 impeller at C=T/2. Halfway between impeller and tank bottom, N=480rpm, f2, 1/60 sec.

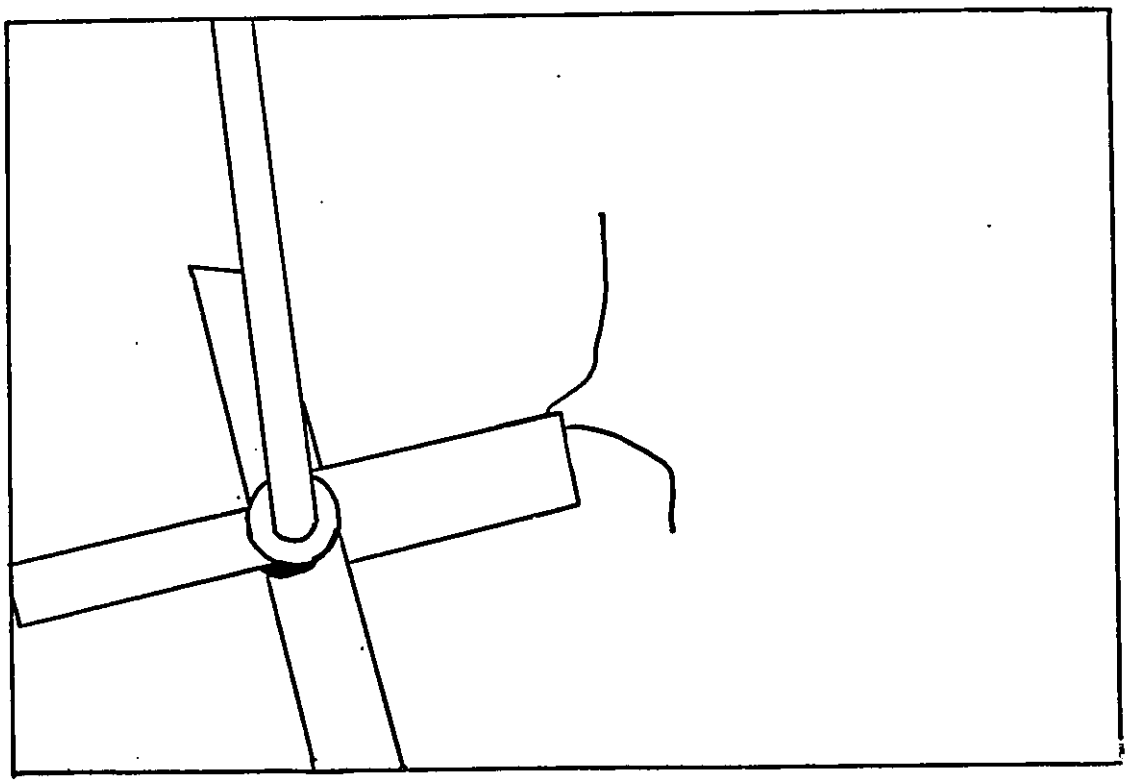

Figure 23. Tuft method showing the configuration needed to capture the trailing vortices.
D=T/2 impeller at C=T/4.
N=0 rpm, f4, 1/2000 sec.

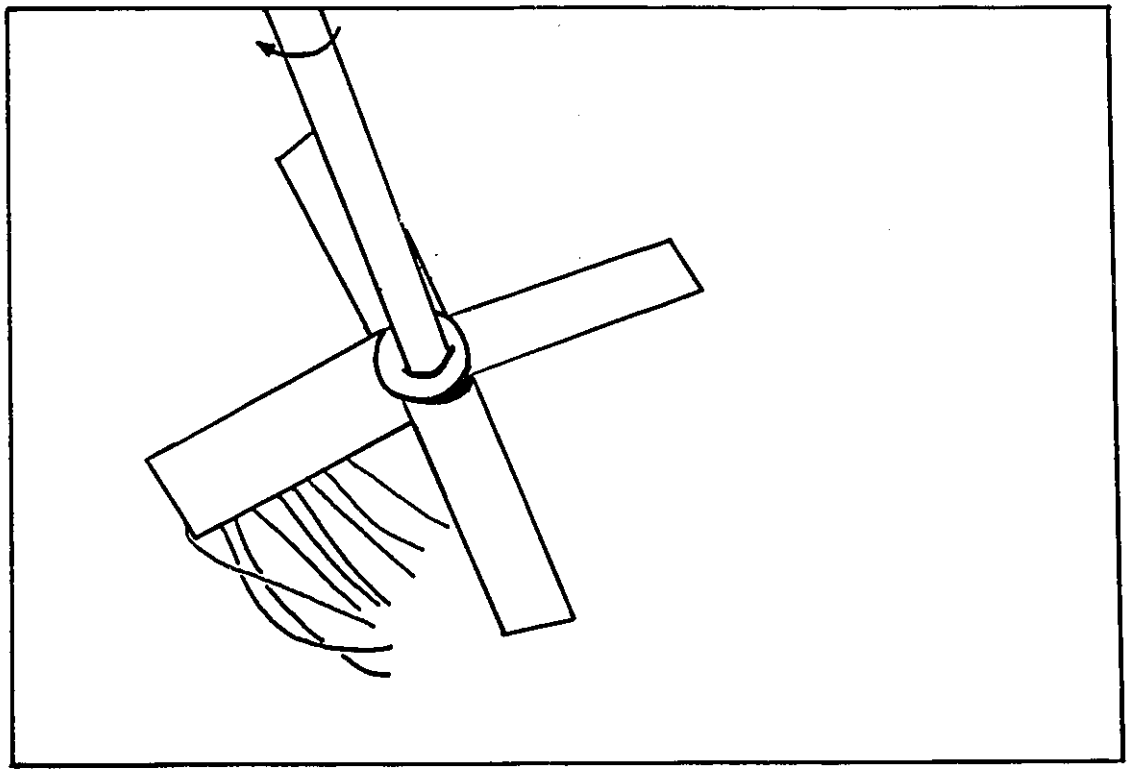

Figure 24. Tuft method showing lower tip vortex and streaming; #1.
D=T/2 impeller at C=T/4.
N=268 rpm, f4, 1/2000 sec.

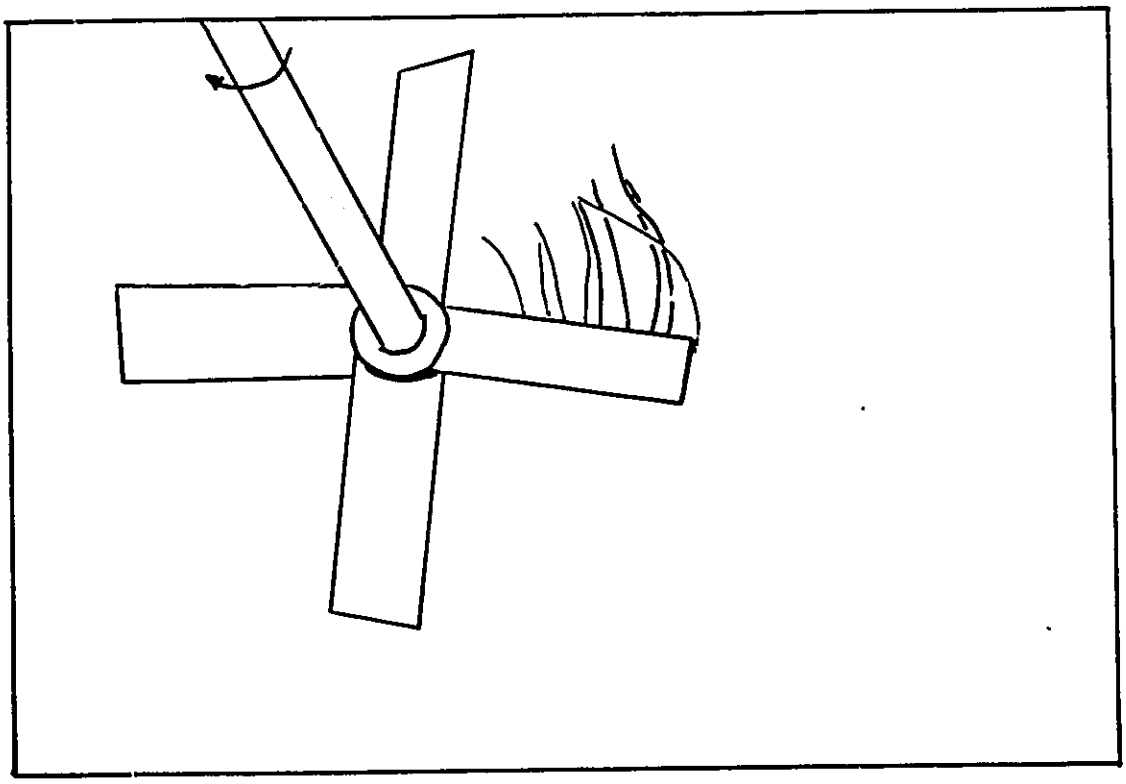

Figure 25. Tuft method showing lower tip vortex and streaming; #2.
D=T/2 impeller at C=T/4.
N=268 rpm, f5.6, 1/2000 sec.

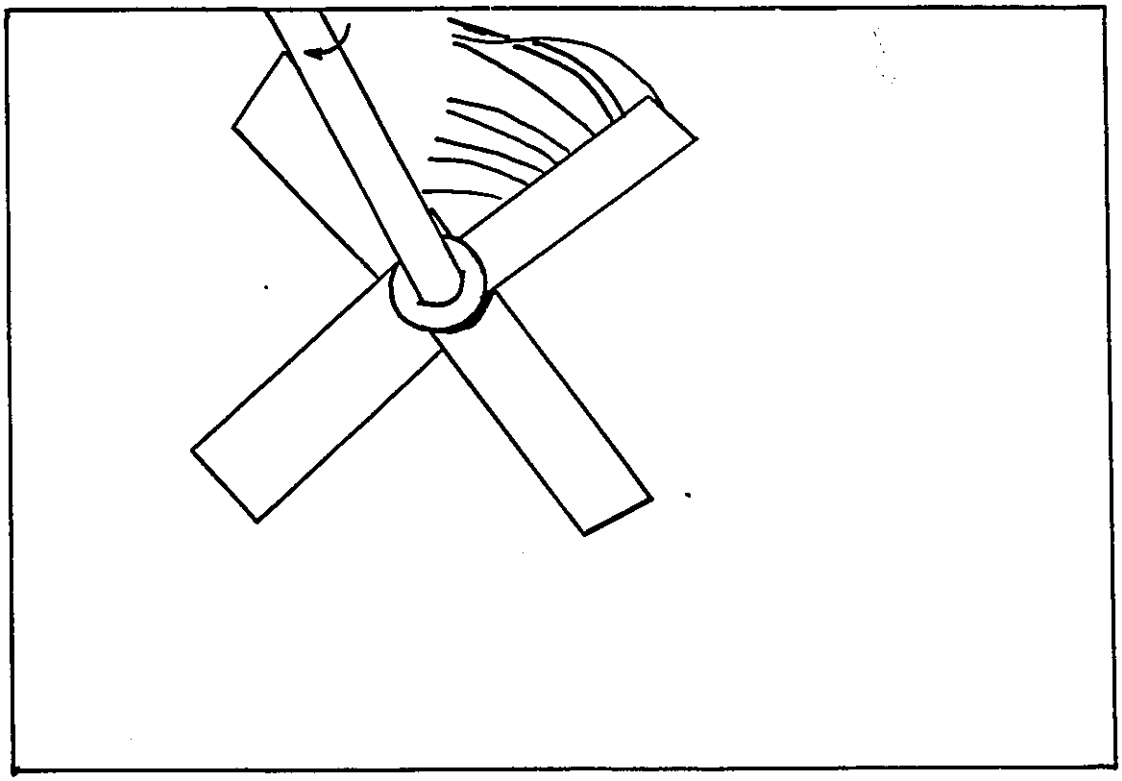

Figure 26. Tuft method showing lower tip vortex and streaming; #3.
D=T/2 impeller at C=T/4.
N=268 rpm, f5.6, 1/2000 sec.

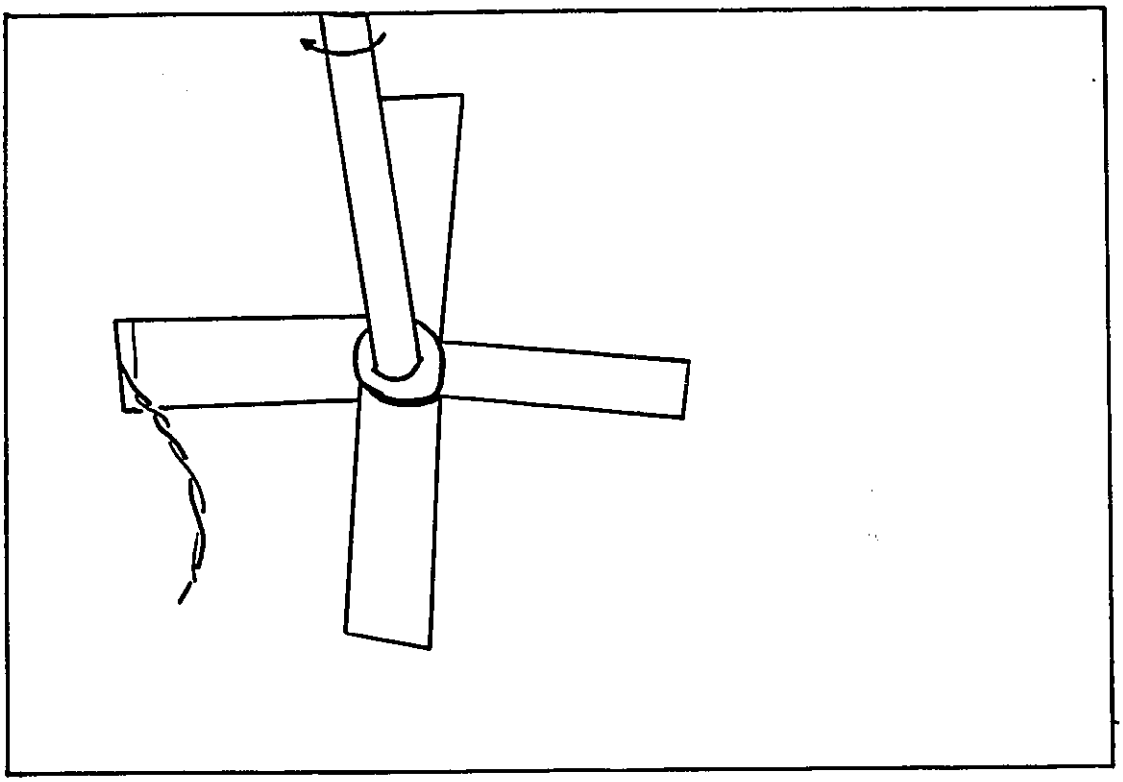

Figure 27. Tuft method showing upper tip vortex.
D=T/2 impeller at C=T/4.
N=268 rpm, f4, 1/1000 sec.

2.7 References

Ali, A. M., H. H. S. Yuan, D. S. Dickey, G. B. Tatterson, "Liquid dispersion mechanisms in stirred tanks: Part 1, pitched blade turbine," Chem. Eng. Comm., v. 10, pp. 205-213, 1981.

Buchave, P., W. K. George, and J. L. Lumley, "The measurement of turbulence with the laser Doppler anemometer," Ann. Rev. Fluid. Mech., v. 11, pp. 443-503, 1979.

Merzkirch, Wolfgang, Flow Visualization, 2nd ed., Academic Press, Toronto, 1987.

Nakayama, Y., W. A. Woods and D. G. Clarke, eds., Visualized Flow: fluid motion in basic and engineering situations revealed by flow visualization, Pergamon Press, Toronto, 1988.

Nouri, J. M. and J. H. Whitelaw, "Flow characteristics of stirred reactors with Newtonian and non-Newtonian fluids," AIChE Journal, v. 36, pp. 627-629, 1990.

Oldshue, James Y., Fluid Mixing Technology, McGraw Hill, New York, 1983.

Rewatkar, V. B., and J. B. Joshi, "Effect of impeller design on liquid phase mixing in mechanically agitated reactors," Chem. Eng. Comm., v. 102, pp. 1-33, 1991.

Shen, Z. J., and M. H. I. Baird, "The delta mixing - some hydrodynamic studies," Chem. Eng. Res. Des., v. 69, pg. 143, 1991.

Tatterson, G. B., H. S. Yuan, and R. S. Brodkey, "Stereoscopic visualization of the flows for pitched blade turbines," Chem. Eng. Sci., v. 35, pp. 1369-1375, 1980.

Uhl, V. W., and F. B. Gray, eds., Mixing, Theory and Practice, vol. 3, Academic Press Inc., Toronto, 1986.

Winardi, S., S. Nakao, and Y. Nagase, "Pattern recognition in flow visualization around a paddle impeller," J. Chem. Eng. Japan, v. 21, pg. 503, 1988.

Winardi, S. and Y. Nagase, "Unstable phenomenon of flow in a mixing vessel with a marine propeller," J. Chem. Eng. Japan, v. 24, pp 243-249, 1991.

Chapter 3. LDA Theory, Apparatus, and Verification

Chapter 2 examined the qualitative aspects of the flow field as obtained using two flow visualization techniques. Laser Doppler anemometry (LDA) is the other major experimental technique which was applied to this sytem. In this chapter, the theoretical basis of LDA is presented, the optical apparatus and automated data collection systems described, and the verification test results are reported. Since LDA depends on the presence of seeding particles to measure the velocity, the results from several different combinations of fluid and seeding particles were examined. The seeding method used had a measureable impact on the results, although there was not enough information available to assess the cause of this variation. The effect of sampling frequency on the measured velocities was examined over the range from 0.1 to 5kHz. It was found that the valid sampling frequency is limited, not by the signal quality, but by the size of the measuring volume. This limit is due to the presence of Doppler ambiguity noise in the signal. An expression for the limiting frequency was assessed and verified. Given an appropriate choice of seeding particles and sampling frequency, the accuracy of the results was verified in four ways; material balances around the impeller, repeats of experiments over several months, comparison with reported results, and comparison with the results of the theoretical swirling radial jet model for the Rushton turbine as proposed in chapter 6. All of the results indicate that LDA gives stable, consistent results, and can be used to accurately measure the mean and fluctuating velocity components for this complex flow field.

3.1 Theory, apparatus, and data collection

Before proceeding to the verification experiments for the flow field to be examined, the basic theory on which LDA is based is summarized. The explanation is based on a one component differential Doppler instrument with a Bragg cell frequency shifter, as used in this work. Readers interested in the reference beam technique, or in other techniques, should consult the general references (Drain (1980), Durst et al. (1976)).

3.1.1 The theory behind laser Doppler anemometry

Laser Doppler anemometry, also known as laser Doppler velocimetry, is an optical velocity measurement technique. Discovered by Yeh and Cummins in 1964 (Drain, 1980), its key advantages over hot wire anemometry are the non-intrusive nature of the probe, the virtually instantaneous response to flow fluctuations, and the linear relationship between the measurement and the fluid velocity. The basic principle of LDA rests on two things: the properties of laser light, and the existence of seeding particles.

The execution of LDA requires a highly focussed beam of light, which has properties similar to those of a plane wave. Laser[1] light has three properties which allow it to meet these requirements. First, it is highly monochromatic, emitting over a very narrow wavelength band. Second, it is coherent, with light waves proceeding in an ordered fashion, rather than randomly. Third, it is highly collimated, producing a beam with a very small divergence angle. In principle, it is possible to focus a

1 light amplification by stimulated emission of radiation

laser beam to a point having the diameter of its wavelength (EChemTech, 1981). In LDA, the focal diameter is larger than this, and is hereafter referred to as the beam waist.

To construct the LDA measuring volume, two beams of linearly polarized laser light are crossed at the beam waists, as shown in figure 28. Where the beams cross, the combined light will have a maximum intensity when the maximum intensities of the light waves (represented by the black lines) coincide. When the minimum intensities of the light waves coincide, the combined intensity will be at a minimum. The aggregate effect of these combinations within the measuring volume is the production of apparent "fringes" of light with a known spacing. The orientation of these fringes is exactly parallel to the bisector of the angle between the two incoming laser beams.

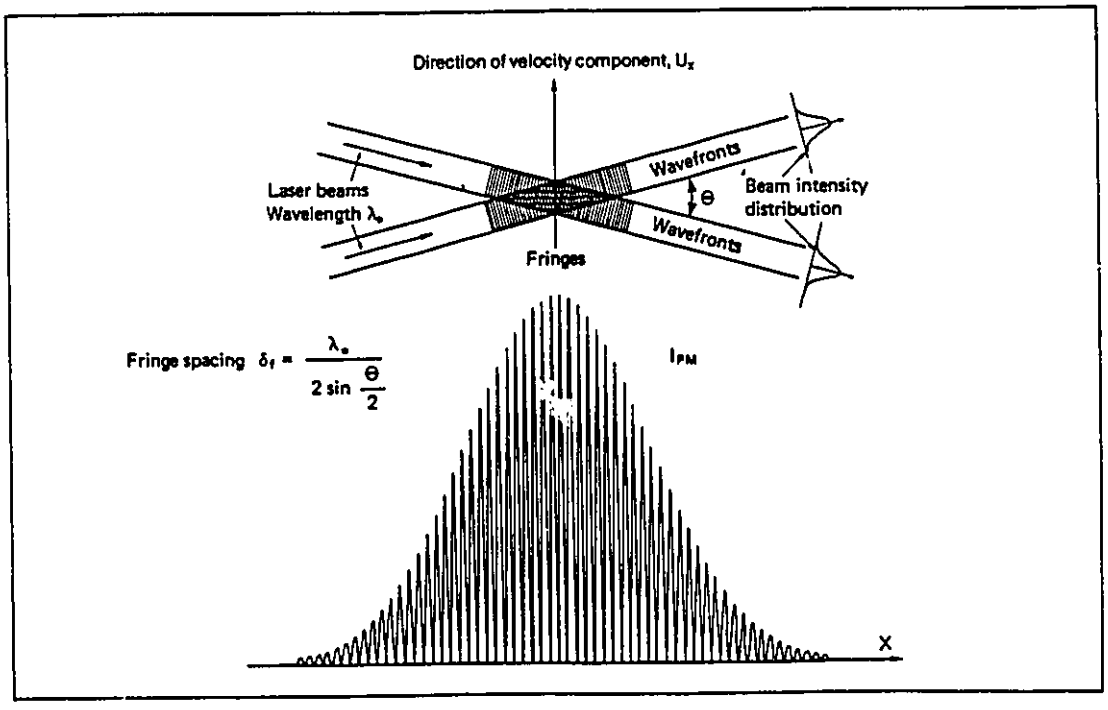

Figure 28. : LDA measuring volume as envisioned by the fringe interpretation. (from George, 1988)

From these fringes, which are stationary in the fluid, the fluid velocity is to be determined. Assume, for a moment, that there exist in the fluid seeding particles which move with exactly the velocity of the fluid. These particles scatter light. When the seeding particles cross the measuring volume described above, they scatter laser light with a modulated intensity corresponding to their passage through the fringes. The frequency of this modulation can be directly related to the component of fluid velocity perpendicular to the fringes, and in the plane of the two laser beams, as follows:

fringe spacing
$$\Delta y = \frac{\lambda_o}{2\sin\theta/2} \tag{5}$$

Doppler frequency
$$f_D = \frac{V_{particle}}{\Delta y} \tag{6}$$

This is referred to as the fringe interpretation of LDA. It is exactly correct for the majority of practical purposes; and is a useful way of thinking about the application of the instrument to a flow. It must be noted that this is not a completely rigorous approach; the scattering wavenumber vector derivation (George, 1988), or others given by Drain (1980) are more rigorously correct.

The boundaries of the measuring volume, or fringes, are defined using the Gaussian distribution of light intensity within a laser beam. The edge of the measuring volume is defined to be the point where the combined beams have decayed to $1/e^2$ of their maximum intensity. This definition results in a measuring volume which is roughly ellipsoidal in shape (1.07mm long with a diameter of 0.12mm for the lens combination used in this work).

If a turbulent, or time varying flow field is to be examined, the velocity will periodically be negative. Since the Doppler frequency is independent of the direction of flow for stationary fringes, some means of directional discrimination must be devised. This is accomplished by shifting the frequency of one of the beams, leaving the wavelength unaffected. This causes the fringes to move with a velocity proportional to the frequency shift. If the frequency shift is chosen so that it exceeds the maximum expected velocity, then directional discrimination of all signals will be possible. Frequency shifting also eliminates the "dead-angle" phenomenon described by George (1988). The desired frequency shift is accomplished using a Bragg cell with a 40MHz shift, and then down mixing to the desired frequency shift of the order of 1MHz.

This discussion has focussed on a single component differential mode LDA. The instrument used for this work was a single component helium-neon (HeNe) LDA. By using a plexiglass tank which allows optical access for the laser beams, ensuring the correct seeding of the fluid, and applying appropriate optics, signal processing, and data analysis, LDA was used to obtain mean and fluctuating velocity components in three directions, and Reynolds stresses. From the experimental records thus obtained, resultant velocities, turbulence kinetic energy levels, turbulence spectra, auto-correlation functions, and the rate of dissipation of turbulence kinetic energy were computed.

3.1.2 Optics

The optical train begins at the 25 mW HeNe laser, and ends at the outgoing signal from the photomultiplier tube. The laser emits a single beam of wavelength

632.8 nm, which is passed through a beam splitter to provide the two necessary beams. These beams are converted from circular to linear polarization; so that all light waves are oriented at the same angle. One of the beams is frequency shifted using a Bragg cell and the Dantec 55N10 frequency shifter, which can provide a frequency shift of up to 40 MHz. The beams then pass through the modular focussing optics. These must be adjusted so that the beams cross at the beam waists before attempting any measurements. Once the beams are correctly aligned, this section can be rotated to set the angle between the plane of the beams and the horizontal, depending on the component of velocity to be measured. The last lens on this train is the focussing lens, of focal length 310 mm. The beams then pass through the model, crossing at the measurement position, and out the other side to disperse. The photomultiplier tube is equipped with a lens of focal length 300 mm, and is focussed on the measuring volume, thus collecting the scattered light signal of interest. The signal from the photomultiplier tube is passed on to the counter processor.

The frequency shift imposed by the Bragg cell must be chosen so that it exceeds the maximum negative velocity. It should not be excessive, however, or quantization errors may result (George (1988)). The minimum frequency shift for this flow is 500kHz. An increase in the validated data rate was observed from 500 to 900kHz, and for some positions, a further increase was observed from 900 to 2000kHz. Increases beyond 2000kHz produced no further improvement. The levelling off of the data rate indicates that the dead angles have been eliminated; the frequency shift required agrees with the minimum shift recommended by George (1988) for this purpose. Based on this information, the frequency shift was set at 900 kHz for most of the experiments, and was increased to 2000 kHz where nec-

essary. A shift of 900 kHz corresponds to a fringe velocity of 5.06 m/s, two and a half times the maximum tip speed, or approximately five times the maximum velocity.

The three principal components of velocity, and the Reynolds stresses, are obtained by varying the optical orientations. Orientations for the determination of the radial, axial, and angular components of velocity in cylindrical coordinates are shown in figure 29. Recall that the measured component of velocity is in the plane of the laser beams, perpendicular to the beam angle bisector.

The Reynolds stresses are determined by rotation as given by Melling and Whitelaw (1976). This method determines the Reynolds stresses from a decomposition of two off-axis measurements which differ by 90°. These rotated measurements contain two components of velocity, and thus portions of the Reynolds stresses as follows:

$$f_D^+ = K(\overline{U_1}\cos\alpha + \overline{U_3}\sin\alpha)$$
$$f_D^- = K(\overline{U_1}\sin\alpha - \overline{U_3}\cos\alpha) \qquad (7)$$

where α is the angle of rotation (from the principle component axis) in the + direction, $\alpha - 90°$ is the angle of rotation in the - direction, and K is the frequency to velocity conversion factor ($K = 2\sin\phi/\lambda$). The RMS frequencies can be expressed

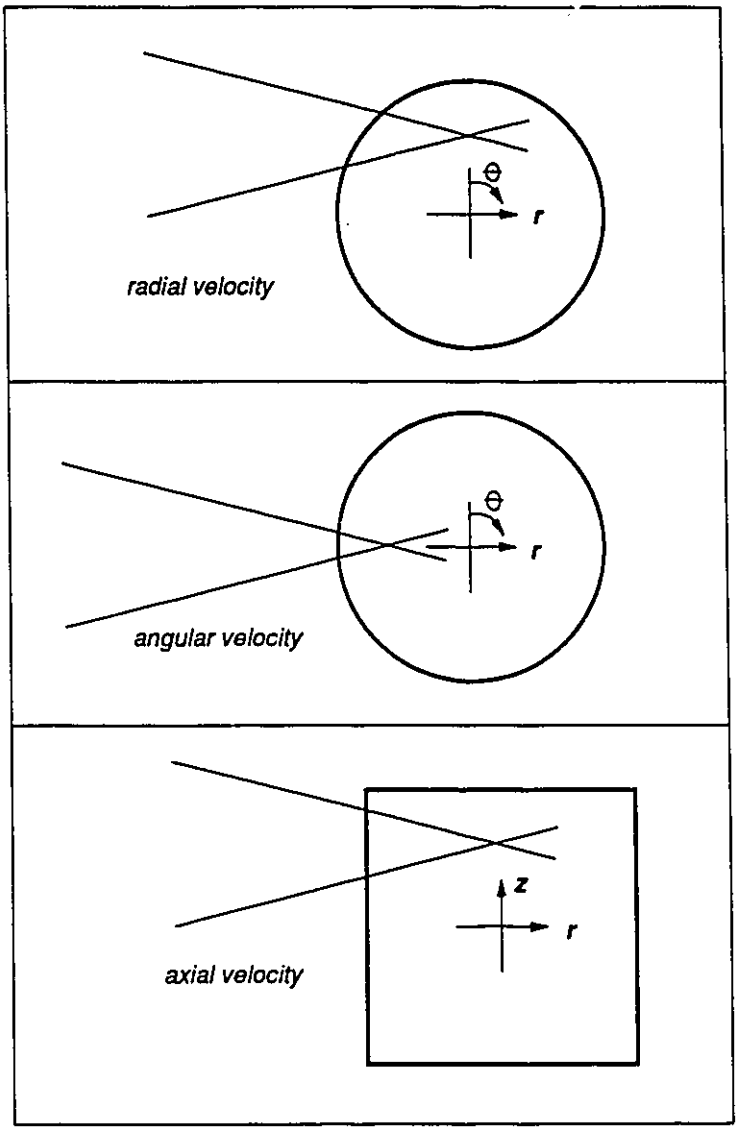

Figure 29. Optical orientations for the determination of three components of velocity as defined in cylindrical coordinates.

$$\overline{f_D^{+'2}} = K^2(\overline{u_1'^2}\cos^2\alpha + 2\overline{u_1'u_3'}\sin\alpha\cos\alpha + \overline{u_3'^2}\sin^2\alpha)$$
$$\overline{f_D^{-'2}} = K^2(\overline{u_1'^2}\sin^2\alpha - 2\overline{u_1'u_3'}\sin\alpha\cos\alpha + \overline{u_3'^2}\cos^2\alpha) \quad (8)$$

giving the Reynolds stress by difference, which simplifies to

$$\overline{u_1' u_3'} = \frac{\overline{f_D^{+2}} - \overline{f_D^{-2}}}{2K^2} = \frac{RMS^{+2} - RMS^{-2}}{2} \qquad (9)$$

for $\alpha = 45°$. This method is also commonly referred to as Logan's method.

There are two experimental details worthy of note in the optical train. The first is the importance of correctly aligning the laser beams. If this is not accomplished correctly, the beams will not cross at the beam waists, and the fringes will not be parallel. This results in a fringe spacing which varies depending on the position in the measuring volume as illustrated in figure 30, and will result in inaccurate determination of the velocity.

The second is the effect of focussing the photomultiplier exactly on the measuring volume. When this is done correctly, the edges of the laser beams will appear sharp, the crossing point will appear as a point, and the center of the bullseye in the viewfinder will coincide exactly with this point. The overall appearance is one of a bullseye (the viewfinder), superimposed on an angular hourglass (the beams and measuring volume). Final adjustment normally requires use of an oscilloscope to monitor signal quality. This stage should not be ignored, as it can result in improvements of up to a factor of three in signal strength. The experimental procedure follows.

Focussing procedure:

1) Locate the measuring volume in the viewfinder.

2) Move the photomultiplier forward and backward to obtain a sharp image.

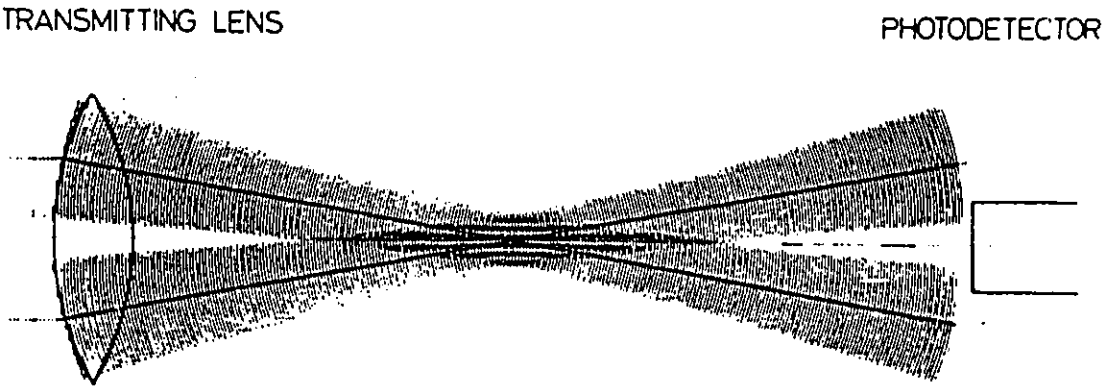

a) crossing of the beams at the beam waist

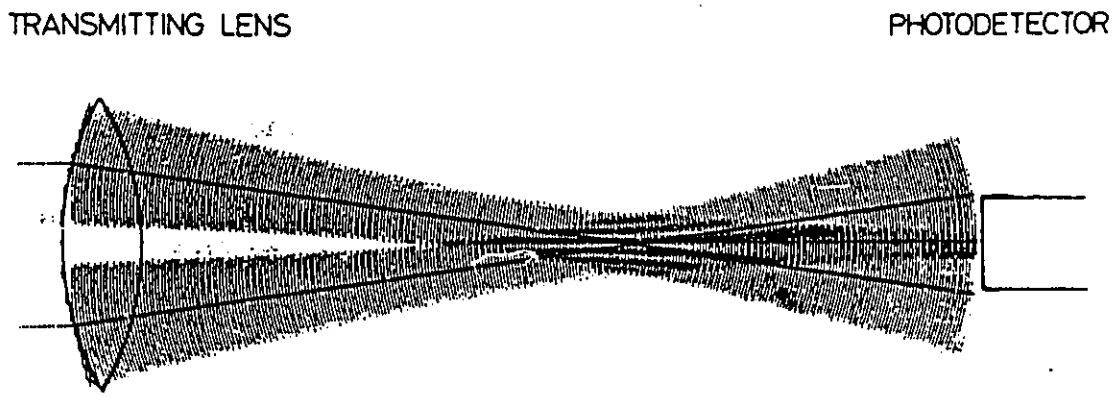

b) crossing of beams after the beam waist

Figure 30. The importance of proper alignment of the laser beams (from Hanson (1974)).

3) Adjust the tuning knobs so that the pinhole (the center of the bullseye) coincides with the beam intersection.

Note: The shadows of any obstructions (eg. the zeroing spike, see next section) will also appear in the viewfinder.

4) Fine tune to get the maximum signal. Monitor the oscilloscope (fast response) and the data rate (slow response) as the position is adjusted to locate the optimum point.

5) Check the anode current indicator on the counter processor. It should not exceed 50μA. If the anode current is below this level, it can be increased to increase the signal strength, and thus the data rate. The validation rate (see the next section for definition) must be monitored if this is done. If the validation rate drops off, the current should be reduced.

3.1.3 Traverses and Positioning Procedures

Computer controlled traversing stages were used for positioning of the model. The x and y traverses were identical Daedal traverses, with a repeatability of 0.004μm/mm. The z traverse, from Thompson, supports a larger load, but has a lower 16μm/mm repeatability. Each traverse is supported by an MC5000 controller board, and the corresponding PC21 controller positioning code.

As the laser beams cross the four model surfaces, they are bent due to changes in the refractive index of the medium. This affects the position of the measuring volume; corrections must be applied during the positioning procedures in order to obtain the desired traverse. A method of calculating these corrections based on vector algebra was developed. Previously, authors used inaccurate assumptions (Ranade, 1990), or trigonometric approximations (Kehoe, 1987) to calculate refractive index effects. The vector algebra approach has proven highly flexible, and exact. Details are given in Appendix 1. Copies of the code are available from the author.

For the purposes of locating the measuring volume at the beginning of a traverse, a 1 mm diameter, 3 mm long zeroing spike was machined at the end of the impeller shaft[1]. The zeroing procedure is as follows:

1) Start with the beams horizontally oriented. Move to approximately the right place, level the impeller, and focus the photomultiplier.
2) Zero on x (towards and away from the laser). Adjust the position such that the beams are clearly visible on the bottom of the hub, just to one side of the zero spike. Line up the zero spike with the intersection of the beams.
3) Zero on y (left and right). At zero, and for approximately 0.2 mm on either side of zero, the data rate is zero and the oscilloscope trace is flat. At ±0.25 to 0.30 mm, the oscilloscope trace looks like watermark taffeta, and the anode current goes off scale. The zero point is located when moving the measuring volume by 0.25 mm to either the left or the right results in the watermark signal. When x and y are correctly zeroed, the beams are fully blocked. Note that a zero signal can also be obtained by blocking one of the beams before it reaches the measuring volume.
4) Zero on z (vertical). The same watermark signal observed at $y = \pm 0.25$ mm shows up at the bottom of the zeroing spike. Accurate measurement of the length of the zeroing spike allows zeroing of z at the lower edge of the impeller.

The visual method used on x is less accurate than the signal method used on y and z, but was the most accurate method available for the x direction for two reasons. Since the measuring volume is long (1.07 mm) in the x direction, signal

1 The impeller was positioned flush with the beginning of the wide portion of the shaft in all cases.

discrimination is more difficult than for either the y or z direction. Secondly, the zero bar interferes with detection of signals generated on the laser side of the zero spike so that only one limit can be observed. Using the zeroing spike, and the procedure given above, it was possible to locate the measuring volume to within ±0.05 mm on y and z, and to within ±0.5 mm on x.

3.1.4 The counter processor

Up until this point, discussion has focussed on how to obtain the Doppler signal. The shift in emphasis now moves to signal processing and data collection. Discussion will be limited to the topics of immediate relevance to a single component, forward scatter LDA, which performs signal processing using a counter processor.

The function of any LDA data processing system is to convert the signal coming from the photomultiplier into a series of Doppler frequencies from which the time series of the velocity can be calculated. The signal which arrives at the processor contains, not only the Doppler burst, but the low frequency Doppler pedestal due to the Gaussian variation of light intensity within the measuring volume (shown in figure 28), and some high frequency noise. These two undesirable components are removed using the high pass (higher frequencies are passed) and low pass (lower frequencies are passed) filters. These filters are initially set based on the range of Doppler frequencies expected. Under experimental conditions, the filter limits are then varied to determine the point at which narrowing the range of frequencies has an observable effect on the data rate. The filters are set outside this range. For these experiments, the high pass filter was set at 256 kHz, and the low pass filter at 2000 kHz.

Once the signal has been treated to remove the undesirable frequencies, the "Doppler frequency burst" associated with the passage of a particle through the measuring volume is centered around zero amplitude. The amplitude of the signal increases as the particle moves into the high intensity core of the measuring volume, and then decreases as the particle moves out the other side. The counter processor (in this case, Dantec model 55L90a) determines the Doppler frequency based on the time required for a set number of zero crossings in the Doppler burst. The timer is activated the second time the signal strength exceeds a threshold value at its maximum amplitude. The time required for the particle to pass through 5 fringes is recorded. Another timer is left open until the same particle has passed through 8 fringes. The two results are compared; if they agree to within 1.5%, the measured frequency is registered as valid, and the value is stored in an intermediate bin, the sampling window.

There is a pair of signal quality indicators on the counter processor which reflect the rates at which data is available from the photomultiplier, and transmitted to the sampling window. The first is the data rate, which reflects the rate of transmission of validated data. This value varied from a low of 0.5 kHz up to a high of 11 kHz, falling between 4 and 7 kHz for the majority of the work. The exact value depends on seeding, focussing, and the position in the tank. The second counter processor read out, the validation rate, is a reflection of the number of validated samples out of a block of 1000. The validation rate also varied substantially, but fell below 65% only rarely. These numbers indicate an intermediate data density, based on criteria suggested by Edwards (1987).

3.1.5 Data collection

Data collection and analysis is performed using the **dostek 1400A** data acquisition board and supporting software as described by Tropea (1987a). Data is available for collection from the counter processor at the "validated data rate" as described above. The data collection system allows collection of all available data (LDA trigger), or of selected data based on a set sampling frequency (timer trigger). If the set sampling frequency mode is used, the "sample and hold" circuit is activated. This means that the most recent valid data point is held in the sampling window, and is replaced as new valid points are collected. Data is collected from the sampling window at exactly the sampling frequency specified by the user, and stored for later analysis of the mean and RMS velocities, the frequency spectrum, and the time series. The sample and hold method thus continues to store data based on the last data point, even after the signal is lost. Observation of the oscilloscope and the validated data rate allows removal of these points in later analysis. A less severe manifestation of this weakness in the method is "drop out." If a new data point has not been stored in the sampling window in the interval between samples, the same data point will be stored twice. This appears in the time series plot as a short horizontal line. Neither of these shortcomings of the sample and hold method were of substantial consequence for these experiments.

3.2 Verification

3.2.1 Seeding

There are three requirements involved in the selection of seeding for LDA. The particles must scatter sufficient light to generate a useful signal, they must be

uniformly distributed throughout the fluid, and they must track the fluid flow so that the measured particle velocity accurately represents the fluid velocity of interest. Several tests of the ability of the particles to follow the flow are used when the flow is both rotational, and oscillatory. In addition to the three experimental criteria suggested in the literature, operational criteria of safety and ease of application are factored into the final choice.

The vast majority of the researchers investigating this problem have chosen tap water with naturally occurring particulate as the fluid/seeding combination. Tap water produces a good signal, is clean, and presents no safety concerns. It is readily available. There are, however, several problems with this choice. The size distribution of particles and the seeding level are outside the control of the researcher. The refractive index of water is substantially different from that of the tank walls, thus increasing refraction effects. The exact particle density is unknown. Based on these concerns, attempts were made to use other seeding particles which can be more exactly characterized and controlled. The seeding methods tested are as follows:

1) distilled water, no particles added
2) tap water, including some particulate
3) mineral oil, with 40 – 60μm polystyrene (PS) particles added
4) mineral oil, with 530 ± 200 nm polymethymethacryate (PMMA) latex particles added
5) heptane, with 530 ± 200 nm PMMA latex particles added

Sufficient particles were added to the last three fluids to generate an optimal signal strength. Too few particles produce a low data rate. Too many particles scatter so much light that little reaches the photomultiplier, producing a weak signal.

The non-aqueous fluid-particle combinations were chosen with several qualities in mind. Light (low viscosity) mineral oil was chosen for its refractive index match with perspex, which is closer than that of water; and for its viscosity, which is approximately equal to that of water. Heptane was used as a control fluid; since it was the original suspending agent for the polymethylmethacrylate (PMMA) latex. Polystyrene (PS) and PMMA have densities close to that of water, which makes them good candidates for flow following purposes.

The first combination (distilled water) was quickly eliminated on the basis of optical properties; the particle concentration was low, giving a very low data rate (of the order of 1 kHz). The other four combinations were satisfactory from the point of view of optical properties, giving a minimum data rate of 4 kHz.

In consideration of the flow following characteristics, four time scales characteristic of the flow were compared with two particle time scales. The characteristic velocity for the mean flow is the tip speed, and the characteristic length is the half-blade width (D/10). This gives a time scale of 3.8×10^{-3}s, or 0.262 Hz. George recommends a particle time constant criterion of one over the rotational speed for rotating flows, in order to ensure that viscous forces on the particle quickly overcome centrifugal forces due to rotation. This is the least stringent of the flow time scales, at a value of 0.12s. A more stringent requirement is that the particles be able to follow oscillations induced by individual blade passages. Using the basic blade passage frequency gives a time scale of $0.02s$, or 50 Hz, but since the oscil-

lations are very sharp, a more conservative estimate would be one tenth of this, 0.002s (500 Hz). The most stringent requirement is the ability to follow the turbulent fluctuations. The Kolmogorov time scale of these fluctuations was estimated from the maximum value of ε using

$$\tau_k = \left(\frac{\nu}{\varepsilon}\right)^{\frac{1}{2}} \tag{10}$$

An estimate of ε was obtained from the SRJ results. This gave a Kolmogorov time scale of $2.25 \times 10^{-4} s$, or 4.4 kHz; based on a rotational speed of 500 rpm, and a maximum impeller diameter of 76.2 mm. In all cases, this most conservative estimate for the flow time scale was used as the selection criterion.

Two particle time scales were considered. The first is a general particle time scale, as recommended by Buchave et al. (1979).

$$\tau_1 = \frac{d_p^2}{36\nu}\left(2\frac{\rho_p}{\rho_f} + 1\right) \tag{11}$$

The second is a limiting frequency used for oscillating flows, as recommended by Dring (1982).

$$\omega = 0.01\left(\frac{18\nu\rho_f}{d_p^2\rho_p}\right) \tag{12}$$

Table 1 gives the particle time scales, and the properties used to calculate them, for combinations 2 through 5.

combination	2	3	4	5
fluid	tap water	mineral oil	mineral oil	heptane
particles	natural	PS	PMMA	PMMA
ρ_f(g/cm^3)	1.0	0.84	0.84	0.684
ρ_p(g/cm^3)	2.0 *	1.10	1.19	1.19
d_p(μm)	1.0 *	60	0.5	0.5
$\nu \times 10^6$(m/s^2)	1.0	1.0	1.0	0.4
τ_1 (s)	1.39×10^{-7}	3.6×10^{-4}	2.68×10^{-8}	7.78×10^{-8}
ω (Hz)	0.9×10^5	38.2	5.08×10^5	1.65×10^5

* estimated

Table 1: Calculation of particie time scales for flow following verification.

From these results, combination 3 can be eliminated, since it will be unable to follow even the fluctuations due to blade passages. Combinations 2, 4, and 5 still appear to be good candidates, with limiting frequencies well above the Kolmogorov criterion.

As a final test of the suitability of these three fluid - seeding particle combinations, the radial velocity profile across the tip of the impeller blades was measured for the Rushton turbine. This profile is well established, and is dominated

by severe fluctuations; thus providing a stringent test of the flow following capability for impeller driven flow fields. The results of these tests, shown in figure 31, show some unexpected differences between the three traverses. Theory states that a dimensionless velocity profile in a fully turbulent flow field is independent of kinematic viscosity. This leads to the initial conclusion that the differences between the profiles must be due to an effect associated with the seeding particles. Consider first combinations 4 and 5; PMMA particles suspended in mineral oil and heptane respectively. The PMMA particles used are from a latex combination, initially suspended in heptane. When the particles were resuspended in mineral oil, there was a substantial decrease in the stability of the suspension. It was hypothesized that particle agglomeration occurred because of the change in suspending agent, resulting in larger effective particle sizes which were unable to effectively follow the flow. A single traverse was performed using heptane to determine if this was the case. This traverse gave a result substantially higher than that for mineral oil, lending some support to the agglomeration hypothesis. This allows elimination of the mineral oil-PMMA combination from consideration.

Considering now the heptane and water combinations, there is still not exact agreement between the two profiles. Since the particle time constants for these two combinations both satisfy all available criteria, another unexplained factor is at work. The most obvious explanation is the change in fluid viscosity to less than half that of water. While the Reynolds number at the impeller indicates fully turbulent flow, the Reynolds number in the outer regions of the tank may not always satisfy the fully turbulent criterion. If the flow field in the outer regions of the tank is transitional, the viscosity will have an effect in these zones, and the heptane flow field will differ

from the water flow field. Since the flow field recirculates back to the impeller, the difference in the velocity profile at the impeller discharge may be due to differences in these outer regions. Later in this thesis, it will be shown that events in the outer regions can have a substantial quantitative effect on the conditions at the impeller boundary. This hypothesis is further supported by earlier work by Gunkel and Weber (1975). They reported experiments performed on an RT impeller flow with a hot wire anemometer in air. Their results showed a deviation from the accepted Rushton turbine profile six times greater than that observed between heptane and water in these experiments. Again, the only discernable difference is in the fluid used for the experiment.

Because of the safety considerations associated with the heptane combination, it was impossible to investigate these issues further. The mineral oil combinations are clearly not satisfactory for tracking the flow. Heptane is unsuitable from the point of view of safety. Since the tap water combination gives the velocity profile in closest agreement with the literature results, is more symmetric than the heptane profile, meets all of the time scale requirements, and is almost certainly evenly seeded, it was deemed a suitable choice for further experiments. To minimize the uncertainties associated with this combination, several measures were undertaken. First, characterization of the particle size distribution and number in a similar tap water was obtained; second, beam tracing calculations were performed to minimize positioning errors due to the changes in refractive index.

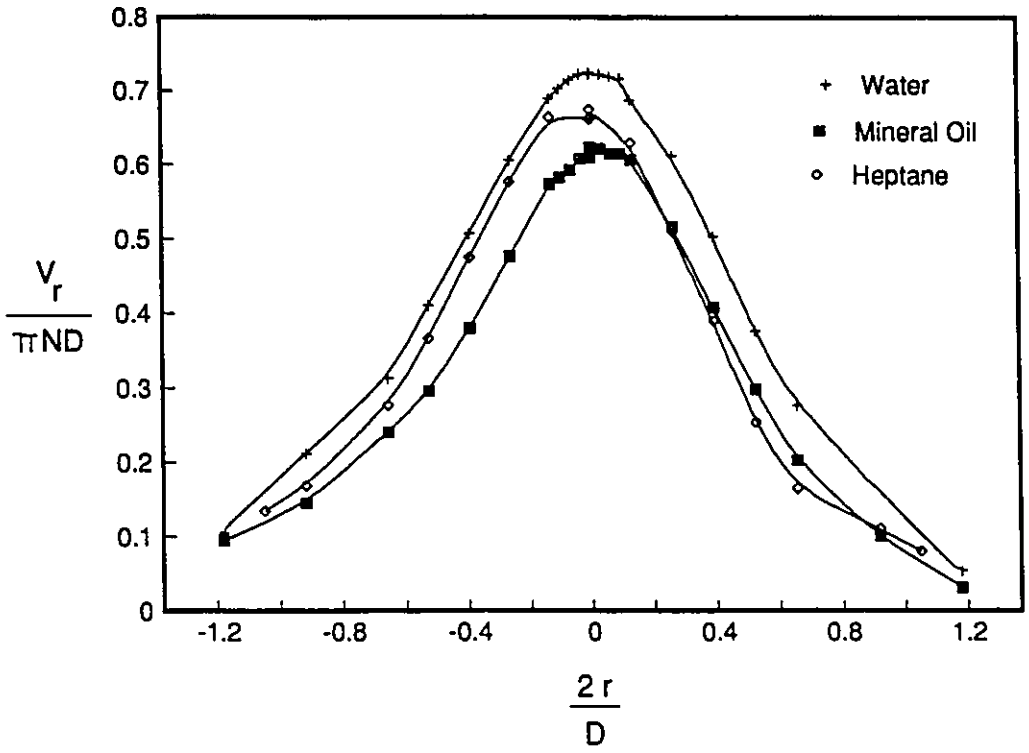

Figure 31. : Comparison of velocity profiles at the tip of the Rushton turbine with different fluid/seeding combinations.

3.2.2 Sampling frequency

The choice of sampling frequency requires consideration of several issues; the objective of complete characterization of the frequency spectrum of the velocity fluctuations must be balanced with limitations imposed by the signal quality, by the size of the measuring volume, and by the need to eliminate velocity bias errors. In order to completely characterize the frequency spectrum, it is necessary to sample the signal at a rate at least twice that of the highest frequency of interest. This is commonly referred to as the Nyquist criterion. The highest frequency of interest can be estimated from the Kolmogorov time scale, which for this flow is of the order

of 0.2 msec, or 4.4 kHz. The actual validated data rate ranged from 0.5 to 11 kHz, with the bulk of the data collected from data rates of 4 to 7 kHz. Since it clearly is not possible to sample at a rate faster than that at which data is available, the Nyquist criterion can not be satisfied at all times for this flow. The data rate can sometimes be increased by increasing the anode current or the frequency shift, but there is always an upper limit to these measures. This means that it is only possible to measure a partial frequency spectrum.

The validated data rate is the first limitation. The second limitation is phase ambiguity, or Doppler ambiguity noise. Up to this point, it has been assumed that there is only one particle in the measuring volume at any given time. In fact, there are normally of the order of 50 particles in the measuring volume at any one time[1], and the signal collected by the photomultiplier is the sum of the light scattered by all of the particles in the measuring volume. As particles move in and out of the measuring volume, the measured (aggregate) velocity fluctuates; this is <u>not</u> however, the turbulent velocity fluctuation we seek to measure. It is phase ambiguity noise.

To estimate the frequency at which phase ambiguity noise becomes a significant factor, consider the dimension of the measuring volume perpendicular to the fringes (0.12mm), and the wavenumber k_1 as defined by Hinze (1987, pg. 203):

$$k_1 = \frac{2\pi f}{\overline{U_1}} = \frac{1}{\lambda} \qquad (13)$$

1 for the tap water combination used here

Substituting in the maximum value of $\overline{U_1}$ at 400rpm, and the dimension of the measuring volume for λ (all wavelengths smaller than this will be completely contained in the measuring volume) gives a maximum measurable frequency of approximately 1.0kHz. Figure 32 shows the measured frequency spectrum for a position at which the limiting frequency is 500Hz (log(500) = 2.7). The sampling frequency, in this case, was 5kHz. According to the Nyquist criterion, this allows measurement of frequencies up to 2.5kHz (log(2500) = 3.4), but because of phase ambiguity noise, the frequency spectrum is clearly composed of white noise above 500Hz, and no useful information is available about the turbulence beyond this point.

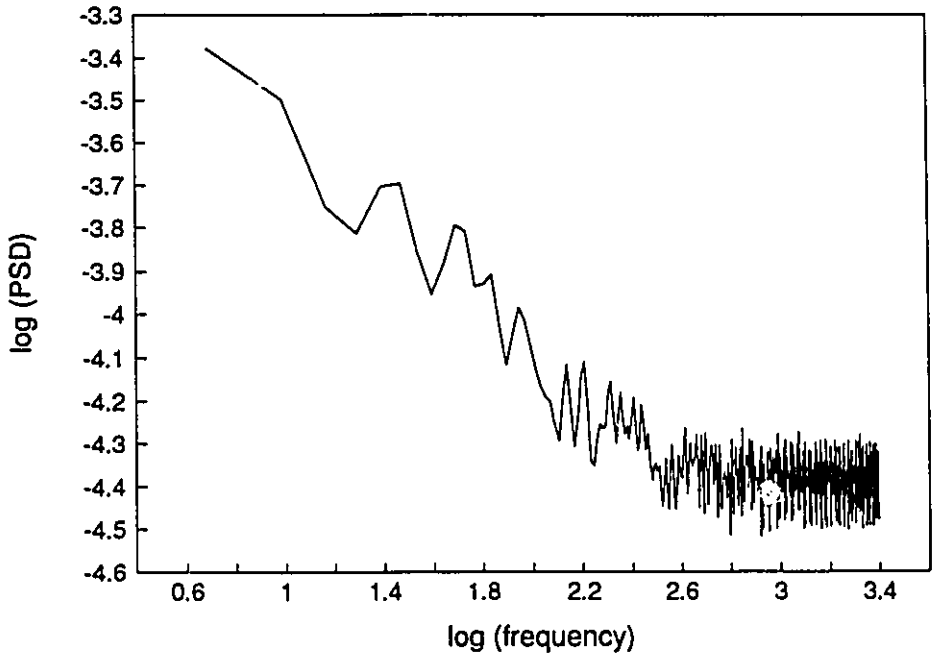

Figure 32. Phase ambiguity noise as it appears in the frequency spectrum. Above the limiting frequency of 500Hz, the spectrum is composed of white noise.

Once the Nyquist criterion and equipment limitations have been evaluated, the only remaining consideration is the elimination of velocity bias errors. These

errors are systematic errors, arising from the number averaging of all available velocity determinations. Assuming that the particles are uniformly distributed in the fluid, more particles will cross the measuring volume in high velocity fluid than in low velocity fluid. If every data point is accepted for averaging, the number averaged velocity will include a systematic bias towards the higher velocities in the flow. The easiest way to correct for velocity bias is to sample at a rate substantially less than the validated data rate. This defines data collection not by particle arrival rates, but by an externally set timer. Based on the velocity bias criterion (Adams and Eaton (1988), Craig et al. (1986), Gould et al. (1989), and Tropea (1987b)), the appropriate sampling frequency is one tenth the validated data rate. A series of tests were conducted to determine the effect of velocity bias on measurements taken in this flow field. If velocity bias errors are affecting the flow, the measured velocity will be reduced by reducing the sampling frequency, up to a certain point. Beyond this point, further reduction in the sampling frequency will not affect the measured velocity. The sampling frequency was varied from 0.2 kHz to 4 kHz, at a validated data rate of approximately 4 kHz. The results are shown in figure 33; there is no observable effect of sampling frequency on measurements of either the mean or the fluctuating velocity.

Since it is unlikely that this flow field is completely immune to the effects of velocity bias, another test was sought. Craig et al. (1986) suggest that the presence of velocity bias may also be indicated by a non-smooth velocity profile. To test the measurement settings under the most extreme conditions possible, radial velocity profiles across the tip of the Rushton turbine were performed, the first time at 0.4 kHz, and the second time allowing all data points to be collected. This is accom-

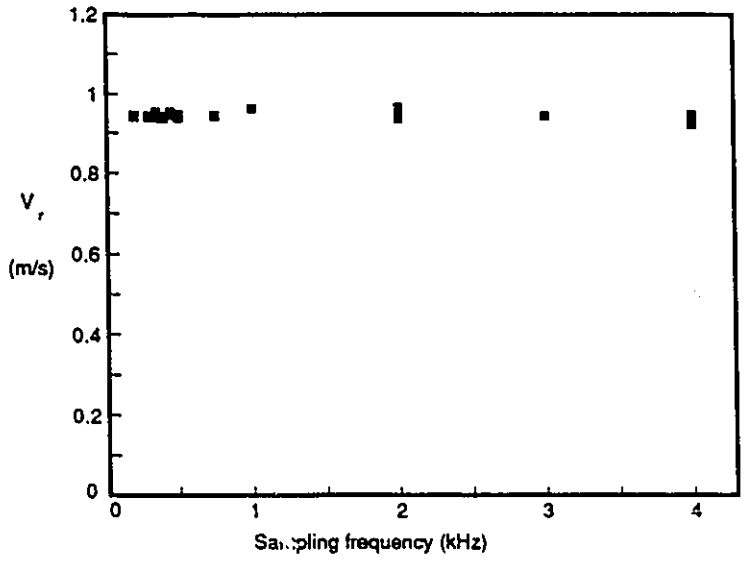

a) mean velocity

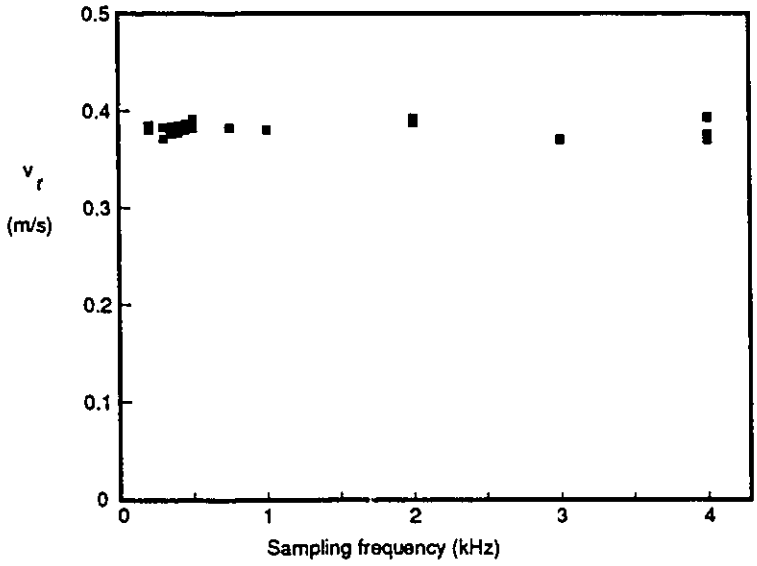

b) RMS velocity

Figure 33. : Effect of sampling frequency on the measured mean and RMS velocity.

plished by changing the data collection mode from timer triggering, to data arrival, or LDA triggering. The results, shown in figure 34, show that it is possible to get a velocity bias effect in this flow, so the precaution of sampling at a set frequency should be heeded.

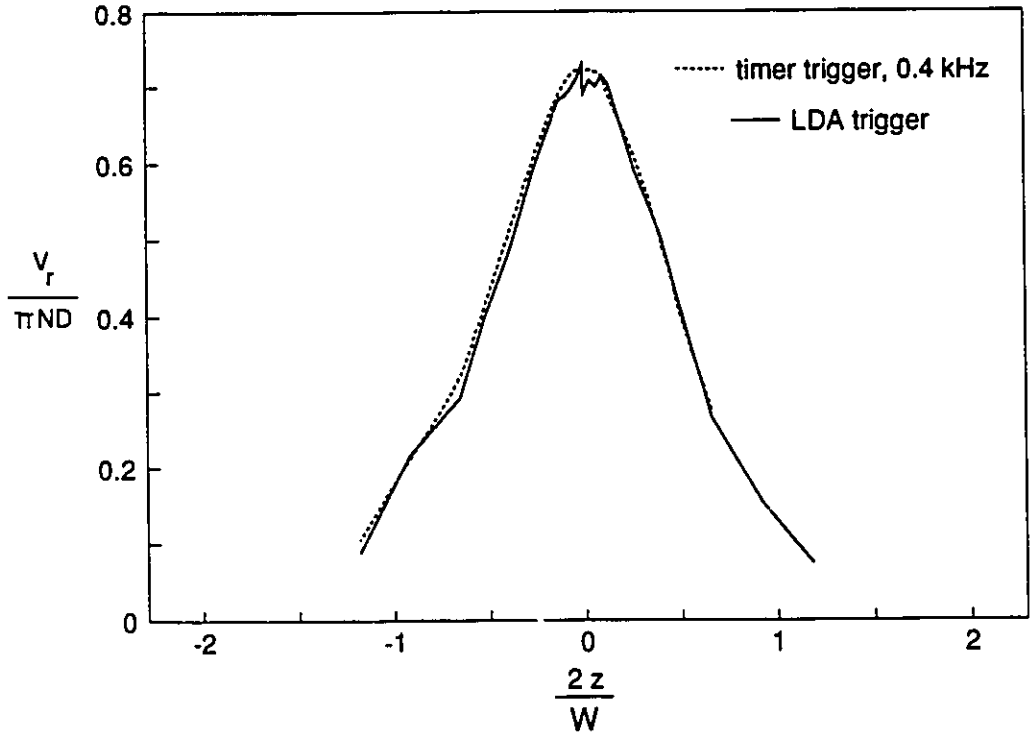

Figure 34. : Fixed sampling rate vs. data triggered collection: effect on the mean radial velocity profile measured at the tip of a Rushton turbine in water.

Figure 35 shows this experiment repeated for the mineral oil - PMMA combination discussed in the seeding section (8.2.1). Note that velocity bias exists for this seeding method, even at a low sampling frequency, and that it is severe for LDA triggered collection. This is further evidence that this seeding method is not a suitable one, even for mean velocity measurements.

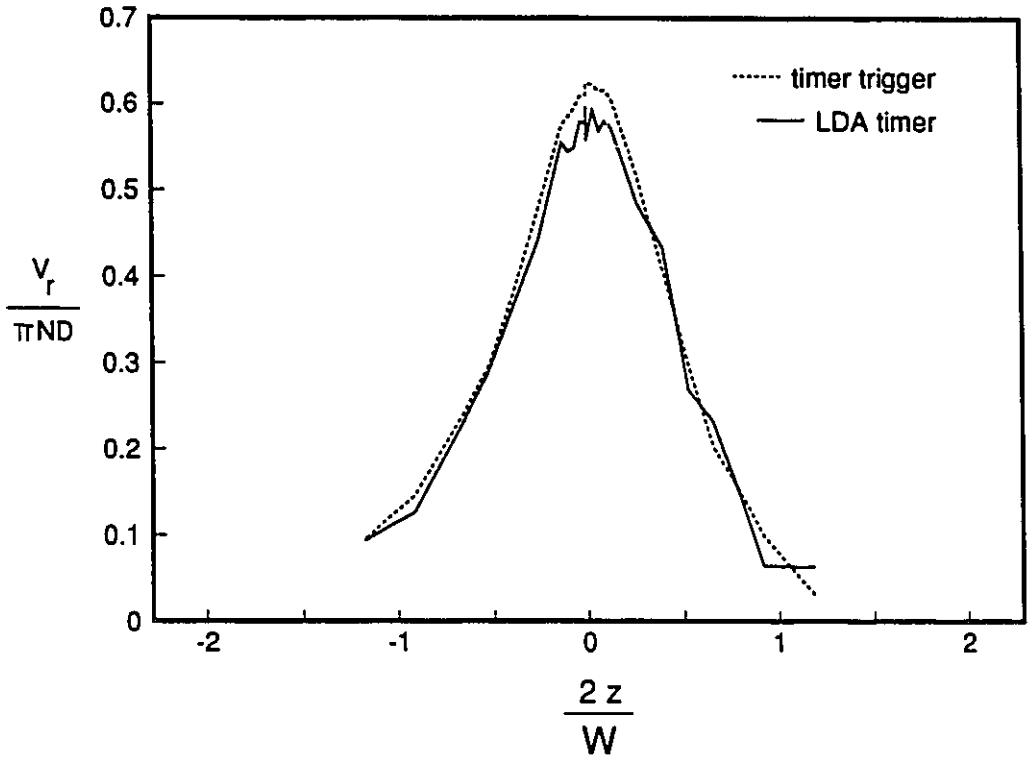

Figure 35. : Fixed sampling rate vs. data triggered collection: effect on the mean radial velocity profile measured at the tip of a Rushton turbine in mineral oil.

Figures 36 and 37 show profiles of the mean and RMS velocity across the lower edge of the PBT for the tap water combination at various sampling frequencies. The mean velocity profile is unaffected by the sampling frequency over the range considered, but the RMS velocity profile is severely affected by the presence of phase ambiguity noise at the 5 kHz sampling frequency.

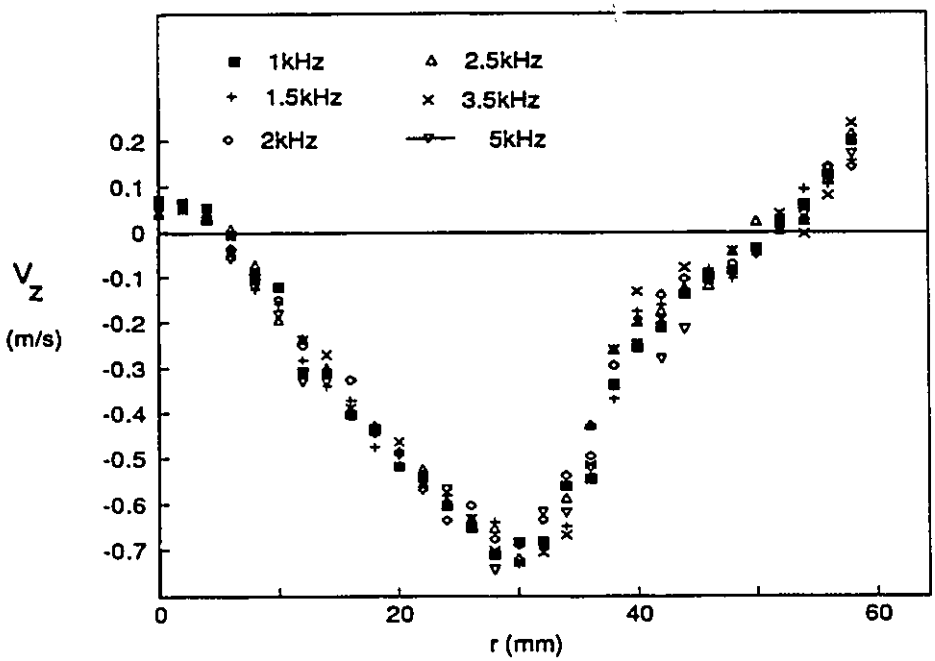

Figure 36. The mean axial velocity profile across the lower edge of the PBT for various sampling frequencies.

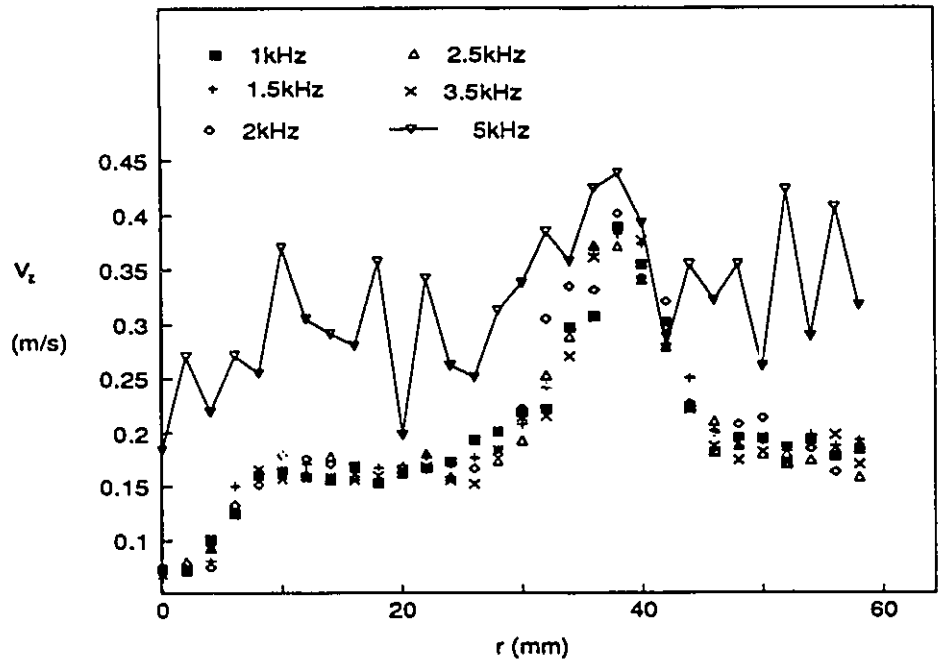

Figure 37. The RMS axial velocity profile across the lower edge of the PBT for various sampling frequencies showing the effect of phase ambiguity noise at a very high sampling frequency.

These experiments have shown that sampling rates ranging from 0.2 to 3.5 kHz will produce accurate results for the mean and RMS velocity profiles. Velocity bias is not a major factor in this flow, but can produce a non-smooth velocity profile if a regular sampling frequency is not imposed. Doppler, or phase, ambiguity noise poses a greater problem, limiting the range of the measurable frequency spectrum, and producing an erroneous RMS velocity profile for excessively high sampling frequencies.

3.2.3 Repeatability

A check on the repeatability of a velocity profile gives two pieces of information. The first is a check on the positioning equipment, the second is a check on the stability of the measurements themselves. Figure 36 shows four axial velocity traverses below the pitched blade turbine. The first two were recorded on the same day; they provide a check on the consistency of the traversing stage. The third and fourth traverses were obtained seven and eleven months later, respectively. Comparison of these traverses shows that the LDA is providing stable, repeatable results that are not substantially affected by small changes in the lab; most particularly by any seasonal variation in the tap water seeding particles.

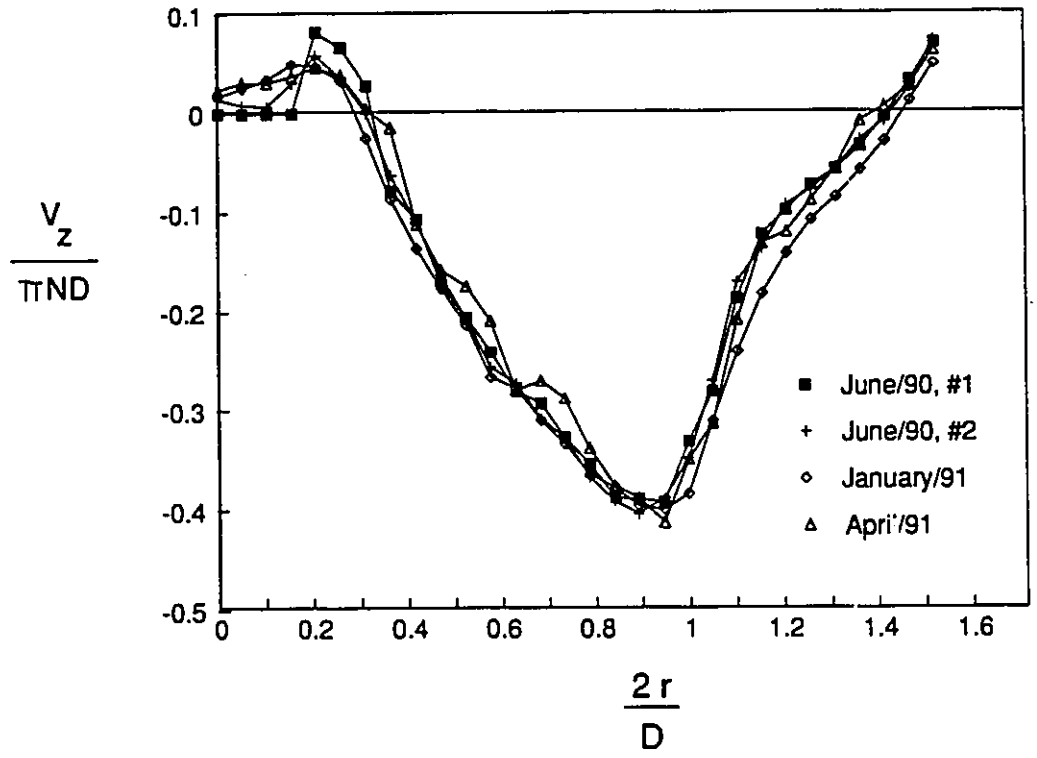

Figure 38. : Four axial velocity traverses across the bottom of the pitched blade turbine, showing the level of repeatability of the measurements.

3.2.4 Material Balances

If the velocity measurements are self-consistent, a material balance around any closed volume of fluid will yield a net flow of zero. The impeller region is the region of greatest interest in this work, and the steepest gradients in the flow are expected to occur on its boundaries; it was chosen as the region for verification of the material balance. Axial velocities across the horizontal surfaces, and radial velocities across the tip were measured at 2 mm intervals. Material balances were performed for both impeller diameters. The balance on the T/2 impeller closed to 0.3% at a clearance of C=T/2, and 0.4% at C=T/3. Results for the T/3 impeller were

not as good, closing to only 9.2% at C=T/2, and 4.3% at C=T/3.

3.2.5 Comparison with Known Results

The best known velocity profile for flow in stirred tanks is the radial velocity profile at the tip of the Rushton turbine, which has been referred to throughout this section. Comparison of experimental results from our lab with results from several other labs, and with the theoretical velocity profile predicted by the SRJ model of chapter 6 was performed. Results are shown in figures 39 and 40. The agreement between experimental and theoretical results is excellent. The only deviation from the theoretical prediction is at the edges of the velocity profile. This is a mathematical limitation of the model, not an experimental error.

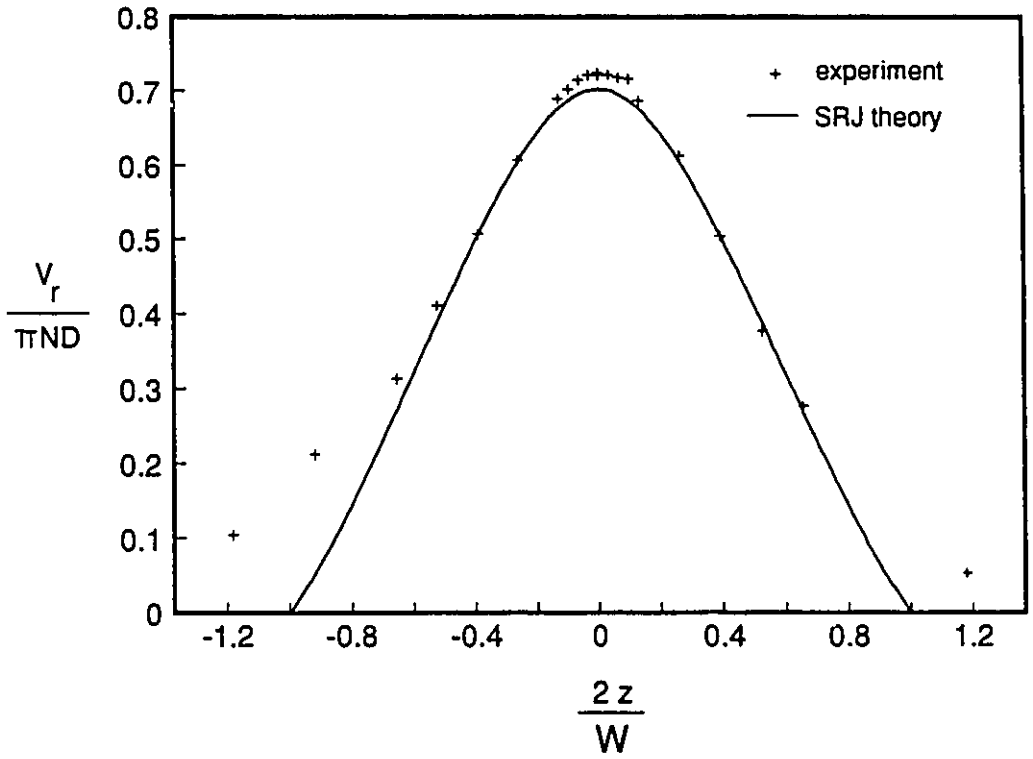

Figure 39. : Comparison of the measured radial velocity profile with the theoretical result predicted by the SRJ model.

The experimental results also agree very well with results reported by other labs. The data shown in figure 40 span twenty years, and all of the major experimental techniques.

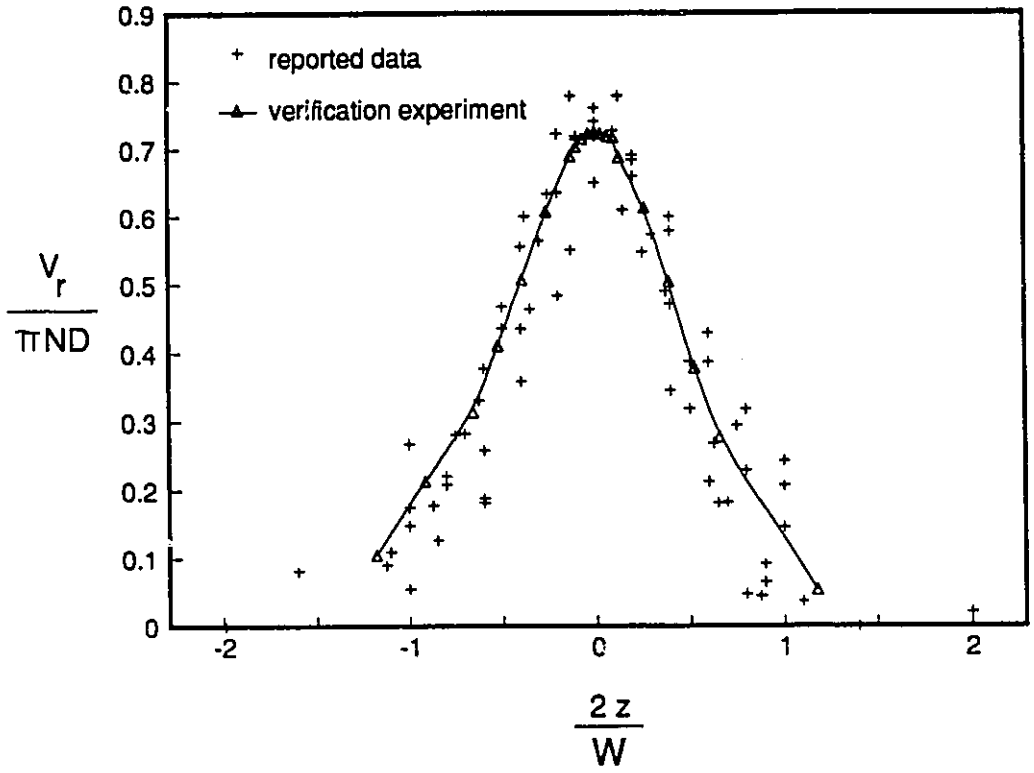

Figure 40. : Comparison of the measured radial velocity profile with the experimental results from other investigators.

Verification of the experimental sytem and the signal obtained has revealed an exceptionally stable experimental result, with a high degree of accuracy. The technique must be applied with caution, however, as errors sometimes emerge with careful secondary verification tests. These errors can only be minimized by understanding the theory behind the method, and by consideration of the unique characteristics of each flow field.

3.3 Notation

D = impeller diameter

d_p = particle diameter

f = frequency

f_D = Doppler frequency

K = conversion factor

k_1 = one dimensional wavenumber

N = impeller rotational speed

PSD = power spectral density (see appendix 2)

$\overline{U_i}$ = mean velocity in the i component direction (1=streamwise component, 2 and 3=cross-stream components); used in general expressions.

u_i' = fluctuating or RMS velocity in the i component direction

$V_{particle}$ =

V_r, V_z = mean radial and axial components of velocity; used in expressions for a specific flow.

v_r, v_z = RMS radial and axial components of velocity

W = blade width

Δy = fringe spacing

greek symbols

α = angle of rotation for Logan's method

ε = dissipation rate of turbulence kinetic energy per unit mass

θ = full angle between the laser beams

λ_o = wavelength of laser light

λ = wavelength of velocity fluctuation

ν = kinematic viscosity

ρ_f = fluid density

ρ_p = particle density

τ_1 = general particle time scale

3.3 Notation

D = impeller diameter

d_p = particle diameter

f = frequency

f_D = Doppler frequency

K = conversion factor

k_1 = one dimensional wavenumber

N = impeller rotational speed

PSD = power spectral density (see appendix 2)

$\overline{U_i}$ = mean velocity in the i component direction (1=streamwise component, 2 and 3=cross-stream components); used in general expressions.

u_i' = fluctuating or RMS velocity in the i component direction

$V_{particle}$ =

V_r, V_z = mean radial and axial components of velocity; used in expressions for a specific flow.

v_r, v_z = RMS radial and axial components of velocity

W = blade width

Δy = fringe spacing

greek symbols

α = angle of rotation for Logan's method

ε = dissipation rate of turbulence kinetic energy per unit mass

θ = full angle between the laser beams

λ_o = wavelength of laser light

λ = wavelength of velocity fluctuation

ν = kinematic viscosity

ρ_f = fluid density

ρ_p = particle density

τ_1 = general particle time scale

τ_K = Kolmogorov time scale

ω = limiting frequency of a particle

3.4 References

Adams, E. W. and J. K. Eaton, "An LDA study of the backward facing step flow, including the effects of velocity bias," J. Fluids Engineering, v. 110, pp. 275-282, 1988.

Buchave, Preben, William K. George, and John L. Lumley, "The measurement of turbulence with the lase Doppler anemometer," Ann. Rev. Fluid Mech., v. 11, pp. 443-503, 1979.

Craig, R. R., A. S. Negad, E. Y. Hahn, and K. G. Schwartzkopf, "Approach for obtaining unbiased laser doppler velocimetry data in highly turbulent flows," J. Propulsion, v. 2, pp. 541-545, 1986.

Drain, L. E., The Laser Doppler Technique, John Wiley and Sons, Toronto, 1980.

Dring, R. P., "Sizing criteria for laser anemometry particles," J. Fluids Engineering, v. 104, pp. 15-17, 1982.

Durst, F., A. Melling, J. H. Whitelaw, Principles and Practice of Laser Doppler Anemometry, Academic Press, New York, 1976.

Edwards, Robert V., ed., "Report of the special panel on statistical particle bias problems in laser anemometry," J. Fluids Engineering, v. 109, pp. 89-93, 1987.

Encyclopedia of Chemical Technology, third ed., "Lasers," v. 14, John Wiley and Sons, Toronto, 1981.

George, William K., "Quantitative measurement with the burst-mode laser Doppler anemometer," Exptl. Thermal and Fluid Sci., v. 1, pp. 29-40, 1988.

Gould, Richard D., Warren H. Stevenson, and H. Doyle Thompson, "Parametric study of statistical bias in LDV," AIAA, v. 27, pp. 1140-1142, 1989.

Gunkel, Alfred A., and Martin E. Weber, "Flow phenomena in stirred tanks, Part I: the impeller stream," AIChE Journal, v. 21, pp. 931-939, 1975.

Hanson, S., "Coherent detection in laser Doppler velocimeters," Opto-electronics, v. 6, pp. 263-269, 1974.

Hinze, J.O., Turbulence, An Introduction to its Mechanism and Theory, 2nd ed., McGraw Hill, Toronto, 1987.

Kehoe, Anthony B., and Prateen V. Desai, "compensation for refractive-index variations in laser Doppler anemometry," Applied Optics, v. 26, pp. 2582-2591, 1987.

Melling, A., and J. H. Whitelaw, "Turbulent flow in a rectangular duct," J. Fluid Mech., v. 78, part 2, pp. 289-315, 1976.

Ranade, V. V., and J. B. Joshi, "Flow generated by a disk turbine: Part I Experimental," Trans. I. Chem. E., v. 68, part A, pp. 19-33, 1990.

Tropea, C., and D. Struthers, "Microprocessor based on-line measurement system for LDA," ISL Proceedings on the Use of Computers in Laser Velocimetry, May 18-20, 1987a.

Tropea, C., "Turbulence induced spectral bias in laser anemometry," AIAA, v. 25, pp. 306-309, 1987b.

Chapter 4. Pitched Blade Turbine Mean Velocity Experiments

Mean velocity measurements were undertaken with several objectives in mind. First, and most important, an accurate understanding of the nature of the impeller discharge stream is needed for both mathematical modelling and physical understanding. Second, once models are available, good data is required throughout the tank for verification of computational fluid dynamic (CFD) experiments. Third, the information from these studies can contribute to a qualitative understanding of the overall flow field, through the bulk circulation patterns, and definition of the flow number. These results should be considered in tandem with the results of the flow visualization experiments presented in chapter 2.

Although the pitched blade turbine (PBT) is the most widely used, general purpose impeller in the process industries, information available in the literature focuses on the Rushton turbine. Very little information is available for comparison with this work. Fort (1986) made some early mean velocity measurements for the PBT using pitot tubes, which are summarized in his 1986 review. Tatterson et al. (1980) and Ali et al. (1981) published some excellent flow visualization work on the details of the impeller discharge flow. Nouri and Whitelaw (1990) have looked at variations in the flow field which occur as the viscosity and Reynolds number are varied, for very low Reynolds numbers. These papers are used here mainly for the evaluation of common trends in the data, and in the flow phenomena observed.

The main source in the literature for quantitative information about the PBT is Ranade and Joshi's 1989 paper. The principal results from this paper are summarized in the first 14 pages of Rewatkar and Joshi (1991). Although much of the work is valuable, several criticisms apply to both papers.

1) In all graphs where the abscissa is labelled "dimensionless radial coordinate," the coordinate has been based not on the impeller radius (as reported), but on the tank radius. This mislabelling makes it appear that the flow is upwards over the outer extent of the downward pumping impeller. Redefinition corrects the trend. It appears that the axial traverse locations are correctly defined in terms of the impeller radius (z/R).

2) With the correction given in (1), the large reported effect of D/T on the axial velocity profile as shown in their figure 15(A) (incorrectly labelled 15(B)) will be substantially reduced.

3) No refractive index corrections were used to determine the position of the measurement volume. The authors claim that this will produce a positioning error of less than 1mm. While this is true for traverses perpendicular to the beam angle bisector, it will result in a positioning error of 25% at 2r/D = 0.66 on traverses parallel to the beam angle bisector. This is due to the lensing effect of the cylindrical tank. This will only affect the angular component of the reported velocities. A relatively simple vector analysis method for calculating these corrections is given in Appendix 1.

The results reported in Ranade and Joshi (1989) will be compared to the results obtained here with the above corrections applied. No quantities involving V_θ will be considered.

The mean velocity results are presented in three parts; first, the bulk of the tank; second, the impeller discharge condition; and third, the flow number. For the bulk of the tank, attention is concentrated on the impeller discharge stream (below the impeller). The effects of variations in off-bottom clearance (C) and impeller diameter (D) on all three components of velocity are presented. In the top half of the tank, the r-z velocity field is given for one configuration. The results obtained in the bulk of the tank indicate that the axial velocity profile at the lower edge of the impeller can be used to characterize changes in the impeller discharge condition. This information will eventually be used for impeller modelling, and for the definition of the impeller boundary conditions for CFD experiments. The discharge condition is thus examined over variations in N, angular position, hub size, C, D, and scale. From this data, the flow number is calculated with particular attention to the effects of C and D.

4.1 The bulk of the tank

4.1.1 Decay of mean velocities in the impeller discharge stream

Since the steepest velocity gradients occur in the region below the impeller, and since this is the locus of energy input to the flow field, the focus of the experimental work is on this "impeller discharge stream." Four geometries were chosen for examination of the effects of off-bottom clearance and impeller diameter. For each geometry, all three components of velocity were measured over radial traverses at six axial positions. Specifics of the four cases and the traverse positions are given in figure 41. Note that the origin is defined at the center bottom edge of the impeller, with z defined to be positive upward.

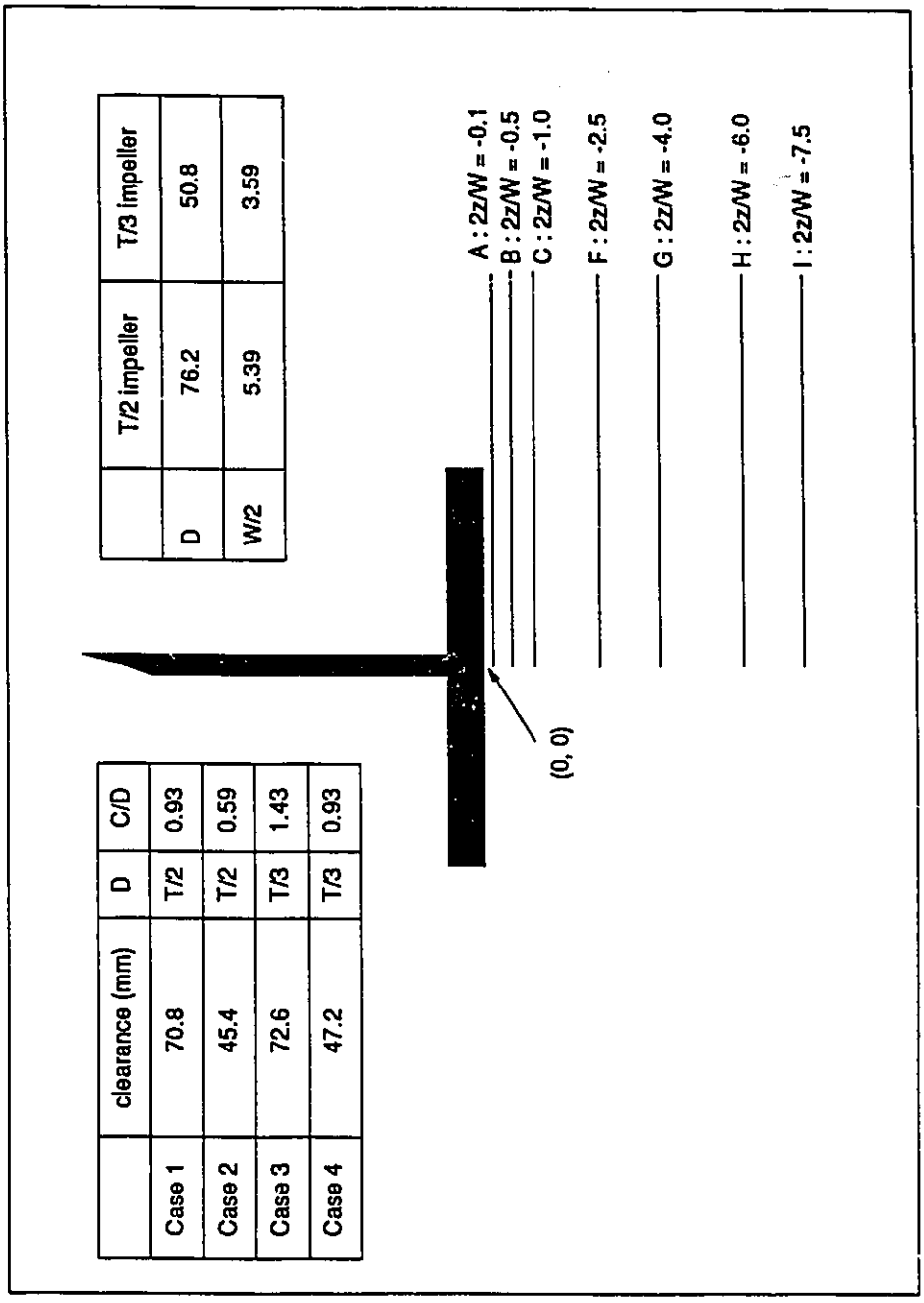

	T/2 impeller	T/3 impeller
D	76.2	50.8
W/2	5.39	3.59

	clearance (mm)	D	C/D
Case 1	70.8	T/2	0.93
Case 2	45.4	T/2	0.59
Case 3	72.6	T/3	1.43
Case 4	47.2	T/3	0.93

Figure 41. Position of traverses below the impeller, relative to the impeller blades.

Direct comparison of the results from these very different geometries is difficult, but is important to establish the extent of the flow field similarity, and thus the appropriate approach for modelling and CFD verification. The basis of comparison chosen here is to define the traverses in terms of projected half-blade widths, giving an equivalent dimensionless distance from the impeller. Another approach would be to define the traverses in terms of the fraction of the distance to the bottom (z/C). The difference between this approach and the blade widths approach is illustrated in figure 42. Note that where the impeller diameter is large, and the clearance is small, a given 2z/W distance from the impeller is much closer to the bottom of the tank than the same 2z/W distance where the impeller is small and the clearance is large. For cases where the clearance is equal to the impeller diameter (1 and 4), the two curves coincide. These differences in perspective must be considered in the analysis of results, especially in regions distant from the impeller edge.

The axial velocity is the most important component of velocity along the lower edge of the impeller, and it is this component which is considered first, as shown in figures 43, 44, 45 and 46. All four cases exhibit a jet-like profile along the impeller edge which peaks somewhere between 2r/D = 0.7 and 0.9, at about 45% of the tip speed. This agrees well with results presented by Ranade and Joshi (1989), who report a maximum axial velocity of 0.47 V_{tip} at 2r/D = 0.8. It can be contrasted with the simplified results of Fort (1986), who found a linear velocity profile starting with zero velocity at the center, and increasing to a maximum at the "critical radius," where decay begins. The peak shown in Fort's results is sharp, unlike the smooth peak shown here. This simplified profile also completely neglects the hub region.

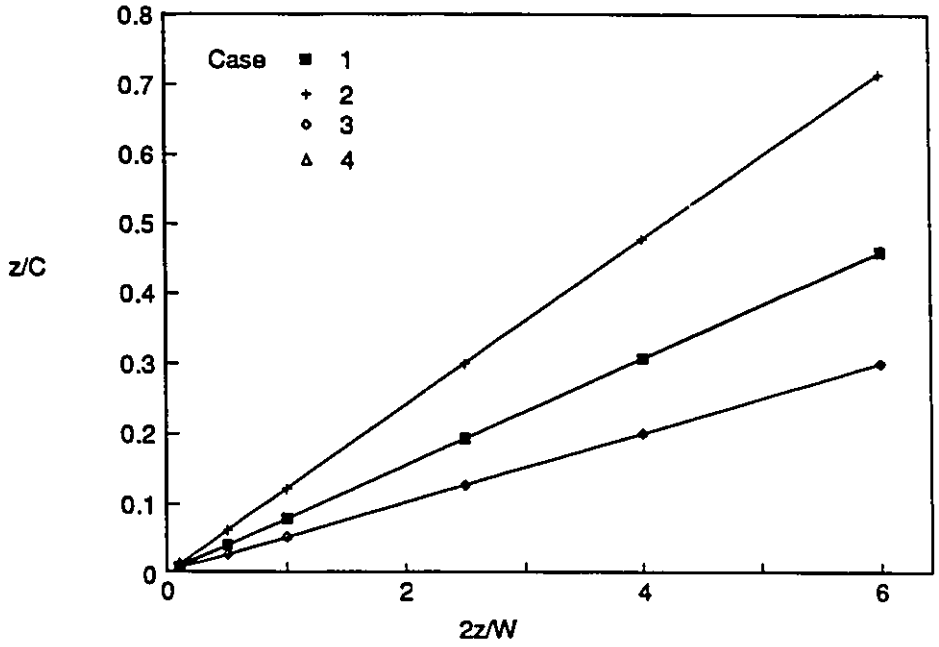

Figure 42. Position of traverses below the impeller as a fraction of the off bottom clearance.

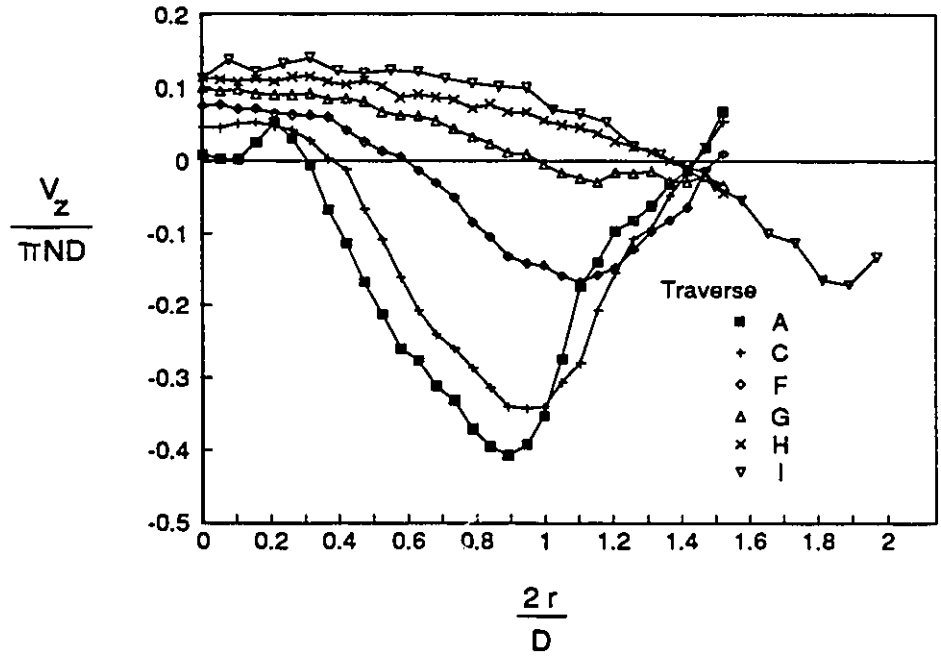

Figure 43. Decay of axial velocity below the impeller for Case 1; D=T/2, C=T/2.

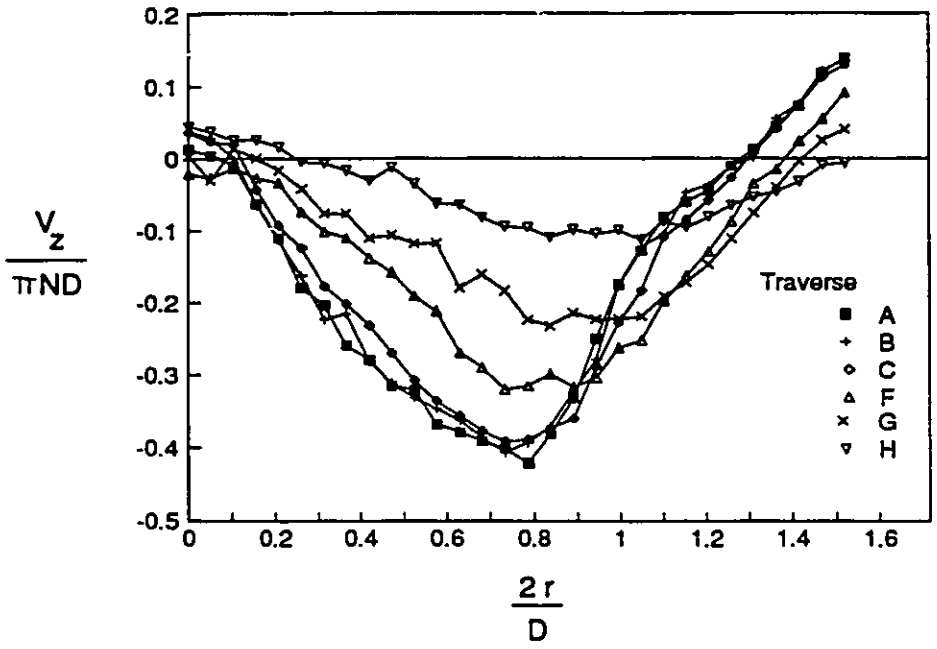

Figure 44. Decay of axial velocity below the impeller for Case 2; D=T/2, C=T/3.

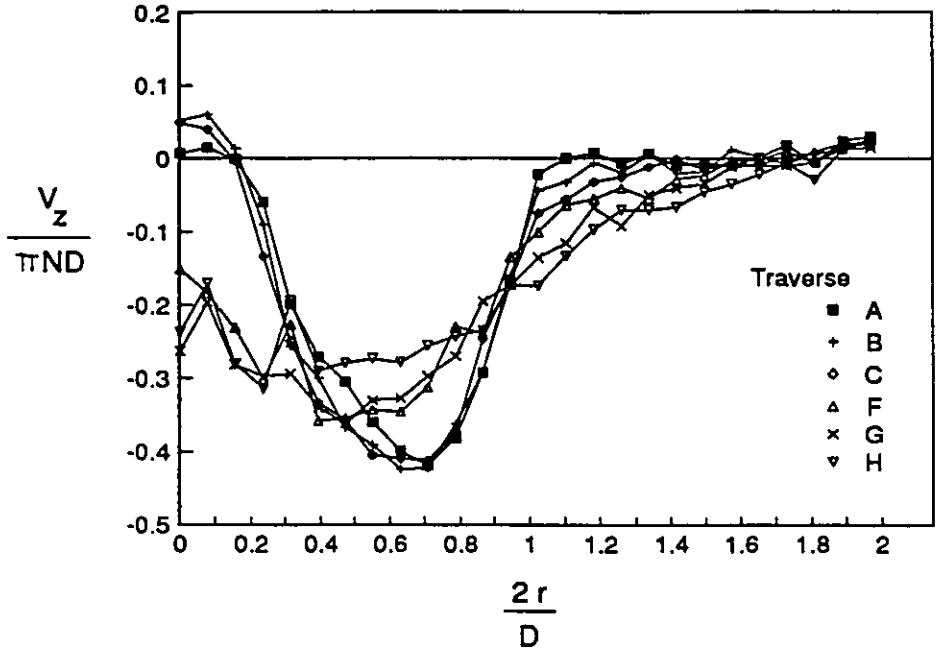

Figure 45. Decay of axial velocity below the impeller for Case 3; D=T/3, C=T/2.

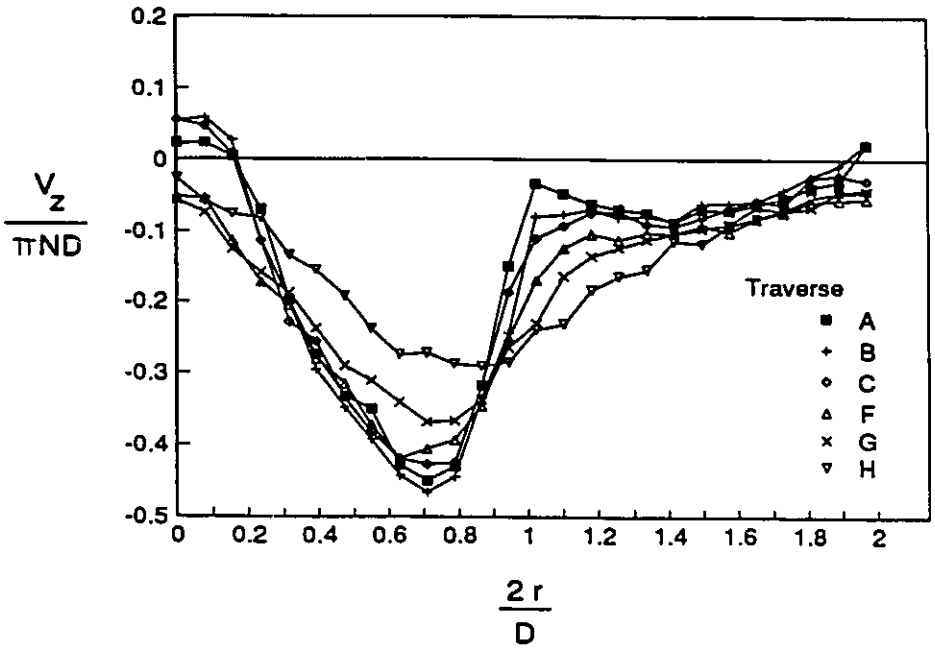

Figure 46. Decay of axial velocity below the impeller for Case 4; D=T/3, C=T/3.

The decay of axial velocity between the impeller and the bottom of the tank is generally steady and smooth, with very little change between 2z/W = -0.1 and -1. There are, however, some important differences between the geometries. From the flow visualization results, there is evidence of a secondary circulation loop in the bottom half of the tank for clearances of T/2. Figure 43 provides conclusive evidence of this loop for Case 1. Traverse I at -7.5 W/2 shows a complete flow reversal from traverse A at the lower edge. The results for Case 3 are more difficult to interpret. This is partly because the traverses extend only 30% of the way to the bottom, so the secondary circulation loop is never intercepted. The most interesting aspect of these results is the transition to a fairly flat axial velocity profile over the extent of the impeller at 2z/W = -2.5 (figure 45). This profile remains fairly constant with further descent to 2z/W = -6. As will be shown later, the radial velocity in this region

is almost zero, and the tangential velocity decays steadily, as expected. This result is supported by flow visualization results, which also show strong axial flow across the T/3 impeller at a T/2 clearance.

Cases 2 and 4 (figures 44 and 46) show the results at a clearance of T/3 for the impeller diameters D=T/2 and D=T/3. Note that the faster decay for case 2 is again due more to the difficulty of comparison in this geometry than to a physically distinct flow.

Comparing the T/2 and T/3 impellers, note that the T/2 impeller shows no dead zone in the eye of the circulation loop (figures 43 and 44), while the T/3 impeller shows a dead zone of at least 1/4 D in extent (figures 45 and 46).

The radial velocity, to be considered next, may or may not be significant; depending on the geometry used. Figures 47, 48, 49, and 50 show the four sets of dimensionless radial velocity profiles. The missing points in figure 49 are due to obstruction of the laser beams by the baffles at one point in the traverse. This occurs in various figures throughout this chapter. Along the lower edge of the impeller, Vr is less than 10% of the tip speed for all but case 1. Again, this agrees with observations by Ranade and Joshi (1989) who found that the radial velocity was negligible along the bottom surface of the impeller. Case 1 is the only exception to this, where the radial velocity along the lower edge quickly reaches 25% of the tip speed, then suddenly reverses at the tip of the impeller (ie. the flow is radially inward at this point). This is an indication of short circuiting of the primary circulation loop, which returns both through the top surface of the impeller, and through the vertical surface at the blade tips for this case. Case 2 shows a smaller reversal at -2.5 and -4 W/2. Short circuiting has been observed by several other authors examining axial flow

impellers (Ranade and Joshi (1989), Nouri and Whitelaw (1990), Winardi and Nagase (1991)). As the bottom is approached, the radial velocity component increases steadily. Again, evidence of the secondary circulation loop appears in the results for case 1, which reaches a maximum radial velocity at 2z/W = -2.5, and then begins to drop off. Measurements did not extend far enough down in the tank to expect to see complete reversal of the radial flow for case 1.

The T/3 impeller cases have a very small radial velocity component (maximum of 0.2 Vtip) relative to the T/2 impeller cases (maximum of 0.5 Vtip). The T/2 impeller produces 3.4 times more volumetric flow than the T/3 impeller at the same rotational speed, and has an area 15% smaller through which to pump the fluid up to the top of the tank. As might be expected, the T/2 impeller produces a much stronger circulation than the T/3 impeller. This is seen both in the shape of the axial velocity profiles, and in the magnitude of the radial velocity profiles.

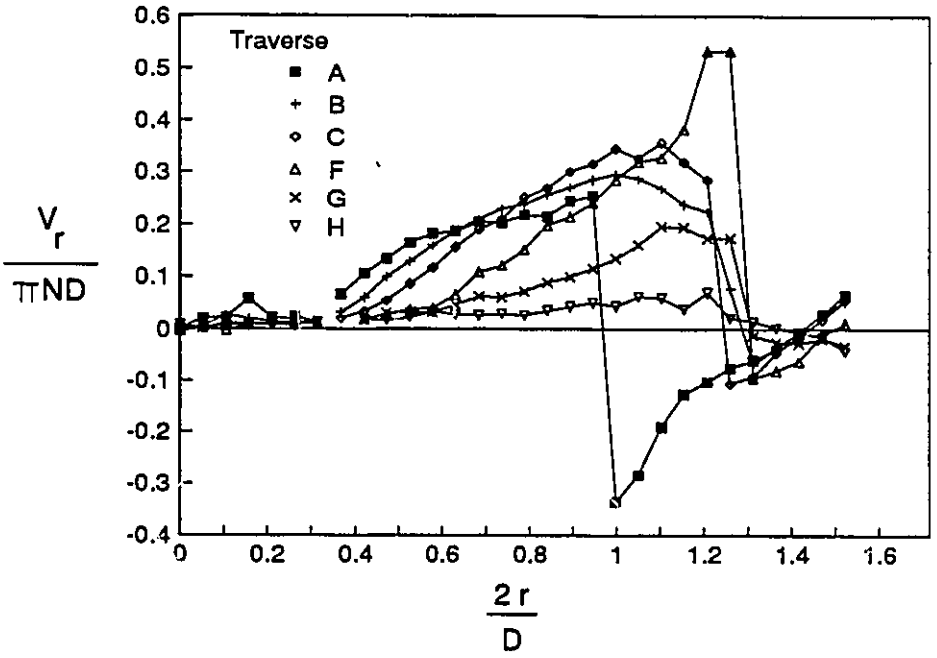

Figure 47. Decay of radial velocity below the impeller for Case 1; D=T/2, C=T/2.

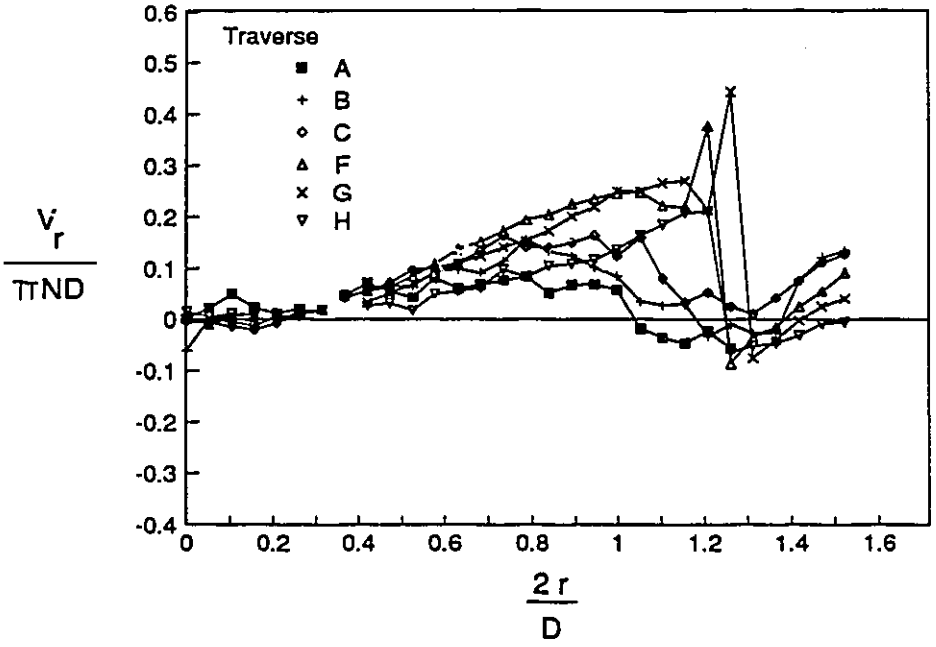

Figure 48. Decay of radial velocity below the impeller for Case 2; D=T/2, C=T/3.

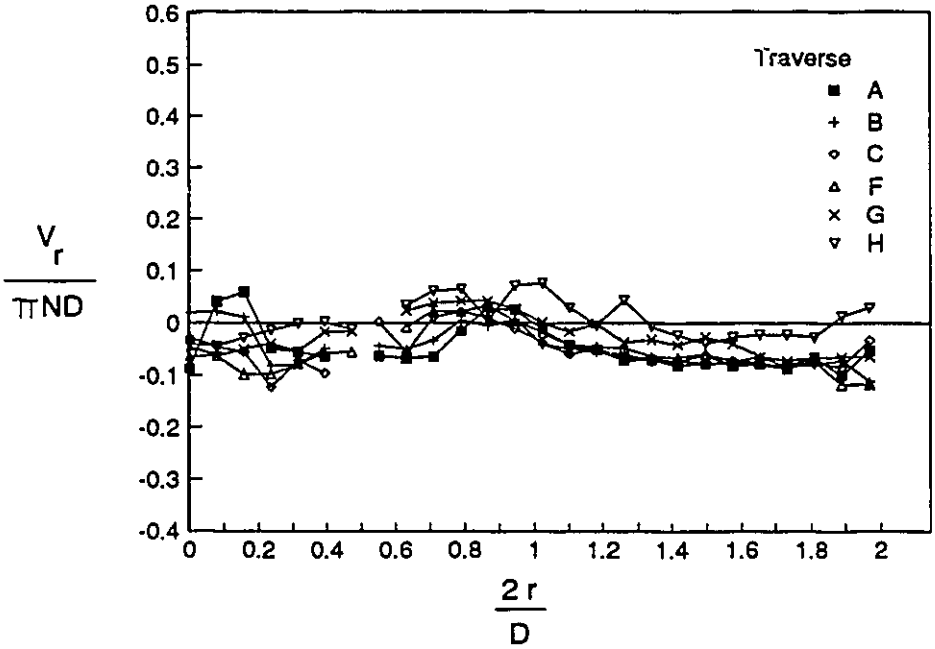

Figure 49. Decay of radial velocity below the impeller for Case 3; D=T/3, C=T/2.

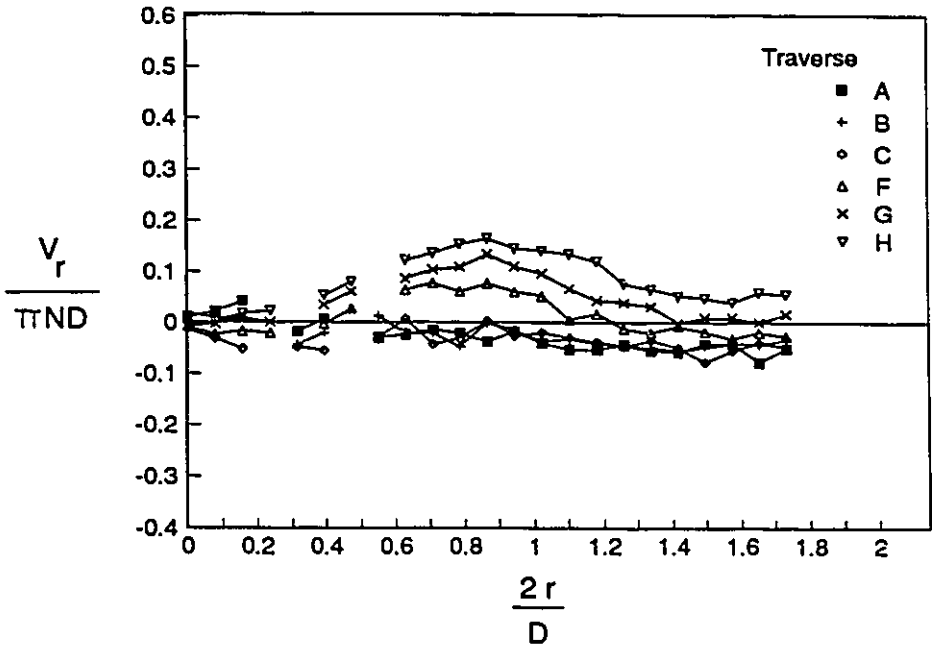

Figure 50. Decay of radial velocity below the impeller for Case 4; D=T/3, C=T/3.

The tangential component of velocity, shown in figures 51, 52, 53, and 54, is at its maximum close to the impeller (traverse A). The peak velocity occurs close to the blade tips, with a magnitude of 35 to 50% of the tip speed. The decay of this component with axial distance is smooth and steady for all four cases. The profiles for the T/3 impeller (figures 53 and 54) show a sharper peak, which decays more rapidly. Again, there is evidence of a dead zone in the eye of the circulation loop for the T/3 impeller, which is not present for the T/2 impeller. Case 1 (figure 51) shows a more rapid decay than the other cases, which may be due to the secondary circulation loop.

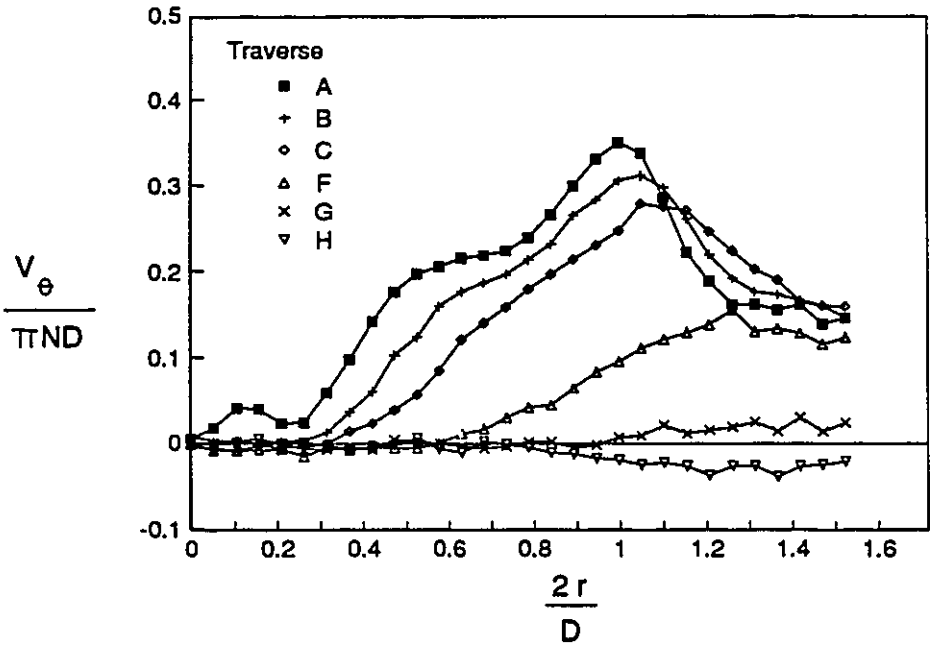

Figure 51. Decay of tangential velocity below the impeller for Case 1; D=T/2, C=T/2.

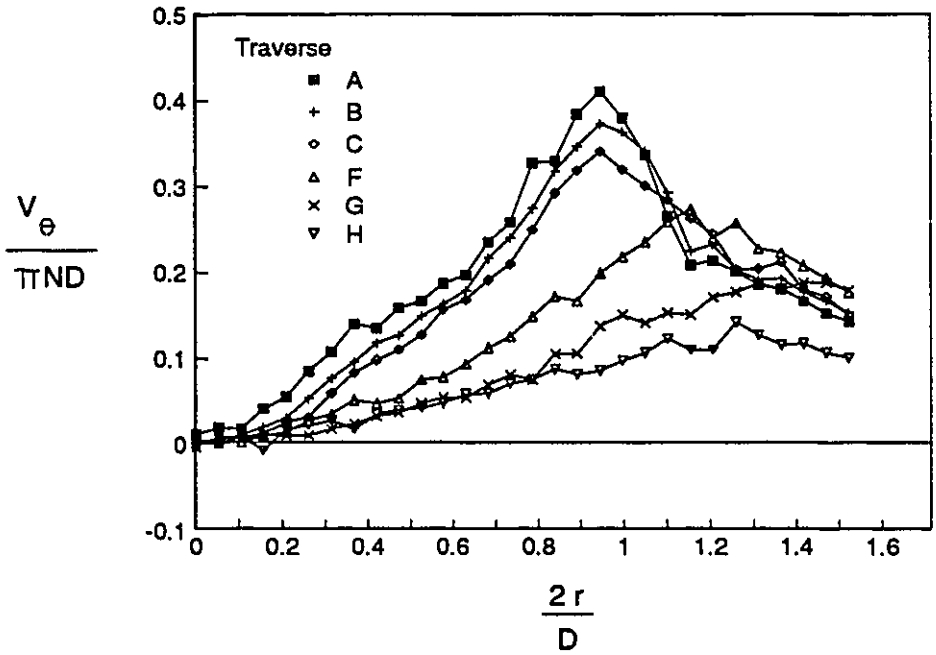

Figure 52. Decay of tangential velocity below the impeller for Case 2; D=T/2, C=T/3.

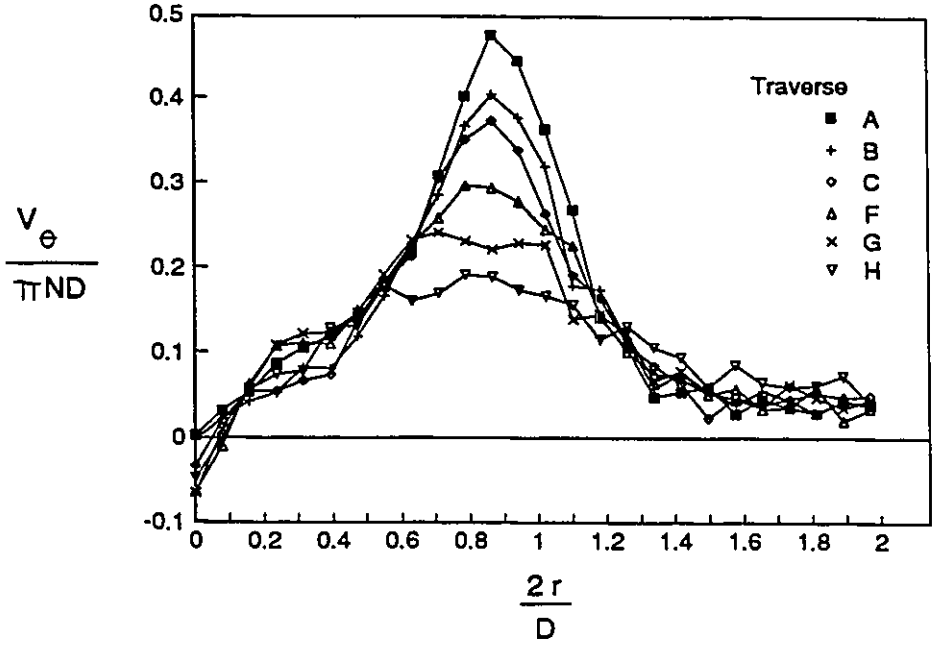

Figure 53. Decay of tangential velocity below the impeller for Case 3; D=T/3, C=T/2.

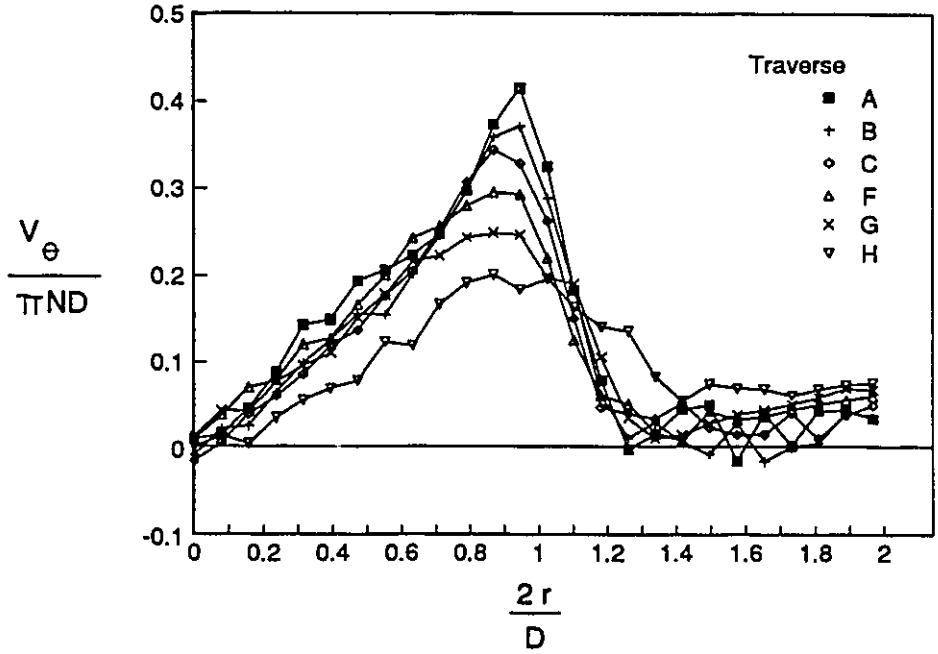

Figure 54. Decay of tangential velocity below the impeller for Case 4; D=T/3, C=T/3.

Examination of the four cases has shown that, while the flow field produced by the PBT in varying geometries is similar, there are substantial quantitative differences between the velocity fields. The further away from the impeller the traverse is performed, the larger the differences observed. Given the flow visualization results presented in chapter 2, which showed differences in the overall circulation pattern in different geometries, these differences are not only not surprising, but are to be expected. With the presence of different flow patterns, the information obtained cannot be reduced to one result using dimensionless variables.

This kind of result makes the PBT a good candidate for computational fluid dynamics experiments, whose main advantage is the ability to examine the effect of variations in geometry quickly, and without repeating time consuming detailed velocity measurements. If a model of the impeller could be defined, and carefully validated for sample geometries, other geometries could be tested computationally. Before such a model can be defined, however, it is necessary to isolate what parameters affect the impeller discharge condition, and to gain as much physical understanding of the impeller discharge as possible. The investigation of these questions is continued in section 1.2 and chapter 7.

4.1.2 Flow above the impeller

To complete the examination of the mean velocity field in the bulk of the tank, axial and radial velocity profiles were measured in the top of the tank. Eight traverses were performed for the geometry D=T/2, C=T/4. Once again, the traverse positions are defined by the projected blade half-width. These experiments were performed at a 6 mm offset from the tank axis to allow the laser beams to pass the

impeller shaft. A test of the effect of y-offset below the impeller showed that the difference in measured velocity due to the offset was not significant beyond a radius of 4 mm.

Although literature reports of the circulation patterns for low clearance impellers frequently show primary circulation loops which extend to the top of the tank (cf. Rewatkar and Joshi (1991)), it is clear from figures 55 and 56 that velocities are very low by a height of z = 12 W/2. The top of the tank is at a height of z = 21.2 W/2, indicating that the main circulation occurs in the bottom 65 to 75% of the tank. The primary circulation loop is clear, especially in the three lower axial velocity profiles. These measurements agree with the results of flow visualization work.

Examination of the top three axial velocity profiles in figure 56 shows no positive velocities. If this were true, it would violate continuity in a mass balance cutting across any of these planes. This indicates that the flow is either dependent on angular position, possibly with all of the upflow behind the baffles; time dependent and unstable; or asymmetric. Bakker and van den Akker (1991) have noted computational instabilities and low velocities in the upper portion of a similar tank. Winardi and Nagase (1991) have reported an unstable, asymmetric flow pattern in the top of a tank agitated by a marine propeller.

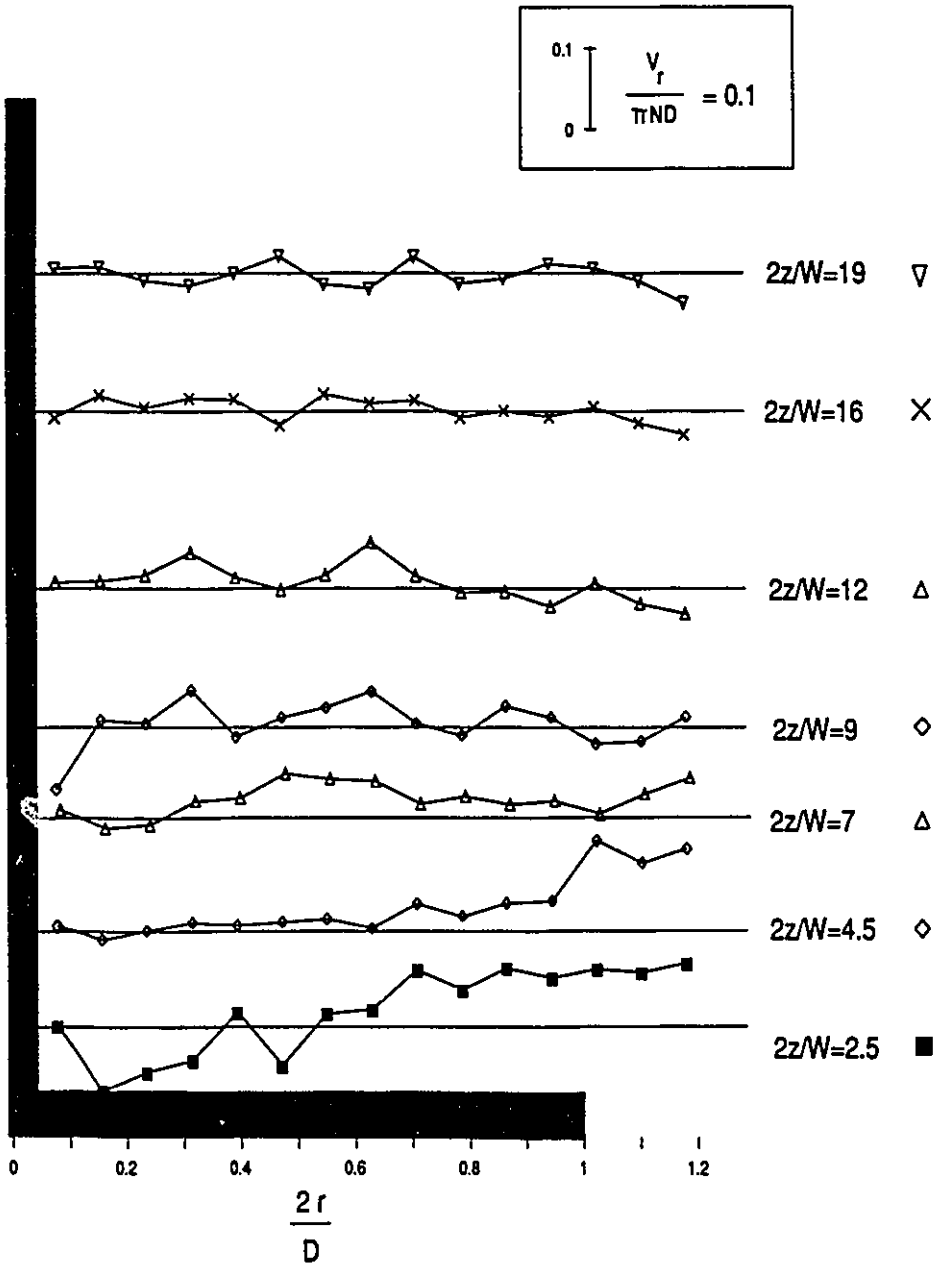

Figure 55. Radial velocity profiles in upper portion of the tank; D=T/2, C=T/4.

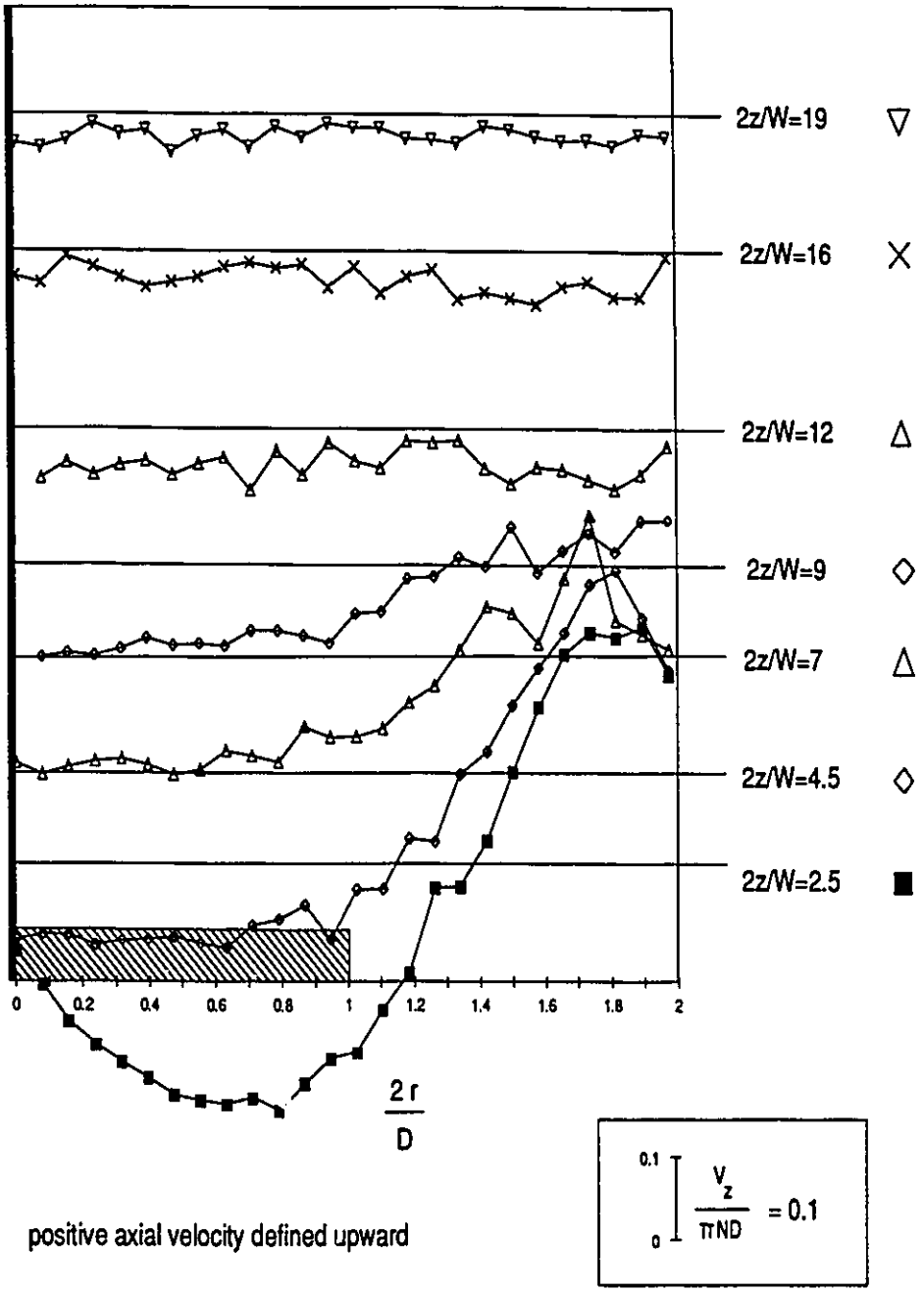

Figure 56. Axial velocity profiles in upper portion of the tank; D=T/2, C=T/4.

4.2 Impeller discharge condition

Since it is the impeller which drives the flow, an accurate representation of the impeller discharge condition (including the three components of the mean velocity, and the turbulence quantities k and ε) is critical to successful modelling and simulation efforts. In chapter 2, and section 4.1.1, it was shown that the flow field in the bulk of the tank depends on the off-bottom clearance, and on the impeller diameter. This sensitivity to tank geometry raises several issues about the generality of the impeller discharge condition, and the design of an impeller model. It becomes necessary to determine whether a PBT generates a flow leaving its periphery that would be the same in any container, or whether the presence of the tank walls is fed back to the impeller and into the impeller discharge stream. Thus either a single boundary condition can be defined, or an impeller model will have to include allowance for the surrounding geometry.

The impeller discharge condition was examined for variations caused by off-bottom clearance and impeller diameter, for variations with angular position in the tank, for half-tank symmetry, for correct scaling with rotational speed, and for the effect of small changes in hub size. Where only one velocity component was examined, the axial velocity profile was chosen as representative, since it gave the clearest means of interpretation in the impeller discharge stream, and is considered the primary velocity component for this impeller. By contrast, less weight was given to the radial velocity results, since these velocities are very small on the mean and exhibit large fluctuations, with relatively poor signal quality.

Unless otherwise stated, these runs were performed for case T7 (see figure 41) at an off-bottom clearance of T/4, with a T/2 impeller rotating at 400rpm. The validated data rate was typically 7kHz (±2.5kHz), at the 1.5% validation level. The sampling frequency was 2.5kHz, with the exception of the T/3 impeller clearance runs and the rotational speed runs, which were sampled at 1kHz. 10 000 data were collected at each point.

Figures 57, 58, and 59 show traverses across the entire tank, as a check on axisymmetry. Very good, if not exact, agreement exists between the two sides of the tank. From this data, there is no reason to believe that there is any fundamental difference in the time averaged flow field from one side of the tank to the other.

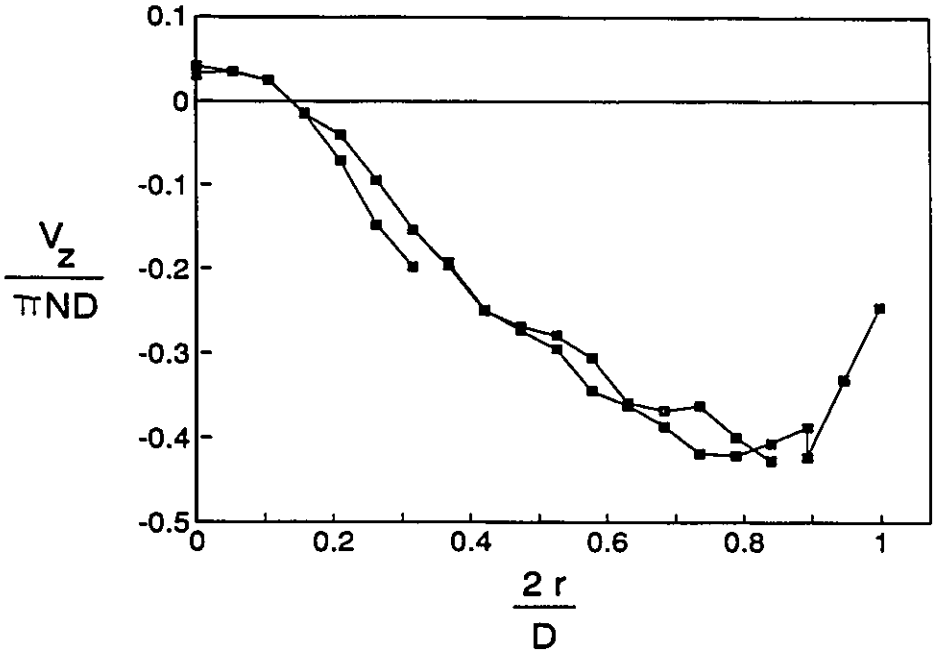

Figure 57. Axisymmetry of axial velocity discharge condition, case T7.

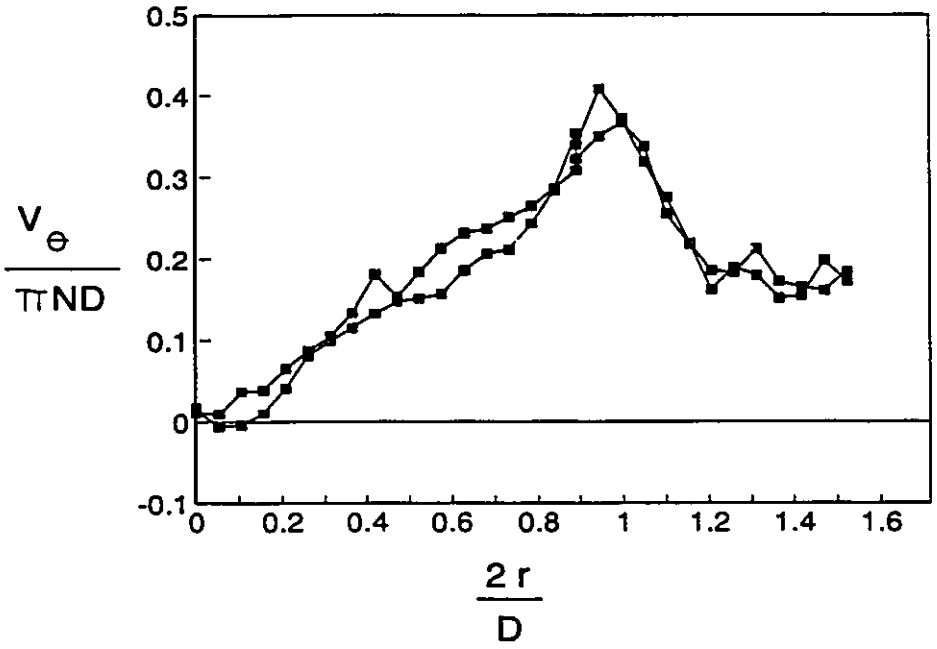

Figure 58. Axisymmetry of tangential velocity discharge condition, case T7.

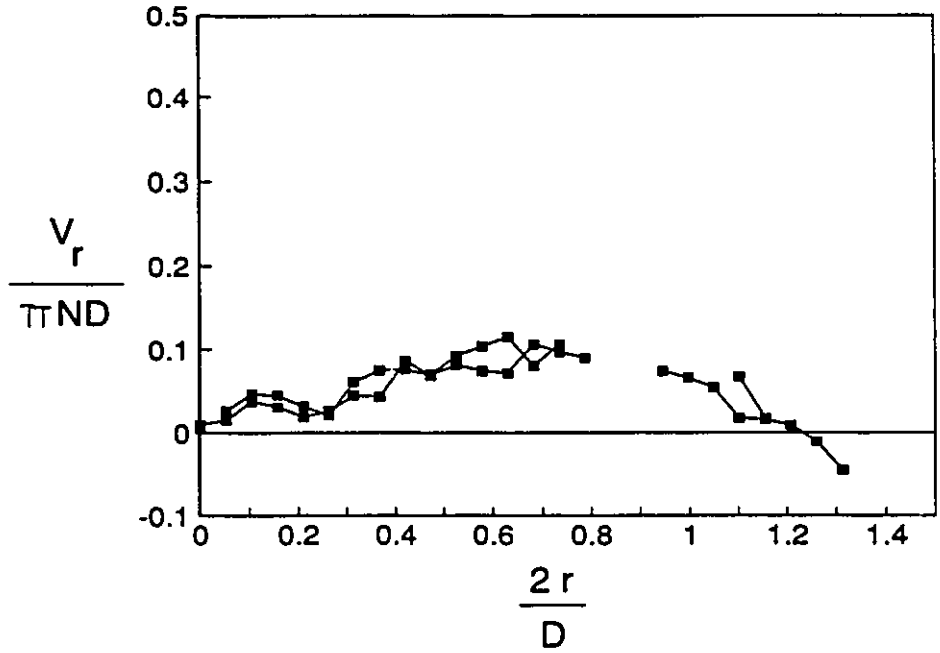

Figure 59. Axisymmetry of radial velocity discharge condition, case T7.

Figures 60, 61, 62 and 63 show the effect of N on the axial, radial, and tangential velocity profiles. The axial velocity profile was checked for both the T/2 and the T/3 impeller. Reynolds numbers ranged from 2.4×10^4 (250rpm) to 5.8×10^4 (600rpm) for the T/2 impeller, and 1.72×10^4 (400rpm) to 2.6×10^4 (600rpm) for the T/3 impeller. At a Reynolds number of 9.7×10^3 (100rpm), the T/2 impeller discharge condition changes, showing that it is no longer in the fully turbulent range. Within the fully turbulent range, all profiles scale with the impeller tip speed independent of the Reynolds number, as is known to be the case for other impellers.

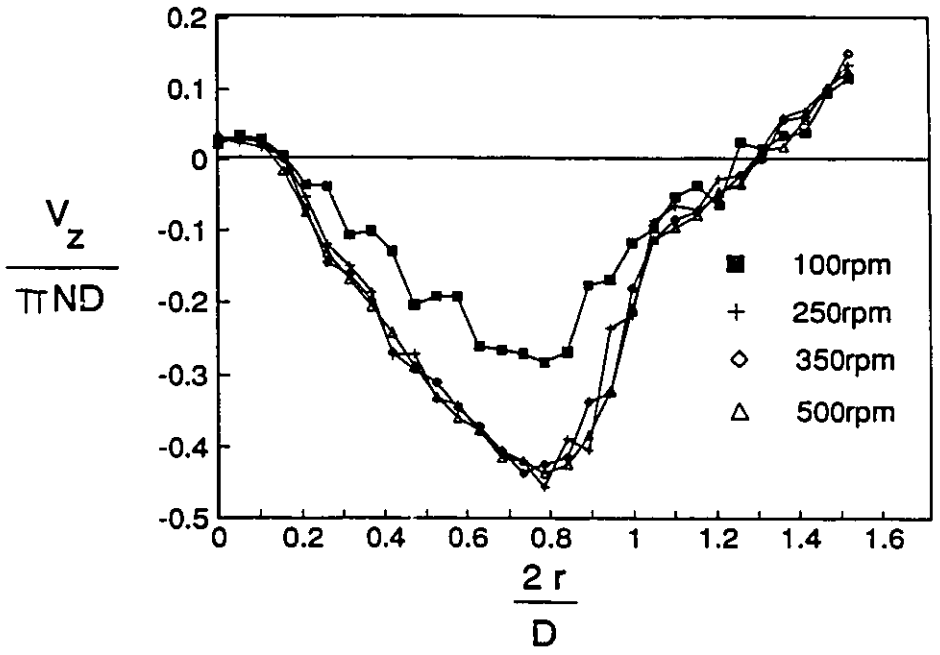

Figure 60. Scaling of axial velocity with tip speed for the T/2 impeller, C=T/4.

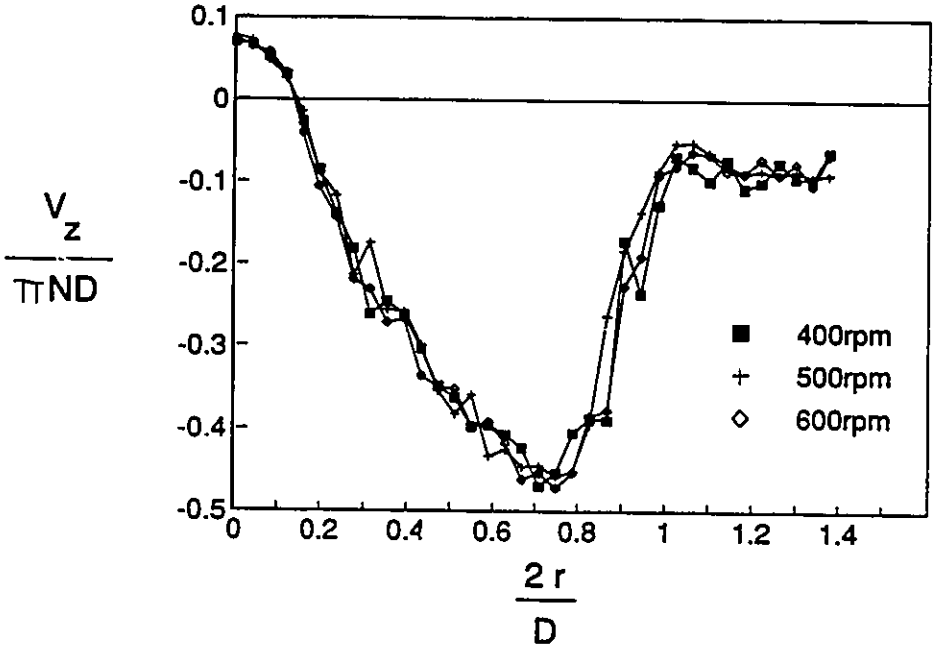

Figure 61. Scaling of axial velocity with tip speed for the T/3 impeller, C=T/4.

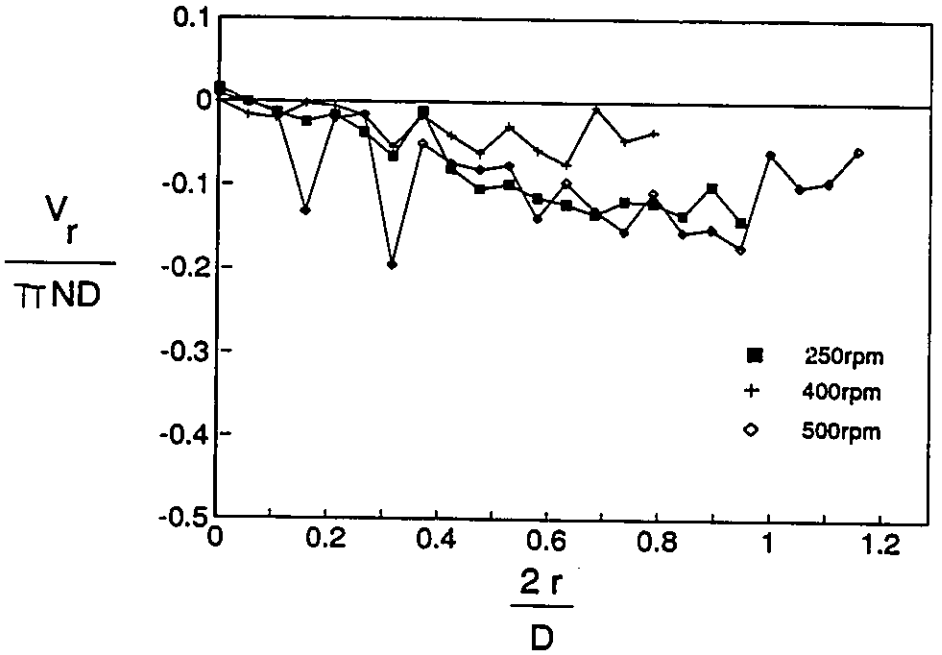

Figure 62. Scaling of radial velocity with tip speed for the T/2 impeller, C=T/4.

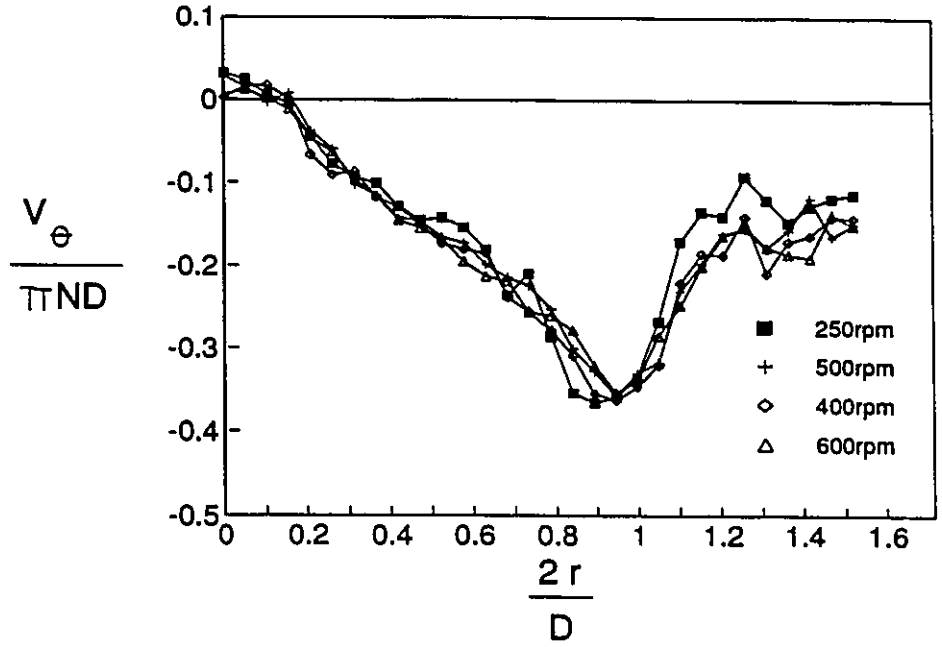

Figure 63. Scaling of tangential velocity with tip speed for the T/2 impeller, C=T/4.

It has been shown (Costes and Couderc (1988), Kresta and Wood (1991)) that the flow field in a fully baffled stirred tank is 3 dimensional, especially in the vicinity of the baffles. Figures 64, 65, and 66 address the effect which this three dimensionality has on the impeller discharge condition. The angular position is defined relative to the baffle, starting with zero degrees at the baffle, and increasing in the direction of impeller rotation. Three angular positions, 22.5°, 45°, and 90° were examined. There is no discernable effect of angular position on the impeller discharge condition; it can be considered axisymmetric over the full 360°. These results should not be interpreted as showing that the entire flow field is completely axisymmetric, since they examine only one axial location (directly below the impeller), and do not extend all the way to the tank wall (2r/D=2). The baffle areas were not examined in detail; nor was the bulk of the tank.

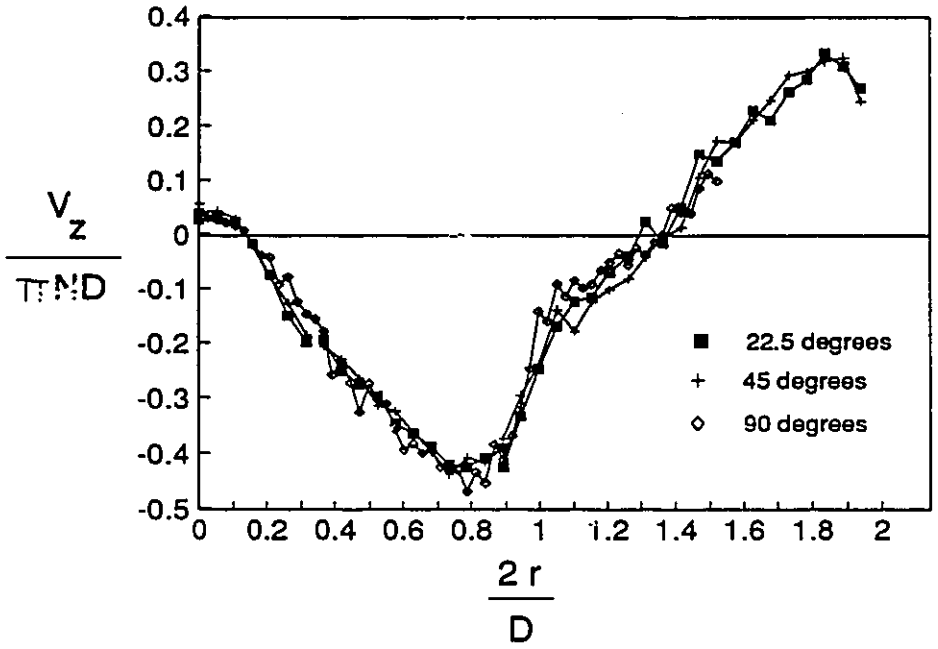

Figure 64. Variation of axial velocity profile with angular position, case T7.

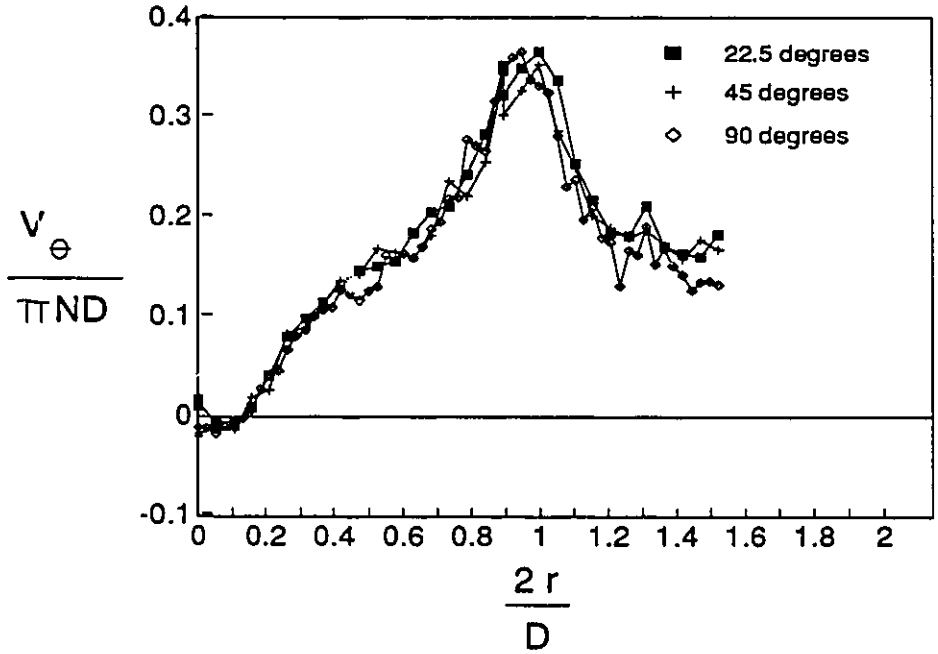

Figure 65. Variation of tangential velocity profile with angular position, case T7.

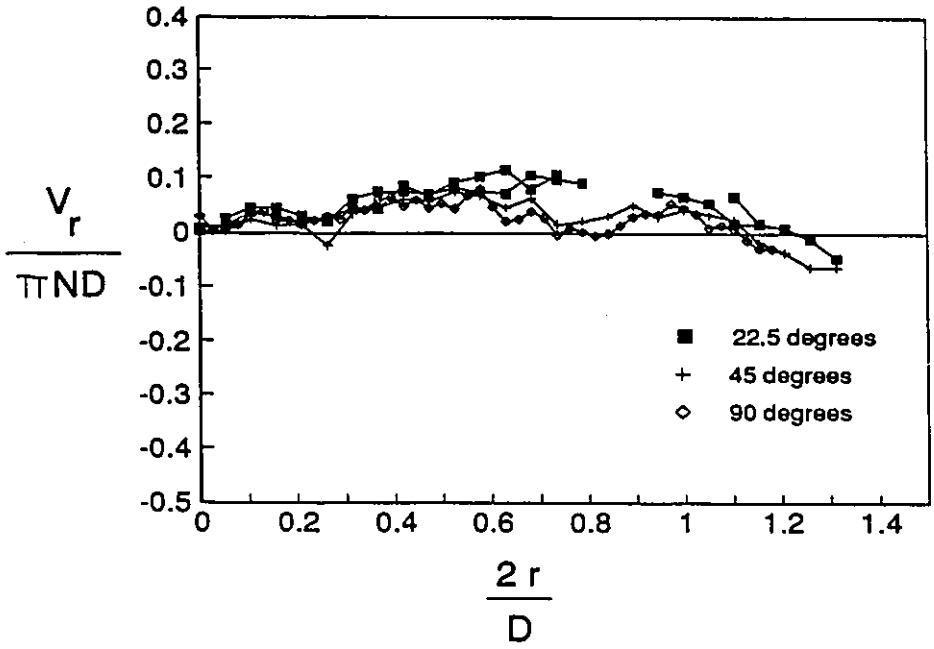

Figure 66. Variation of radial velocity profile with angular position, case T7.

There has been increasing concern in the literature with exact geometric scale-up of stirred tanks, including details such as the blade thickness (Bujalski et al. (1987), Tatterson et al. (1980)). The two impellers used in this study were made from the same stock, and while no attempt was made to examine the effect of blade thickness, it was considered that the hub size might be of some importance. Using putty, the hub on the T/2 impeller was built up to have the same dimensionless size as the hub on the T/3 impeller, and the resulting axial velocity profile was compared with that of the original impeller. The results are shown in figure 67. The original hub extends to 2r/D=0.16, and the built up hub to 0.25. The larger hub induces a small zone of upflow under the impeller, but beyond 0.25, the profile rapidly aligns itself with the profile produced with the smaller hub.

Note the change in slope of the large hub velocity profile at the point where the two profiles coincide. In many of the velocity profiles reported, there is a similar change in slope at some point in the profile. Extension of the outer slope back towards the origin frequently results in a (0,0) intercept. This brings to mind Fort's (1986) model for the PBT, which proposes a linear velocity profile from the origin to the point of maximum velocity. The fundamental weakness of this modelling approach is that it is necessary to know the slope and the point of maximum velocity in the velocity profile before the model can be applied. Once the velocity profile is known, a model for it is no longer useful, unless this model can be extended to predict results for other configurations. This extension would require the assumption of a constant velocity profile under changing configurations. The validity of this assumption, fundamental to all modelling work which does not consider the surrounding geometry, is addressed next.

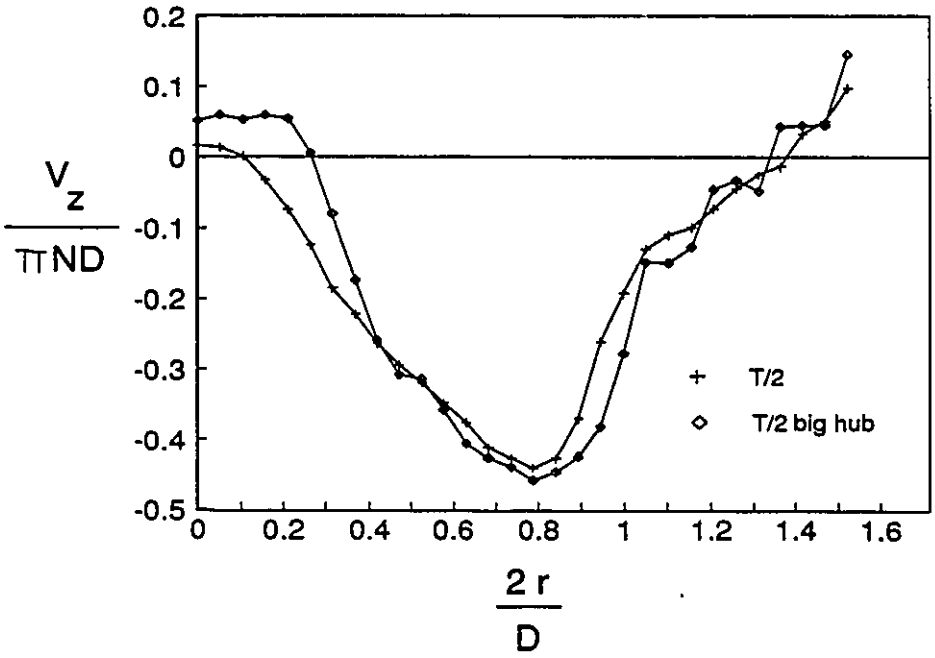

Figure 67. Effect of hub size on axial velocity profile.

In the examination of the impeller discharge stream at the beginning of this chapter, it was shown that the flow field depends on the off-bottom clearance, and the impeller diameter. To gain a better understanding of the impact of these variables on the impeller discharge condition, axial velocity profiles were studied for two impellers and several clearances. The clearances were varied from the minimum clearance still allowing laser beam access to a clearance of 1.5 times the impeller diameter; in increments of 6.35mm (1/4 inch). The two impellers were of T/2 and T/3 diameter. Clearances are reported in terms of C/D (clearance/impeller diameter), not in fractions of the tank diameter, because the impeller diameter is the characteristic dimension. It was found that this allowed better comparison of the two impellers of interest.

The results are presented in three parts; first, the T/3 impeller is examined, second, the T/2 impeller, and last, a comparison of the two. It was found that each impeller had two or more characteristic axial velocity profiles, and that the shift from one profile to another occurred over a very narrow range of clearances. Figure 68 shows the high clearance axial velocity profile for the T/3 impeller, with the data from all six associated traverses. The profiles collapse onto a single curve for all clearances from C/D=1.5 to 0.75. Figure 69 shows the second profile for the T/3 impeller, this time over a much narrower range of clearances, from C/D=0.59 to 0.5. Below a C/D ratio of 0.5, the T/3 impeller discharge condition is strongly affected by the proximity of the tank bottom, as is apparent from figure 70. This last figure combines the two characteristic profiles from figures 68 and 69 with the data for the two lowest traverses. The difference between the profiles is clear, and the transition

is sharp. The high clearance discharge condition peaks at a radial position of 2r/D=0.7, the low clearance at 0.8. As the bottom is approached, the peak moves further out into the tank, and the maximum decreases.

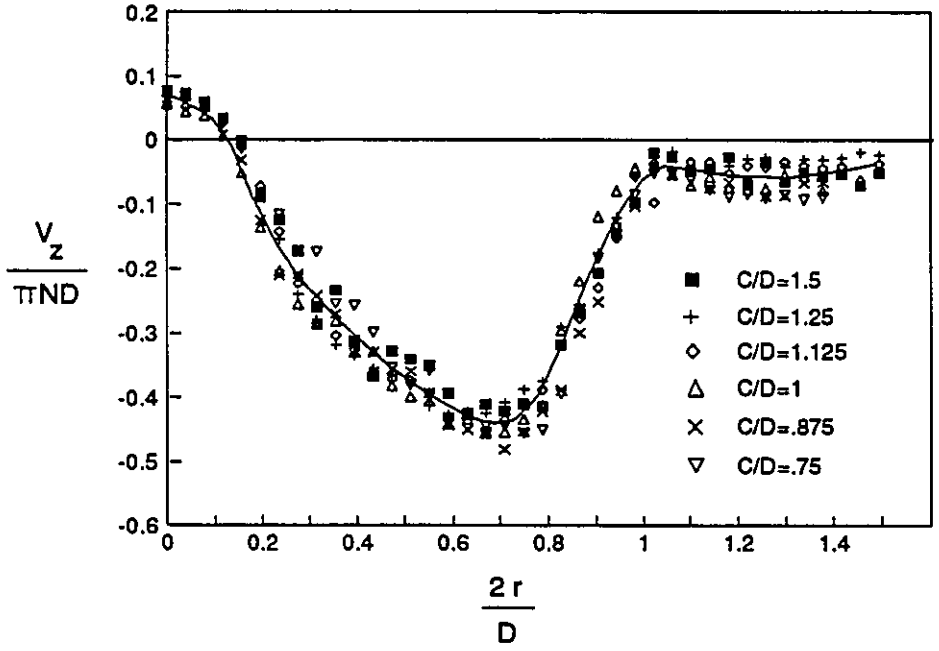

Figure 68. High clearance discharge condition for T/3 impeller.
C/D = 1.5 to .75

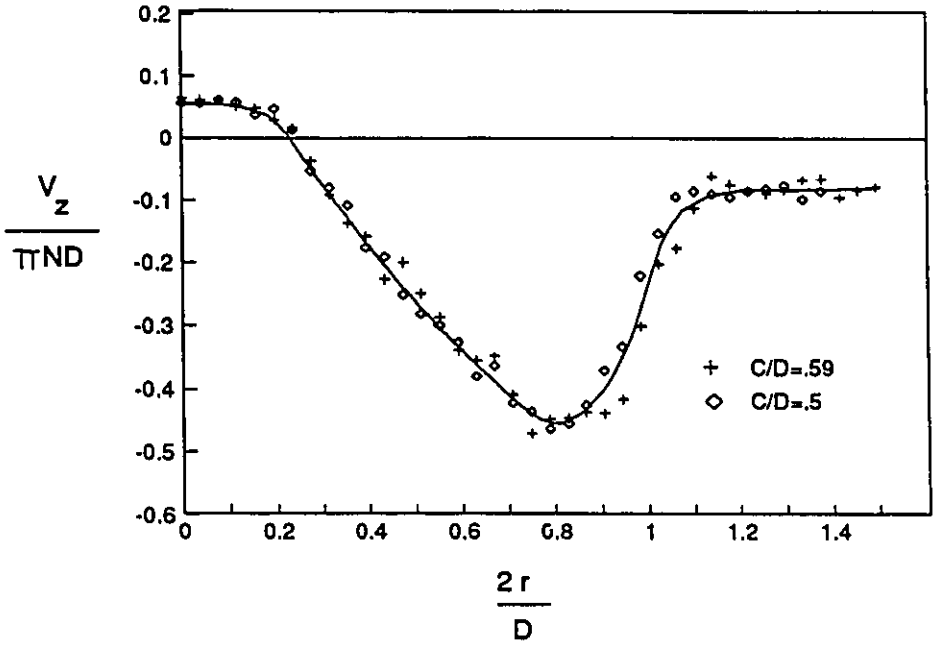

Figure 69. Low clearance discharge condition for T/3 impeller.
C/D = 0.59 to .5

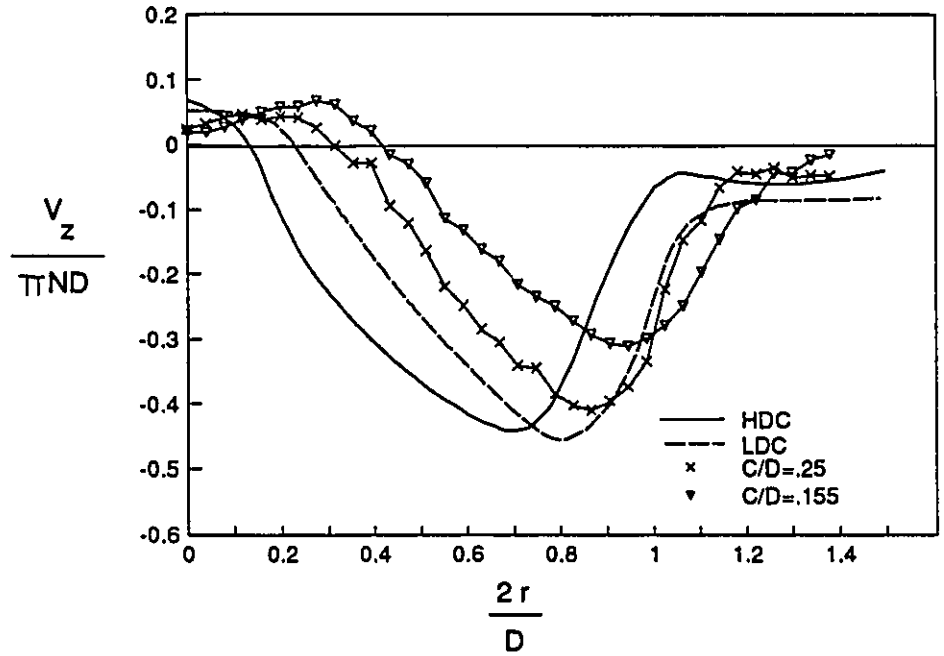

Figure 70. Impeller discharge conditions for the T/3 impeller.

The data for the T/2 impeller follows a similar pattern. Figure 71 shows the high clearance axial velocity profile, which applies from C/D=1 to 0.667. The second profile is shown in figure 72, applicable from C/D=0.583 to 0.33. The two characteristic profiles and a low traverse at C/D=0.25 are combined in figure 73. Once again, the difference between traverses is clear, and the transition is sharp. With the T/2 impeller, however, the velocity peak does not start towards the center of the tank at the highest clearance and move radially outward as the clearance is decreased. Instead, the radial position of the maximum velocity peak in the high clearance discharge condition almost coincides with the radial position of the peak for the lowest clearance tested. The low clearance discharge condition has a peak position closer to the tank axis, and then the profile starts to decay as the bottom is approached. This apparent reversal of trends between the two impellers can be explained by recalling the flow visualization results. At a clearance of T/2, a secondary circulation loop appears in the bottom of the tank for both impellers. For the T/2 impeller, this loop is clear, and strong, while for the T/3 impeller, it is unstable and less evident. It appears that this counter-rotating flow in the bottom of the tank deflects the impeller discharge towards the tank wall (compare figures 8 and 15 in chapter 2). This displacement of the discharge flow is reflected in the displacement of the axial velocity profile, and in the increase of radial velocity observed in figure 47. The transition in the axial velocity profile appears even within 1.5mm of the impeller blades, indicating significant feedback from the tank to the impeller (ie. the tank geometry affects not only the overall flow field, but also the impeller discharge condition).

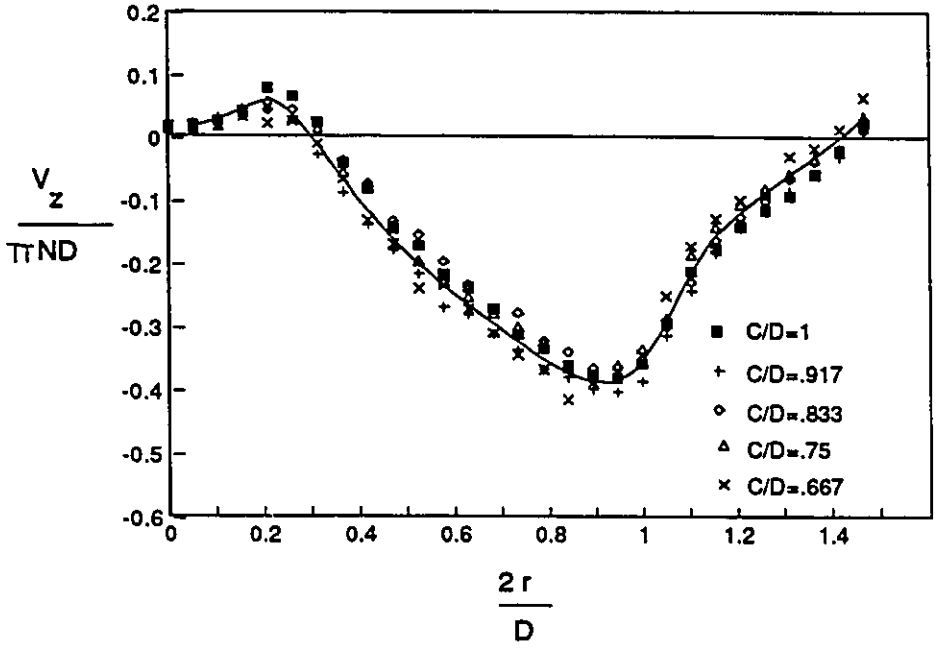

Figure 71. High clearance discharge condition for T/2 impeller.
C/D = 1 to .667

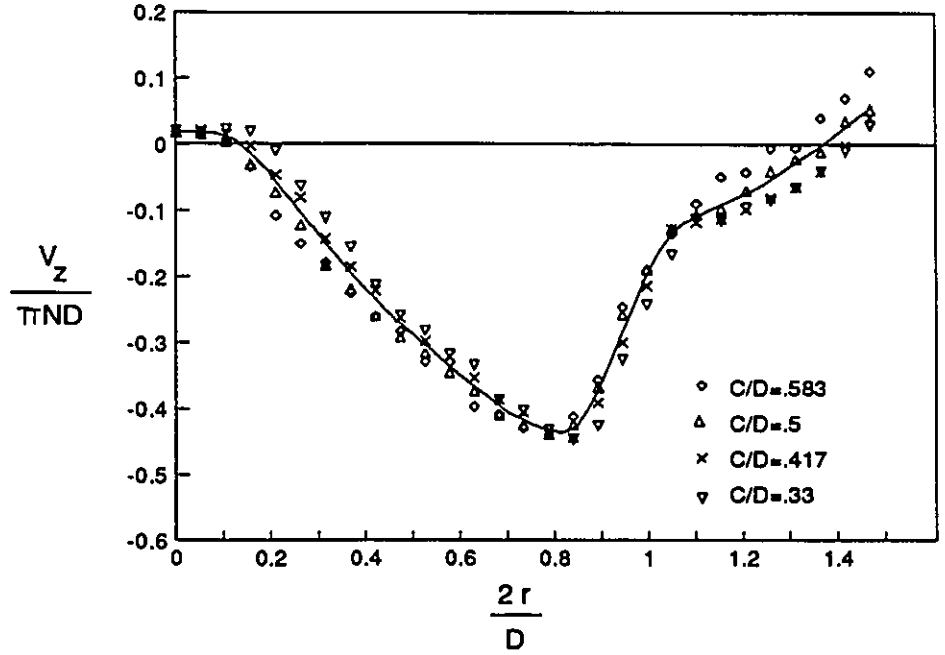

Figure 72. Low clearance discharge condition for T/2 impeller.
C/D = 0.583 to .333

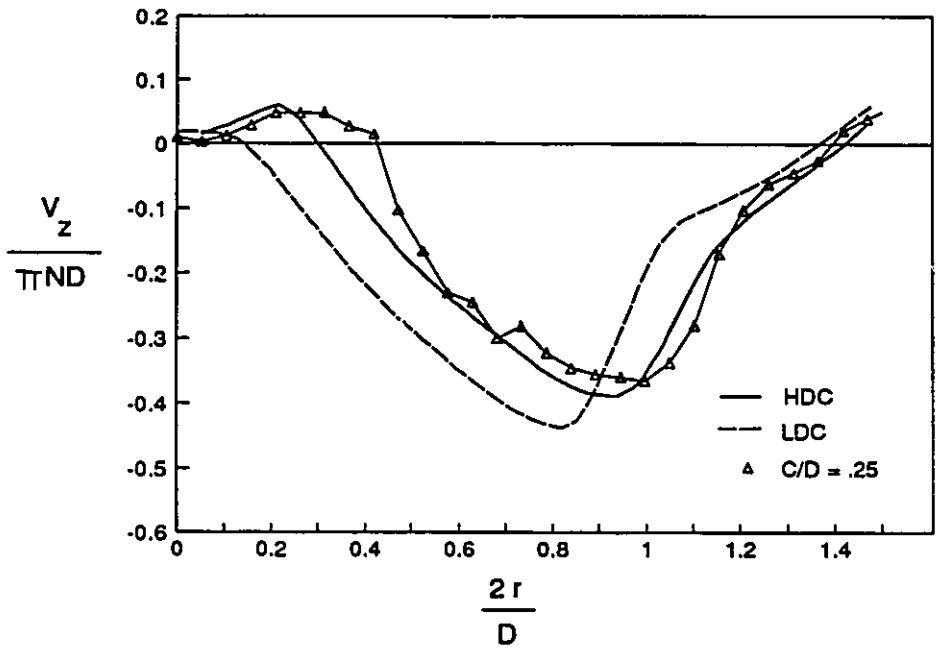

Figure 73. Discharge conditions for the T/2 impeller.

All four characteristic profiles are grouped together in figure 74. There are two things to note here. The first is that the transition between profiles happens at the same C/D ratio for both impellers. The second is that the low clearance discharge conditions (where the effects of the secondary circulation loop are removed) roughly coincide over the extent of the impeller blades. If the hub effects shown in figure 27 are considered, the agreement between the two profiles becomes even greater.

Nouri and Whitelaw (1990) reported a similar sudden transition between circulation patterns in their examination of low Reynolds number tank flows with high viscosity fluids. Their transition point occurred a Reynolds number of 650. The effect of clearance was not examined. Ranade and Joshi (1989) report data showing the same behavior of the velocity profile with varying clearance in their figure 10. They consider a D=T/3 impeller with six blades having W/D=0.3. Using

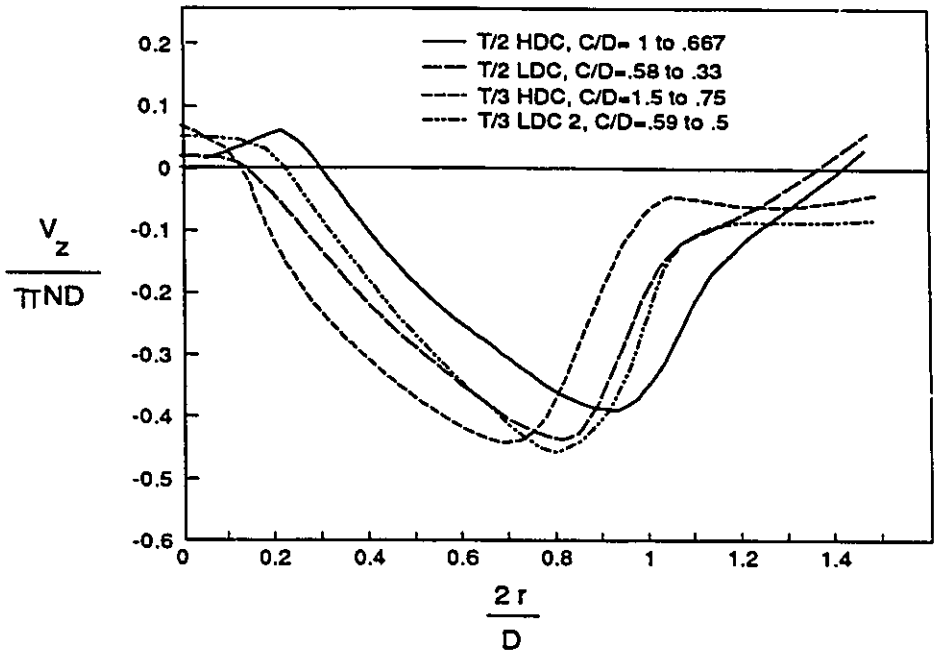

Figure 74. Comparison of D=T/2 and D=T/3 axial velocity discharge conditions.

their figure 14A, which gives the effect of blade width on the velocity profile; the two results can be compared. Ranade and Joshi report profiles for C/D=1.5, 1.0, 0.75, and 0.5. The peak in the axial velocity profile shifts outward at C/D=0.5 by a dimensionless radial distance of 0.1 (from 2r/D=0.9 to 2r/D=1.0), while the maximum axial velocity is reduced by 0.1. The results given here do not show a decrease in the maximum axial velocity, but the radial displacement and the C/D location of the shift are the same as those shown in the data by Ranade and Joshi.

Given this information about the ranges over which the various impeller discharge conditions apply, let us return for a moment to the four cases for which the impeller discharge was examined in the bulk of the tank. Case 1, for the T/2 impeller, is at a C/D of 0.93 - corresponding to the high clearance impeller discharge condition with the secondary circulation loop. Case 2, for the T/2 impeller, falls in

the range of the low clearance discharge condition, with C/D=0.59. Cases 3 and 4, for the T/3 impeller, both fall in the range of the high clearance impeller discharge condition; C/D=1.43 and 0.93 respectively. Comparison of the axial, radial, and tangential velocity profiles at 2z/W=-1.0 for these four cases are shown in figures 75, 76, and 77. There is consistently good agreement between the case 3 and 4 profiles, and significantly different results for the case 1 and 2 profiles. This is consistent with the defined transition regimes.

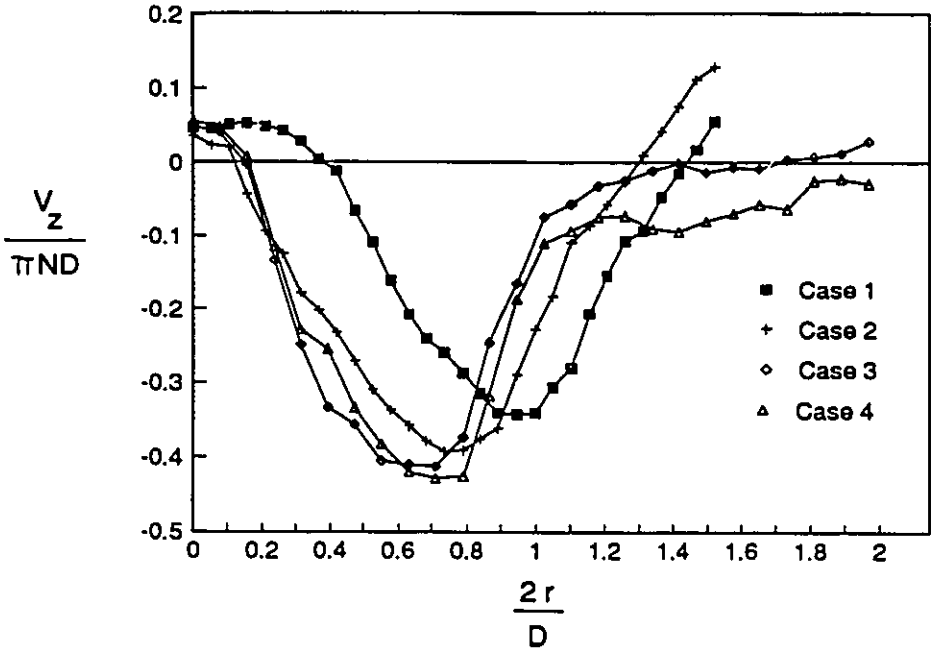

Figure 75. Comparison of cases 1 to 4 at 2z/W = -1.0: axial velocity.

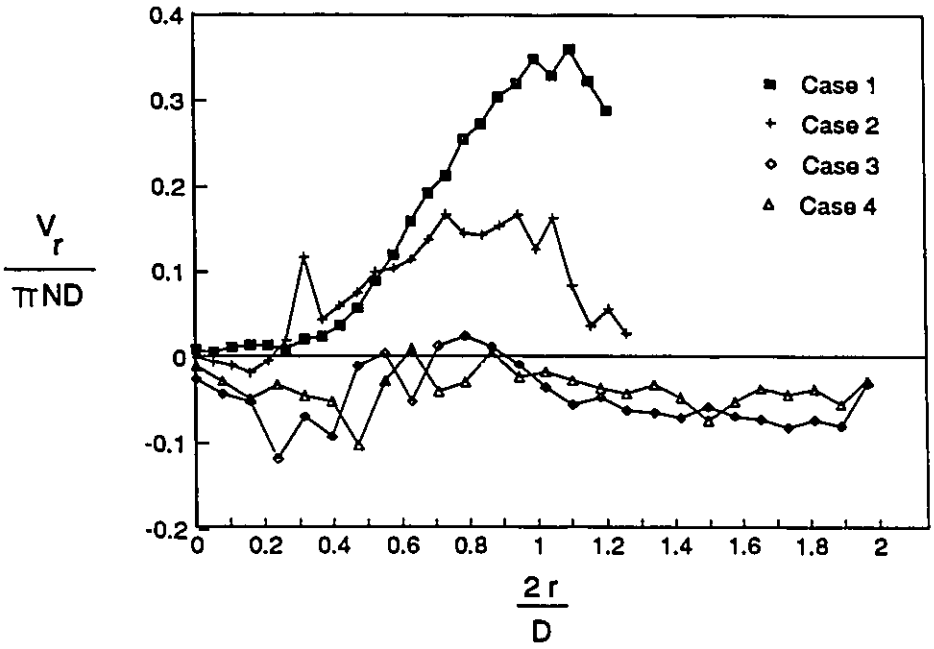

Figure 76. Comparison of cases 1 to 4 at 2z/W = -1.0: radial velocity.

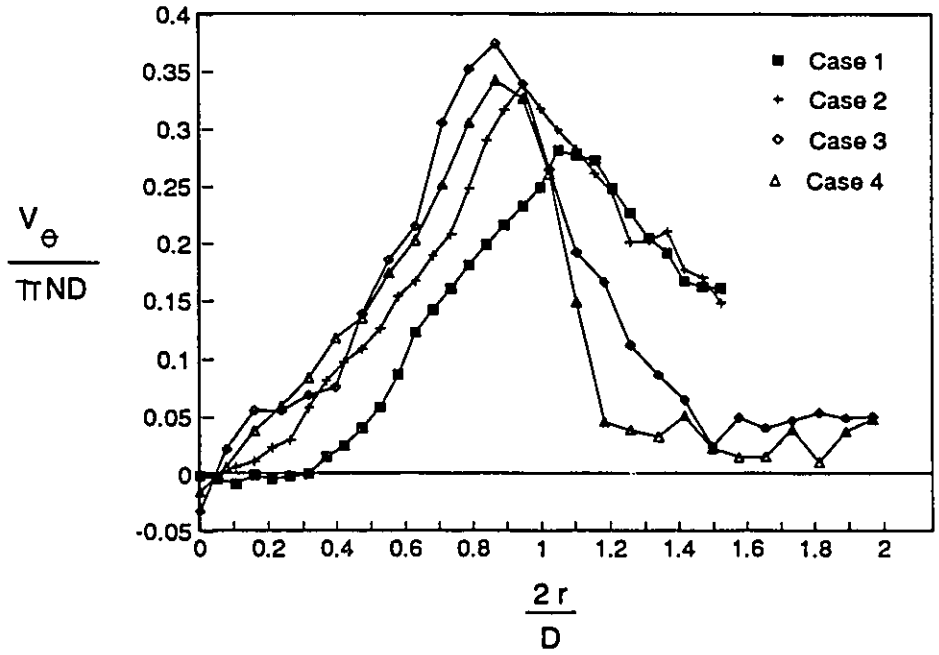

Figure 77. Comparison of cases 1 to 4 at 2z/W = -1.0: angular velocity.

If the three components of velocity are combined into a single, resultant velocity at 2z/W=-0.1, the profiles appear much more similar. This is shown in figure 78. If a slightly lower traverse at 2z/W=-1.0 is considered (figure 79), the differences and similarities between cases reappear. It must be emphasized that this last approach compares only the magnitude of the velocity vector; all directional information is lost. Examination of individual velocity components for the four cases at 2z/W=-0.1 reveals some significant differences.

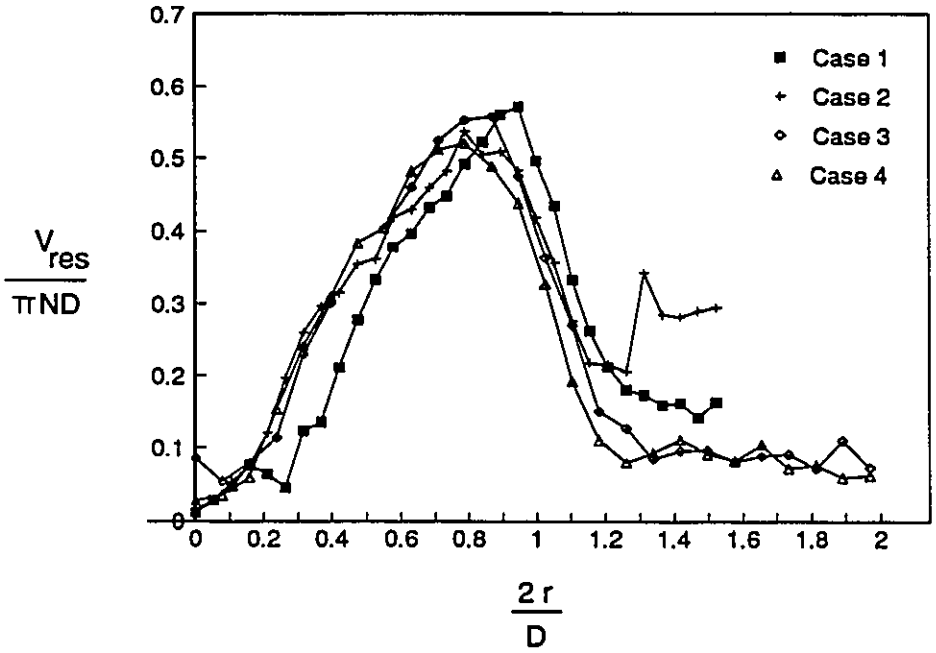

Figure 78. Comparison of cases 1 to 4 at 2z/W = -0.1: resultant velocity.

The last variable which is considered is the effect of scale on the flow. Due to the limited amount of information available about the PBT, this is a difficult issue to address. Industrial vessels are typically of the order of 2m in diameter. Tatterson et al. (1980) reported different flow phenomena for a scale-up factor of three, from a six bladed to a four bladed impeller. It was not clear whether this was due to the

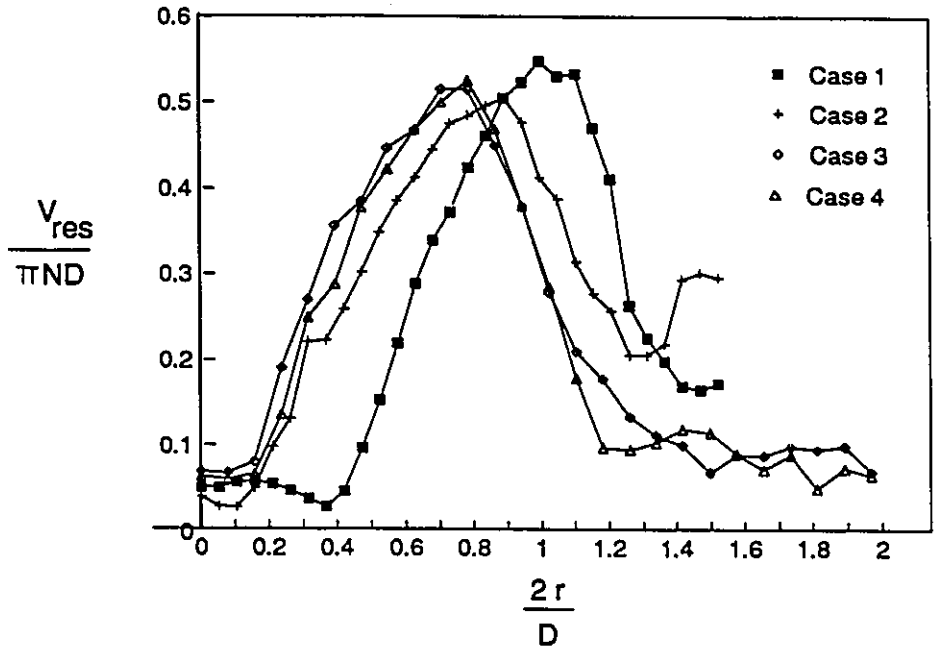

Figure 79. Comparison of cases 1 to 4 at 2z/W = -1.0: resultant velocity.

scaling, or to the change in the number of blades. The tank used in the present work has a diameter of 150mm, with a four bladed impeller. Ranade and Joshi (1989) report experiments in 300mm and 500mm tanks, with a six bladed impeller. Three sets of axial velocity data are compared to the high clearance discharge condition for a T/3 impeller in figure 80. The six blade data is from Ranade and Joshi (1989); the 4 bladed data and the low clearance impeller discharge condition are from this work. Agreement over the extent of the impeller blades (up to 2r/D=1.0), while not exact, is very good; it is certainly within the range of the data used to define the impeller discharge condition.

Conclusions

Detailed examination of the mean velocity field at the discharge of a PBT has led to the following conclusions:

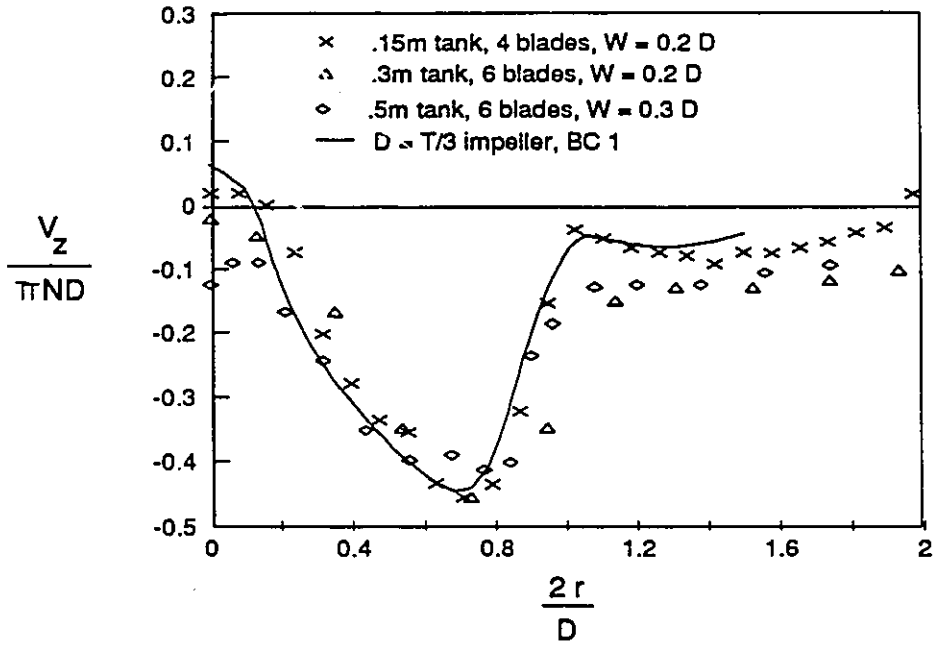

Figure 80. Effect of scale on axial velocity profile. Results for the six bladed impeller are from Ranade and Joshi (1989).

1) The circulation flow does not necessarily extend to the top of the tank.

2) At a Reynolds number of $2.4x10^4$, the flow is fully turbulent.

3) Above this Reynolds number, the mean velocity profiles scale with the tip speed.

4) The impeller discharge condition can be considered axisymmetric.

5) Variations in hub size due to scale-up have only a small effect on the velocity profile. An explanation of these effects may be useful for model development.

6) The effect of scale on the time averaged axial velocity discharge condition is very small, if it exists at all.

7) The impeller discharge condition, and the overall circulation patterns, are affected by the proximity of the tank walls.

8) This effect is not continuously varying, but undergoes definite transitions at well defined positions.

9) The impeller discharge condition is independent of impeller diameter for some clearances, but not for others. This is due to the formation of a secondary circulation loop at higher clearances of the T/2 impeller. This secondary circulation loop displaces the impeller discharge stream, changing the axial velocity profile, and increasing the radial velocity.

10) Any predictive model of the PBT must be able to account for differences in the discharge condition due to impeller placement and size.

11) Simulations of the flow field using computational fluid dynamics should be verified for several different configurations before they are used for predictive purposes in new geometries.

4.3 Pumping, or flow number

The flow number is used to characterize the amount of circulation provided by an impeller. It is defined as

$$N_q = \frac{Q}{ND^3} \tag{14}$$

where Q is the volumetric flow rate. Two definitions of Q have commonly been applied in the literature. The first uses the normal component of velocity at the discharge surface of the impeller, and integrates it from the center of the impeller, to the blade tip.

$$Q = 2\pi \int_0^{D/2} r V_z dr \tag{15}$$

This quantity gives what is often called the "primary flow number." Another quantity, the "total flow number," is obtained by integrating from the center of the impeller, to the velocity zero crossing at the eye of the primary circulation loop. The primary flow number was found to give more repeatable results for the pitched blade turbine. It is tabulated, for all of the clearances and diameters studied, in table 2.

The mean flow numbers for each discharge condition (as defined in the last section) were examined, using a t-test, to determine if there was a significant difference between them. At the 90% confidence level, none of the differences were found to be significant. Within the accuracy of the experiments performed, there is no significant dependence of the flow number on off bottom clearance. The overall mean flow number was calculated, excluding clearances with C/D < 0.33. The value obtained was 0.789. This is somewhat lower than the value of 0.85 reported by Ranade and Joshi (1989). It would appear, however, that their result is based on only one traverse for the T/3 impeller at a C/D=1.0. From Table 1, it is clear that this single value is well within the range of observations for these conditions. Oldshue (1983, table 8-3) reports flow numbers of 0.75 and 0.79, which agree extremely well with this data.

Table 2: Flow numbers calculated for varying clearance and impeller diameter.

D=T/2			D=T/3		
C/D	Nq	mean	C/D	Nq	mean
			BC 1		
1.5	.782		1.5	.721	
1.25	.759	.758	1.25	.721	
1.25	.732		1.125	.765	.793
BC 1			1	.837	
1	.640		.875	.885	
.917	.725		.75	.829	
.833	.614	.832	BC 2		
.75	.641		.591	.838	
.667	.706		.5	.767	.758
BC 2			.5	.668	
.583	.802		decay		
.5	.802		.335	.709	
.417	.792	.798	.25	.594	
.333	.795		.25	.637	
decay			.155	.349	
.25	.607				

4.4 References

Ali, A. M., H. H. S. Yuan, D. S. Dickey, and G. B. Tatterson, "Liquid dispersion mechanisms in stirred tanks: Part 1, Pitched blade turbine," Chem. Eng. Comm., v. 10, pp. 205-213, 1981.

Bakker, Andre, and H. E. A. van den Akker, "A Parametric study of the internal structure of stirred gas-liquid dispersions," Mixing XIII, Banff, Canada, June 10-15, 1991.

Bujalski, W., A. W. Nienow, S. Chatwin and M. Cooke, "The dependency on scale of power numbers of Rushton disc turbines," Chem. Eng. Sci., v. 42, pp. 317-326, 1987.

Costes, J. and J. P. Couderc, "Study by laser Doppler anemometry of the trubulent flow induced by a Rushton turbine in a stirred tank: influence of the size of the units - I Mean flow and turbulence," Chem. Eng. Sci. v. 43, pp 2751-2764, 1988.

Fort, Ivan, "Flow and turbulence in vessels with axial impellers," in Mixing: Theory and Practice v. 3, V.W. Uhl and J.B. Gray, eds., Academic Press, Toronto, 1986.

Kresta, S. and P.E. Wood, "Prediction of the three dimensional turbulent flow in stirred tanks," AIChE Journal, v. 37, pp. 448-460, 1991.

Nouri, J. M. and J. H. Whitelaw, "Flow characteristics of stirred reactors with Newtonian and non-Newtonian fluids," AIChE Journal, v. 36, pp. 627-629, 1990.

Oldshue, James Y., Fluid Mixing Technology, McGraw Hill, New York, 1983.

Ranade, V. V., and J. B. Joshi, "Flow generated by pitched blade turbines I: measurements using laser Doppler anemometer," Chem. Eng. Comm., v. 81, pp. 197-224, 1989.

Rewatkar, V. B. and J. B. Joshi, "Effect of impeller design on liquid phase mixing in mechanically agitated reactors," Chem. Eng. Comm., v. 102, pp. 1-33, 1991.

Tatterson, Gary B., H. S. Yuan, and R.B. Brodkey, "Stereoscopic visualization of the flows for pitched blade turbines," Chem. Eng. Sci., v. 35, pp. 1369-1375, 1980.

Winardi, Sugeng, and Yoichi Nagase, "Unstable phenomenon of flow in a mixing vessel with a marine propeller," J. Chem. Eng. Japan, v. 24, pp.243-249, 1991.

Chapter 5. Characterization of turbulence in a stirred tank

While it is the mean flow field which governs circulation times, dead zones, and macro-mixing, it is the turbulent flow field which governs the flow on the small scale. The turbulent flow phenomena dominate the transport processes (heat, mass, and momentum transfer), and thus reaction rates, and mixing times. Since prediction of these phenomena is the ultimate objective, the solution of the turbulent flow field is central to solution of the larger problem. In this chapter, turbulence theory as it pertains to stirred tanks is presented. The nature of classical turbulence and of turbulence in this flow field is discussed; the classic equations and assumptions used to describe the physical phenomenon are recounted; and then the methods currently used for predicting, measuring, and otherwise estimating the quantities of interest are reviewed. Careful attention is given to the assumptions required to obtain the standard equations of turbulence, and to the validity of these assumptions in a complex flowfield.

5.1 The nature of turbulence

Tennekes and Lumley (1972) decline to give a precise definition of turbulence, relying instead on a list of its characteristics: irregular, diffusive, three-dimensional, rotational, dissipative, and occuring at high Reynolds numbers. Hinze (1987) gives the following definition, "Turbulent fluid motion is an irregular condition of flow in which the various quantities show a random variation with time and space coordinates, so that statistically distinct average values can be discerned." Over much of the volume of a stirred tank, either of these conceptual definitions can

be applied with no reservations. Close to the tip of the impeller blades, however, the trailing vortices discussed in chapter 1, and shown in chapter 2, lead to some questions regarding irregularity. The vortices impose a periodicity on the instantaneous velocity, which occurs at exactly the frequency of the blade passages. Because these fluctuations are not completely random, several questions arise: Should they be included with the turbulence? Can the flow field be considered stationary? Is the mean velocity meaningful; or is most of the useful information lost in the averaging process (as is the case for the mean of a sine wave)? Can an impeller model which does not explicitly deal with these vortices provide any useful information about the turbulence? How should measurements be performed? Do the standard turbulence models still apply? Before these questions can be addressed, it is important to define the nature of turbulence.

The quantity central to all turbulence studies is the fluctuating velocity, u_i'. This is defined as follows:

$$u_i' = u_i - \overline{U_i} \tag{16}$$

where u_i is the instantaneous velocity, and $\overline{U_i}$ is the time averaged (mean) velocity. The instantaneous velocity is divided into two components in order to isolate the study of the turbulent flow field from that of the mean flow field. Some authors (Tropea et al. (1989), Evans (1975)) suggest that a further separation is necessary for a flow field containing regular oscillations.

$$u_i' = u_i - (\overline{U_i} + \tilde{u}_i) \tag{17}$$

In this representation, $\overline{U_i}$ and u_i are defined as before. $\tilde{u}_i$ is the regular oscillatory component, and the sum $\overline{U_i}+\tilde{u}_i$ is the ensemble average velocity for that point in the oscillatory cycle. In the stirred tank literature, several authors have used the ensemble average velocity very successfully to illuminate the structure of the trailing vortices produced by a Rushton turbine (Yianneskis et al. (1987), Calabrese and Stoots (1989), Van't Riet and Smith (1975), Van der Molen and Van Maanen (1978)). Van't Riet and Smith (1976) and Rao and Brodkey (1972) concluded that the turbulence in the impeller discharge stream is highly anisotropic because of the presence of the periodic component. They claim that it is necessary to remove the "pseudo-turbulence" from the signal before the turbulence can be properly characterized. Various ways of doing this have been proposed (Wu and Patterson (1989), Wu et al. (1989), Rao and Brodkey (1972), Okamoto (1981)). Placek et al. (1986) develop and apply a two scale model of turbulence in order to separate the periodic from the random fluctuations. All of these authors treat the fluctuations due to the vortices as fundamentally different from the purely random fluctuations.

Fundamentally, however, the trailing vortices are very similar to the large scale eddies found in a boundary layer, in the plume of a smoke stack, and, for that matter, in most turbulent shear flows. The primary physical difference is in the nature of the source of momentum; instead of arising from a single, stationary source, the trailing vortices arise periodically from the passage of successive blades. Notwithstanding this similarity, Wu et al. (1989) hold the opinion that the trailing vortices should not be included in the calculation of ε because they are "non-dissipative" eddies. From the concept of the turbulence energy cascade, it is clear that no large scale eddies are dissipative to any significant degree. It is universally accepted that

fluctuations of all scales should be included in an integral kinetic energy balance because they all contain kinetic energy. It is clear that this energy must be dissipated somewhere in the flow, so the basis of Wu et al.'s claim is unclear. Considering the physical phenomena to be predicted provides another perspective for approaching the analysis of the flow. Ali et al. (1981), and Chang et al. (1981) used flow visualization to examine liquid dispersion mechanisms in stirred tanks. They found two principal mechanisms; ligament stretching and turbulent fragmentation, both of which were shown to occur at the tip of the impeller blades. They concluded that most of the dispersion is in the trailing vortices. The importance of defined vortices to the mixing processes is further supported by the development of efficient ring vortex mixers (see Latto et al. (1990) for a review), which rely solely on this transport mechanism for mixing. Since it is widely accepted that most of the mixing in stirred tanks occurs in the same region over which the trailing vortices persist, and since the mathematical, theoretical, and experimental complexity introduced by separate consideration of the trailing vortices is not clearly justified by the potential benefits of a more complex model, an alternate approach is followed in this work. **First, it is assumed that the physical processes induced by the regularly occuring trailing vortices are not fundamentally different from those induced by randomly occuring large scale eddies. Second, it is assumed that stationarity can be defined based on a time scale long enough to damp out the effects of individual blade passages. Third, it is assumed that the flow is locally isotropic.** These assumptions are not trivial, and their implications will be discussed in some detail.

When these simplifying assumptions are used, it must be done with the understanding that, as with any assumptions, mathematical simplicity is bought at

the cost of physical understanding of the process. The meaning of the assumptions must be clearly stated so that weaknesses in the approach can be isolated. Of the three assumptions made above, the first is the weakest. It is not clear whether the fluctuations due to the trailing vortices provide a diffusive and dissipative mechanism similar to that of the largest turbulent eddies, or whether they in some way interfere with these processes. These questions cannot be answered when the trailing vortices are lumped together with all other fluctuations in the flow. It is possible that the equations arising from this analysis will not adequately describe the underlying physics of the problem, so that attempts at prediction fail. These are important issues, and wherever possible, the effect of these assumptions on the results obtained is examined. Whenever information is available, secondary phenomena are observed, and discussed.

The assumption of stationarity is a powerful one, and is applied in many fields to mean that *the physical processes of interest do not change with time.* Stationarity of the mean is a fundamental assumption in all analysis of turbulence. Once stationarity breaks down, it is necessary to change the method of analysis to an ensemble averaging approach, as discussed above. For stirred tanks, the validity of applying stationarity depends on the time scale that is chosen. In chemical processes, the time scale chosen is typically of the order of minutes. In the stirred tank used for this work, a time scale of the order of 3 seconds reveals a stationary process. A time scale of one blade passage, on the other hand, would lead to adoption of ensemble averaging. If one examines the turbulence literature, there is no indication of what time scale should be considered to define stationarity. Hinze (1987) does not invoke ensemble averaging until time or space averaging is not possible. No

assumptions are required concerning the randomness of the fluctuating component in the derivation of the time averaged equations of motion. The stationarity assumption allows a considerable simplification of the mathematics used to describe the flow, and provides access to the theory and solutions surrounding classical turbulence.

The last assumption is that the flow is locally isotropic. Fully isotropic turbulence is defined by von Karman and Howarth (1938) as follows:

> ...the average value of any function of the velocity components and their derivatives at a particular point, defined in relation to a particular set of axes, is unaltered if the axes of reference are rotated in any manner and if the coordinate system is reflected in any plane through the origin...

Local isotropy is a less severe constraint, and allows the same mathematical simplifications to stand; it requires only that there be no directional preference at the smaller scales of the flow. The local isotropy assumption is based on the concept of the *turbulent energy cascade*. Energy is supplied to the fluctuating flow field from the mean flow field at the scale of the larger eddies. These eddies break up into and exchange energy with successively smaller eddies, until the forces maintaining the eddy velocity gradients cannot overcome the viscous forces, and the energy is dissipated into heat. This occurs at the smallest scales of motion, in the dissipative range. If the cascade of energy is maintained so that very little energy is dissipated between the large, energy containing eddies, and the small, dissipative eddies, the flow is said to be in *local equilibrium*, the intermediate eddies will tend to have no directional preference, and the frequency spectrum will exhibit a -5/3 slope when plotted on a log-log scale.

The size of the dissipative eddies determines many things of practical interest; drop and bubble size, floc size, scale of segregation. The characteristic size of the smallest scales of flow is closely related to the rate of energy dissipation, and to the Reynolds number[1]. The scales of turbulence are generally determined indirectly, through the rate of dissipation of turbulence kinetic energy. Determination of these quantities is the most important objective of turbulence studies in stirred tanks. In the next section, the governing equations of turbulence, which include the dissipation term, are introduced.

5.2 The mathematical expression of turbulence

By expressing the flow field in terms of the governing partial differential equations and solving these equations, we look to predict the mean velocity and turbulence fields. These fields serve as input to models of the process variables of interest. The governing equations describing momentum transfer in a Newtonian fluid are the Navier-Stokes equations. Using the decomposition given in equation 16, the instantaneous form of these equations is written

$$\frac{\partial(u_i' + \overline{U_i})}{\partial t} + (u_j' + \overline{U_j})\frac{\partial(u_i' + \overline{U_i})}{\partial x_j}$$

$$= -\frac{1}{\rho}\frac{\partial(p' + \overline{P})}{\partial x_i} + \nu\frac{\partial^2(u_i' + \overline{U_i})}{\partial x_j^2} + g_i \qquad (18)$$

1 Above the critical Reynolds number, the flow field is fully turbulent; increases in the Reynolds number beyond this point result in a reduction of the size of the smallest scales of turbulence.

Solution of these equations, while possible for some conditions, is expensive, and gives much more information than is useful for this flow field. In their time averaged form, these equations become

$$\frac{\partial \overline{U_i}}{\partial t} + \overline{U_j}\frac{\partial \overline{U_i}}{\partial x_j} = -\frac{1}{\rho}\frac{\partial \overline{P}}{\partial x_i} + \nu\frac{\partial^2 \overline{U_i}}{\partial x_j^2} - \frac{\partial(\overline{u_i' u_j'})}{\partial x_j} + g_i \qquad (19)$$

In the time averaged Navier Stokes equations, a new term, $\overline{u_i' u_j'}$ appears. This term represents the stresses appearing in the flow field due to the turbulent velocity fluctuations; known as the Reynolds stresses. The Reynolds stresses form a symmetric second order tensor, which in general has 6 components. There are now 10 unknowns to solve for, and only 4 equations. If we wish to follow the path of flow field prediction, some way must be found to model the Reynolds stress field in terms of known quantities.

Before continuing in this direction however (see section 5.3.7), it is useful to consider the problem from the perspective of gaining additional physical understanding of the mechanisms of turbulent momentum transfer. First, recall that one derivation of the Navier-Stokes equations is based on the balance of momentum fluxes over a differential volume (Whitaker, 1981). Within this interpretation, the velocity becomes a volume flux (m^3/m^2s), $\rho u_i'$ becomes a mass flux (kg/m^2s) and $\rho\overline{u_i' u_j'}$ becomes a momentum flux - the turbulent flux of momentum.

A second approach comes from considering another of the four basic tools for the mathematical description of momentum tranfer. These tools are differential and integral momentum and mechanical energy balances; the Navier-Stokes equations are a differential momentum balance. Integral balances are good for predicting

overall results, but obscure details of the mechanisms - so the most promising candidate for obtaining increased understanding of the mechanisms of turbulent momentum transfer is a differential mechanical energy balance. This can be derived starting either from the first law of thermodynamics (see Hinze, 1987, pg. 68), or from the Navier Stokes equations (see Tennekes and Lumley, pg. 59). Following the second approach, the momentum balance (momentum = mass x velocity) is multiplied by the velocity to obtain the energy balance (energy = mass x velocity squared). The derivation for the turbulent flow field is summarized as follows:

1) The TOTAL kinetic energy balance; multiply the instantaneous Navier Stokes equations by $(u_i' + \overline{U_i})$, apply time averaging.

2) The MEAN kinetic energy balance; multiply the time averaged Navier Stokes equations by $\overline{U_i}$.

3) The turbulent kinetic energy (TKE) balance; subtract (2) from (1).

The resulting equation is written

$$\underset{I}{\frac{1}{2}\frac{D\overline{(u_i'u_i')}}{Dt}} = \underset{II(+\text{or}-)}{-\frac{\partial}{\partial x_i}\overline{u_i'\left(\frac{p}{\rho}+\frac{(u_j'u_j')}{2}\right)}} \underset{III(+)}{-\overline{u_i'u_j'}\frac{\partial \overline{U_j}}{\partial x_i}}$$

$$\underset{IV(+)}{+\nu\frac{\partial}{\partial x_i}\overline{u_j'\left(\frac{\partial u_i'}{\partial x_j}+\frac{\partial u_j'}{\partial x_i}\right)}} \underset{V(-)}{-\nu\overline{\left(\frac{\partial u_i'}{\partial x_j}+\frac{\partial u_j'}{\partial x_i}\right)\frac{\partial u_j'}{\partial x_i}}} \qquad (20)$$

Note that the terms $\overline{u_i'u_i'}/2$ are often written $q^2/2$ or simply k, and represent the turbulence kinetic energy per unit mass. Hereafter, this quantity will be referred to as k. The physical meaning of each term is ascribed by Hinze (1987) as follows:

I) k accumulation and convection by the mean flow

II) work done by the total dynamic pressure of turbulence

III) work of deformation of the mean flow by the turbulence stresses

IV) work done by the viscous shear stresses of turbulent motion

V) viscous dissipation by the turbulent motion.

The + and - signs denote what are normally positive and negative contributions to the energy balance. Term III is normally a source of energy in the turbulent flow, and a sink of energy in the mean flow; it is often referred to as the "production term" in the TKE equation. This energy is dissipated principally through term V. Terms IV and V both arise directly from the viscous dissipation term in the original instataneous Navier Stokes equations ($\nu\partial^2(u_i' + \overline{U_i})/\partial x_j^2$). The viscous dissipation by the turbulence is normally orders of magnitude larger than the analogous term in the mean equations.

Term V can be simplified to

$$\varepsilon = \nu\overline{\left(\frac{\partial u_i'}{\partial x_j}\right)^2} \tag{21}$$

if the flow field is (locally) isotropic, and thus

$$\overline{\frac{\partial u_i'}{\partial x_j}\frac{\partial u_j'}{\partial x_i}} = 0 \tag{22}$$

This term turns out to be the most important term in the description of turbulence, at least from the point of view of process modelling: ε is, in more ways than one, the "bottom line." It is the point in the dynamic equations where most of the dissipation occurs; where limiting length scales are determined, and where most of the productive process work is accomplished. Up to this point, the assumptions

made about the flow are only that it is stationary in time, and that it is locally isotropic. The derivations followed to obtain equation 20 are familiar manipulations of the well established Navier Stokes equations. It is useful to make careful note of this basic definition of ε: the methods used to estimate and model this important term will not always be as straight forward as those used to define it!

Examination of the fundamental equations of turbulence leads to two conclusions. One, the turbulence equations are not closed, and their solution will require modelling of the Reynolds stress field; two, the dissipation term is of substantial practical interest, and should be measured if at all possible.

5.3 Prediction, estimation, and/or measurement of turbulence

The three variables of greatest interest in the characterization of turbulence are k, ε, and the Reynolds stresses ($\overline{u_i' u_j'}$). Given these quantities, it is possible to gain some understanding of the turbulent energy distribution, and of the various length scales in the flow. The length scales are central to modelling of transport phenomena, reaction rates, and mixing times. In this section, the available methods for measurement of these quantities by direct and indirect means, and for their prediction through model equations, will be surveyed.

Measurement of k is straight forward, since it is simply one half of the sum of the RMS components of velocity, or the variances. With a single component LDA, this requires three separate measurements, and thus the assumption of stationarity of the mean. The Reynolds stresses are determined using Logan's method of beam rotation, which is detailed in chapter 3. Again, the assumption of stationarity is required. Direct measurement of ε is virtually impossible, since this would require

two probes differentially close to each other in space providing simultaneous measurements of the instantaneous velocity so that the instantaneous velocity gradient could be computed at a point. Instead, ε is estimated by indirect measurement, and from turbulence models.

Several routes are available for the development of methods of determining ε. It can be calculated by difference from either the integral kinetic energy balance or the differential kinetic energy balance (specifically, the TKE balance). The assumption of local isotropy provides special properties for the correlation functions, which can thus be used to provide a starting point for determinations of ε based on length scales. These length scales can be calculated from the dissipation spectrum, from the autocorrelation function, or from the time derivative of the velocity using Taylor's frozen turbulence hypothesis; they can be approximated based on physical arguments; or they can be predicted using turbulence models.

There are four types of turbulent length scales; integral length scales, length microscales, integral time scales, and time microscales. Both of the length scales can be defined in several ways. These are explained in detail in Hinze (1987, pp. 39-57) and in Tennekes and Lumley (1972, pp. 14-25). The definitions of greatest interest for this work are based on the shape of the correlation functions in the limit of zero separation as follows:

$$f(r) = \frac{\overline{(u_1')_A\,(u_1')_B}}{u'^2} \tag{23}$$

$$\frac{1}{\lambda_f^2} = -\frac{1}{2}\left[\frac{\partial^2 f}{\partial r^2}\right]_{r=0} = \frac{1}{2\overline{u_1'^2}}\left[\overline{\left(\frac{\partial u_1'}{\partial x_1}\right)^2}\right]_{x_1=0} \tag{24}$$

$$g(r) = \frac{\overline{(u_2')_A (u_2')_B}}{\overline{u'^2}} \tag{25}$$

or equivalently,

$$g(n) = \frac{\overline{(u_1')_A (u_1')_B}}{\overline{u'^2}} \tag{26}$$

$$\frac{1}{\lambda_g^2} = -\frac{1}{2}\left[\frac{\partial^2 g}{\partial r^2}\right]_{r=0} = \frac{1}{2\overline{u_1'^2}}\left[\overline{\left(\frac{\partial u_1'}{\partial x_2}\right)^2}\right]_{x_2=0} \tag{27}$$

$$R_E(t) = \frac{\overline{u'(t')u'(t'-t)}}{\overline{u'^2}} \tag{28}$$

$$\tau_E = \int_0^\infty R_E dt \tag{29}$$

Where λ_f and λ_g are the Taylor microscales, and τ_E is an integral time scale. f(r), g(r), and $R_E(t)$ are the longitudinal, lateral, and time correlations respectively. A and B define two points in the flow, separated by a distance r in the streamwise direction (or n in the cross stream direction).

Once one of the flow scales is measured, ε is determined using one of the scale-dissipation relationships. The starting point for many of these relations is equation (3-99) from Hinze (1987)

$$\varepsilon = -15\nu u'^2\left[\frac{\partial^2 f}{\partial r^2}\right]_{r=0} = 30\nu\frac{u'^2}{\lambda_f^2} = 15\nu\frac{u'^2}{\lambda_g^2} \tag{30}$$

This equation follows directly from the definition of ε, and from equation (3-20, Hinze, 1987), which relates the velocity gradients to the correlation function. The derivation of this equation, once again, requires the assumption of isotropic turbulence.

Once ε is known, any other length scale of interest can be estimated. However, since the methods of obtaining ε are indirect, and often approximate, it is advisable to apply several different estimates before drawing any conclusions about the results.

5.3.1 Experimental application of the TKE balance

In some flow fields, it is possible to obtain an estimate of ε by difference using the TKE balance (Turan, 1988). This requires the assumption of a zero pressure velocity correlation, and the measurement of the triple velocity correlations, the Reynolds stresses, the mean velocity gradients, and k. In a stirred tank, the main region of interest is the impeller discharge. As the fluid passes over and around the impeller blades, a pressure difference is created. This pressure difference quickly equilibrates to an increase in the mean velocity (Prandtl (no date)). With this equilibration process in mind, an assumption of a zero pressure velocity correlation close to the impeller blades is questionable. Furthermore, with the experimental apparatus available (a single component LDA), it is not possible to measure the triple velocity correlations. These two limitations precluded the determination of ε by difference from the differential TKE balance.

5.3.2 Kinetic energy balance over a control volume

One of the four main tools of fluid mechanics not yet discussed is the integral kinetic energy balance. In the application of this balance, all of the velocity fluctuations (random and periodic) are included. Two authors (Cutter (1966), Wu and Patterson (1989)) apply this equation to determine the dissipation rate within a control volume. This gives an average value of ε over the volume, rather than a single point-wise value. The control volume must be carefully defined so that the variations of ε within it are acceptably small. Since the magnitude of ε is known to vary over two or more orders of magnitude within the tank, the accuracy of the method is highly dependent on the control volume definition.

Applied over the whole tank, this tool has been used to determine the constants required for other methods (Laufhutte and Mersmann (1987), Wu and Patterson (1989), Wu et al. (1989), Costes and Couderc (1988)), and as a check on the results (Cutter (1966), Rao and Brodkey (1972)). If the determination of ε is accurate, the sum of the dissipation over the whole tank will equal the power input.

5.3.3 The dissipation spectrum

The frequency spectrum $E_1(k_1)$ is defined

$$\overline{u_1'^2} = \int_0^\infty E_1(k_1)dk_1 \tag{31}$$

ε can be related to the frequency spectrum by

$$\varepsilon = 15\nu \int_0^\infty k_1^2 E_1(k_1)dk_1 \tag{32}$$

which arises from the expressions

$$\frac{1}{\lambda_f^2} = \frac{1}{2\overline{u_1'^2}} \int_0^\infty k_1^2 E_1(k_1) dk_1 \tag{33}$$

for the length microscale, and from equation 30. In these expressions, the factor k_1^2 appears in the Fourier domain due to differention of the velocity in the time domain. The quantity $k_1^2 E_1(k_1)$ is frequently referred to as the dissipation spectrum.

This approach has been applied to stirred tanks by Okamoto et al. (1981), Komasawa et al. (1974), Yuu and Oda (1980), Costes and Couderc (1988), and Rao and Brodkey (1972). Some of these authors report equation 33 in its frequency form, which is related to the 1-D wavenumber by

$$k_1 = \frac{2\pi f}{\overline{U_1}} \qquad \text{and} \qquad E_1(k_1) = \frac{\overline{U_1}}{2\pi} E_1(f) \tag{34}$$

The experimental tools used by these authors were video (Yuu and Oda (1980)), hot-film current meter (Okamoto et al. (1981)), hot wire anemometry (Komasawa et al. (1974) and hot film anemometry (Rao and Brodkey (1972)). Costes and Couderc (1988) appear to have applied this method using an LDA system. The frequency spectrum obtained using our LDA does not extend to high enough wavenumbers to apply the dissipation spectrum method.

5.3.4 Taylor's frozen turbulence hypothesis

Starting from equation 30 and the definition of λ_f gives

$$\varepsilon = 30\nu \frac{u'^2}{2u_1'^2} \left[\overline{\left(\frac{\partial u_1'}{\partial x_1} \right)^2} \right]_{x_1 = 0} \tag{35}$$

While the spatial derivative is almost impossible to measure, the time derivative can be calculated from the time series of the data. Taylor's frozen turbulence hypothesis assumes that for a small time interval, the turbulent structure is frozen in space and is convected along with the mean flow velocity as shown in figure 81. By taking measurements at a fixed point, b, and relating the measured time interval and the mean velocity to the spatial separation, the spatial derivative can be extracted from the time derivative as follows:

$$\left(\frac{\partial u_1'}{\partial x_1}\right) = -\frac{1}{\overline{U_1}}\left(\frac{\partial u_1'}{\partial t}\right)$$

$$\overline{\left(\frac{\partial u_1'}{\partial x_1}\right)^2} = \frac{1}{\overline{U_1}^2}\overline{\left(\frac{\partial u_1'}{\partial t}\right)^2} \qquad (36)$$

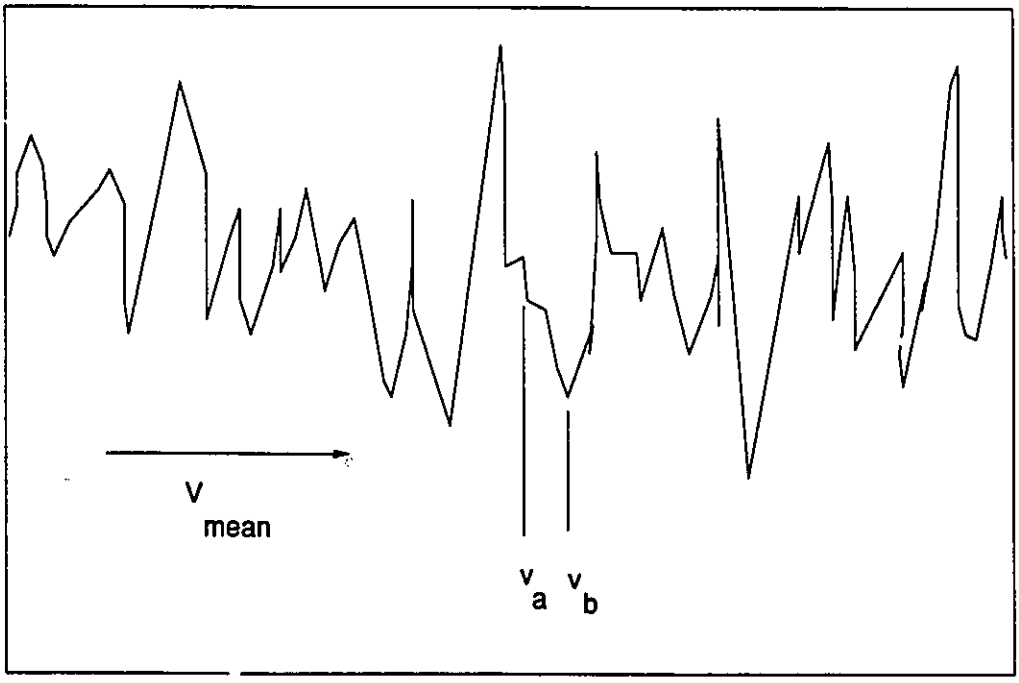

Figure 81. The frozen turbulence hypothesis

This relationship between the time and space derivatives is based on the assumption that the streamwise component of the mean velocity is the only significant component (the flow is one dimensional). This is true where the principle direction of flow is aligned with the chosen co-ordinate axes, and the turbulence intensity is low (eg. flow in a pipe, or a boundary layer). It is not true for the flow in a stirred tank. Heskestad (1965) and Van Doorn (1981) have derived a correction for three dimensional flows with high turbulence intensity by replacing $\overline{U}$ with the convection velocity U_c.

$$U_c^2 = \overline{U_1}^2 \left[1 + 2\frac{\overline{U_2}^2}{\overline{U_1}^2} + 2\frac{\overline{U_3}^2}{\overline{U_1}^2} + \frac{\overline{u_1'^2}}{\overline{U_1}^2} + 2\frac{\overline{u_2'^2}}{\overline{U_1}^2} + 2\frac{\overline{u_3'^2}}{\overline{U_1}^2} \right] \tag{37}$$

If $\overline{U_2} = \overline{U_3} \sim 0$, and the turbulence is isotropic, this expression reduces to

$$U_c^2 = \overline{U_1}^2 \left[1 + 5\frac{\overline{u_1'^2}}{\overline{U_1}^2} \right] \tag{38}$$

Van Doorn has found that the intermediate result

$$U_c^2 = \overline{U_1}^2 + \overline{u_1'^2} + 2\overline{u_2'^2} + 2\overline{u_3'^2} \tag{39}$$

is approximately true.

When applying this method, care must be taken to consider a short enough time interval between samples. In theory, the time derivative obtained will reach a constant value at some small time interval. In practice, Wu and Patterson (1989) found that the time scale decreases continuously as the time interval is decreased from 0.4 to 0.15 msec (2.5 to 6.6 kHz sampling frequency). There is a practical limit on the sampling frequency possible with an LDA, which is imposed by the size of

the measuring volume, as discussed in chapter 3.

5.3.5 Dimensional argument

One of the most commonly used expressions for ε is

$$\varepsilon = A\frac{u'^3}{L} \qquad (40)$$

where A is a constant of proportionality, u is a characteristic turbulent velocity, and L is a characteristic length scale. This expression is based on dimensional arguments, and can be obtained in several ways:

I. Tennekes and Lumley (1972) argue as follows:

> "All of the available experimental evidence suggests that the spectral energy transfer proceeds at a rate dictated by the energy of the large eddies (of the order of u^2) and their time scale (of the order of L/u). Thus, the dissipation rate may always be estimated as ..." (energy/time)

Hinze (1987) follows a similar, but more detailed line of reasoning (pp. 218-225), also based on the turbulence energy cascade. Note that this assumes a) most of the energy enters the turbulent flow at the largest scales of motion (L), b) most of the energy (k) is contained in the larger eddies, c) the flow is in local equilibrium, and d) some constant fraction of the total TKE is dissipated once every time scale.

II. Starting from the equation (3-99, Hinze, 1987)

$$\varepsilon = 15\frac{\nu u'^2}{\lambda_g^2} \qquad (30)$$

and using Brodkey's (1975) derivation as reinterpreted by Laufhutte and Mersmann (1985a);

$$\lambda \propto \sqrt{L\nu/u'} \tag{41}$$

where L can be set to some fraction of the impeller diameter, $L = D/constant$. ε then becomes

$$\varepsilon = C_1 \frac{u'^3}{D} \tag{42}$$

III. Brodkey (1975, pg. 80) gives an alternate derivation, starting from the definition of the low wavenumber cut-off point, k_o:

$$\varepsilon = \frac{k_o u_1'^3}{(2/3)^{3/2}} \tag{43}$$

using an estimate of $k_o = L/2$ gives

$$\varepsilon = 3.68 \frac{u_1'^3}{L} \tag{44}$$

IV. Antonia and Satyaprakash (1980), and Wood and Chen (1985) report similarity solutions for jets. In the derivation of the similarity functions, it is shown that the ε function must have the same form as equation 40. This result, and its applicability to this flow, is discussed further in chapter 6.

Different authors have chosen various values for u and L, as summarized in Table 3. All of the results are for Rushton turbines, with the exception of Laufhutte and Mersmann (1987), and Rao and Brodkey (1972) who used various other impellers. While the characteristic velocities chosen are consistent for isotropic turbulence, there is a wide variation in the length scales. The constant A is known to be approximately 1 for isotropic turbulence (Batchelor (1970, pg. 106), Cutter (1966), Wu and Patterson (1989)), and this value is sometimes applied in stirred tanks. When the length scale is set to some fraction of the impeller diameter, the constant C_1 becomes a combination of A, and the adjustment needed to obtain the correct length scale. If A is set to 1 for the cases where it would otherwise include part of the length scale (Laufhutte and Mersmann (1985a,b, 1987), Costes and Couderc (1988), Rao and Brodkey (1972)) and the resulting length scales are compared, some agreement appears between the apparently divergent results. The impeller discharge from a Rushton turbine is jet-like, with a jet width equal to one half the width of the impeller blades. This indicates that the characteristic integral length scale at the impeller discharge should be W/2, or D/10. The results of the SRJ (swirling radial jet) model of the Rushton turbine (presented in the next chapter), when substituted into equation 40, support this claim, as do Wu and Patterson's results (L = D/12.5), and Rao and Brodkey's results (L = D/8.8). It should be noted that this theoretically based estimate of the integral length scale is also exactly equal to the length scale of the trailing vortices for both the RT and the PBT. Laufhutte and Mersmann (1985 a,b, 1987) and Costes and Couderc (1988) report results that are averaged over the whole tank, which leads to an average integral length scale larger than that at the impeller discharge, but smaller than the true value in the outer

regions of the tank. The remaining results are due to Cutter (1966), who expressed some reservations about the result, and to Stoots and Calabrese (1989) who assumed values of both L and A. It can be concluded that the variations shown in table 3 depend on the choice of control volume used in the integral kinetic energy balance (as discussed earlier), where this is the method used to determine the value of the constant A or C_1.

Table 3: Characteristic length and velocity scales used in equation 40.

reference	velocity scale	length scale	A or constant
Laufhutte and Mersmann (1985a and b)	u_1'	D	6 to 6.6
Laufhutte and Mersmann (1987)	u_1'	D	5.5 to 7.2, recommends 6.25
Costes and Couderc (1988)	$k^{1/2}$	D	4.4 ± 2.4
Rao and Brodkey (1972)	u_1'	D/2	4.4
Wu et al. (1989)	$k^{1/2}$	from autocorrelation	0.946
Wu and Patterson (1989)	$k^{1/2}$	from autocorrelation	$0.85 \pm 10\%$
Cutter (1966)	u_1'	from correlation coefficient	0.51
Stoots and Calabrese (1989)	$k^{1/2}$	D/5	1
SRJ	$k^{1/2}$	D/10	1

The dimensionally based expression for ε derived in this section contains a length scale, a velocity scale, and a constant of proportionality. The choice of velocity scale is straightforward; either $k^{1/2}$, or u_1' (if the flow is isotropic) will yield a correct result. The length scale, while related to the impeller diameter at positions in the impeller stream, is not a constant fraction of this dimension - even within the impeller stream. Determination of the constant C_1 based on a constant length scale will yield distorted values of ε; too low close to the impeller, and too high in the outer regions of the tank. The constant A can be assumed equal to 1, and verified using the integral kinetic energy balance, where the length scale is determined pointwise.

5.3.6 The autocorrelation function

Table 3 notes several determinations of the length scale from the autocorrelation coefficient. This method has recently been applied in stirred tanks by Wu and Patterson (1989), and Wu et al. (1989).

Recall the autocorrelation coefficient, defined as

$$R_E = \frac{\overline{u_1'(t')u_1'(t'+t)}}{\overline{u_1'^2}} \tag{45}$$

and the Eulerian integral time scale, obtained by taking the integral of the autocorrelation function;

$$\tau_E = \int_0^\infty R_E dt \tag{46}$$

This can be related to the desired length scale (L_f) in one dimensional flow via the mean velocity

$$L_f = \overline{U_1}\tau_E \tag{47}$$

and then substituted into equation 40.

Wu and Patterson (1989) and Wu et al. (1989) have suggested that several corrections to these relations are necessary because a) the flow is three dimensional, and b) the fluctuating velocity contains a periodic component. Since this is a three dimensional flow with high turbulence intensity, the velocity $\overline{U_1}$ is changed to the convection velocity U_c as presented in section 5.3.4. This correction should be applied with some caution, since it was derived for time and velocity derivatives, and is applied here to length scales.

The authors also suggest a three dimensional correction to the length scale, using a vector sum of the length scales determined from the three coordinate directions

$$L_{f,i} = \frac{U_c}{\overline{u_i'^2}} \int_0^\infty R_E dt \qquad L_{res} = \sqrt{L_{f,i} L_{f,i}} \tag{48}$$

Their actual calculations, however, seem to return almost completely to the one dimensional case, leaving

$$\varepsilon = \frac{A u_1'^3}{\tau \sqrt{\overline{U_1}^2 + \overline{u_1'^2}}} \tag{49}$$

where τ is determind from the streamwise component, and A is assumed to be 1. The authors base this simplification on their observation that the RMS components are very nearly equal. As noted in Table 3, A was later verified by the authors, and found equal to 0.946.

The second set of corrections proposed by Wu and co-authors is directed at removing the periodic component of the fluctuating velocity. The methods presented have produced impressive results when applied to the data in question. However, if the equation for the upper frequency limit of an LDA experiment (see chapter 3) is appled to the experimental conditions reported in Wu and Patterson (1989), it appears that only frequencies up to 217 Hz have been measured. Above this limit, fluctuations in the signal are due only to the Doppler ambiguity noise. The authors express concern about this source of error at several points in the paper, and even refer to the flattening of the spectrum at 200 Hz, which is a characteristic of white noise. Their filtering method, however, appears to have covered up the severity of the problem, coincidentally producing a -5/3 slope. The locally isotropic range of turbulence occurs entirely above 200 Hz, so that any turbulence results obtained by these authors must be treated with great care. Given the limitation of these measurements, further discussion of the methods is deferred until chapter 7, under discussion of the PBT results.

Rao and Brodkey (1972) and Yuu and Oda (1980) use the autocorrelation coefficient to obtain τ_E. Rao and Brodkey integrate to the second zero crossing (0.1 sec) in an effort to remove the effect of the periodic component. They find very low values of the integral length scale, and conclude that this method is not appropriate for complex flow fields. They then approximate the value of the integral length scale by integrating only to the first zero crossing (approximately 12 msec) of the autocorrelation, finding an integral scale of 0.25W = D/20. Yuu and Oda also integrate only to the first zero crossing (approximately 10 msec). They find that τ_E varies by a factor of 4 over the tank, and that there is very little difference between

the results for the three components of velocity.

Use of the autocorrelation for determination of length scales has several advantages. First, it is averaged over a large number of data points, so that experimental errors are damped out. Second, it provides a good physical understanding of the large scale regular fluctuations, their frequencies, and the effect of their removal.

5.3.7 The k-ε model

In the second section of this chapter, the time averaged Navier Stokes equations were derived, and it was shown that for a turbulent flow field, there are 4 equations, with 10 unknowns. In order to solve these equations, it is necessary to model the Reynolds stress field by relating it to known quantities. As always, the modelling effort begins with a consideration of the physical meaning of the terms in question.

Recall the time averaged Navier Stokes equations. The terms

$$\nu\frac{\partial}{\partial x_j}\frac{\partial \overline{U_i}}{\partial x_j} \qquad \text{and} \qquad -\frac{\partial(\overline{u_i' u_j'})}{\partial x_j} \tag{50}$$

represent the momentum sinks due to mean velocity gradients and Reynolds stresses respectively. From the examination of the TKE balance, we know that the second term above eventually appears as a turbulent viscous dissipation (ε). Based on this physical analogy, a mathematical analogy is often made between the two terms above, and the Newtonian constitutive equation;

$$\tau_{ij} = -\rho\overline{u_i' u_j'} = \rho\nu_t\frac{\partial \overline{U_i}}{\partial x_j} \tag{51}$$

In this analogy, ν_t is a property not of the fluid, but of the flow. In Prandtl's mixing length hypothesis, ν_t is taken to be a constant over all space and time. In fact, it is not constant, and will require further modelling.

The units of ν_t are m^2/s, indicating that a velocity scale, and a length scale may be used to characterize the variable. Since the flow field in question is the turbulent field, whose dynamics are described by equation 20, the velocity scale is chosen as one of the principle variables in that equation;

$$u' = \left(\frac{1}{2} \overline{u_i' u_i'} \right)^{1/2} = k^{1/2} \tag{52}$$

A length scale is still required to complete the definition of ν_t. The length scale could be (and has been) modelled (see Bradshaw (1972)). An alternative to this is to consider ε, which appears in the k equation, and which is of considerable practical interest. ε has units of m^3/s^2, so it can be interpreted as

$$\varepsilon = \underset{\text{energy}}{u'^2} \underset{\text{per time}}{\frac{u'}{\ell}} \Rightarrow \text{the energy out of size range } \ell \text{ per unit time} \tag{53}$$

Substituting these arguments back into ν_t gives

$$\nu_t \propto u' \ell$$

$$= C_\mu \frac{k^2}{\varepsilon} \tag{54}$$

This is refered to as the turbulence constitutive equation. In the turbulence modelling literature, there are frequent references to "zero equation models," "one equation

models," and "two equation models." These models are classified according to the way in which the characteristic velocity and length scales in the constitutive equation above are specified. Zero equation models will specify both the velocity and length scale algebraically; 0 PDE's are used. One equation models determine the velocity scale using a transport equation, and specify the length scale algebraically; 1 PDE is used. Two equation models model both the length scale and the velocity scale using transport equations (2 PDE's). The effort required to model both the length and velocity scales is justified on the grounds that

1) by modelling terms of a higher order, the errors introduced by the necessary approximations are reduced. (ie. We model the transport of stresses to determine the stress field - we don't directly model the stress field.)
2) extra information is obtained about the Reynolds stresses.
3) both the length and velocity scales (in this case k and ε) vary as the flow develops, so ν_t will be allowed to vary, as it is known to do.

However, even with a two equation model, the theory is still local and instantaneous. The stress and strain fields are linked: a change in the mean velocity gradients will result in an immediate change in the Reynolds stresses. This is another way of saying that the flow field is assumed to be in local equilibrium. It is a consequence of using a model which makes no allowance for the effects of flow field memory, and for the effects of events spatially removed from the local differential volume.

These are some of the basic ideas which motivate turbulence closure models. Many of these models have been proposed, and various developmental arguments have been forwarded over the years. The model used in this work is the k-ε model, which is attributed to Launder and Spalding (1972). There has been considerable

discussion about the validity of the model, particularly concerning the ε equation. Perhaps in response to this, several means of obtaining the k and ε equations have been developed over the years. Although these approaches will not be given in detail here, the key arguments behind three quite different methods will be discussed.

First, consider modelling of the k equation based on physical arguments. Beginning with a rearrangement of equation 20;

$$\underset{[1]}{\frac{Dk}{Dt}} = \underset{[2]}{-\overline{u_i' u_j'}\frac{\partial \overline{U_i}}{\partial x_j}} - \underset{[3]}{\frac{\partial}{\partial x_k}\left(\underset{(i)}{\overline{k u_k'}} + \underset{(ii)}{\overline{u_k' p'}} + \underset{(iii)}{\nu \frac{\partial k}{\partial x_k}} \right)} - \underset{[4]}{\varepsilon} \qquad (55)$$

term [3] is a diffusion term, combining (i) turbulent diffusion, (ii) pressure diffusion, and (iii) molecular diffusion[1]. By substituting the turbulent constitutive equation into term [2], and modelling term [3] as a single diffusive term, the k equation is obtained:

$$\frac{Dk}{Dt} = \frac{\partial}{\partial x_k}\left[\frac{\nu_t}{\sigma_k}\frac{\partial k}{\partial x_k} \right] + \nu_t \left(\frac{\partial \overline{U_i}}{\partial x_k} + \frac{\partial \overline{U_k}}{\partial x_i} \right)\frac{\partial \overline{U_i}}{\partial x_k} - \varepsilon \qquad (56)$$

Development of the ε equation based solely on physical arguments is less straight forward, and is not discussed further. It is fair to say that the ε-equation is the simplest dimensionally correct equation which accounts for the production of dissipation by mean shear, the dissipation of dissipation, and the diffusion by a gradient mechanism. For further details, the reader is referred to Hanjalic and Launder (1975).

1 As an aside, consider the integral of either term [1] or term [3], which are both the gradient of a flux, over a control volume where u_i' and $\overline{U_i}$ are zero over the boundaries. In all cases, these integrals will be zero, so terms [1] and [3] can be neither sources nor sinks of TKE.

Speziale (pg. 490, 1990) has taken a different approach. He has shown that if one performs a volume integration over the 2-point correlation function, the result is a tensor length scale multiplied by k. A transport equation for the trace of this tensor length scale has the same form as the ε-equation. Thus the ε-equation is consistent with an equation for the average of the integral length scales in the three component directions.

Finally, Wood (1978) has presented a general, rigorous method for model development, which proceeds from the TKE balance, through the mean Reynolds stress model, to the k and ε equations. This method provides a means of isolating the assumptions made along the way, so that modifications to proposed models can be based on a rational assessment of weaknesses in proposed assumptions. The development of the k-ε model starts with the TKE balance, derived in section 5.2, with the individual normal stresses left in. The ε equation is derived by differentiation of the TKE balance for u_i' with respect to x_j, followed by multiplication by $2\nu\frac{\partial u_i'}{\partial x_k}$ and time averaging. Up to this point, the exercise is purely mathematical.

The unknown terms in each equation are modelled using functional equations

$$\text{term} = \text{functional}\left(\frac{\partial U_i}{\partial x_j}, \overline{u_i' u_j'}, \varepsilon\right)$$

By using a functional, or integral, approach, one considers the variables over all space and time. Assumptions are made based on physical reasoning to reduce the complexity of the model, finally ending up with the general MRS model. This modelling is done at the level of the second order equations because it is known that the first order equations are not sufficient, and because the third order equations a)

require too much experimental input, and b) are removed from the flow to a degree that decreases the physical understanding of the individual terms. The terms remaining in this model include several constants, which are determined by a systematic method of parameter estimation. Progressively more complex flows are examined in order to isolate the physical phenomena and determine the constants uniquely. The model is then tested on more difficult flow fields. This is analogous to a viscometric experiment; *thus precluding later adjustments of the model constants* in order to fit the results to a specific flow field. The validity of the model will depend on the quality of the experimental data on which it is based.

Only after the constants have been determined is the MRS model simplified to the k-ε model, which is designed for use primarily in free shear flows. The simplifications are as follows:

1) lump the three normal stress equations together to obtain the k equation
2) assume that advection = diffusion (the same as saying that the flow is in local equilibrium) to simplify the τ_{12} equation to the constitutive equation arrived at earlier.

This leaves the governing equations for k and ε;

$$\frac{Dk}{Dt} = \frac{\partial}{\partial x_k}\left[\frac{\nu_t}{\sigma_k}\frac{\partial k}{\partial x_k}\right] + \nu_t\left(\frac{\partial \overline{U_i}}{\partial x_k} + \frac{\partial \overline{U_k}}{\partial x_i}\right)\frac{\partial \overline{U_i}}{\partial x_k} - \varepsilon \tag{57}$$

$$\frac{D\varepsilon}{Dt} = \frac{\partial}{\partial x_k}\left[\frac{\nu_t}{\sigma_\varepsilon}\frac{\partial \varepsilon}{\partial x_k}\right] + C_{\varepsilon 1}\nu_t\frac{\varepsilon}{k}\left(\frac{\partial \overline{U_i}}{\partial x_k} + \frac{\partial \overline{U_k}}{\partial x_i}\right)\frac{\partial \overline{U_i}}{\partial x_k} - C_{\varepsilon 2}\frac{\varepsilon^2}{k} \tag{58}$$

and the turbulent constitutive equation

$$\frac{\tau_{ij}}{\rho} = \nu_t \frac{\partial \overline{U_i}}{\partial x_j}$$

$$\nu_t = C_\mu \frac{k^2}{\varepsilon} \qquad (59)$$

This model has been applied to a wide variety of problems, and has proved both stable, and efficient; especially for thin shear flows such as that induced by the Rushton turbine. Wood and Chen (1986) have shown that the model is able to predict jet flows, even in their developing region. By modelling the flow at the edge of the impeller, it is possible to predict expected values of k and ε. This provides a valuable check on the validity of the proposed experimental methods, in addition to providing much needed quatitative information.

5.3.8 The gradient hypothesis

The constitutive equation developed in conjunction with the k-ε model can also be used for experimental determination of ε as per Yianneskis et al. (1987). To apply this method measurements of k, the Reynolds stress, and the corresponding velocity gradient are needed for substitution into the equation

$$\varepsilon = -\frac{0.09k^2}{\overline{u_i' u_j'}} \frac{\partial \overline{U_i}}{\partial x_j} \qquad (60)$$

Note that several combinations of i and j are possible, so several determinations of ε can be compared. If the flow is truly isotropic, the choice of i and j will have no effect on the result.

5.3.9 Summary

Eight methods for obtaining ε, and their applications to stirred tanks, have been surveyed. Two of these methods (the TKE balance and the dissipation spectrum) are not suitable for this application. Four experimental methods, plus the k-ε model will be applied. The experimental methods, with the equations to be applied, are listed below.

Dimensional argument (equation (61)):

$$\varepsilon = A\frac{u'^3}{L}$$

Autocorrelation coefficient (equation (62)):

$$\varepsilon = A\frac{u'^3}{\tau_E U_c} \text{ or } A\frac{u'^2}{\tau_E}$$

Taylor's hypothesis (equation (63)):

$$\varepsilon = 30\nu\frac{u'^2}{2u_1'^2 U_c^2}\overline{\left(\frac{\partial u_1'}{\partial t}\right)^2}$$

Gradient hypothesis (equation (64)):

$$\varepsilon = -\frac{0.09k^2}{\overline{u_i' u_j'}}\frac{\partial \overline{U_i}}{\partial x_j}$$

These equations are the most general forms. In chapter 7, the experimental determination of ε is examined further. Where several possibilities exist for terms in one of the four equations above, the effect of these variations will be examined. The

effects of the periodicity and stationarity assumptions will also be examined. The next chapter concerns prediction of a turbulent flow field produced by a Rushton turbine, using the k-ε model.

5.4 Notation

A = constant in dimensional method

C_1 = constant in dimensional method

$C_{\epsilon 1}$, $C_{\epsilon 2}$, C_μ = constants in k-ε model

D = impeller diameter

$E_1(k_1)$ = one dimensional energy spectrum

f = frequency

$f(r)$ = longitudinal correlation coefficient

$g(r)$ = lateral correlation coefficient

g_i = i'th component of gravity

k = turbulence kinetic energy per unit mass

k_o = low wave number cut off point

k_1 = one dimensional wave number

ℓ = characteristic length scale

L = characteristic length scale

$L_{f,i}$ = i'th component of the length scale calculated from the integral of the correlation coefficient

p' = fluctuating component of the pressure

$\overline{P}$ = time averaged (mean) component of the pressure

R_E = autocorrelation coefficient function

t = time (time lag in definition of $R_E(t)$)

t' = time in definition of $R_E(t)$

u_i' = fluctuating component of the i'th component of velocity

u_i = instanteous component of velocity

$\overline{u_i' u_j'}$ = Reynolds stress

$\tilde{u}_i$ = ensemble average component of velocity

U_c = convection velocity

$\overline{U_i}$ = time averaged component of velocity

W = blade width

x_i = directional co-ordinate i

ε = dissipation rate of the turbulence kinetic energy per unit mass

λ_f, λ_g = differential length scales calculated from correlation functions

greek letters

ν = kinematic viscosity

ρ = density

σ_k, σ_ε = constants in the k-ε closure model

τ_E = Eulerian integral time scale, calculated from the autocorrelation function

5.5 References

Ali, A. M., H. H. S. Yuan, D. S. Dickey, G. B. Tatterson, "Liquid dispersion mechanisms in stirred tanks: Part 1, pitched blade turbine," Chem. Eng. Comm., v. 10, pp. 205-213, 1981.

Antonia, R. A. and B. R. Satyaprakash, "Measurements of dissipation rate and some other characteristics of turbulent plane and circular jets," Phys. Fluids, v. 23, pp. 695-700, 1980.

Batchelor, G.K., The theory of homogeneous turbulence, Cambridge University Press, London, 1970.

Bradshaw, P., "The understanding and prediction of turbulent flow," Aeronautical Journal, pp. 403-418, 1972.

Brodkey, R. S., ed. Turbulence in Mixing Operations, Academic Press, New York, 1975.

Calabrese, R. V., and C. M. Stoots, "Flow in the impeller region of a stirred tank," Chem. Eng. Prog., pg. 43, May 1989.

Chang, T. P. K., Y. H. E. Sheu, G. B. Tatterson, and D. S. Dickey, "Liquid dispersion mechanisms in agitated tanks: Part II, straight blade and disc style turbines," Chem. Eng. Comm., v. 10, pp. 215-222, 1981.

Costes, J. and J.P. Couderc, "Study by laser Doppler anemometry of the turbulent flow induced by a Rushton turbine in a stirred tank: influence of the size of the units - II Spectral analysis and scales of turbulence," Chem. Eng. Sci., v. 43, pp. 2765-2772, 1988.

Cutter, Louis A., "Flow and turbulence in a stirred tank," AIChE Journal, v. 12, pp. 35-45, 1966.

Evans, R. L., "Turbulence and unsteadiness measurements downstream of a moving blade row," J. of Eng'g. for Power, v. 97, pp. 131-139, 1975.

Hanjalic, K. and B.E. Launder, "A Reynolds stress model of turbulence and its application to thin shear flows," J.Fluid Mech., v. 52, part 4, pp. 609-638, 1972.

Heskestad, Gunnar, "A generalized Taylor hypothesis with application for high Reynolds number turbulent shear flows," J. Appl. Mech., v. 32, pp. 735-739, 1965.

Hinze, J. O., Turbulence, An Introduction to its Mechanism and Theory, 2nd ed, McGraw Hill Classic Textbook Reissue, McGraw Hill, Toronto, 1987.

Komasawa, I., R. Kuboi, and T. Otake, "Fluid and particle motion in turbulent dispersion - I Measurement of turbulence of liquid by continual pursuit of tracer particle motion," Chem. Eng. Sci., v. 29, pp. 641-650, 1974.

Latto, B., M.L.C. Papple, M. Shoukri, and M.H.I. Baird, "Mixing of thermally stratified fluids by injecting a series of vortex rings - a numerical simulation," Trans. I. Chem. E., Part A, 1990.

Laufhutte, Hans Deitrich, and Alfons Mersmann, "Dissipation of power in stirred vessels," Fifth European Conference on Mixing, Wurtzberg, June 10-12, 1985.

Laufhutte, Hans Deitrich, and Alfons Mersmann, "Laser Doppler velocimetry as a suitable measuring technique for the determination of flow behavior in stirred fluids," Ger. Chem. Eng., v. 8, pp. 371-379, 1985.

Laufhutte, Hans Deitrich, and Alfons Mersmann, "Local energy dissipation in agitated turbulent fluids and its significance for the design of stirring equipment," Chem. Eng. Technol., v. 10, pp. 56-63, 1987.

Launder, B. E. and D. B. Spalding, Lectures in Mathematical Models of Turbulence, Academic Press, New York, 1972.

Okamoto, Y., N. Nishikawa, K. Hashimoto, "Energy dissipation rate distribution in mixing vessels and its effects on liquid-liquid dispersion and solid-liquid mass transfer," International Chemical Engineering, v. 21, pp. 88-94, 1981.

Placek, J., L. L. Tavlarides, G. W. Smith and I. Fort, "Turbulent flow in stirred tanks, Part II: a two scale model of turbulence," AIChE Journal, v. 32, pp. 1771-1786, 1986.

Prandtl, Ludwig, Essentials of Fluid Dynamics with applications to hydraulics, aeronautics, meteorology and other subjects, Hafner Publishing, (no date).

Rao, M. A. and R. S. Brodkey, "Continuous flow stirred tank turbulence parameters in the impeller stream," Chem. Eng. Sci., v. 27, p. 137-156, 1972.

Speziale, in Whither Turbulence? Turbulence at the Crossroads, J.L. Lumley ed., Springer Verlag,1990.

Tennekes, H. and J. L. Lumley, A First Course in Turbulence, MIT Press, Cambridge, Mass., 1972.

Tropea, C., M. Stieglmeier, W. Dursthoff, L. Zhan. "The application of LDA to the measurement of wave induced velocity fields," IAHR workshop on instrumentation for hydraulics laboratories, CCIW, Burlington, Canada, August 16-18, 1989.

Turan, Ozden, "Further development of a new method of evaluating turbulence dissipation," PhD thesis, University of Manitoba, 1988.

Van der Molen, K. and H. R. E. Van Maanen, "Laser doppler measurements of the turbulent flow in stirred vessels to establish scaling rules," Chem. Eng. Sci., v. 33, pp. 1161-1168, 1978.

Van Doorn, M., "On Taylor's hypothesis in turbulent shear flows," Internal note 811123, University of Missouri-Rolla.

Van't Riet, K. and J. M. Smith, "The trailing vortex system produced by Rushton turbine agitators," Chem. Eng. Sci., v. 30, pp. 1093-1105, 1975.

Van't Riet, K., W. Bruijn, and J. M. Smith, "Real and pseudo-turbulence in the discharge stream from a Rushton turbine," Chem. Eng. Sci., v. 31, pp. 407-412, 1976.

Von Karman and Howorth, "On the statistical theory of isotropic turbulence," Proc. Roy. Soc., v. 164A, pp. 192-215, 1938.

Whitaker, Stephen, Introduction to fluid mechanics, Robert E. Kreiger Publishing, Florida, 1981.

Wood, P. E., "Studies of Mean Reynolds Stress Models of Turbulent Flow," PhD thesis, Cal. Tech., 1978.

Wood, P. E., and C.P. Chen, Numerical Heat Transfer, v. 9, pp. 115-123, 1986.

Wood, P. E. and C. P. Chen, "Turbulence model prediction of the radial jet - a comparison of k-ε models," Can. J. Chem. Eng., v. 63, pg. 177-182, 1985.

Wu, H. and G. K. Patterson, "Laser Doppler measurements of turbulent flow parameters in a stirred mixer," Chem. Eng. Sci., v. 44, pp. 2207-2221, 1989.

Wu, H., G. K. Patterson and M. Van Doorn, "Distribution of turbulence energy dissipation rates in a Rushton turbine stirred mixer," Expts. in Fluids, v. 8, pp. 153-160, 1989.

Yianneskis, M., Z. Popiolek and J. H. Whitelaw, "An experimental study of the steady and unsteady flow characteristics of stirred reactors," J. Fluid Mech., v. 175, pp. 537-555, 1987.

Yuu, S., and T. Oda, "Measurement of turbulence parameters in a non-baffled stirred tank with high rotation speeds," Chem. Eng. Journal, v. 20, pp. 35-42, 1980.

Chapter 6. Prediction of turbulence quantities using the swirling radial jet model of the Rushton turbine impeller

6.1 Introduction

Mathematical modelling of a fundamental kind where conservation equations are solved subject to initial and boundary equations can provide detailed information about the flow field which would be very difficult to obtain experimentally. This has been attempted by Harvey and Greaves (1982a and b), Placek and Tavlarides (1985), Placek et al. (1986), Ju et al. (1987 and 1990) and Kaminoyama et al. (1988). Progress in this area has been difficult, however, due to a shortage of experimental information on higher order turbulence quantities, which has only recently become available. This data is needed not only to build the mathematical models, but also to validate them.

In this chapter the 2-equation ($k-\varepsilon$) turbulence model described in section 5.3.7 is used to investigate the turbulent flow field in a stirred tank agitated by a Rushton turbine. This same $k-\varepsilon$ model has been used by several authors previously to study the flow patterns within stirred tanks [cf. Placek and Tavlarides (1982), Harvey and Greaves (1982a and b), Middleton et al. (1986), Ju et al. (1987 and 1990), Pericleous and Patel (1987), Kaminoyama et al. (1988), Hutchings et al. (1989)]. It is crucial to the model predictions that accurate boundary conditions be applied and it is clear from these earlier papers that an appropriate set of boundary conditions, especially with respect to turbulence modelling, has not yet been established for the agitator zone. This problem is similar to the $k-\varepsilon$ model predictions of the com-

plicated flow patterns that exist in the swirl combustor. With different boundary conditions at the combustor inlet, the predicted flow field in the combustor can change dramatically from no recirculation zone to a toroidal recirculating vortex at the center of the combustor (Ramos (1984)); hence it is clear that accurate boundary conditions are required to give accurate predictions of the flow field in the bulk.

The boundary conditions near the impeller blades which characterize the highly inhomogeneous turbulence generated by the impeller have been studied quite extensively. Experimental observations (Van't Riet and Smith (1975), Yianneskis et al. (1987), and Stoots and Calabrese (1989)) suggest that the flow generated by the passing turbine blades consists mainly of trailing vortices which are being continuously shed. Velocity measurements at a single point in the impeller stream show a strong periodic component with super-imposed fluctuations. One model for the impeller discharge stream was put forward by Placek and Tavlarides (1985). This is a mechanistic model based on the trailing vortex concept initially proposed by Van't Riet and Smith (1975) which is capable of providing estimates of the turbulence energy, k_p, of the large scale vortices in the impeller discharge stream. The model cannot however, be used to provide estimates of the turbulence dissipation rate ε, which is also required near the impeller blades. Furthermore, it is the average values of the velocities and turbulence quantities that are required as input to the $k-\varepsilon$ model, so it is not likely that dynamic modelling of the vortices being shed from the impeller is required. These dynamic predictions must be averaged in some sense to obtain useful boundary conditions. On the average, the flow generated by the turbine is jet-like. Because the impeller is rotating this jet is not purely radial but also has a swirl (or tangential) component. The concept of using a tangential jet

as a model to simulate the impeller discharge flow has been proposed by several authors (cf. DeSouza and Pike (1972), Obeid et al. (1982)). Ju et al. (1987 and 1990) compute the flow field using the tangential jet boundary condition, which requires knowledge of three experimental parameters, and assumes a zero gradient of k and ε at the impeller periphery. They concentrate their comparisons on the velocity field in the bulk of the tank, where agreement with experimental results is good. Agreement of the model results with the turbulence quantities k and ε, however, is qualitative at best (Ju et al. (1987)). The weaknesses of the tangential jet model are discussed by Kolar et al. (1984), who developed the more general swirling radial jet (SRJ) model to obtain outlet velocity profiles. Unfortunately, these models cannot give any information about the turbulence characteristics near the impeller blades, and it is this information which is required as input for a $k-\varepsilon$ model simulation for the turbulence in the entire tank.

Extension of impeller zone modelling to provide reliable predictions of k and ε at the impeller periphery is crucial to progress. It has been shown experimentally that the mean velocity field in the impeller discharge stream has a similarity profile that is established only a very short distance from the impeller. In particular, the observed velocity field is the same as that which would be produced by a turbulent, swirling radial jet. Velocity profiles predicted by Kolar et al. (1984) using this idealization show very good agreement with experimental data, however; problems in this earlier version of the SRJ model resulted in a number of parameters of unclear physical significance. In this chapter, the SRJ model is further developed and clarified, so that the only parameters required for its application are the peak discharge velocity and flow angle at the impeller tip. Based on the detailed experimental

results available in this region, optimum parameters are suggested, which require only the rotational speed and diameter of the impeller as input. Instead of the mixing length hypothesis used in Kolar et al. (1984), the $k-\varepsilon$ model is used to close the governing equations, and to quantify the turbulence characteristics. One of the major objectives of this work then, is to extend the phenomenological, swirling radial jet model of the impeller region (Kolar (1982)) by using a $k-\varepsilon$ turbulence model to obtain direct estimates of k and ε on the impeller periphery.

Modelling of this flow field is further complicated by the addition of baffles around the tank wall. These baffles encourage top to bottom circulation in the tank, but also make the flow field three dimensional over part of the volume, and introduce a drag which makes it difficult to represent the flow realistically as an axisymmetric (ie. two dimensional) one, especially with regard to the turbulence quantities k and ε. Harvey and Greaves (1982a) and Pericleous and Patel (1987) model the effects of the baffles by introducing a pressure induced drag term in the θ - component of the equations of motion. This drag term contains a coefficient, which is, in essence, a tuning parameter. Chen and Wood (1988) found that (for the SRJ boundary condition) if this parameter is set to zero, an incorrect velocity field results. The most reasonable predictions were obtained when it was set to 10^{-5}. For the boundary conditions used by Harvey and Greaves (1982a), the best value for the parameter was 1. Placek and Tavlarides (1982, 1985), Placek et al. (1986), and Ju et al. (1987 and 1990) model the stirred tank by introducing modifications to the turbulence model and boundary conditions, which meet with limited success. Hutchings et al. (1989) deal with the baffles by complete suppression of the tangential velocity in the axisymmetric case, and its suppression in the baffle region for the three

dimensional case. It was found that, while this irrotational treatment results in reasonable mean velocity profiles, it has severe implications for the prediction of turbulence quantities, resulting in differences of up to three orders of magnitude from a full 3-dimensional, swirling case. In this work, the baffles are not modelled, but are included as part of the three dimensional calculation domain. This has allowed reproduction of details of the flow field around the baffles as they are observed in flow visualization experiments, and very good prediction of the turbulence quantities. This approach also requires much less a priori knowledge of the flow field than previous methods.

6.2 Turbulence Model

The reported simulations consist of two parts:

1) Solution of the SRJ model to obtain the boundary conditions at the tip of the impeller as described in Wood and Chen (1985).
2) Three dimensional simulations of the flow using FLUENT, a commercial software package.

The two equation ($k-\varepsilon$) model described in chapter 5 is used in both the modelling and simulation parts of this study because it is the most tested and reliable turbulence model available. Although it will not give the amount of information that a Mean Reynolds Stress model will give, it requires an order of magnitude less computation time and gives predictions of the mean velocities that are of comparable accuracy to the higher order models. The model constants used are given in Table 4.

Table 4: $k-\varepsilon$ model constants used in simulations

Simulation	C_μ	$C_{\varepsilon 1}$	$C_{\varepsilon 2}$	σ_ε	σ_k
SRJ model	0.09	1.43	1.92	1.3	1.0
FLUENT	0.09	1.44	1.92	1.3	1.0

6.3 Swirling Radial Jet Model of Impeller Discharge Flow

It has been known for some time that the turbulent stream ejected from a Rushton turbine behaves like a "tangential jet" (DeSouza and Pike (1972)), and subsequently this model was modified to the more general case of a swirling radial jet (Kolar (1984)). In the analysis presented in Kolar (1982, 1984) the mixing length hypothesis was used to close the mean momentum equations and solutions were obtained for the radial component of the mean velocity profile. The results were in good agreement when compared to the radial velocity data for several different types of radial impellers. This suggests that the basic model is a good one for predicting the mean velocity in the impeller stream. This type of closure, however, gives no information whatever about the turbulence kinetic energy and its dissipation rate in the vicinity of the impeller blades. If the $k-\varepsilon$ model is to be used to predict the turbulence quantities in the tank, then profiles of k and ε are needed along every boundary surface. The approach used here is to apply the model of the swirling radial jet to predict profiles of both the mean velocity and turbulence quantities along the periphery of the volume swept out by the impeller. The standard $k-\varepsilon$ model

subject to the boundary layer and high Reynolds number approximations is used for establishment of boundary conditions. The same model, in its unsimplified form, is used for tank simulations.

6.3.1 Reduction and Transformation of Governing Equations

The radial turbulent jet with swirl is governed by the mean equations of motion and the continuity equation. A cylindrical coordinate system was selected, with its origin at the center of the impeller. At steady state, the momentum and continuity equations, subject to the assumptions of high Reynolds number and the boundary layer approximation, reduce to:

$$\frac{\partial(rV_r)}{\partial r}+\frac{\partial(rV_z)}{\partial z}=0 \tag{65}$$

$$V_r\frac{\partial V_r}{\partial r}+V_z\frac{\partial V_r}{\partial z}-\frac{V_\theta^2}{r}=\frac{1}{\rho}\frac{\partial \tau_{rz}}{\partial z} \tag{66}$$

$$V_r\frac{\partial V_\theta}{\partial r}+V_z\frac{\partial V_\theta}{\partial z}+\frac{V_rV_\theta}{r}=\frac{1}{\rho}\frac{\partial \tau_{\theta z}}{\partial z} \tag{67}$$

A standard $k-\varepsilon$ model (Launder and Spalding (1972)) is used to close this set of equations. The constitutive equations for the turbulent fluxes are given by:

$$\tau_{rz}=-\rho\overline{v_r'v_z'}=\rho\nu_t\frac{\partial V_r}{\partial z} \tag{68}$$

$$\tau_{\theta z}=-\rho\overline{v_\theta'v_z'}=\rho\nu_t\frac{\partial V_\theta}{\partial z} \tag{69}$$

With the eddy viscosity defined by:

$$\nu_t = 0.09\frac{k^2}{\varepsilon} \tag{70}$$

The governing transport equations for k and ε, subject to the boundary layer approximation are:

$$V_r\frac{\partial k}{\partial r} + V_z\frac{\partial k}{\partial z} = \frac{\partial}{\partial z}\left(\frac{\nu_t}{\sigma_k}\frac{\partial k}{\partial z}\right) + B - \varepsilon \tag{71}$$

$$V_r\frac{\partial \varepsilon}{\partial r} + V_z\frac{\partial \varepsilon}{\partial z} = \frac{\partial}{\partial z}\left(\frac{\nu_t}{\sigma_\varepsilon}\frac{\partial \varepsilon}{\partial z}\right) + \frac{\varepsilon}{k}\left[c_{\varepsilon_1}B - c_{\varepsilon_2}\varepsilon\right] \tag{72}$$

$$B = \nu_t\left(\frac{\partial V_z}{\partial z}\right)^2 + \nu_t\left(\frac{\partial V_\theta}{\partial z}\right)^2 \tag{73}$$

The momentum integrals which express the conservation of radial momentum and angular momentum may be written:

$$\lim_{r\to\infty}\int_{-\infty}^{\infty}\rho r V_r^2 dz = M_\infty \tag{74}$$

$$\int_{-\infty}^{\infty}\rho r^2 V_r V_\theta dz = G \tag{75}$$

This gives a total of 4 governing equations, 2 momentum integral constraints, and 2 constitutive equations, plus continuity, in 3 dimensions. Solution of these differential equations would be a difficult task. By performing a coordinate transformation $(r,\theta,z)\rightarrow(r,\xi)$, the problem can be substantially reduced. This

transformation is depicted graphically in figure 82, where r and θ are the radial and azimuthal directions, and ξ is the direction of flow in the impeller discharge. From figure 1, the following observations can be made:

1) the angle β is exactly 90° at the circle of radius e, where ξ is equal to zero: ie. this is the origin of the system of tangential half planes

2) the angle β decreases as r increases, going to zero as $r \rightarrow \infty$.

3) at any radial position, given the angle of declination of the flow from the purely radial direction, e can be determined from

$$\sin\beta = \frac{e}{r} \qquad \text{or} \qquad \cos\beta = \frac{\xi}{r} \quad (76)$$

4) the position of the impeller periphery relative to e is thus fully determined by the flow angle β_o at the periphery, or at any other radial position where the SRJ model holds. For a given impeller diameter, a single measurement of the flow angle allows e to be determined explicitly.

5) $$\xi = \sqrt{r^2 - e^2} \quad (77)$$

Following Riley (1962) and Kolar (1982), the flow field in this system of tangential half planes can be expressed by the following geometrical relations:

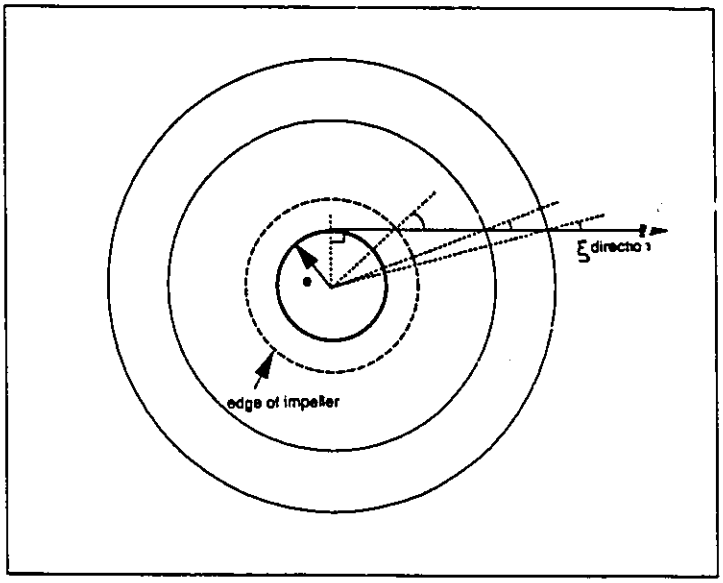

Figure 82. Graphical depiction of coordinate transformation $(r,\theta,z) \rightarrow (r,\xi)$

$$V_r = q\frac{\xi}{r} \qquad V_\theta = q\frac{e}{r} \tag{78}$$

$$\tau_{rz} = \tau_{\xi z}\frac{\xi}{r} \qquad \tau_{\theta z} = \tau_{\xi z}\frac{e}{r} \tag{79}$$

Where q is the velocity component in the ξ direction, and $\tau_{\xi z}$ is the turbulent shear stress in the ξ direction.

Using the transformation $(r,\theta,z) \rightarrow (\xi,z)$, the governing equations (65 - 75) for the SRJ become:

$$\frac{\partial}{\partial\xi}(\xi q) + \frac{\partial}{\partial z}(\xi V_z) = 0 \tag{80}$$

$$q\frac{\partial q}{\partial\xi} + V_z\frac{\partial q}{\partial z} = \frac{1}{\rho}\frac{\partial\tau_{\xi z}}{\partial z} \tag{81}$$

$$q\frac{\partial k}{\partial \xi}+V_z\frac{\partial k}{\partial z}=\frac{\partial}{\partial z}\left(\frac{\nu_t}{\sigma_k}\frac{\partial k}{\partial z}\right)+\frac{\tau_{\xi z}}{\rho}\frac{\partial q}{\partial z}-\varepsilon \tag{82}$$

$$q\frac{\partial \varepsilon}{\partial \xi}+V_z\frac{\partial \varepsilon}{\partial z}=\frac{\partial}{\partial z}\left(\frac{\nu_t}{\sigma_\varepsilon}\frac{\partial \varepsilon}{\partial z}\right)+\frac{\varepsilon}{k}\left[c_{\varepsilon_1}\frac{\tau_{\xi z}}{\rho}\frac{\partial q}{\partial z}-c_{\varepsilon_2}\varepsilon\right] \tag{83}$$

The constitutive equations collapse to:

$$\tau_{\xi z}=\rho\nu_t\frac{\partial q}{\partial z} \tag{84}$$

and the momentum integral constraints reduce to:

$$J=\int_{-\infty}^{+\infty}q^2\xi dz=M_\infty=\frac{G}{e} \tag{85}$$

This transformed set of equations expresses the impeller stream turbulent flow field in the system of tangential half-planes to the cylinder of radius e with its axis coinciding with the axis of the jet symmetry.

6.3.2 Similarity Solution and Resulting Profiles

On closer examination, it becomes apparent that these equations have exactly the same form as those defining the turbulent radial jet with no swirl studied by Wood and Chen (1985). These equations admit a similarity solution, with similarity length and velocity scales defined as:

$$\delta(\xi)=\lambda\xi \qquad \text{and} \qquad q_M(\xi)=\frac{\gamma}{\xi} \tag{86}$$

respectively. The stream function is defined by:

$$q=\frac{1}{\xi}\frac{\partial \psi}{\partial z} \qquad \text{and} \qquad V_z=-\frac{1}{\xi}\frac{\partial \psi}{\partial z} \tag{87}$$

and the dimensionless similarity functions are:

$$\eta = \frac{z}{\delta(\xi)} \tag{88}$$

$$f(\eta) = \frac{\psi}{q_M(\xi)\delta(\xi)\xi} \tag{89}$$

$$g(\eta) = \frac{\overline{v_\xi' v_z'}}{q_M^2(\xi)} \tag{90}$$

$$p(\eta) = \frac{k}{q_M^2(\xi)} \tag{91}$$

$$m(\eta) = \frac{\varepsilon}{q_M^3/\delta(\xi)} \tag{92}$$

Using these transformations and variable definitions, the coupled set of partial differential equations (eqs. 80 - 84) can be reduced to a coupled set of ordinary differential equations in the single similarity variable η. This set of ordinary differential equations has boundary conditions at the jet centerline and jet edge, and can be solved using the calculation procedure described in Wood (1978) and Wood and Chen (1985) to yield the similarity profiles of f, g, p, and m. The similarity profiles are untransformed to obtain the stream function, Reynolds stress, k and ε respectively, all as functions of η. The computed values of the similarity variables are given at a series of points in Table 5.

Table 5: Similarity profiles as a function of η, determined using $k-\varepsilon$ model

η	q'	$g(\eta)$	$f(\eta)$	$p(\eta)$	$m(\eta)$
0.0	1.000	0.000	0.000	0.158	0.061
0.1	0.978	0.016	0.590	0.159	0.061
0.2	0.915	0.030	1.153	0.160	0.061
0.3	0.821	0.039	1.670	0.158	0.061
0.4	0.707	0.043	2.124	0.150	0.057
0.5	0.582	0.041	2.507	0.136	0.051
0.6	0.454	0.036	2.815	0.114	0.042
0.7	0.327	0.028	3.047	0.088	0.031
0.8	0.204	0.018	3.204	0.057	0.019
0.9	0.088	0.008	3.291	0.026	0.008
1.0	0.000	0.000	3.310	0.000	0.000
	$\lambda =$	0.16838			

There are two important things which must be considered due to the nature of this solution, both intimately related to the jet width. The first concerns the value of λ, the second relates to the virtual origin of the jet.

The jet spreading rate, or λ, is in fact, not a variable in these equations. It is an eigenvalue which is determined in the course of the problem solution. This is a direct consequence of the fact that the equations are singular in form, due to the complete neglect of molecular diffusion in their formulation. The locus of the singularity is at $z = \delta(\xi)$, which defines the jet width. This means that at the jet boundary, the profiles will not just approach zero, but will be identically equal to zero. This mathematical limitation will allow some simplifications in the development of predictions of e and β_o.

The lack of freedom in specification of λ leads to an apparent contradiction between the definition of $\delta(\xi)$ and the value of λ. Experimental results lead to the conclusion that the jet width is equal, or nearly equal to, the blade width at the impeller periphery. The origin of ξ is fully specified by the direction of flow at the impeller boundary, as discussed earlier. This leads to an over specified problem. In the similarity length scale at the impeller tip, all three variables are fixed. This conflict is resolved by realizing that the similarity equations are invariant to the transformation $(\xi) \rightarrow (\xi + \xi_v)$. This allows specification of the jet width at the impeller periphery, without violation of the previously defined origin of the coordinate ξ. The virtual origin, ξ_v and the jet geometry, are depicted in figure 83.

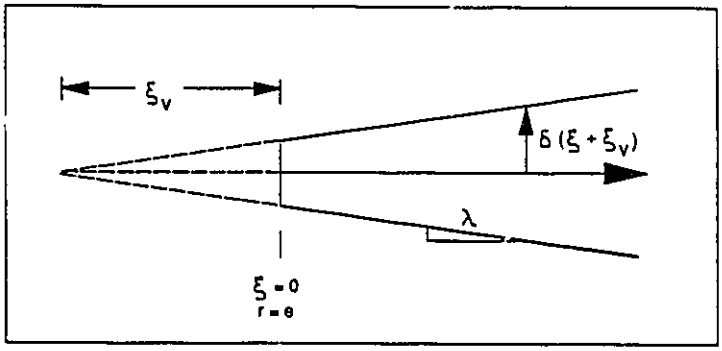

Figure 83. Jet geometry illustrating virtual origin

6.3.3 Experimental and Theoretical Predictions of e and β

Deconvolution of the similarity variables f, p, and m into the SRJ variables q, V_z, k and ε requires knowledge of γ, λ (calculated as part of the solution), $\delta(\xi)$ and $q_M(\xi)$. Further deconvolution of q into V_r and V_θ requires the use of e. As stated earlier, e can be defined in two ways: by the declination of flow (β) at any radial

The lack of freedom in specification of λ leads to an apparent contradiction between the definition of $\delta(\xi)$ and the value of λ. Experimental results lead to the conclusion that the jet width is equal, or nearly equal to, the blade width at the impeller periphery. The origin of ξ is fully specified by the direction of flow at the impeller boundary, as discussed earlier. This leads to an over specified problem. In the similarity length scale at the impeller tip, all three variables are fixed. This conflict is resolved by realizing that the similarity equations are invariant to the transformation $(\xi) \rightarrow (\xi + \xi_v)$. This allows specification of the jet width at the impeller periphery, without violation of the previously defined origin of the coordinate ξ. The virtual origin, ξ_v and the jet geometry, are depicted in figure 83.

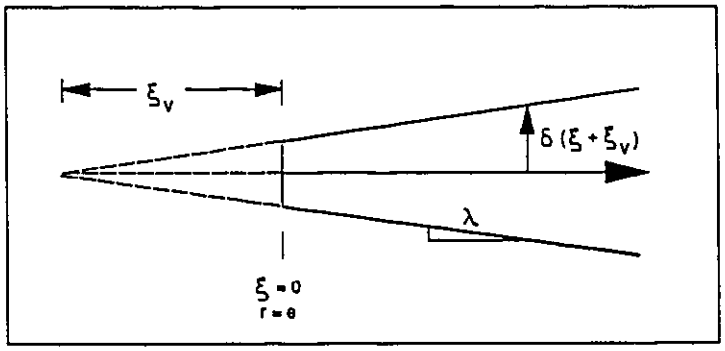

Figure 83. Jet geometry illustrating virtual origin

6.3.3 Experimental and Theoretical Predictions of e and β

Deconvolution of the similarity variables f, p, and m into the SRJ variables q, V_z, k and ε requires knowledge of γ, λ (calculated as part of the solution), $\delta(\xi)$ and $q_M(\xi)$. Further deconvolution of q into V_r and V_θ requires the use of e. As stated earlier, e can be defined in two ways: by the declination of flow (β) at any radial

position where the SRJ model holds, or through the equality

$$e = \frac{G}{M_\infty} = \frac{G}{J}$$

Since the objective is to define the boundary conditions at the impeller tip, the values required for deconvolution should be defined as close to that point as possible. Consideration of experimental evidence, as shown in Table 6 and figure 84, leads to adoption of the values

$$q_{M,o} = V_{TIP} = \pi N D$$

$$\beta_o = 45° \qquad (93)$$

$$\delta_o = \frac{D}{10}$$

Although the value of $q_{M,o}$, averaged over all cited experimental results, is $1.18V_{TIP}$, the median is $1.05V_{TIP}$. The median is more useful in this case, because it minimizes the influence of faulty data. The jet width δ_o is set equal to the half blade width. This means that there may be some under prediction of the velocities close to the edges of the blade; but from figure 84, this deviation is still within the range of the experimental results. Note that these results span a period of 20 years, and all of the major experimental techniques. Only two authors have been omitted from this comparison; the first performed early LDV work which has since been questioned (Bertrand (1980, 1980b), and the second performed his experiments in air,

rather than water (Gunkel and Weber (1975)). The value for which the least information is available, and which is thus the least reliable, is β_o. Again, the median value is used.

Table 6: Experimental data for maximum velocity and flow angle at impeller tip [123]

Author	Instrument	C	2r/D	$\frac{V_{r,m}}{\pi ND}$	β	$\frac{V_{\theta,m}}{\pi ND}$	$\frac{q_m}{\pi ND}$
Keller (85)	LDA	T/3	1.18	0.55	-	-	-
Armstrong (88)	LDA	T/3	1.02	0.74	-	-	-
Wong (88)	HFAnem	T/2,T/3	1.2	0.68	40	-	(.888)
Gunkel (75)	HWAnem	T/2	1.018	0.99	(42)	0.89	1.267
Cooper (68)	HWAnem	T/3	-	0.74	52 to 68	(.75)	1.054
V.d.Molen (78)	LDA	-	-	0.85	45	(.85)	1.02
Bertrand (80a)	HFAnem	T/2	1.11	1.043	45	0.935	(1.4)
		T/3	1.11	1.196	42	1.054	(1.5)
Bertrand (80b)	HFAnem	T/2	1.11	1.08	45	0.95	(1.44)
		T/2	1	0.868	-	-	-
Fort (82)	pitot	T/3	-	0.718	-	-	-
Wu (89)	LDA	T/3	1.11	0.745	-	0.663	(.997)
Costes (82)	HFAnem	T/2	1.11	0.76	-	0.66	(1.01)
Nouri (87)	LDA	T/3	1.2	0.822	-	-	-
Mahouast (87)	LDA	T/3	1.03	0.50	-	-	-

1 first author only listed
2 HWAnem = hot wire anemometer, HFAnem = hot film anemometer
3 bracketed values are calculated

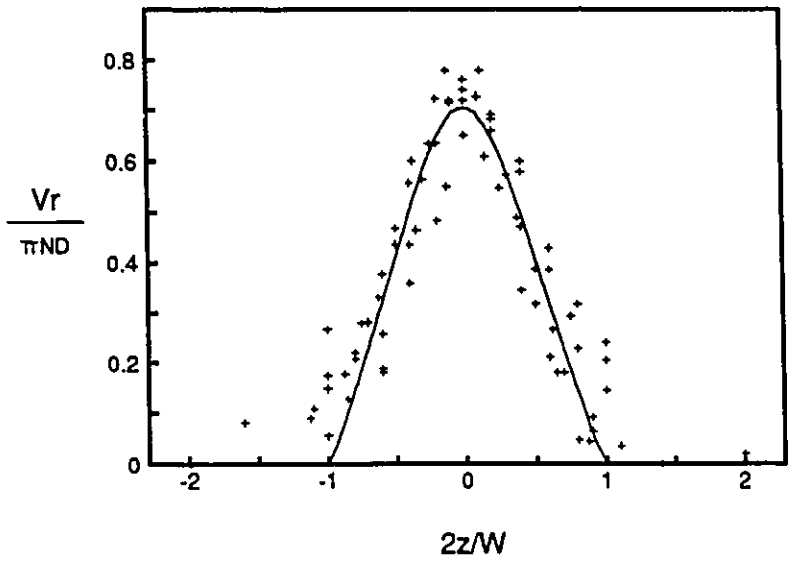

Figure 84. Radial velocity profile at impeller tip
Experimental data points from Wu and Patterson (1989), Armstrong and Ruszkowski (1988), Wong and Huang (1988), Nouri et al. (1987), Keller (1985), Fort and Mala (1982), Costes and Couderc (1982), Cooper and Wolf (1968). Line from SRJ model prediction.

It is also possible to predict e from theory, following equation 21. J can be simplified to

$$J = 2\lambda\xi^2 q_{M,o}^2 \int_0^1 q'^2 d\eta \tag{94}$$

given the sharp boundaries inherent in the model. Further, the integral can be evaluated numerically, using the values of q' from Table 5, to give

$$\int_0^1 q'^2 d\eta = 0.4167 \tag{95}$$

Given a way to evaluate G, e could be computed using equation (85). Kolar (1984) uses the same analysis as that applied to centrifugal pumps (McCabe and Smith (1967) to evaluate the angular momentum integral constraint (equation 75). This approach, however, requires the assumption of constant velocity profiles in V_r and V_θ across the tip of the impeller blade, which leads to a significant error in the integral of their product. Another approach is to apply a time averaged macroscopic mechanical energy balance (Bird et al. (1960)), which reduces to

$$\left[\frac{1}{2}\frac{\langle V_r^3\rangle}{\langle V_r\rangle}\right]_{\Sigma_V} - \left[\frac{1}{2}\frac{\langle V_z^3\rangle}{\langle V_z\rangle}\right]_{\Sigma_H} + \hat{W} + \hat{E}_v = 0 \tag{96}$$

for the impeller control volume, defined as the volume swept out by the impeller blades. Here Σ_V and Σ_H are the vertical and horizontal surfaces of this disk-like volume.

$\langle V_r^3\rangle$ can be written

$$\langle V_r^3 \rangle = \frac{1}{W}\int_{-\frac{W}{2}}^{+\frac{W}{2}} V_r^3 dz = \frac{2}{W}\left(\frac{2\xi_o}{D}\right)^3 (q_{M,o})^3 \frac{W}{2}\int_0^1 q'^3 d\eta \qquad (97)$$

the integral

$$\int_0^1 q'^3 d\eta = 0.6881 \qquad (98)$$

is calculated numerically from the SRJ similarity profile. From the definition of N_Q

$$\langle V_r \rangle = \frac{1}{W}\int_{-\frac{W}{2}}^{+\frac{W}{2}} V_r dz = \frac{Q}{\pi D W} = \frac{5N_Q N D^3}{\pi D^2} \qquad (99)$$

Taking V_z to be constant over Σ_H, and defined by a material balance around the impeller:

$$\frac{1}{2}\frac{\langle V_z^3 \rangle}{\langle V_z \rangle} = \frac{1}{2}V_z^2 = \frac{1}{2}\left(\frac{4ND^3N_Q}{2\pi D^2}\right)^2 \qquad (100)$$

By definition,

$$\hat{W} = \frac{-P}{m} = \frac{-N_p \rho N^3 D^5}{\rho N_Q N D^3} \qquad (101)$$

$\hat{E}_v$, the dissipation rate within the control volume, is difficult to define or measure. It is dealt with by inserting an efficiency term, η_{eff}, which is the fraction

of the power drawn which is not dissipated within the impeller control volume ($\hat{W} + \hat{E}_v = \eta_{eff}\hat{W}$). $q_{M,o}$ will be some fraction of the impeller tip speed: assume this to be one.

Substituting 97 - 101 back into 96 gives:

$$\left(\frac{\xi_o}{D}\right)^3 = \frac{5}{8\pi^3(0.688)}\left[\frac{2}{\pi}N_P\eta_{eff} + 4\frac{N_Q^3}{\pi^3}\right] \qquad (102)$$

for a standard impeller where $W = D/5$. Finally,

$$\frac{e}{D} = \sqrt{\left(\frac{1}{2}\right)^2 - \left(\frac{\xi_o}{D}\right)^2} \qquad (103)$$

This shows that e does not depend on N, except possibly through η_{eff}. The only information remaining which is required for the prediction of e is η_{eff}. η_{eff} can be calculated from the results of tank simulations, by integrating ε over the tank volume. This provides a check on the assumptions used for establishment of the boundary conditions (equations 93).

6.4 Tank Simulations

Simulations were carried out for two and three dimensional cases, using two tank geometries and two finite difference programs. The system chosen was a standard geometry, with T = 0.456 m, H = T, C = T/2, b = T/10, and the impeller dimensions D:L:W in the ratio 20:5:4. The impeller speed was 950 rpm, and two impeller diameters were considered: D = T/2 and D = T/3.

The code used for three dimensional calculations was FLUENT, a commercial finite difference package. The calculation domain considered comprised 1/8 of the tank volume. The grid used was $26 \times 30 \times 30$; $z \times r \times \theta$ with domain division for both D=T/2 and D=T/3 cases as follows:

1) uniform division of the 28 internal cells in the r direction.
2) in the θ direction, a contraction factor of 0.85 was applied from cells 2-15 (where 15 is the baffle cell), and an expansion factor of 1.1765 from cells 16-29.
3) in the z direction, uniform division was applied over the extent of the impeller (cells 2-7), and an expansion factor of 1.11 was applied over the remaining 18 cells.

This gave finer definition in the impeller region in the z direction, and refinement around the baffle in the θ direction, as sketched in figure 85.

The boundary conditions were defined as follows:

1) symmetry at the tank axis, and at the impeller centerline
2) cyclic, or repeating, at the mid-baffle plane: to satisfy a continuous pressure gradient condition
3) no slip at the tank wall, on the baffle, and along the bottom. These boundary conditions were computed using wall functions built into the FLUENT program.
4) vertical impeller boundary, Σ_V, according to the SRJ predictions of q, k, and ε, using the recommended experimental values for $q_{M,o}$ and β (equations 93).

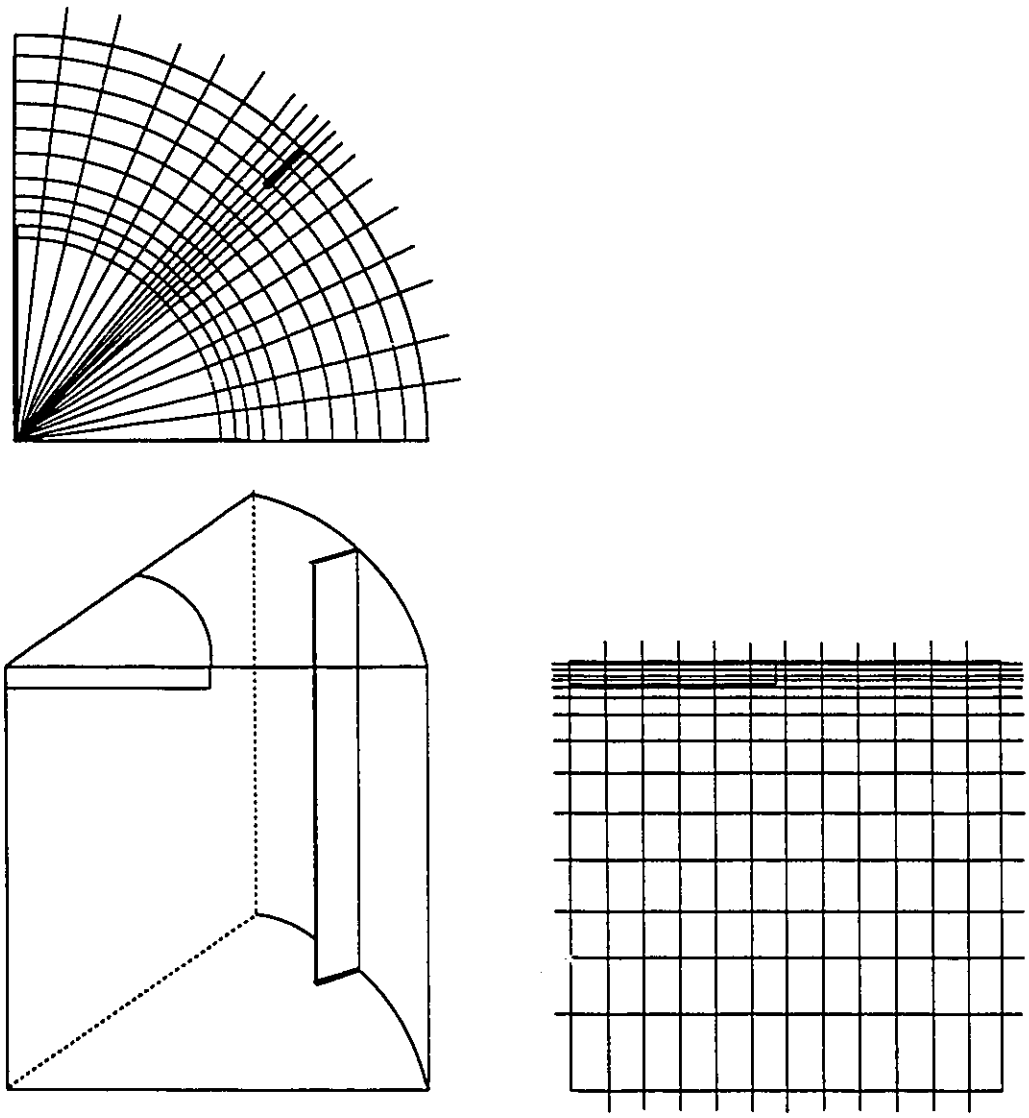

Figure 85. Sketch of calculation domain for three dimensional finite difference calculations.

5) horizontal impeller boundary (Σ_H) with V_z assumed constant over the impeller: determined from a material balance around the impeller; V_θ taken as solid body rotation; V_r, k, and ε set to zero.

Vertical symmetry across the impeller centerline was checked in two dimensions with a free surface at the top of the tank. It was found that deviations from symmetry were slight, and were at their maximum in the center of the tank, a region of minor importance in this flow field.

The normalized residuals of all variables converged to less than 5×10^{-3} within 600 iterations.

6.5 Results

The quantity of data acquired from three dimensional simulations such as these is immense. In this case, each of the 23400 cells has 5 values associated with it. Experimental data is not as plentiful, and if attention is confined to comparing the predictions with the data, then evaluation of the model predictions can be reduced to a reasonable task. The region of the tank with the steepest gradients, and the most intense turbulence, is the impeller discharge zone. This is the region of greatest interest for mixing and drop size distribution models, as it is the zone of highest shear. Since the aim of modelling the flow field in the tank is to improve the information available for these models, comparisons of the SRJ predictions with experimental results are concentrated on the impeller discharge zone. The comparisons proceed from the well established bulk properties of the flow field (the flow number, the power number, and overall circulation patterns), to quantitative comparisons for which experimental results are fairly plentiful (radial decay of V_r, k and ε) to details of the flow field for which data is scarce (profiles of k and V_r, behavior of the vortex behind the baffle). Given the excellent agreement of the

model predictions with all of these experimental criteria, the SRJ model results are used to provide additional information about the flow field, in the form of average values of ε.

6.5.1 Dimensionless Numbers

Two dimensionless numbers, N_p and N_Q, are well established for the Rushton turbine. The flow number (Revill (1982)) has been defined, and set to a value of approximately 0.75. Integration of the radial velocity profile predicted by the SRJ model at the tip of the impeller gives $N_Q = 0.78$, a difference of 4%. The power number is usually reported [cf. Bates et al. (1963) and Neinow and Miles (1971)] as 5.0, although there is significant experimental deviation in this number. Bujalski et al (1987) did a careful study of the power number, and found that for high Reynolds numbers, variations in N_p arose from changes in the disk thickness, as compared to the impeller diameter, and changes in scale. N_p was independent of D/T.

The mechanical energy balance discussed in section 6.3.3 can be used to calculate the fraction of the power dissipated in the tank, ie. η_{eff}. Substituting the established experimental values $N_p = 5.0$, $N_Q = 0.75$ and $\beta = 45°$ into equation (102) gives $\eta_{eff} = 0.46$. An independent estimate of η_{eff} can be computed by integrating the dissipation rate of each computational cell over the free volume of the tank. If the integral

$$\frac{\rho \int \varepsilon dV}{\rho N^3 D^5} = \eta_{eff} N_P \qquad (104)$$

is computed from the 3-dimensional simulation results, the prediction of η_{eff} is 0.46 for D=T/2 and 0.56 for D=T/3 where $N_p = 5.0$ has been used in both cases. This means that approximately 50% of the energy is dissipated before the fluid reaches the impeller periphery. A similar fraction of energy dissipation in the impeller control volume (50%) is reported by Placek and Tavlarides (1982). A similar trend, of increasing η_{eff} with decreasing D/T, was reported by Placek and Tavlarides (1986).

These two equations (102 and 104) are also used to check the assumption of constant β_o, made in order to establish the boundary conditions. If N_p and N_Q are constant, and computational results show that η_{eff} varies with D/T, then β_o cannot be constant. If β_o is calculated based on the computational results, $\beta_o = 44.9°$ for D=T/2 and $\beta_o = 39.7°$ for D=T/3. Examination of available experimental results (table 6) shows that this variation is very small compared to that seen in experiments. Given the excellent agreement of model results with experiment, even using the assumption of constant β_o, and the lack of reliable experimental evidence for a better evaluation, it seems best to accept this approach. The variation in η_{eff} appears to be related to the changing tank geometry. The implications of this are discussed further in section 6.5.6.

Comparing the SRJ results to those given by other authors shows an unprecedented emphasis on the impeller stream. If considered in terms of the total power, these results can be stated as 54% dissipated inside the impeller, 35% in the impeller stream, and 11% in the bulk of the tank, or the circulation zone. Cutter (1966) suggests only 20% dissipation in the impeller, 50% in the impeller stream, and 20-40% in the bulk of the tank. Gunkel and Weber (1975) state that 38% of the energy is dissipated inside the impeller boundaries. Okamoto (1981) finds that none

of the energy is dissipated inside the impeller. Wu (1989) states that 30% of the energy is dissipated in the impeller, 30% in the impeller stream, and 40% in the bulk of the tank. A reported experimental uncertainty of ±15% brings these measurements into the range of the SRJ model predictions.

6.5.2 Mean Velocity Fields

The flow pattern in a stirred tank with a radial impeller is known to consist of two toroidal vortices, or circulation loops; one above and one below the impeller, which rotate such that the impeller stream is radially directed outward. This was observed in the results of the simulations, and has been reported in detail elsewhere (Costes and Couderc (1988), Yianneskis et al. (1987)). In the r-θ planes, it has been reported that there is a vortex behind the baffles. Flow visualization experiments show that this vortex persists only in the vicinity of the impeller plane, and decays rapidly with increasing or decreasing z. This was also shown in the results of the simulations, as illustrated in figure 86.

The decay of V_r on the impeller centerline at the mid-baffle plane for D=T/3 is shown in figure 87. Since all available experimental results are for D=T/3, the computed decay for D=T/2 is not shown. The similarity solution predicts decay of $V_{r,m}$ with ξ^{-1}, which is not the case for the outer region of the tank. This is due to the influence of the baffle.

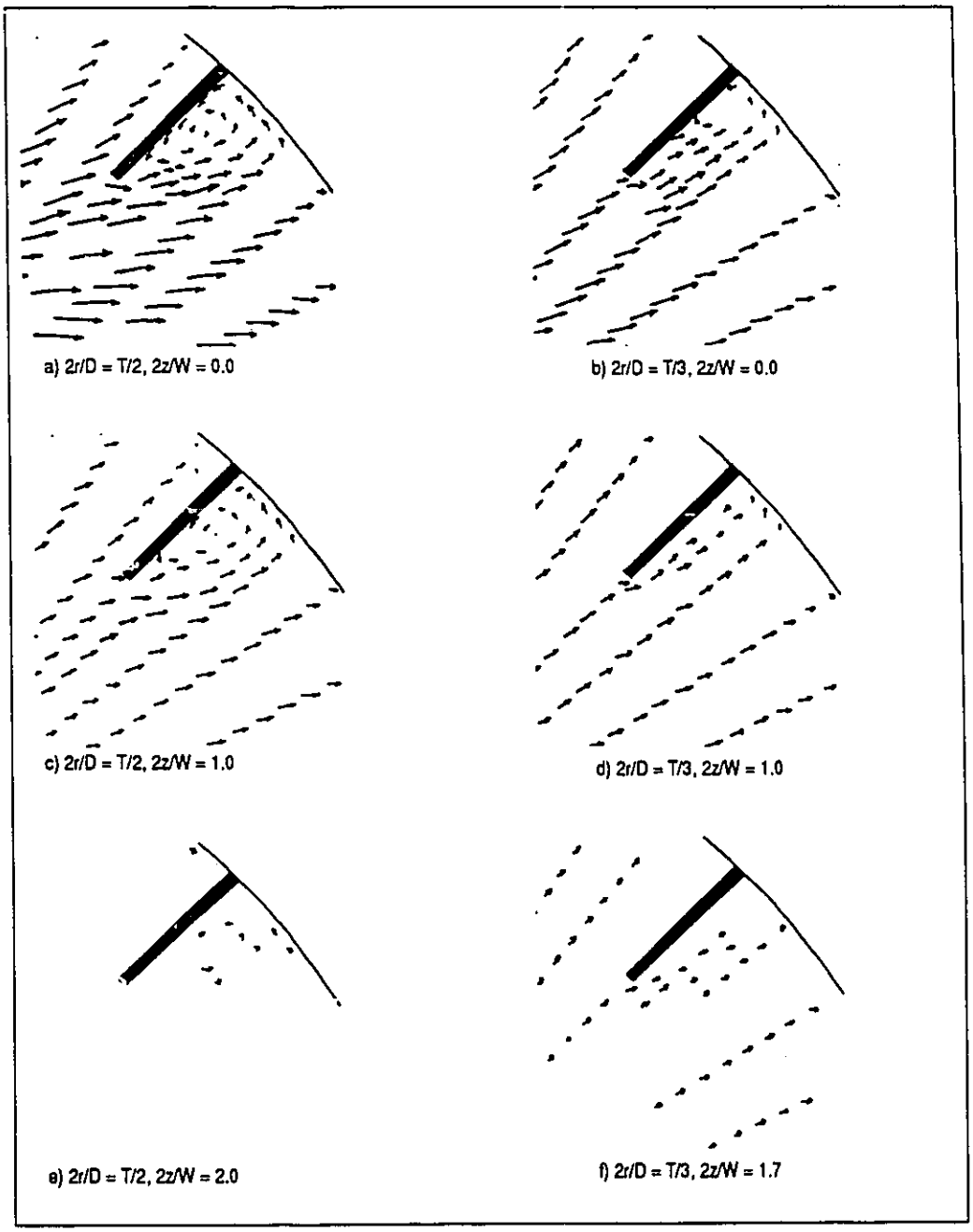

Figure 86. Axial variation in the velocity field showing the baffle vortex decay.

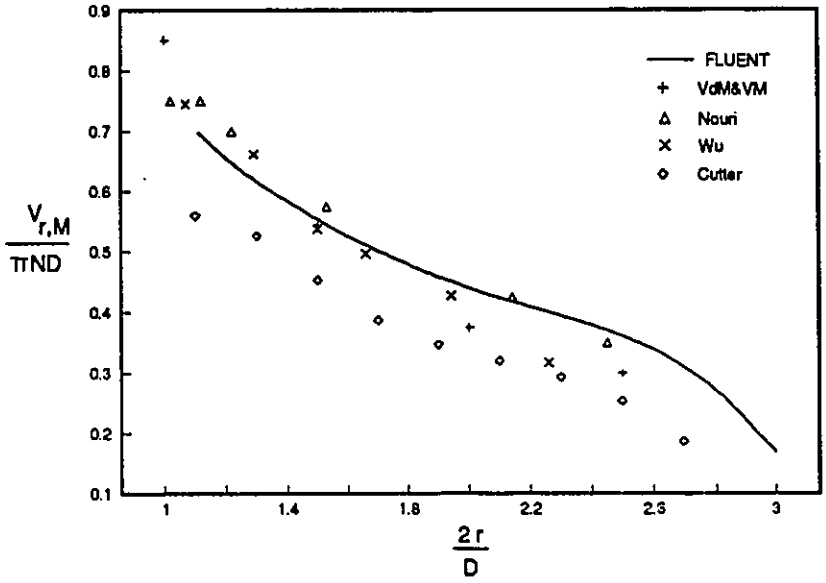

Figure 87. Decay of V_r on impeller centerline at mid-baffle plane for D=T/3.

Figure 88 shows the computed profile of V_r at 2r/D = 1.5 for D=T/3. All of the experimental profiles shown in this figure are for cases where the impeller was set at a clearance of C=T/3. Because of this asymmetry, the experimental velocity profiles are skewed to one side. They are also more elongated than the computed profile. Given the uncertainty in comparing asymmetric data to a symmetric case, agreement between experimental and computational results is good.

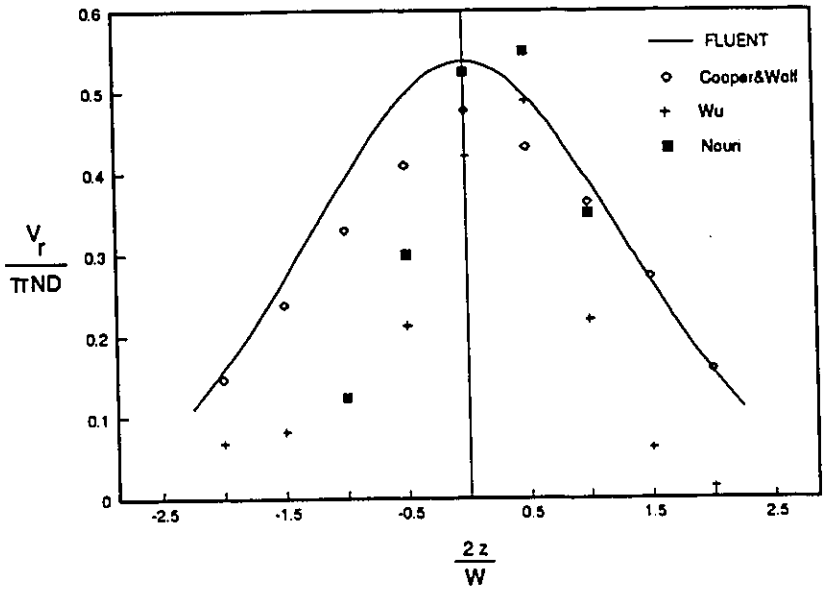

Figure 88. Profile of the radial component of velocity at 2r/D = 1.5 on the mid-baffle plane.

6.5.3 Two Dimensional Versus Three Dimensional

Figure 89 gives an example of the three dimensional character of the flow field in the outer 25% of the tank. The decay of k is virtually independent of angular position, from 4 degrees behind the baffle to 3.5 degrees ahead of the baffle. In the baffle zone, however, changes are rapid and extreme. Out to a radial position of $2r/D \approx 1.48$, the effects of the baffle are negligible, for the D=T/2 case. This lends credence to the assumption of axisymmetric flow at the impeller periphery, while showing the importance of an accurate representation of this complex geometry.

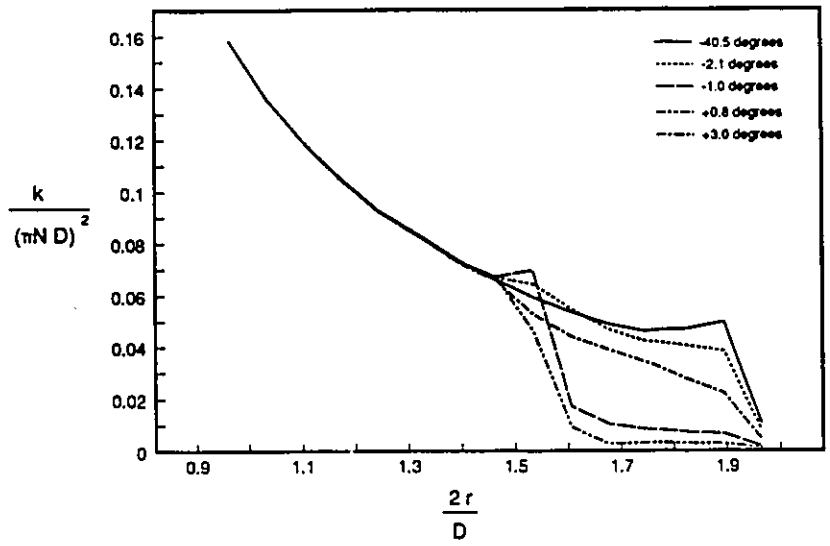

Figure 89. Angular variation in the centerline decay of the dimensionless turbulence kinetic energy (D=T/2).

6.5.4 Turbulence Kinetic Energy, k

The decay of k on the impeller centerline at the mid-baffle plane is shown in figure 90 for both impeller diameters, and three sets of experimental data. Only those values of k which include all three components of the velocity fluctuation are considered; those which ignore v_θ' ignore the second largest component of k and are thus subject to severe underprediction. Mahouast (1989) and Wu (1989) both report measurements taken using an LDV. Cutter's (1966) data was obtained by use of a photographic technique. Agreement between the model predictions and the experimental results is very good. The turbulence kinetic energy, made dimensionless with V_{TIP}, is shown to scale exactly with $2r/D$.

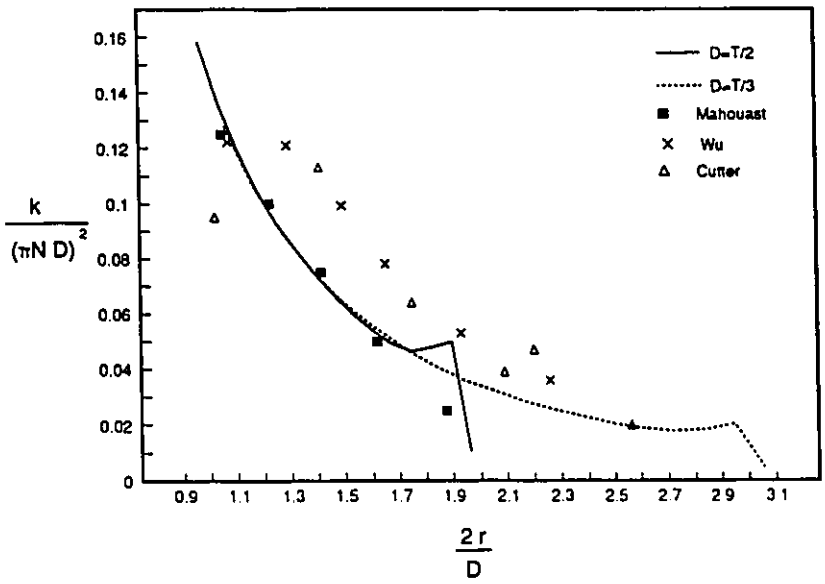

Figure 90. Decay of dimensionless turbulence kinetic energy on the impeller centerline at the mid-baffle plane - comparison with experimental results.

The profiles of k across the impeller tip at three radial positions are shown in figure 91. It appears that the curvature in the model is more extreme than that seen in experiments, but that the spreading and decay are fairly well predicted. Agreement down to this level of detail in the flow field has not previously been reported.

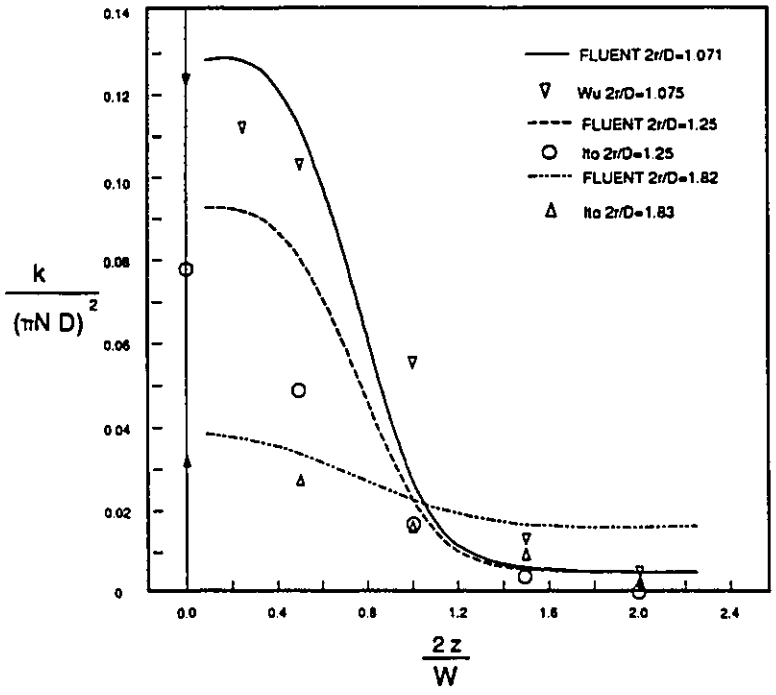

Figure 91. Profiles of turbulence kinetic energy in the impeller stream at various radial positions.

6.5.5 Turbulence Kinetic Energy Dissipation Rate ε

The decay of ε on the impeller centerline at the mid-baffle plane is shown in figure 92 for both impeller diameters, and four sets of experimental data. The radial decay of ε closely follows several previously reported experimental studies. The degree of agreement shown here, especially in the immediate vicinity of the impeller, indicates that the SRJ model accurately describes the impeller boundary condition.

Previous authors (Wu (1989) and Laufhutte (1987)) have reported surveys of ε data which showed a wide variations in the results. The primary cause of this

apparent deviation is not, as was suggested, the experimental technique or evaluation theory used, but incorrect scaling of ε. The general practice has been to plot $\varepsilon/\bar{\varepsilon}$ vs. $2r/D$, where $\bar{\varepsilon}$ is the power input per unit mass. Use of $\bar{\varepsilon}$, although it is appealing from a design point of view, contaminates the data with introduction of the tank diameter, cubed. If the scaling suggested by the more theoretically rigorous similarity solution is used, the data collapses very nicely, as shown in figure 92. This new scaling divides the value of ε by (V_{TIP}^3/D). Use of this modified dimensionless variable allows exact scale-up, over the axisymmetric region, from D=T/2 to D=T/3.

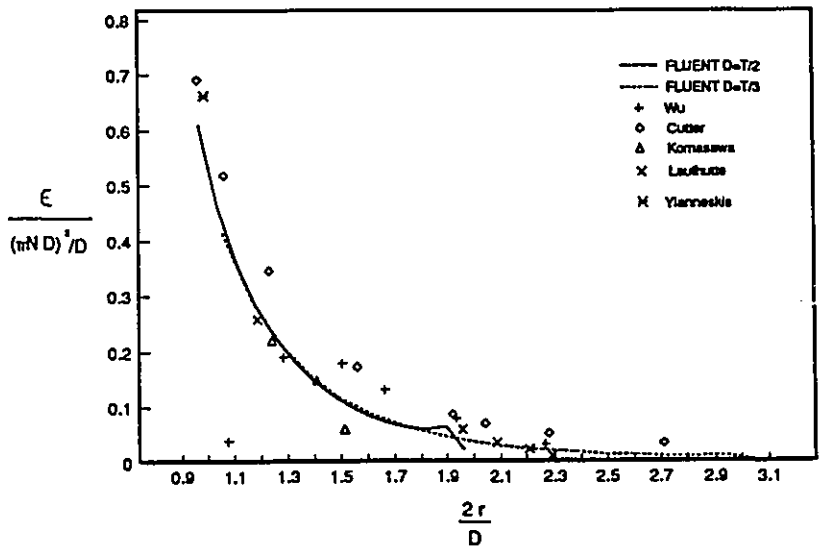

Figure 92. Decay of ε on impeller centerline - comparison with experimental results.

Comparison of the SRJ model predictions with other model predictions is shown in figure 93. Harvey and Greaves (1982) set k and ε equal to zero at the impeller boundary. Their predictions of ε are not only low, but show an incorrect trend; increasing as the wall is approached. Placek and Tavlarides' (1986) model

gives very low predictions close to the impeller, but approaches experimental results in outer regions. Their calculations concentrated on a case where D=T/4, so the effects of this under prediction close to the impeller were minimized. The SRJ model correctly predicts the exponential rise of ε as the impeller is approached. No other model is close to the data in this region.

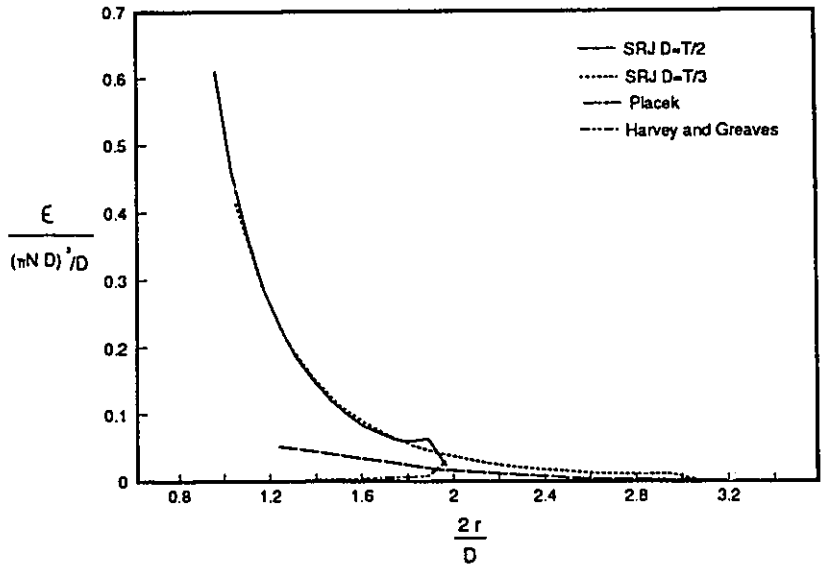

Figure 93. Comparison of various model predictions of the decay of ε on the impeller centerline.

6.5.6 Average Values

For the purposes of further modeling of reactors and chemical processes where computation of the detailed fluid mechanics is not practical due to the large number of variables involved, it is useful to define zones in the stirred tank where average values of the turbulence quantities may be applied. Based on the results of these simulations, two zones have been defined. The first is the impeller discharge

zone. This zone extends over the region where the SRJ dominates, and the effects of the baffles are not felt. The value of ε_{ave} for this zone is virtually independent of D/T. The second zone comprises the remaining free volume of the tank, and reflects the influence of changing D/T. More detailed zones (eg. baffle zone) could not be defined because of the changing geometry. While the impeller zone does not "see" its surroundings, the geometry has significant effects outside this zone. Of the total power drawn (calculated from N_p), approximately 50% is dissipated within the impeller control volume. The volume averaged, dimensionless, dissipation rate is constant with varying D/T within the impeller discharge zone (defined using dimensionless coordinates). The power remaining is dissipated in the bulk of the tank. This means that the bulk value can be expected to vary, depending on the tank geometry (especially D/T).

In order to define these zones rigorously, the dimensionless, volume averaged ε is defined as:

$$\varepsilon_{ave} = \frac{\int \varepsilon dV}{\frac{(\pi N D)^3}{D} \int dV} \qquad (105)$$

This was computed for each of the r, z, and θ planes, so that the variation of ε_{ave} could be examined, and appropriate zones chosen. Most of the variation occurs in the immediate vicinity of the impeller, from 2z/W = 0 to 1.0 (ε_{ave} decays to 10% of its initial value), and 2r/D = 1 to 1.45 (ε_{ave} decays to 30% of the boundary value). The limiting value of 2r/D must be chosen with some care if ε_{ave} for the impeller discharge zone is to remain constant from D=T/2 to D=T/3 : the zone cannot extend

into the region where the influence of the baffles begins to be felt (see figure 89). For the limits given above, $\varepsilon_{ave} = 0.195$ for D=T/2 and $\varepsilon_{ave} = 0.192$ for D=T/3, a difference of 1.6%.

The only variation in ε_{ave} which is not covered by the impeller discharge zone is that due to the influence of the baffles. This variation is shown for both cases in figure 94. Note that while the trends are clearly analogous for the two cases, no way of scaling the results so that they collapse onto one curve was found. It was concluded that this is mainly because the power input, and therefore the energy available to be dissipated, is dependent only on the impeller diameter and rotational speed: a smaller impeller in the same size tank (with constant N) has much less power available to be dissipated in the bulk of the tank. The volume of the tank relative to the volume of the impeller is much larger. Because any value of ε_{ave} defined for this zone would only be applicable to a specific case, no baffle zone has been defined.

For the bulk of the tank, ε_{ave} is $5.59x\,10^{-3}$ for D=T/2, and $2.07x\,10^{-3}$ for D=T/3. The volume covered by these averages is the free volume in the tank not included in the impeller zone. The baffle variations have been lumped into these averages.

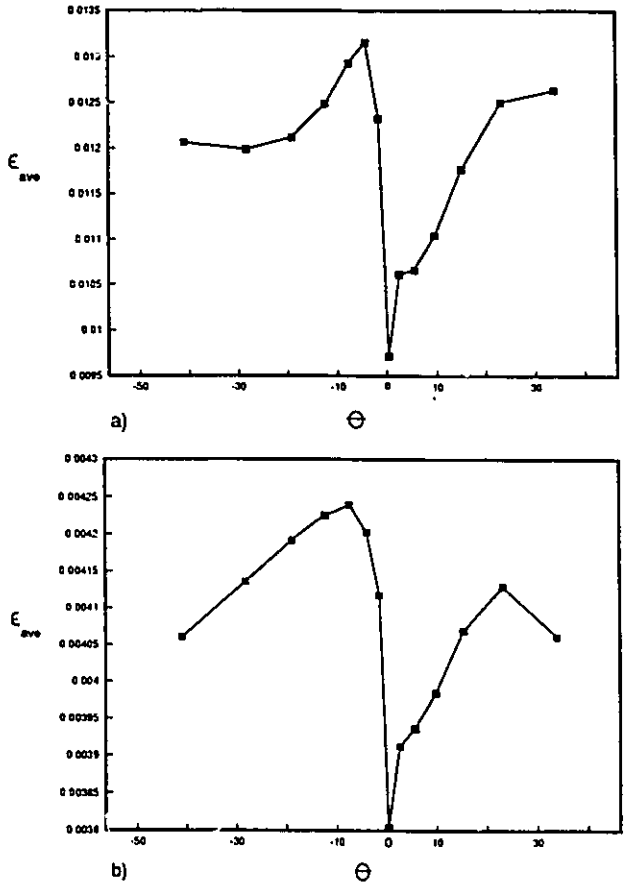

Figure 94. Variation of ε_{ave} with θ for a) D=T/2 and b) D=T/3

6.6 Conclusions

The turbulent swirling radial jet model can successfully be applied to the modelling of flow in stirred tanks with radial impellers, specifically the Rushton turbine. This model has been extended from the case of closure using the mixing length hypothesis, to closure using the $k-\varepsilon$ model. In addition, the model parameters have been clarified so that they have clear physical meaning. The success of this

modelling effort indicates that the modified $k-\varepsilon$ models recently proposed by several authors are not necessary, provided the proper boundary conditions are applied when using the standard $k-\varepsilon$ model.

The most reliable way to treat the drag introduced by the baffles around the tank periphery is to specify them as part of a three dimensional computational geometry. This allows elimination of the pressure induced drag term, (which is in essence a tuning parameter) so that the flow field can be calculated with much less a priori knowledge of the result.

Three dimensional simulations based on these principles yielded excellent agreement with experimental results. Details of the velocity field, decay of k and ε on the impeller centerline, profiles of V_r and k at various radial positions, and the total power dissipated were all accurately predicted. Previous studies have concentrated on predictions of the mean velocity field, and have shown only qualitative agreement with the turbulence quantities k and ε.

Appropriate zones were recommended for use in modelling efforts where the main interest is not the detailed fluid mechanics, but other processes such as mixing or reaction. Average values of ε were presented for these zones.

6.7 Notation

b = baffle width = T/10

B = holding variable

C = impeller clearance = T/2

C_{ε_1} = $k-\varepsilon$ model constant

C_{ε_2} = $k-\varepsilon$ model constant

C_μ = $k-\varepsilon$ model constant

D = impeller diameter

e = radius of cylinder, centered at $r = 0$, which defines the origin of the system of tangential half planes

$\hat{E}_v$ = rate at which system loses energy through dissipation, per unit mass

$f(\eta)$, $g(\eta)$, $p(\eta)$, $m(\eta)$ = similarity variables

G = total radial flux of angular momentum, or moment of momentum

H = height of liquid in the tank = T

J = total ξ flux of ξ momentum

k = turbulence kinetic energy per unit mass (m^2/s^2)

k_{ave} = volume averaged k

k_p = turbulence kinetic energy of large scale vortices (Placek and Tavlarides (1985))

L = length of impeller blades = D/4

m = mass rate of flow through impeller

M_∞ =total radial flux of radial momentum at infinity

N = rotational speed of impeller, rps

N_P = power number = $P/(\rho N^3 D^5)$

N_Q = flow number = $Q/(ND^3)$

P = power input

Q = primary flow

q = component of velocity in ξ direction

$q' = q/q_M$ = dimensionless q velocity determined from similarity solution

q_M = centerline q velocity

$q_{M,o}$ = centerline q velocity at impeller periphery

r = radial coordinate, origin at center of impeller

T = tank diameter

V_r = component of velocity in r direction

v_r' = turbulent velocity fluctuation of r component of velocity

V_{TIP} = impeller tip speed = πND

V_θ = component of velocity in θ direction

v_θ' = turbulent velocity fluctuation of θ component of velocity

V_z = component of velocity in z direction

v_z' = turbulent velocity fluctuation of z component of velocity

W = width of impeller blade = $D/5$

$\hat{W}$ = rate at which system performs mechanical work on surroundings, per unit mass

z = axial coordinate, origin at center of impeller

greek symbols

β = angle of declination of flow

β_o = β at impeller periphery

γ = constant

δ(ξ) = jet width

δ_o = jet width at impeller periphery

ε = turbulence kinetic energy dissipation rate (m^2/s^3)

$\bar{\varepsilon}$ = power input per unit mass

ε_{ave} = volume averaged ε

η = similarity coordinate

η_{eff} = impeller efficiency

θ = angular coordinate, origin at baffle plane

λ = jet spreading rate = constant = eigenvalue

ν_t = turbulent viscosity

ξ = coordinate in direction of flow (see figure 1)

ξ_o = value of ξ at impeller periphery

ξ_v = "virtual" origin of SRJ (see figure 2)

ρ = fluid density (kg/m^3)

$\sigma_k = k - \varepsilon$ model constant

$\sigma_\varepsilon = k - \varepsilon$ model constant

Σ_H = horizontal impeller boundary

Σ_V = vertical impeller boundary

τ = shear stress (rz,θz or ξz)

ψ = stream function

$\langle\rangle$ = quantity averaged over a surface

6.8 References

Armstrong, S. G. and S. Ruszkowski, "The flow field in the discharge stream of disk turbines," pp. 1-6, Proceedings of the Sixth European Conference on Mixing, Pavia, Italy, 24-26 May, 1988; BHRA Fluid Engineering Center, Springer Verlag.

Bates, Robert L., Philip L. Fondy, and Robert R. Corpstein, "An examination of some geometric parameters of impeller power," I. and E. C. Process Des. and Dev., v. 2, pp. 311-314, 1963.

Bertrand, J., J. P. Couderc and H. Angelino, "Power consumption, pumping capacity, and turbulence intensity in baffled stirred tanks: comparison between several turbines," Chem. Eng. Sci., v. 35, pp. 2157-2163, 1980.

Bertrand, J., J. P. Couderc and H. Angelino, "Ecoulement dans le courant de refoulement d'une turbine a disque et six pales plates dans une cuve munie de chicanes," The Chemical Engineering Journal, v. 19, pp. 113-123, 1980.

Bird, R. B., Warren E. Stewart and Edwin N. Lightfoot, Transport Phenomena, John Wiley and Sons, Toronto, 1960.

Bujalski, W., A. W. Nienow, S. Chatwin and M. Cooke, "The dependency on scale of power numbers of Rushton disc turbines," Chem. Eng. Sci., v. 42, pp. 317-326, 1987.

Chen, C. P. and P. E. Wood, "Numerical modelling of the turbulent flow in a stirred tank," 79th AIChE annual meeting, Miami Beach, Nov. 1-6, 1988.

Cooper, R. G. and D. Wolf, "Velocity profiles and pumping capacities for turbine type impellers," Can. J. Chem. Eng., v. 46, pp. 94-100, 1968.

Costes, J., and J. P. Couderc, "Pumping capacity and turbulence intensity in baffled stirred tanks: influence of the size of the pilot unit," Fourth European Conference on Mixing, Leewenhorst, April 27-29, 1982.

Costes, J., and J. P. Couderc, "Study by laser Doppler anemometry of the turbulent flow induced by a Rushton turbine in a stirred tank: influence of the size of the units - I Mean flow and turbulence," Chem. Eng. Sci., v. 43, pp. 2751-2764, 1988.

Cutter, Louis A., "Flow and turbulence in a stirred tank," AIChE Journal, v. 12, pp. 35-45, 1966.

Desouza, Abel, and Ralph W. Pike, "Fluid dymanics and flow patterns in stirred tanks with a turbine impeller," Can. J. Chem. Eng., v. 50, pp. 15-23, 1972.

Fort, Ivan, and Jana Mala, "Hydraulic characteristics of turbine impeller," Coll. Czech. Chem. Comm., v. 47, pp. 421-429, 1982.

Gunkel, Alfred A., and Martin E. Weber, "Flow phenomena in stirred tanks, Part 1: The impeller stream," AIChE Journal, v. 21, pp. 931-939, 1975.

Harvey, P. S., and M. Greaves, "Turbulent flow in an agitated vessel, Part I: A predictive model," Trans. I. Chem. E., v. 60, pp. 195-200, 1982.

Harvey, P. S., and M. Greaves, "Turbulent flow in an agitated vessel, Part II: Numerical solution and model predictions," Trans. I. Chem. E., v. 60, pp. 201-210, 1982.

Hutchings, Barbara J., R. J. Weetman, and B. R. Patel, "Computation of flow fields in mixing tanks with experimental verification," paper TN-481, ASME annual meeting, San Francisco, Dec. 10-15, 1989.

Ito, Shiro, Hohei Ogawa, Nobuo Yoshida, "Turbulence in impeller stream in a stirred vessel," J. Chem. Eng. Japan, v. 8, pp. 206-209, 1975.

Ju, S. Y., T. M. Mulvahill and R. W. Pike, "Turbulent, three dimensional velocity profiles in a turbine stirred vessel," Mixing XI - Engineering Foundation Conference on Mixing, Henniker, New Hampshire, August 1987.

Ju, S. Y., T. M. Mulvahill and R. W. Pike, "Three-dimensional turbulent flow in agitated vessels with a nonisotropic viscosity turbulence model," Can. J. Chem. Eng., v. 68, pp. 3-16, 1990.

Kaminoyama, M., F. Saito, M. Kamiwano, "Numerical analysis of three dimensional flow behavior of pseudoplastic liquid in a stirred vessel with turbine impellers," Kag. Kog, Ron., v. 14, #6, pp. 786-793, 1988.

Keller, D. B. A., "To determine the pumping capacity of a disk turbine impeller at different Reynolds numbers," Fifth European conference on Mixing, Wurtzberg, West Germany, 10-12 June, 1985.

Kolar, V., P. Filip, and A. G. Curev, "The swirling radial jet," Appl. Sci. Res., v. 39, pp 329-335, 1982.

Kolar, V., P. Filip, and A. G. Curev, "Hydrodynamics of a radially discharging impeller stream in agitated vessels," Chem. Eng. Comm., v. 27, pp 313-326, 1984.

Komasawa, I., R. Kuboi, T. Otake, "Fluid and particle motion in turbulent dispersion I: Measurement of turbulence of liquid by continual pursuit of tracer particle motion," Chem. Eng. Sci., v. 29, pp. 641-650, 1974.

Laufhutte, Hans Deitrich, and Alfons Mersmann, "Local energy dissipation in agitated turbulent fluids and its significance for the design of stirring equipment," Chem. Eng. Technol., v. 10, pp. 56-63, 1987.

Launder, B. E. and D. B. Spalding, "Mathematical Models of Turbulence," Academic Press, London, 1972.

Mahouast, M., and G. Cognet, "Analysis of turbulent mixing in a CFSTR from LDV measurements," ASME Third International Symposium on Laser Anemometry, ASME, FED, v. 55, pg. 157, Boston 1987.

Mahouast, M., G. Cognet, R. David, "Two component LDV measurements in a stirred tank," AIChE Journal, v. 35, pp. 1770-1778, 1989.

McCabe, Warren L., and Julian C. Smith, Unit Operations of Chemical Engineering, 2nd ed., McGraw Hill, Toronto, 1967.

Middleton, J. C., F. Pierce, P. M. Lynch, "Computations of flow fields and complex reaction yield in turbulent stirred reactors, and comparison with experimental data," Chem. Eng. Res. Des., v. 64, pp. 18-22, 1986.

Nienow, Alvin W., and David Miles, "Impeller power numbers in closed vessels," Ind. Eng. Chem. Process Des. Develop., v. 10, pp. 41-43, 1971.

Nouri, J. M., J. H. Whitelaw and M. Yianneskis, "The scaling of the flow field with impeller size and rotational speed in a stirred reactor," Second International Conference on Laser Anemometry - Advances and Applications, Strathclyde, UK, Sept. 1987.

Obeid, Ahmed, Ivan Fort, and Joel Bertrand, "Hydrodynamic characteristics of flow in systems with turbine impellers, Part LXI, Studies in Mixing," Coll. Czech. Chem. Comm., v. 48, pp. 568-577, 1982.

Okamoto, Y., N. Nishikawa, K. Hashimoto, "Energy dissipation rate distribution in mixing vessels and its effects on liquid-liquid dispersion and solid-liquid mass transfer," International Chemical Engineering, v. 21, pp. 88-94, 1981.

Pericleous, K. A., and M. K. Patel, "The source-sink approach in the modelling of stirred reactors," Physico Chemical Hydrodynamics, v. 9, pp. 279-297, 1987.

Placek, Jiri, and Lawrence L. Tavlarides, "A turbulent flow model applied to fluid flow in a stirred tank," Paper 101c, AIChE meeting, Los Angeles, Nov. 14-19, 1982.

Placek, Jiri, and Lawrence L. Tavlarides, "Turbulent flow in stirred tanks, Part I: Turbulent flow in the turbine impeller region," AIChE Journal, v. 31, pp. 1113-1120, 1985.

Placek, Jiri, Lawrence L. Tavlarides, G. W. Smith and I. Fort, "Turbulent flow in stirred tanks: Part II: A two scale model of turbulence," AIChE Journal, v. 32, pp. 1771-1786, 1986.

Ramos, J. I., "Turbulent nonreacting swirling flows," AIAA Journal, v. 22, pp. 846-848, 1984.

Revill, B. K., "Pumping capacity of disc turbine agitators - a literature review," Fourth European Conference on Mixing, Leewenhorst, April 27-29, 1982.

Riley, N., "Radial jets with swirl: Part 1, Incompressible flow," Quart. Journ. Mech. and Applied Math, v. 15, pp. 435-458, 1962.

Stoots, Carl M., and Richard V. Calabrese, "The trailing vortex system behind a Rushton turbine blade," Mixing XIII - Engineering Foundation Conference on Mixing, 1989.

Van der Molen, K., and H. R. E. Van Maanen, "Laser doppler measurements of the turbulent flow in stirred vessels to establish scaling rules," Chem. Eng. Sci., v. 33, pp. 1161-1168, 1978.

Van't Riet, K., and John M. Smith, "The trailing vortex system produced by Rushton turbine agitators," Chem. Eng. Sci., v. 30, pp. 1093-1105, 1975.

Wong, C. W., and C. T. Huang, "Flow characteristics and mechanical efficiency in baffled stirred tanks with turbine impellers," Proceedings of the Sixth European Conference on Mixing, Pavia, Italy, 24-26 May, 1988; BHRA Fluid Engineering Center, Springer Verlag.

Wood, P. E., "Studies of Mean Reynolds Stress Turbulence Models of Turbulent Flow," Ph.D. Thesis, California Institute of Technology, 1978.

Wood, P. E., and C. P. Chen, "Turbulence model predictions of the radial jet - a comparison of $k-\varepsilon$ models," Canadian Journal of Chemical Engineering, v. 63, pp. 177-182, 1985.

Wu, H. and G. K. Patterson, "Laser doppler measurements of turbulent flow parameters in a stirred mixer," Chem. Eng. Sci., v. 44, pp. 2207-2221, 1989.

Yianneskis, M., Z. Popiolek, and J. H. Whitelaw, "An experimental study of the steady and unsteady flow characteristics of stirred reactors," J. Fluid. Mech., v. 175, pp. 537-555, 1987.

Chapter 7. Turbulence characterization for the pitched blade turbine

Of all of the flow variables available to describe a turbulent flow field for the modelling of industrially important processes, the rate of dissipation of turbulence kinetic energy is the most important. In chapter five, the methods available for determining ε in stirred tanks were discussed in some detail, and four methods were chosen for experimental application. The principles upon which these methods rest can be summarized as follows: the *gradient hypothesis* method uses the constitutive equation from the k-ε model; *Taylor's hypothesis* is used to convert time derivatives to velocity derivatives; *dimensional* arguments lead to estimation of ε from k using a constant length scale; and finally, the *autocorrelation* coefficient function is used to calculate the Eulerian integral time scale, which is then combined with k to estimate ε. Various corrections have been suggested for all of these methods. In this chapter, the four methods will be applied to the flow produced by a 45° pitched blade turbine (PBT).

Previous measurements of ε in stirred tanks have always been confined to one method, and corrections have been applied with little or no indication of the effect which they have on the results. In this study, the four methods listed above are all applied to the same set of data, and the various corrections are examined with some care. The first comparisons are applied at the impeller outlet, across the edge of the blade. This is the most difficult part of the tank to characterize accurately, and the most demanding experimentally, due to the high turbulence intensity, and

the flow disruptions induced by individual blade passages. The methods which perform best at the impeller discharge are extended out into the bulk of the tank, both to provide further comparisons of the methods, and to provide data for verification of CFD experiments. Previous data has concentrated on the less efficient Rushton turbine impeller, which is no longer widely used in industry. These are the first reported measurements of ε for PBT systems. This is also the most complete ε data set currently available for any stirred tank system.

In order to calculate ε, many other intermediate turbulence quantities are needed. These include mean velocity gradients, Reynolds stresses, time derivatives of the fluctuating velocity, the turbulence kinetic energy, k, and the Eulerian integal time scale, τ_E. Wu and Patterson (1989) were the first to use the autocorrelation method, and thus τ_E, extensively for measurement of ε in stirred tanks. In this work, the methods for measurement and analysis of τ_E have been developed to the point where the steps required to obtain repeatable, physically meaningful values of τ_E can be recommended. The validity of various assumptions such as stationarity and isotropy, and the effects of variables such as the blade passage frequency (BPF), impeller rotational speed, and the LDA sampling frequency on the results have been considered.

Since all of the intermediate measured quantities are time averaged, statistical values, it is prudent to examine the time dependent characteristics of the data. This was done using the time series, frequency spectrum, and autocorrelation coefficient function representations of the data. The examination of time dependent characteristics revealed the dominance of the blade passage frequency, and of a low frequency about one twentieth of the blade passage frequency in the signal. These

are most clearly apparent in the curves of the autocorrelation function, R_E. The low frequency variation has not previously been reported. The effect of these frequencies on the turbulence quantities is examined throughout the chapter. They are found to have little or no effect on any quantity except the integral time scale, τ_E, which drops by 50% when the low frequency component is removed from the signal.

7.1 Signal characteristics

The data collected by the LDA is stored in the form of a series of Doppler frequencies, which are converted to velocities in the data processing step. The interval between successive data points is exactly one over the sampling frequency. The resulting series of velocity data points over time is referred to as the instantaneous velocity signal, or simply the signal. The principal tools available for its examination are the frequency spectrum, the autocorrelation coefficient function (R_E), and a time series plot of the data. The frequency spectrum and the autocorrelation are calculated using FFT's and the NAP code, which is discussed in detail in Appendix 2.

7.1.1 Time series

A time series of the axial velocity signal at the tip of the impeller blade, recorded at a sampling frequency of 1kHz, is shown in figure 95. The three horizontal lines show the mean, plus and minus one standard deviation. The time series shows the turbulent fluctuations, the fluctuations due to individual blade passages, and a 0.8s periodicity (one cycle for every 20 blade passages). Similar signals reported for the Rushton turbine (Yianneskis et al. (1987), Stoots and Calabrese (1989)) show no variations at time scales longer than the time required for one blade passage.

In this record, the high frequency velocity fluctuations obscure the details of the slower variation in the mean. These high frequency variations can be removed, and a much longer record of the slow variations in the signal examined, if the mean as averaged over a short interval of data is plotted as shown in figure 96. An averaging window of 0.2s was chosen, since this is the usual location of the first zero crossing of the auto-correlation function. This represents the smallest time lag for which velocities are not related to each other. The resulting record of the short time mean shows a much less regular, but still significant, low frequency pattern. The reduction in regularity was attributed to shaft run-out. It was found that the regularity of the low frequency fluctuations improved for runs where the shaft exhibited little run-out at the tip (for example, figure 95).

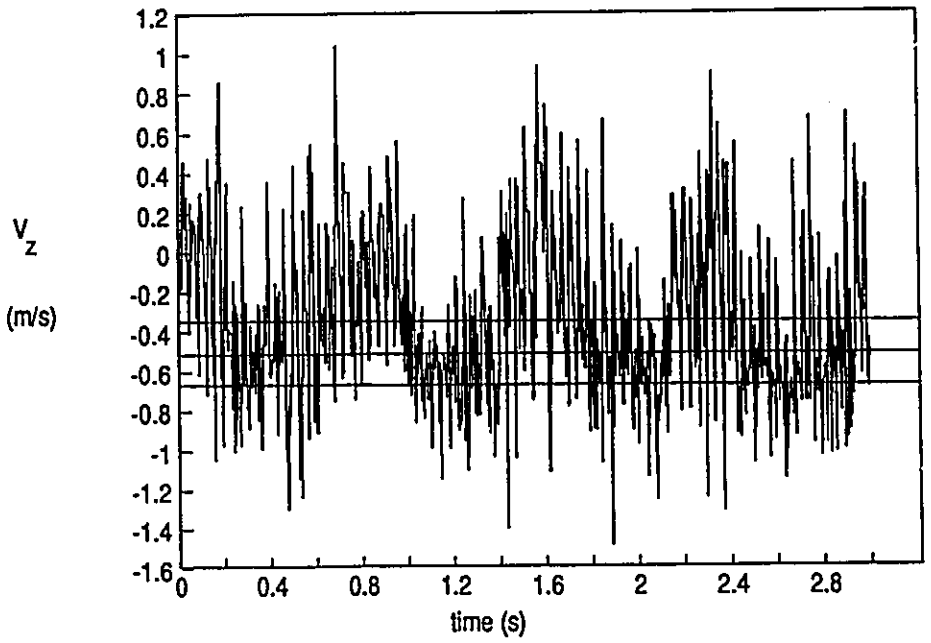

Figure 95. Time series record of the instantaneous axial velocity. N=400rpm, sampling frequency=1kHz, minimal shaft run out.

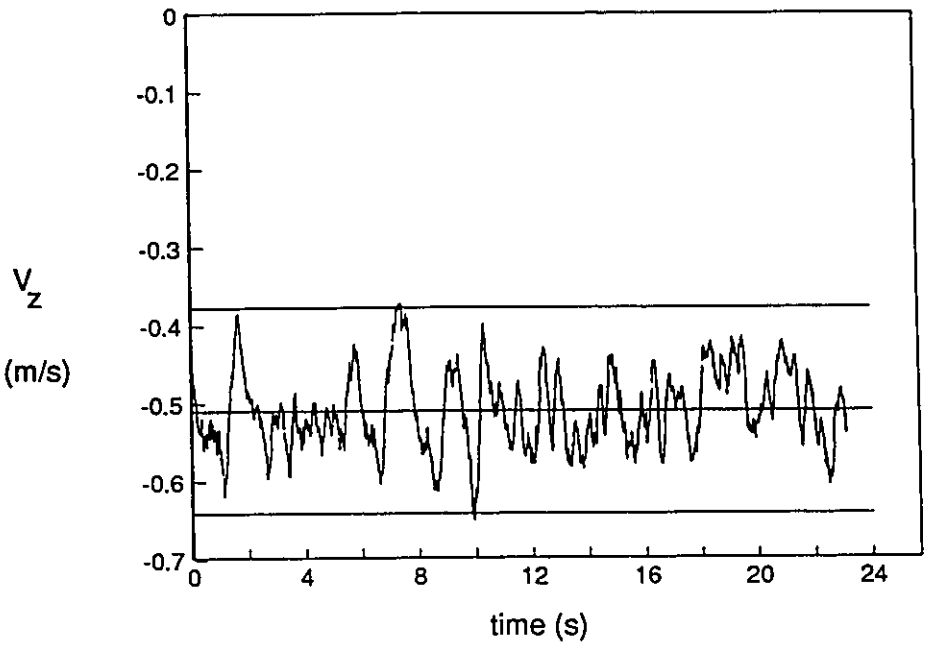

Figure 96. Time series record of the short time mean, averaged over a window of 0.2 seconds. N=450rpm, significant shaft run out.

One possible explanation of this low frequency oscillation is a tank time constant, or mean circulation time. This can be estimated using the flow number $N_q = 0.78$ defined in chapter 4 as $Q = N_q N D^3$. The volume of the tank is $V = 2\pi D^3$ when the impeller diameter D=T/2. Combining these equations into a time constant of V/Q gives an expected mean circulation time of 8 rotations of the impeller. The observed frequency of 1.28Hz (period = 0.8s) corresponds to 5 rotations at 400rpm, which would imply that the effective volume of the tank is only 60% of the total volume. From the mean velocity results in chapter 4, and the flow visualization results in chapter 2, it is apparent that the velocities in the top 40% of the tank are very low, which lends support to this proposal. It is not clear, however, why (or how) some parts of the circulation loop should move faster than others. Several other explanations are possible, such as the presence of a precessing vortex, or a

time varying flow field. The reader is referred to papers by Winardi and co-authors (1988, 1991) and Tatterson et al. (1980) for discussions of the time varying flow fields created by other axial impellers. The work by Winardi et al. (1991) on the average lifetimes of flow patterns produced by marine and paddle impellers is particularly interesting.

The fundamental hypothesis of this work, however, is that it is possible to analyse the flow without removing the regular oscillations, providing this is done carefully. In order to check this hypothesis, many of the results were calculated with the oscillations included, and with the oscillations removed. Wu and Patterson (1989) were able to remove the BPF oscillations from a Rushton turbine velocity signal using the first two terms of a Fourier expansion. The oscillations produced by a pitched blade turbine are not as regular, and it was found that a notch filter (see Appendix 2) was much more effective in this case. Costin et al. (1982) have applied the same method to the signal produced by instantaneous pressure fluctuations in a plasticating screw extruder, which is remarkably similar to figure 95. The low frequency oscillations were also removed using the notch filter, however, subtraction of the short time mean (0.2s window) from the instantaneous signal was found to be at least as effective for isolation of the higher frequency fluctuations.

7.1.2 Frequency spectrum

Figure 97 shows the frequency spectrum, or power spectral density (PSD) at 2r/D=0.8, along the lower edge of the impeller blades. The BPF appears at 26.67Hz, (1.42 on the log scale) with the first and second harmonics evident. For the upper end of the spectrum, the slope is -5/3. This satifies one of the conditions

necessary for validation of the assumption of local isotropy. Figure 98 shows the spectrum for a lower sampling frequency at a position in the tank (2r/D=1.4) where the BPF no longer appears. Again, the -5/3 slope is apparent. For a T/2 impeller, the BPF persists to 2z/W=-2.5 (C=T/2); for a T/3 impeller (C=T/3), it persists much further to 2z/W=-6.

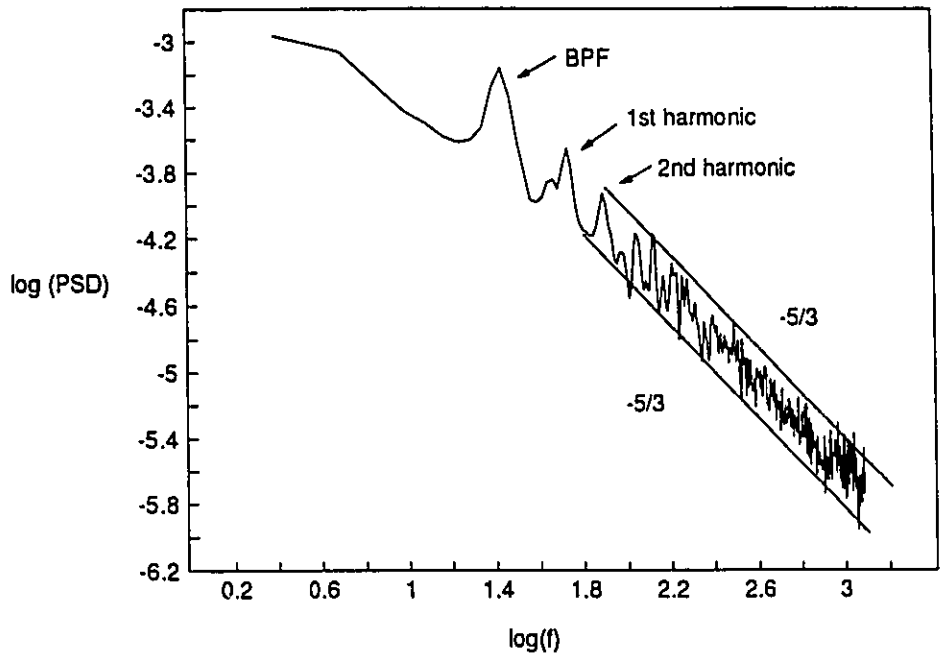

Figure 97. Frequency spectrum for the axial component of velocity at 2r/D=0.8 showing the presence of the blade passage frequency (BPF). Sampling frequency of 2.5kHz, 400rpm.

If the frequency spectrum were plotted on a linear-linear scale, and the area under the BPF peak was determined as a percentage of the total area under the curve, it would give the fraction of total power contained in the BPF frequency band. Similarly, the peak height gives a qualitative picture of the importance of the BPF at various positions. Figures 99 and 100 show the variation in the magnitude of the BPF peak in the frequency spectrum as compared to the axial velocity profile across

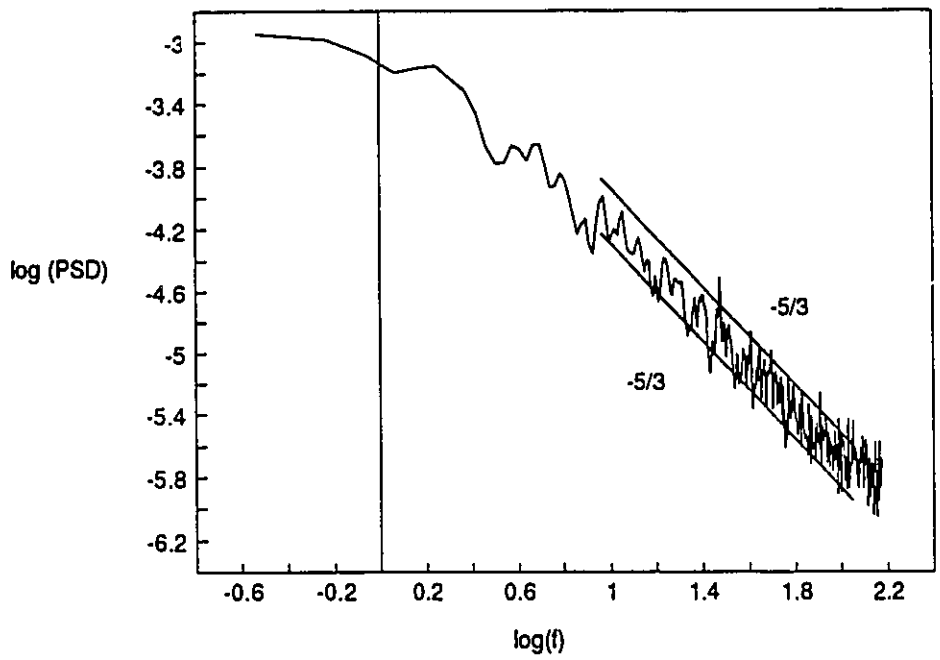

Figure 98. Frequency spectrum of the axial component of velocity at 2r/D=1.4 showing no peak at the BPF. Sampling frequency of 0.3kHz, 400rpm.

the lower edge of the impeller. Note that in both cases, the maximum BPF height occurs at a dimensionless radial distance 0.3 beyond the velocity peak, and extends over 0.4 radial units. Combining this information with the flow visualization results leads to the conclusion that the BPF has its greatest influence over the extent of the trailing vortices at the blade tips.

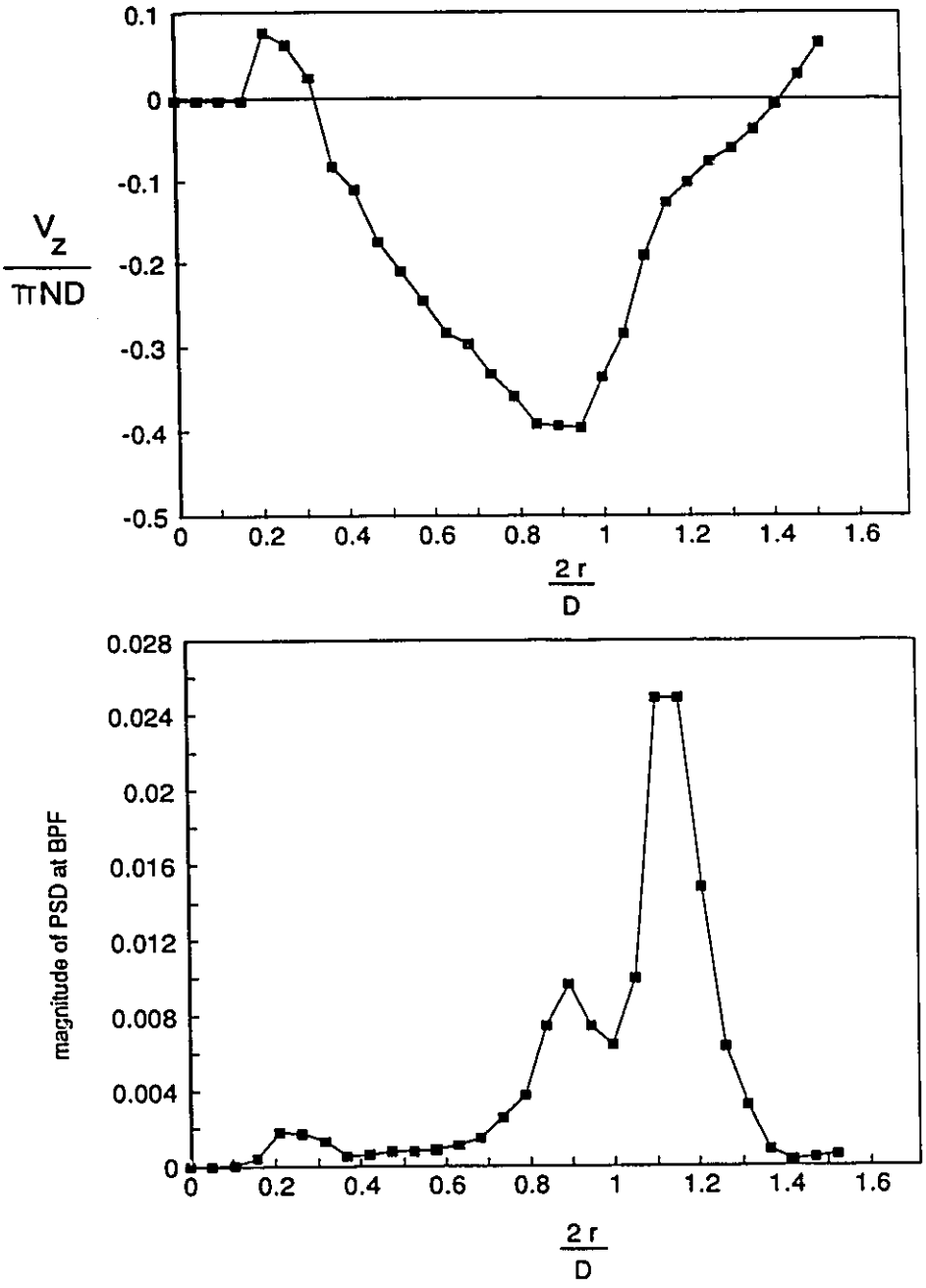

Figure 99. Comparison of the axial velocity profile with the magnitude of the BPF peak in the frequency spectrum. D=T/2, C=T/2, sampling frequency of 0.3kHz, 400rpm.

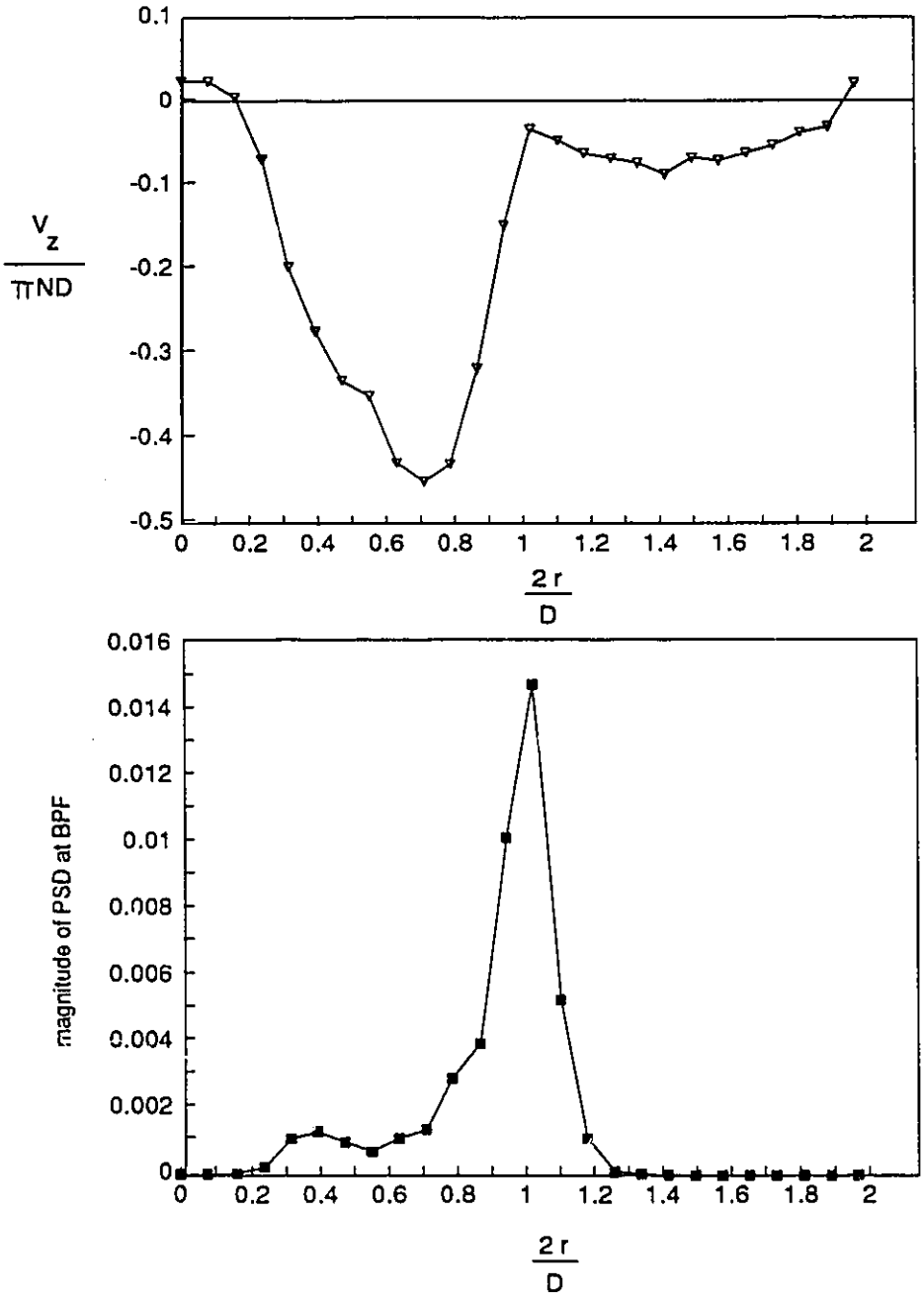

Figure 100. Comparison of the axial velocity profile with the magnitude of the BPF peak in the frequency spectrum. D=T/3, C=T/3, sampling frequency of 0.3kHz, 400rpm.

7.1.3 Autocorrelation coefficient

The autocorrelation coefficient function is a key component in the analysis of ε later in this chapter, so its features are verified in some detail here. Figure 101 shows a typical autocorrelation curve. Note the regular 0.8s period (this is a different data point than that used for the time series). This autocorrelation has been computed for time lags up to 2.5s, or just over three times the longest period in the flow. Previous authors typically compute only to about 0.1s, which is enough time for several blade passages to occur, but not enough to examine the low frequency oscillations which occur in this flow. The repeatability of R_E over three runs is shown in figure 102. It is not exact, but is acceptable to at least a 1.5s lag. The effect of sampling frequency is shown in figure 103. For clarity, the BPF has been removed from these results. It appears that the agreement between runs with differing sampling frequencies is much worse than that between runs where the sampling frequency is held constant. In theory (see appendix 2), the effect of an increased sampling frequency on R_E is only to increase the resolution of the function. If the sf=1kHz, the lag step is 0.001s; if the sf=3kHz, the lag step is 0.00033s. Based on this information, and the earlier effect of the shaft run out on the time series, it is concluded that the variations in this plot are due more to flow instabilities than to inaccurate determinations of R_E.

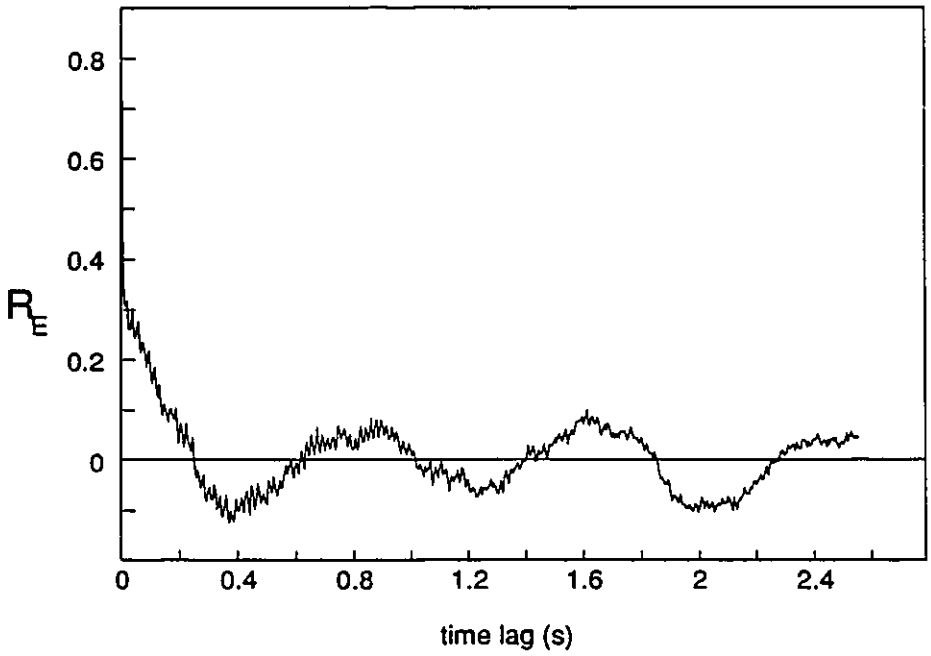

Figure 101. Typical autocorrelation coefficient function at the impeller tip. Sampling frequency 2.5kHz, 400rpm.

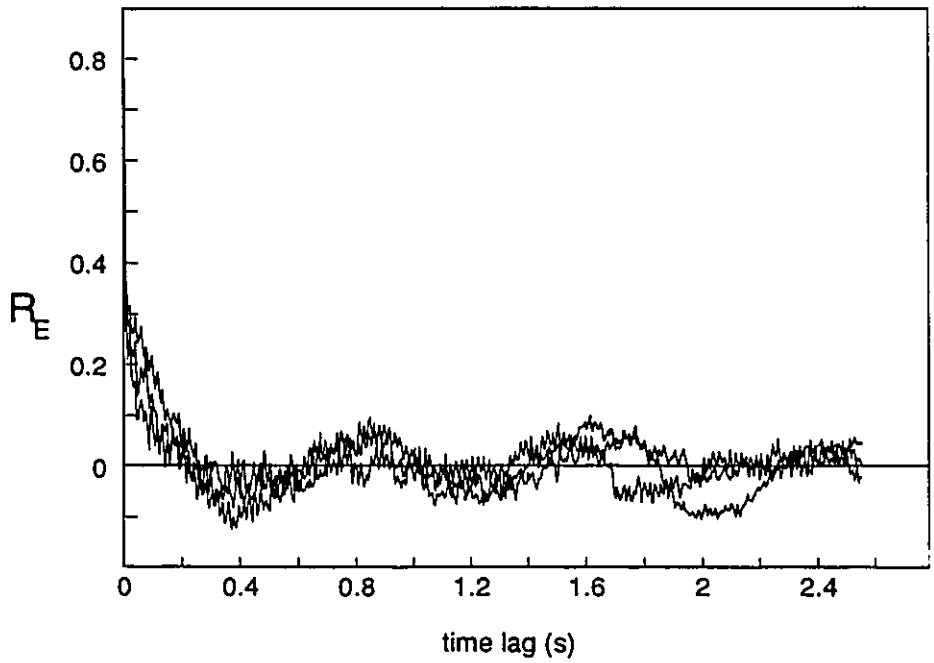

Figure 102. Repeatability of the autocorrelation coefficient function. Sampling frequency 2.5kHz, 400rpm.

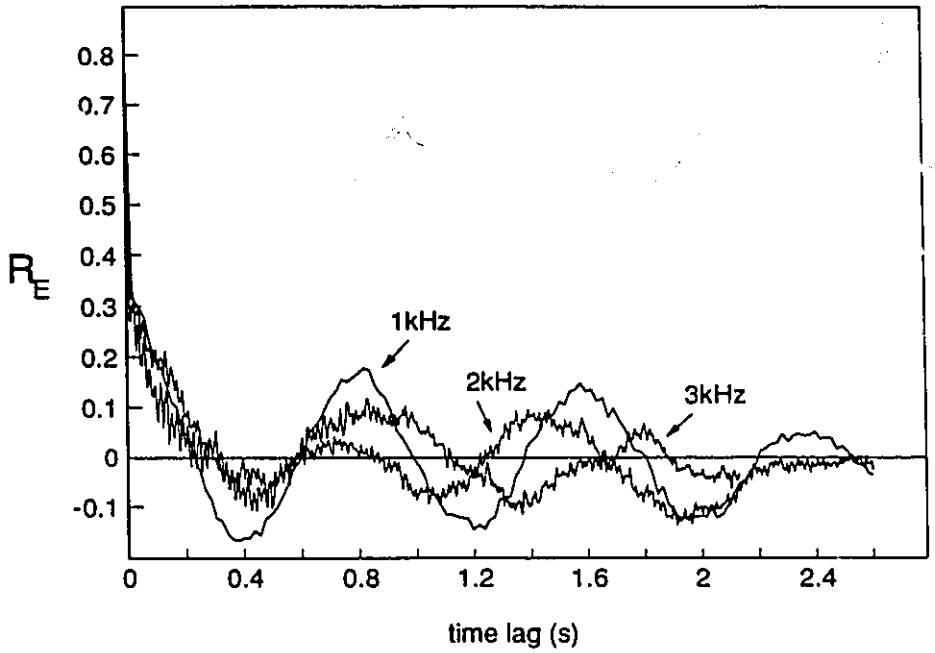

Figure 103. Effect of sampling frequency on the autocorrelation coefficient function at the impeller tip. 400rpm.

Earlier in this section, the 0.8s periodicity was related to the flow number and N. In order to determine whether the low frequency scales correctly with N, R_E is plotted versus the dimensionless time lag (t*N=number of rotations of the impeller) in figure 104. Given the effect of shaft run out, and the limited repeatability discussed above, the agreement between the four rotational speeds tested is very good. The four curves coincide to peak at 16 rotations after 3 cycles, which gives a mean period of oscillation of 5.33 rotations. This agrees well with the initial value of 5 rotations (or 0.8 s for N=400rpm) taken from figure 101.

Examination of the signal characteristics has revealed two dominant frequencies, one at the BPF, and a second low frequency oscillation at a frequency roughly corresponding to 5 rotations of the impeller. The BPF is most evident in

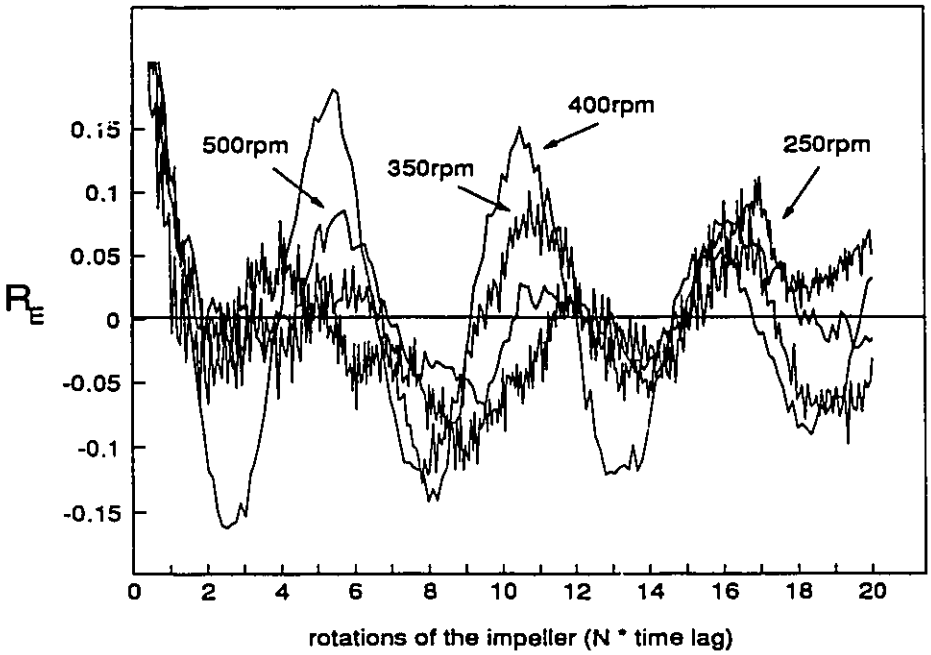

Figure 104. Effect of rotational speed on the period of the low frequency variation at the impeller tip. Sampling frequency 1kHz.

frequency spectra plots, while the low frequency oscillation is easier to observe in plots of R_E, the autocorrelation. The effect of each of these frequencies on the results will be examined wherever possible.

7.2 Measurements of turbulence quantities at the impeller discharge

To estimate ε using the methods outlined in chapter 5, the turbulence quantities k, ν_z, $\overline{\left(\frac{\partial \nu_z}{\partial t}\right)^2}$, $\overline{\nu_r \nu_z}$, $\overline{\nu_\theta \nu_z}$, $\frac{\partial V_r}{\partial z}$, $\frac{\partial V_\theta}{\partial z}$, $\frac{\partial V_z}{\partial r}$, and τ_E are needed. The only turbulence quantity which is measured directly is the instantaneous velocity. From this, the RMS velocity, the mean velocity, and the time derivative are calculated. Using the RMS velocities for the three components of velocity, k is obtained. Using the smoothed mean velocity profiles for two traverses, time averaged spatial derivatives

are obtained. The Reynolds stresses are measured indirectly, using off-axis orientations of the optics to discern the combined effects of two components of velocity (Melling and Whitelaw (1976)) as explained in chapter 3. Before proceeding to the calculation of ε, the results of the intermediate calculations are discussed. All of the results to be used in the ε calculations in section 1.3 are for the case T7 (D=T/2 and C=T/4). This is representative of the low clearance discharge condition for the T/2 impeller, which was shown to coincide with the low clearance discharge condition for the T/3 impeller in chapter 4. It also covers the range of the most common industrial configurations. Since only one traverse was examined, the results are presented in dimensional form wherever possible. As in chapter 6, ε should be made dimensionless with $(\pi ND)^3/D$ if it is to be applied in other configurations.

7.2.1 Turbulence kinetic energy and turbulence intensity

Of all the turbulence results, the turbulence kinetic energy is the least susceptible to experimental error. RMS velocities are stable in time, and unaffected by the presence (or absence) of periodic components. The three components of RMS velocity (shown in figure 105 for case 4, and figure 106 for case T7) differ by only 25-50% (components in highly anisotropic flows are expected to vary by up to 200%). The trends followed by each of the three components are exactly the same, peaking at the impeller tip.

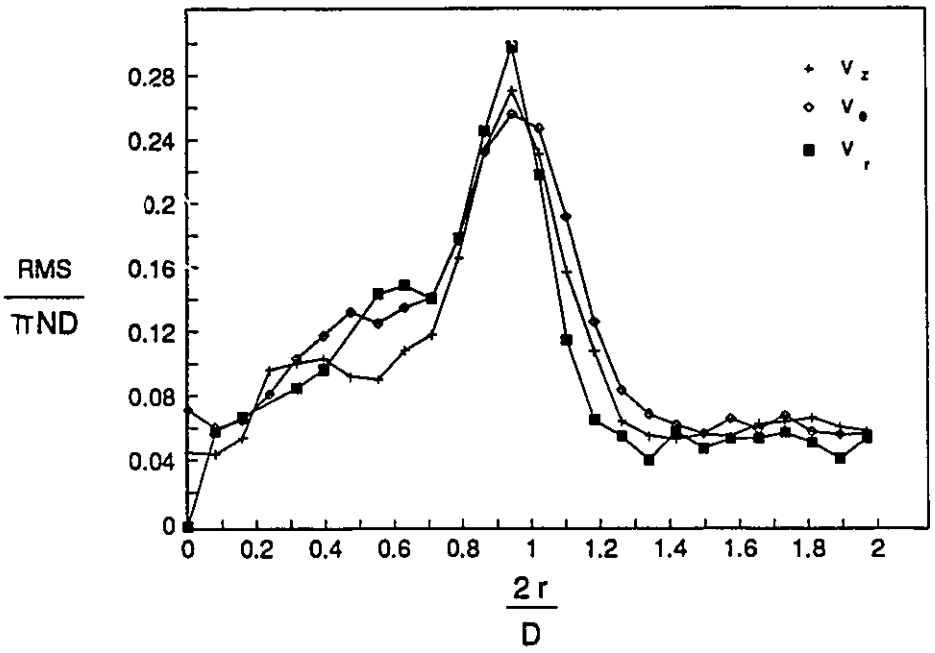

Figure 105. Comparison of the magnitude of the three RMS components of velocity. D=T/3, C=T/3, 400rpm.

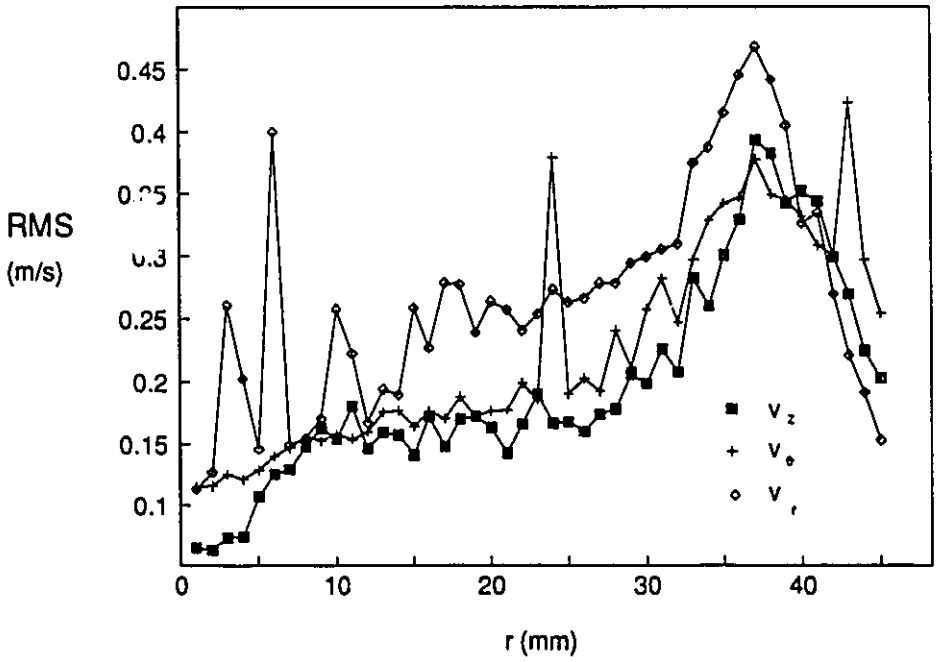

Figure 106. Comparison of the magnitude of the three RMS components of velocity. D=T/2, C=T/4, 400rpm.

The resulting profiles of k in figures 107 and 108 cover all five of the major cases studied. Once again, case 1 is a significant outlier, due to the dominance of the secondary circulation loop discussed in chapters 2 and 4. The results for case T7 are smoothed to reduce the error introduced in the later ε calculations.

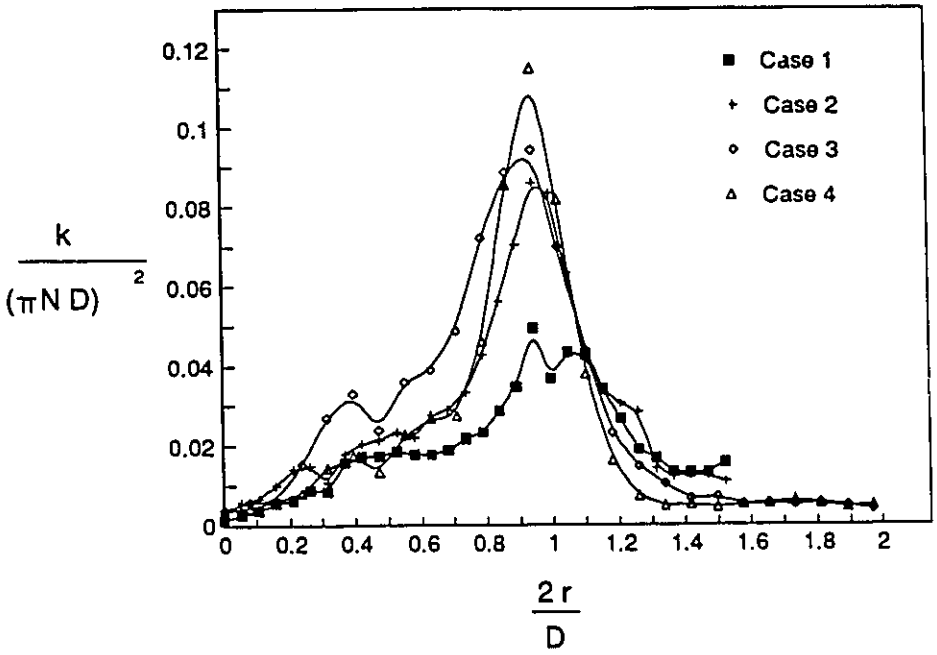

Figure 107. Profile of k at the impeller discharge for the cases 1 to 4 defined in chapter 4.

Another turbulence quantity of interest is the turbulence intensity. This is shown for case T7 in figure 109. Note that it is virtually constant, at 25%, over the extent of the impeller where the flow is not dominated by trailing vortices. The intensity is very sensitive to the value of the mean velocity, and so is not reported for the r component where the mean velocity is small and difficult to measure.

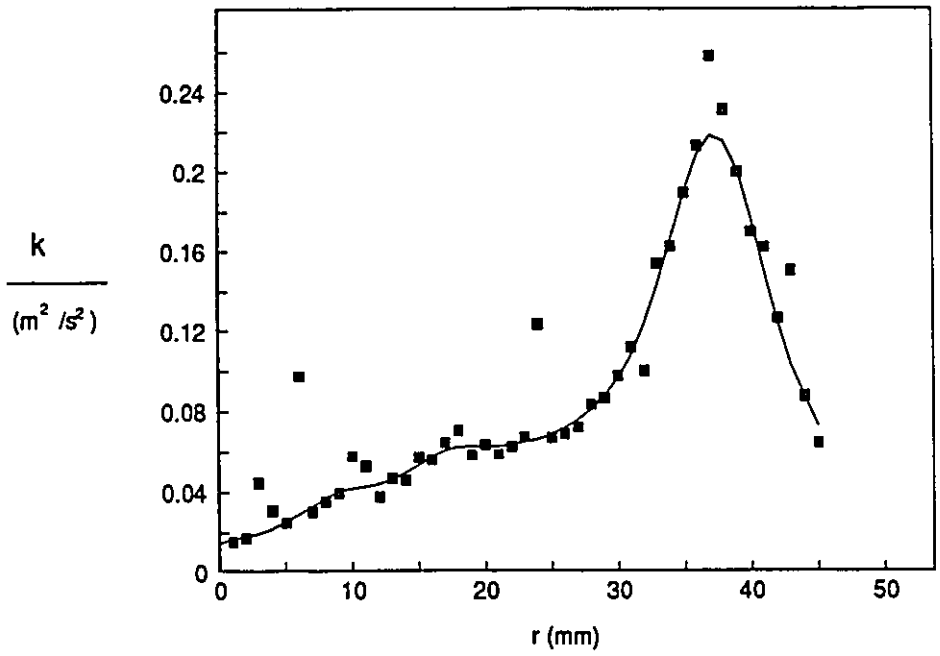

Figure 108. Profile of k at the impeller discharge for case T7. D=T/2, C=T/4, N=400rpm.

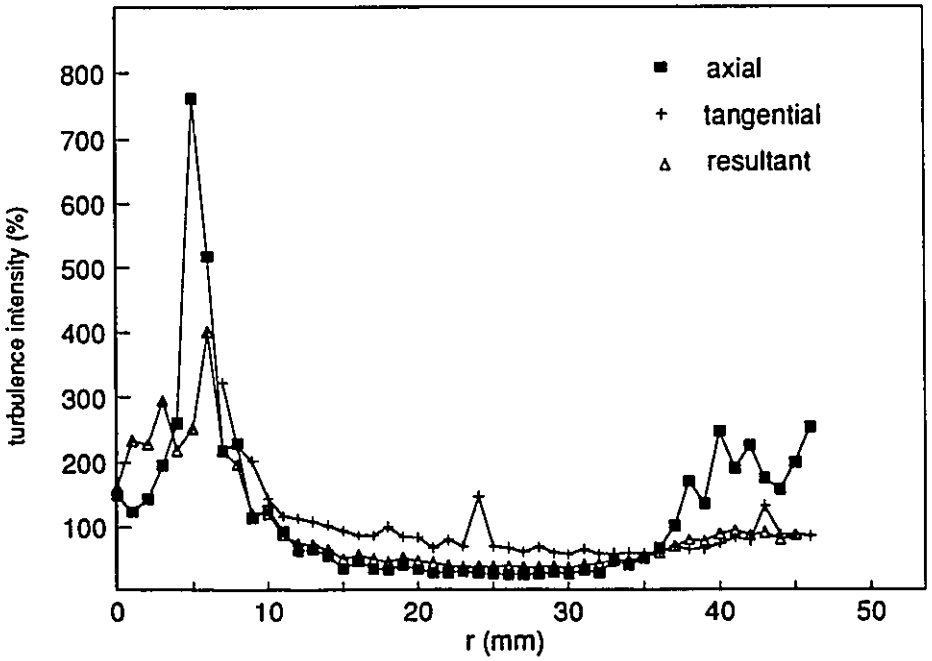

Figure 109. Turbulence intensities at the impeller discharge for case T7.

7.2.2 Mean velocity gradients

From smoothed profiles of the axial, radial, and tangential mean velocity profiles, the spatial gradients as reported in figure 110 are calculated. Note that small variations in the slope, which are probably not repeatable, have a profound influence on the values obtained for the derivatives. It is unlikely that the oscillations which appear in this figure have any physical significance. The mean velocity and its gradients are unaffected by removal of the periodic components.

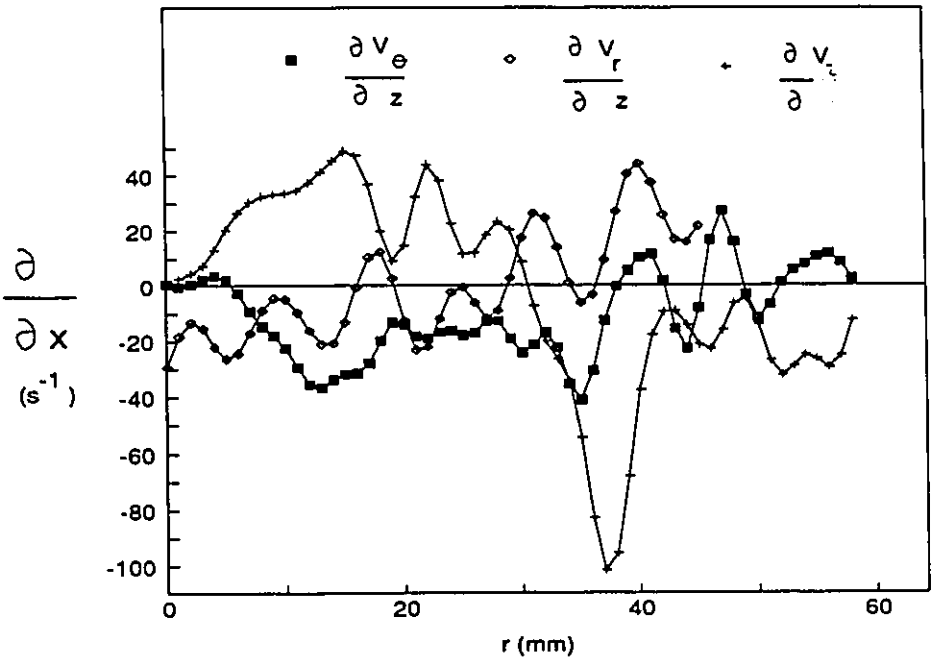

Figure 110. Spatial derivatives of the mean velocity at the impeller discharge for case T7.

7.2.3 Reynolds stresses

The rotational method for obtaining Reynolds stresses descirbed in chapter 3 has been criticized for using the difference between two large numbers. For this flow field, that was not the case. The difference between the two RMS velocities

(see eq'n 9) was always at least 12% of the largest velocity, and often 25%. The RMS velocities used to calculate the Reynolds stresses are stable, and unaffected by the removal of the periodic components. The relationship between the Reynolds stresses and the mean velocity gradients is, however, complicated by the complexity of the flow field. This will be discussed further when the two quantities are used to calculate ε. The two measured Reynolds stresses, $\overline{v_r v_z}$ and $\overline{v_\theta v_z}$, are shown in figure 111. The solid lines represent the smoothed profiles, which are used in the calculation of ε.

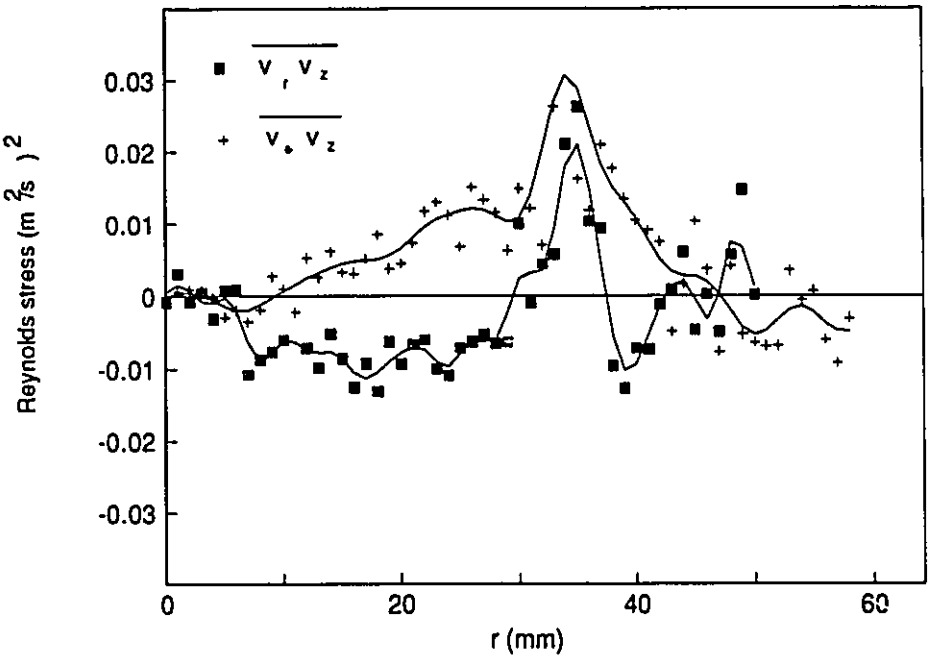

Figure 111. The Reynolds stresses, $\overline{v_r v_z}$ and $\overline{v_\theta v_z}$ at the impeller discharge for case T7.

7.2.4 Time derivatives

The instantaneous time derivative is the least reliable of all of the measured turbulence quantities. It is highly dependent on the sampling frequency (see figure 112), and shows poor repeatability in the tip region (figure 113). The effects of these inaccuracies will be seen later, when the time derivative is used to calculate ε.

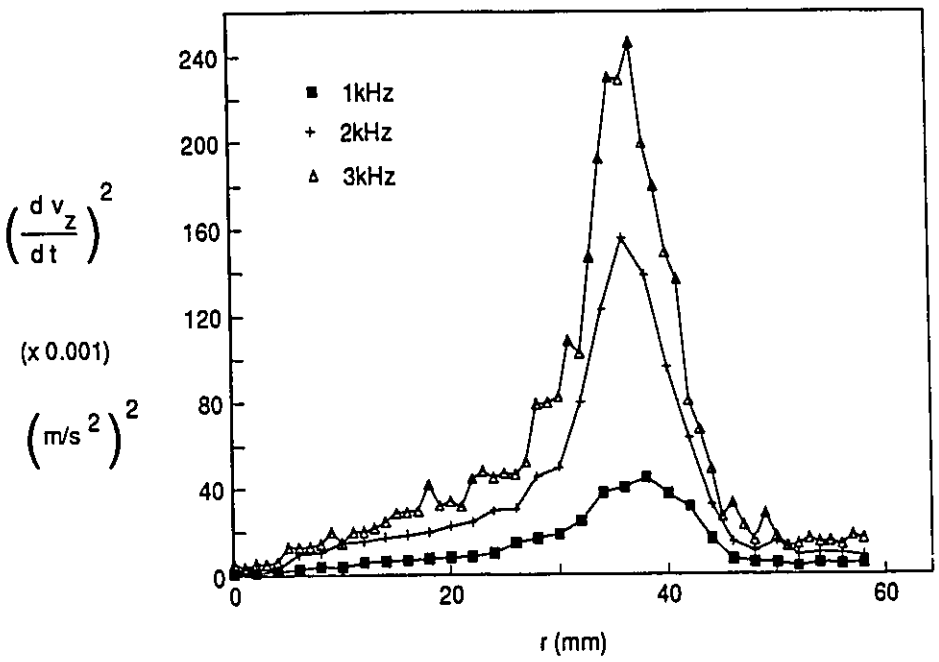

Figure 112. Effect of sampling frequency on the time derivative of the instantaneous velocity. Three traverses at 400rpm, case T7.

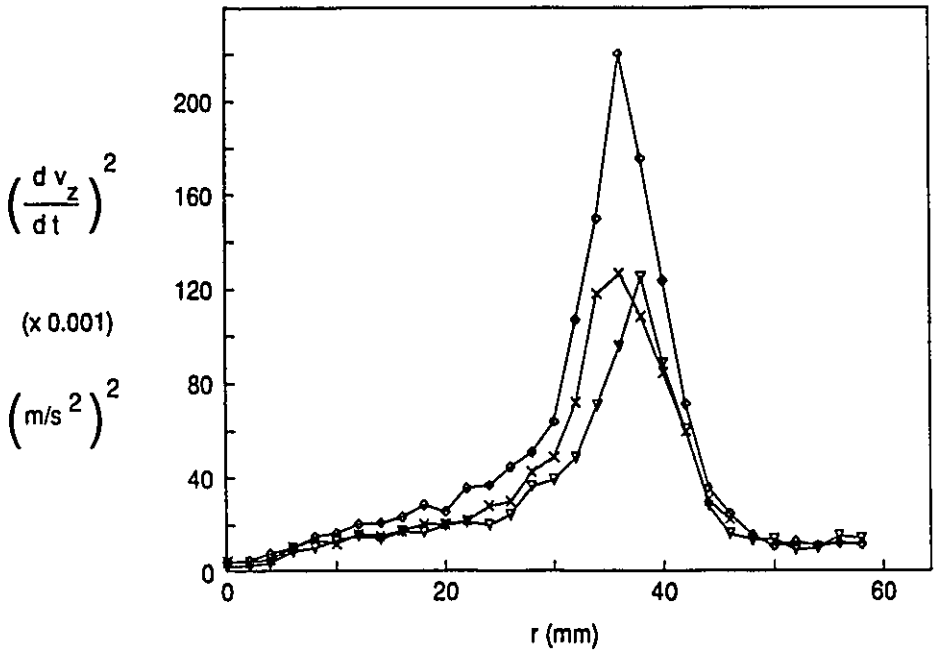

Figure 113. Repeatability of the time derivative of the instantaneous velocity. Three traverses at 2.5kHz, 400rpm, case T7.

7.2.5 Eulerian integral time scale

The Eulerian integral time scale

$$\tau_E = \int_{t=0}^{t=\infty} R_E(t)dt$$

is calculated from numerical integration of the autocorrelation coefficient function. For ideal turbulence, this function decays away quickly to zero, so that the integral can easily be evaluated. The presence of periodic components in this complex flow makes the evaluation more difficult, since the function oscillates about zero in an irregular manner. Several methods of analysing the data were considered, with particular attention to the influence of the chosen limits of integration and of the periodic components on the calculated time scale.

When the integral of the raw data out to the maximum time lag (5 seconds) is considered (figure 114), the results show large fluctuations, and can not be considered repeatable. The interval up to the first zero crossing is the first interval over which the flow is related to itself, and thus is more likely to be characteristic of the underlying turbulence. If the integral is evaluated only up to the first zero crossing (around 0.2 seconds), the results are more repeatable (figure 115), but still unacceptable for detailed analysis.

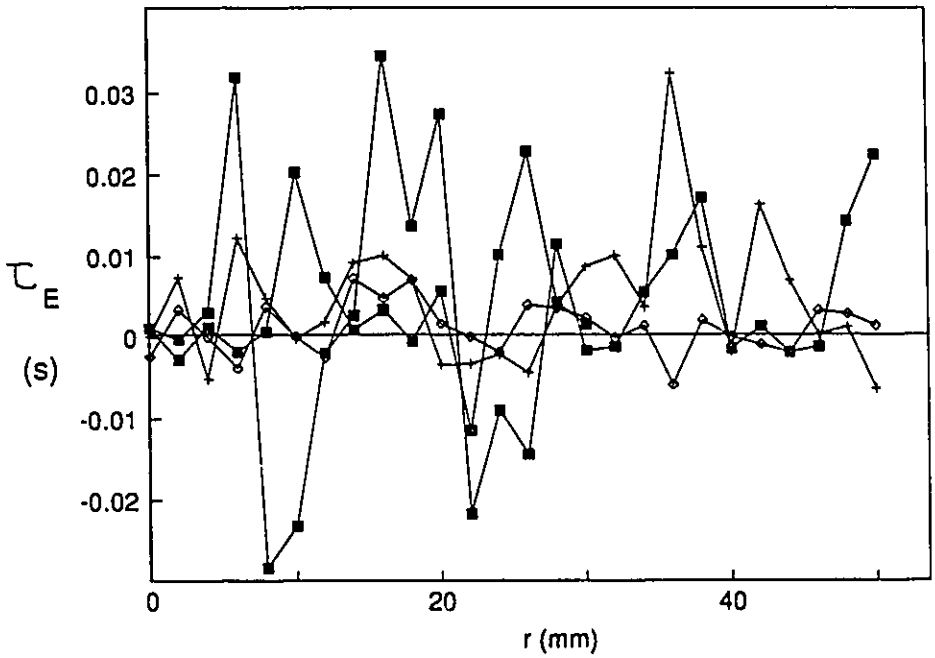

Figure 114. Repeatability of the integral time scale resulting from the maximum integration limits on raw data. The results shown are for three identical runs, where the squares represent a traverse covering both sides of the tank.

Since the time scale of interest is that which represents the turbulent fluctuations, and the presence of other fluctuations may introduce an undesirable distortion in the time scale, notch filters are applied to remove the regular frequencies. The effect of these filters on the calculated time scale is shown in figure 116. Removal

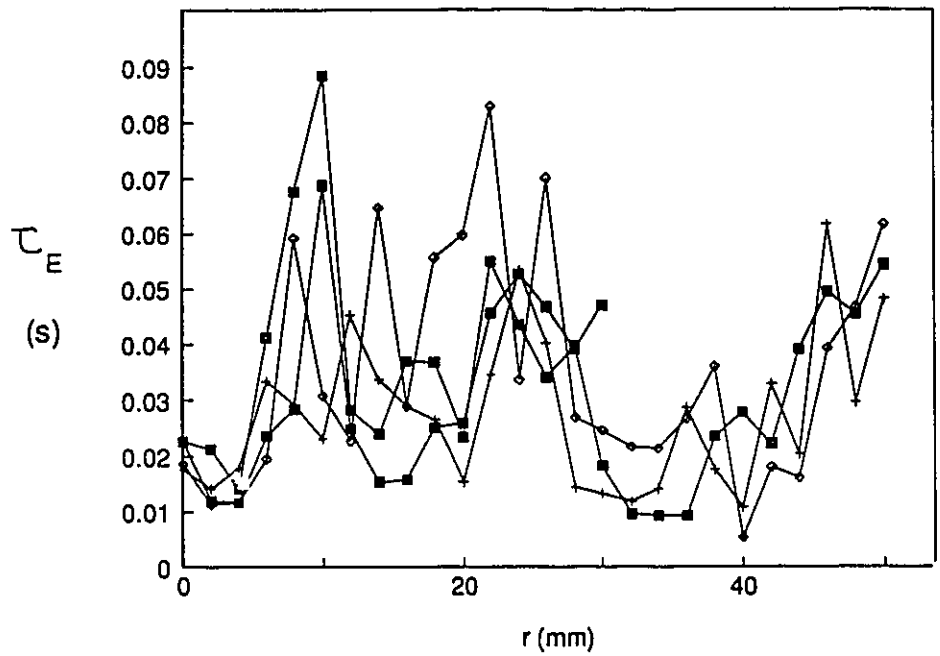

Figure 115. Repeatability of the integral time scale resulting from integrating raw data to the first zero crossing. The results shown are for three identical runs, where the squares represent a traverse covering both sides of the tank.

of the BPF has *no effect* on the value of the integral; this runs contrary to results reported by Wu and Patterson (1989), which are discussed later in this section. The fact that removal of the BPF has no effect on the result supports the hypothesis that it is valid to include all of the fluctuations with the turbulence; ie. that the pseudo-turbulence induced by blade passages is not fundamentally different from the random fluctuations found in other turbulent flows. Removal of the low frequency oscillation, however, does affect the calculated time scale. The result is reduced; however, the general trends are maintained. Filtering of the low frequency component, combined with integration only to the first zero crossing, drastically improves the repeatability of the integral time scale measurement, as shown in figure 117. This indicates that the low frequency variation is not stationary, according to the

definition given in chapter 5.

In all of the above graphs, the squares represent a traverse used to check the axisymmetry of the results. For the first two methods of analysis, where no filters are applied, the two halves of the traverse do not coincide; for the last, where the low frequency oscillation has been removed, agreement is very good. By removing the low frequency oscillation, the characteristic time scale of the turbulence has been measured, rather than the effect of the varying flowfield. The underlying turbulence is repeatable, and axisymmetric, lending support to the ideas which led to the assumption of local isotropy.

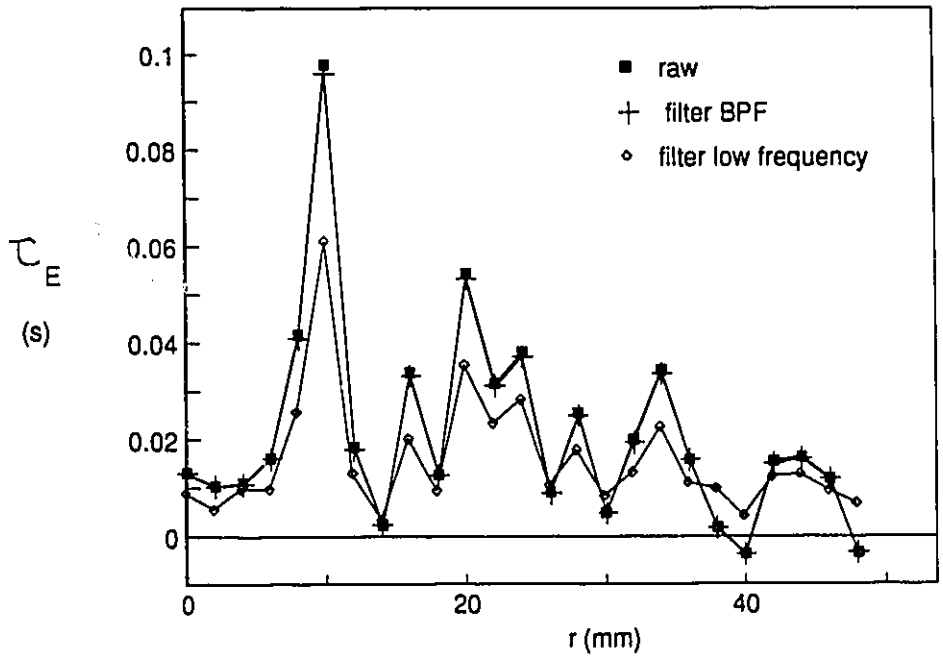

Figure 116. Effect of removing the dominant frequencies; BPF (26.67Hz) and the low frequency (1.28Hz) on the integral time scale as calculated to the first zero crossing.

Closer examination of figure 117 reveals several points which differ substantially from their neighbors, and from other determinations at the same point.

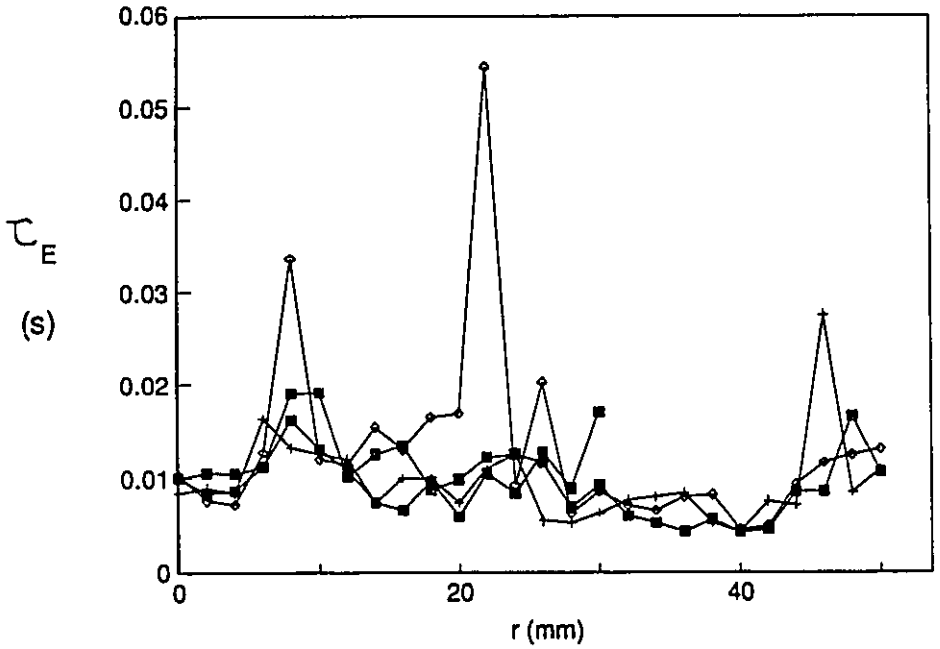

Figure 117. Repeatability of the integral time scale as calculated from the filtered signal, up to the first zero crossing. The results shown are for three identical runs, where the squares represent a traverse covering both sides of the tank.

When the raw autocorrelation functions for these points are compared with their neighbors, the source of the difficulty becomes clear. The notch filter used to remove the low frequency fluctuations is set to 1.28Hz (0.8s period) with a bandwidth of 50%. This frequency would lead to a first zero crossing around 0.2s, as is the case for the points which neighbor the outliers. As shown in figures 118 and 119, however, the outliers cross zero for the first time at 1s and 0.4s respectively. Neither of these would be included in the filtered bandwidth, even at a 50% width. This result was verified for many other outlying points not reported here. Since the deviation is clearly caused by inadequate analysis and has no useful physical interpretation for the turbulence time scale, the points will not be considered further. Where the outlying points fall on the figure, however, they will be reported as they can give

some indication of the degree of instability of the flow.

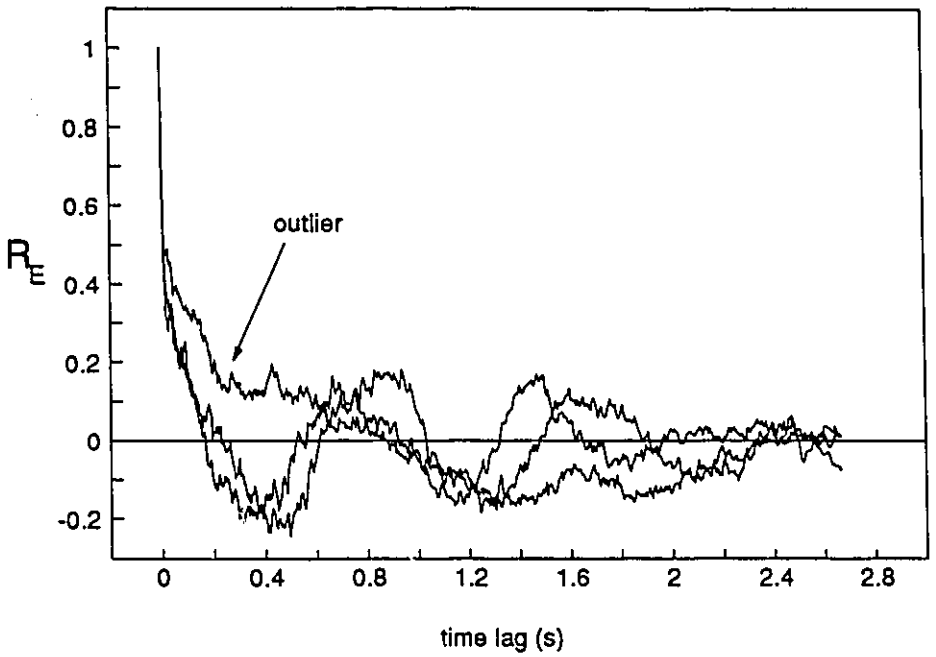

Figure 118. Outlying point caused by a zero crossing which occurs at a time lag significantly greater than 0.2s in the raw data; first example.

The measures required for the evaluation of the integral time scale, and the marked effect of removing the low period fluctuations, indicate that the assumption of stationarity can only be considered as an approximation for some aspects of the flow analysis. Henceforth, the autocorrelation function will only be integrated to the first zero crossing, and the low frequency oscillation will be removed from the signal before analysis. Integrating to the first zero crossing improves the repeatability of the results, and limits the evaluation to the initial interval over which the flow is related to itself. Removal of the low frequency oscillation elimates the effect of the relatively unstable slow variations in the flow field on the characteristic time scale.

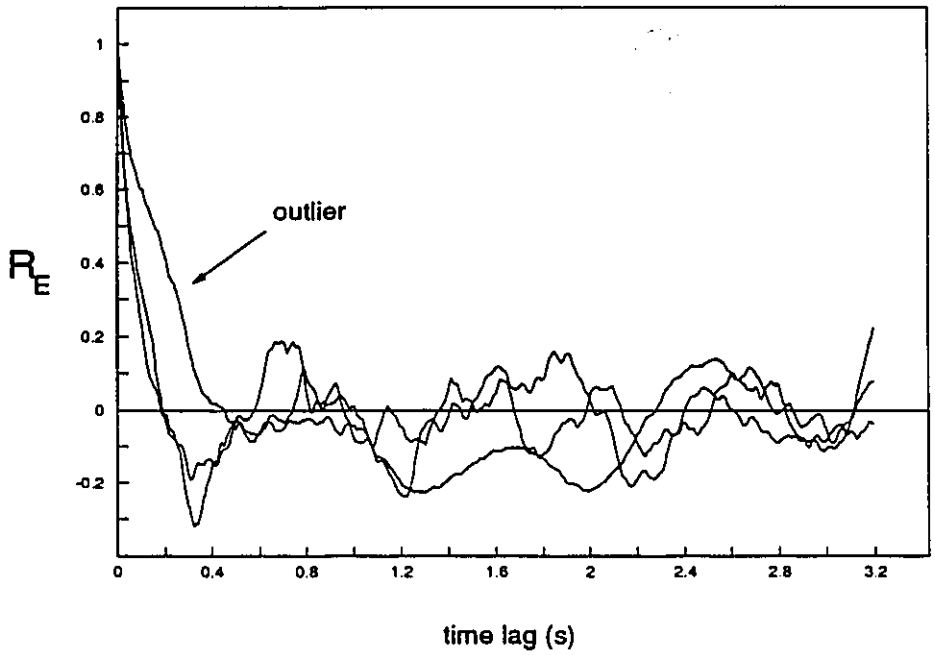

Figure 119. Outlying point caused by a zero crossing which occurs at a time lag significantly greater than 0.2s in the raw data; second example.

As a precaution, the BPF is also removed; this allows examination of the results with no influence from regular oscillations. Whether the BPF is removed or not is immaterial, however, as was shown in figure 116.

As explained in the examination of the autocorrelation, the sampling frequency affects only the resolution of the curve, not its shape. The effect of improved resolution on τ_E is negligible over the range of sampling frequencies shown in figure 120. If the sampling frequency is increased to the point that the RMS profile is affected by the presence of excessive noise (see chapter 3), then τ_E is also affected. This occurs at 5kHz. If the sampling frequency is reduced to very low values, however, agreement is still extremely good (see figure 121). Figure 122 shows τ_E as calculated from the raw data for the same runs as shown in figure 120. Although quantitative repeatability is poor, the trend which emerges is interesting. Moving

radially outward, the time scale first increases, then decreases to a minimum close to the tip of the impeller, then increases rapidly again outward into the bulk of the tank.

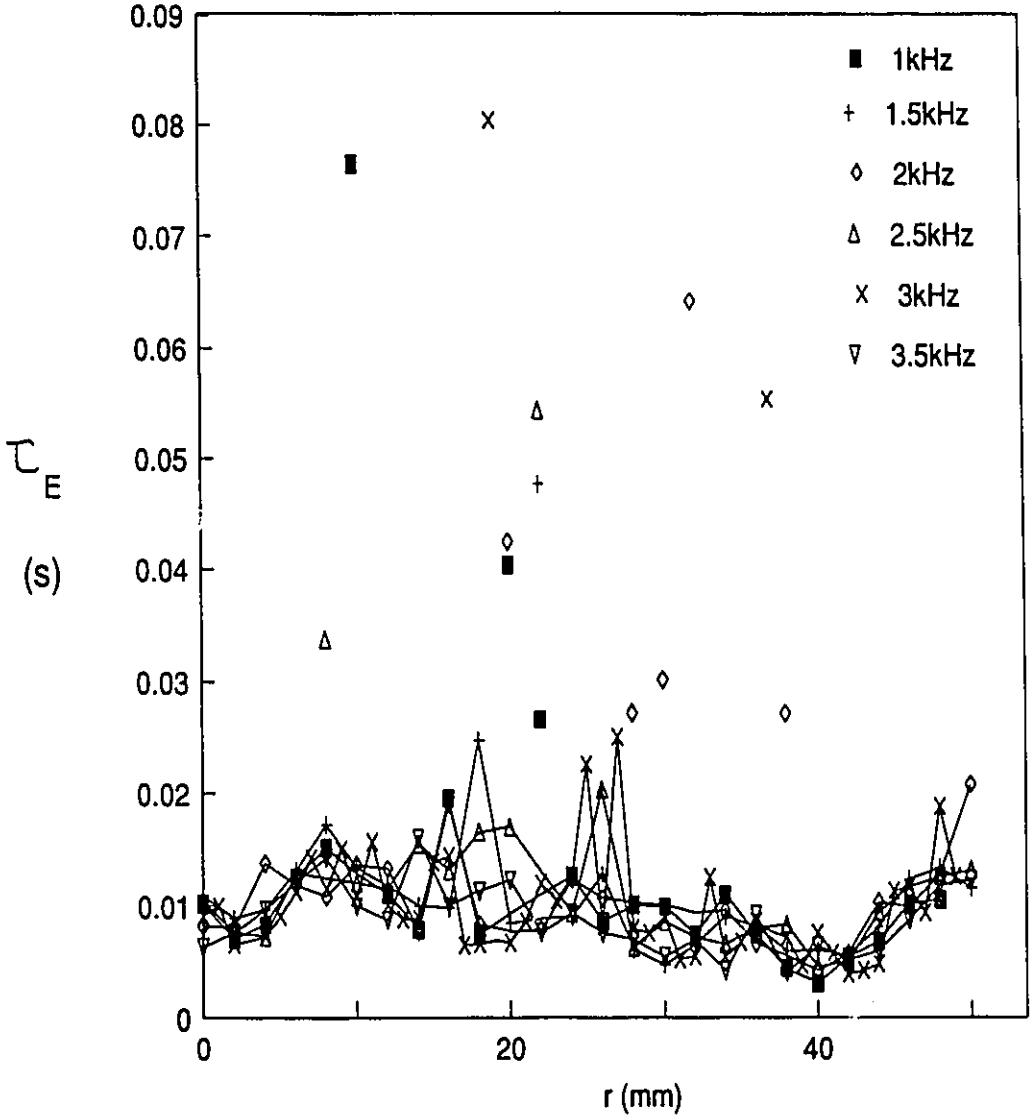

Figure 120. Effect of the sampling frequency on the integral time scale for the filtered data. Outlying points are not included on the line.

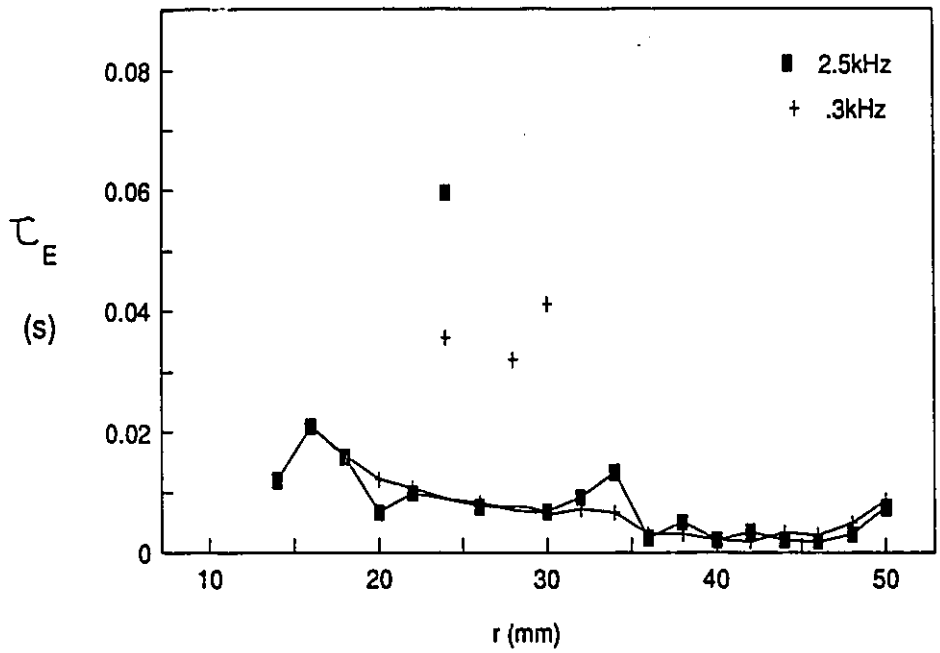

Figure 121. Validity of the calculation method, even for extremely low sampling frequencies.

It is now appropriate to address the concerns raised earlier concerning the validity of results reported by Wu and Patterson (1989) which show a large change in the turbulence characteristics due to the removal of the BPF. This runs contrary to the results reported here, which show no effect of the BPF on the final results, whereas removal of the low frequency oscillation is important. While it should be remembered that they studied the Rushton turbine, which shows no evidence of the low frequency fluctuations observed here for the PBT, the concerns raised in chapter 5 concerning the experimental method used can now be addressed. While even very low sampling frequencies give accurate results, an excessively high sampling frequency (5 times the frequency limit of the LDA measuring volume) gives results due more to the measurement of white noise than to the measurement of random turbulence (see chapter 3). Wu and Patterson (1989) performed their experiments

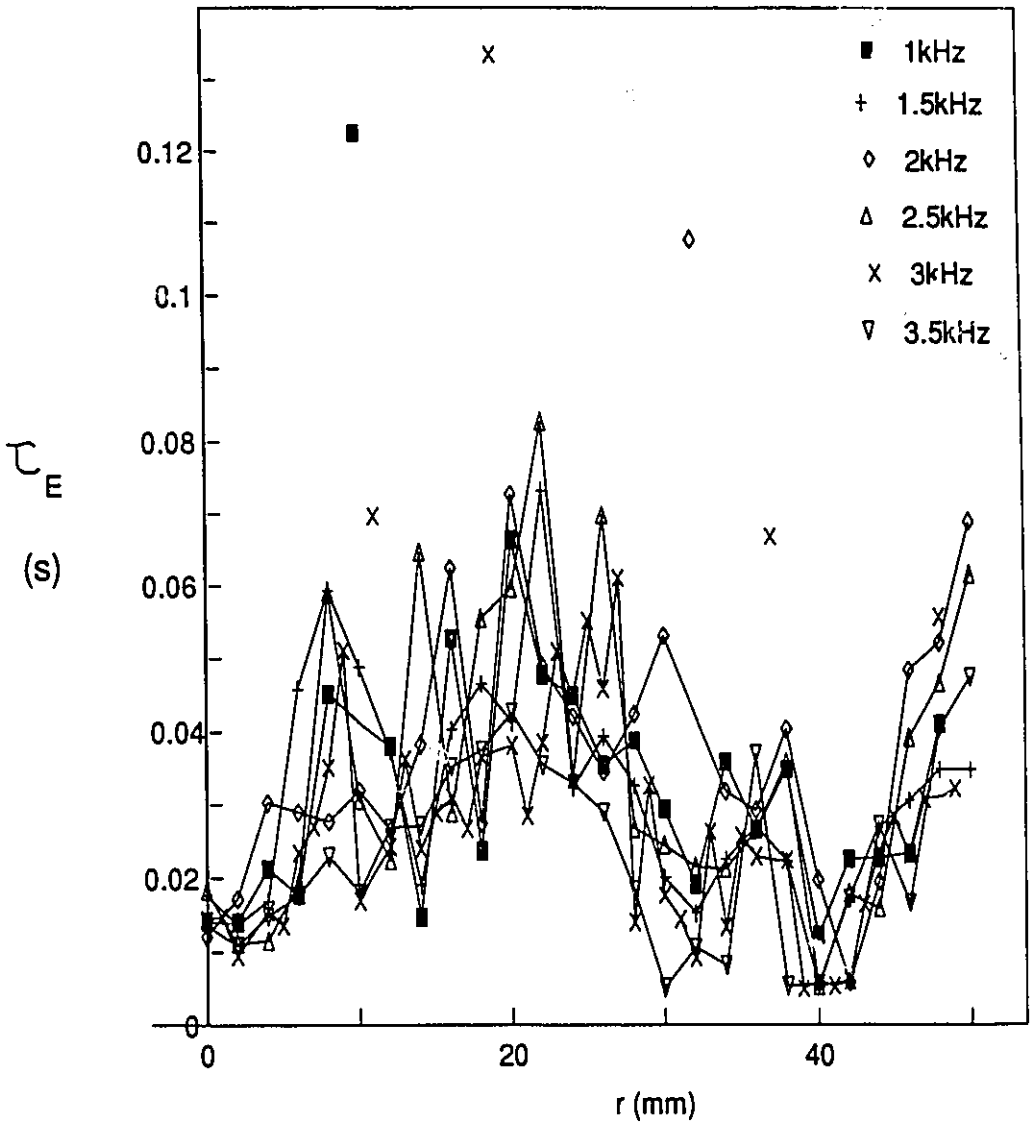

Figure 122. Integral time scale calculated from the raw data, integrated to the first zero crossing. Shows the effect of sampling frequency, and reduced repeatability due to the lack of filtering.

in data arrival mode (all valid data received is recorded), which means that given an average signal (3kHz), their sampling rate was of the order of fifteen times the frequency limit of their measuring volume (217Hz). When Wu and Patterson removed the BPF, it appears that any remaining measured turbulence was swamped

out by the Doppler ambiguity noise, over which they repeatedly express concern. As they move out of the region where the BPF dominates, subtraction of the BPF no longer removes all of the true measurement, and the "corrected" and "uncorrected" sets of results come back into agreement. For this method of turbulence characterization, it is much better to use a low sampling frequency (as shown in figure 121), than an excessively high one. We now return to further consideration of the effect of basic experimental variables on τ_E.

As shown in figure 123, τ_E scales correctly with the rotational speed (ie. the dimensionless τ_E is independent of N). To confirm that this agreement is not due to an insensitive method of analysis, the same profiles are shown in figure 124 with a dimensional time scale, and no filtering.

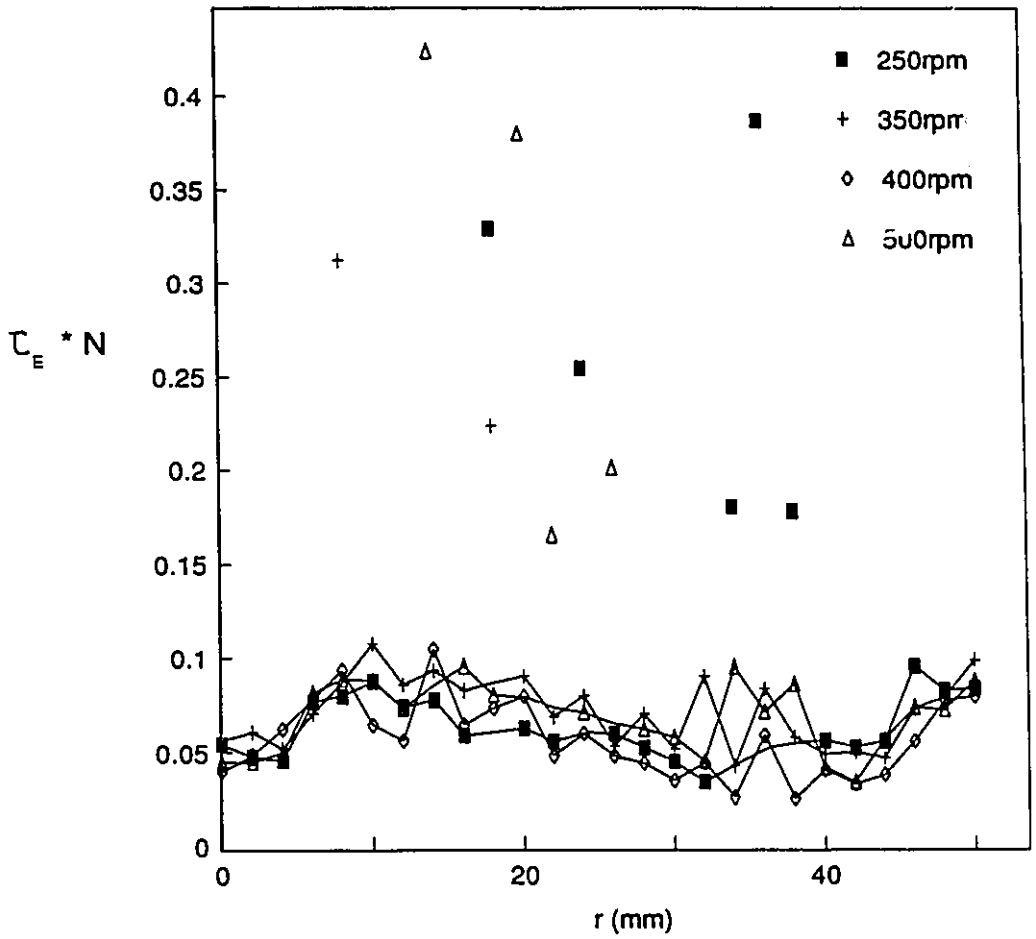

Figure 123. Effect of rotational speed on the dimensionless integral time scale.

The τ_ε's calculated at one point from three different components of velocity agree very well, as shown in figure 125. Once again, no directional preference is shown in the time averaged turbulence characteristics, which supports the ideas leading to the assumption of local isotropy.

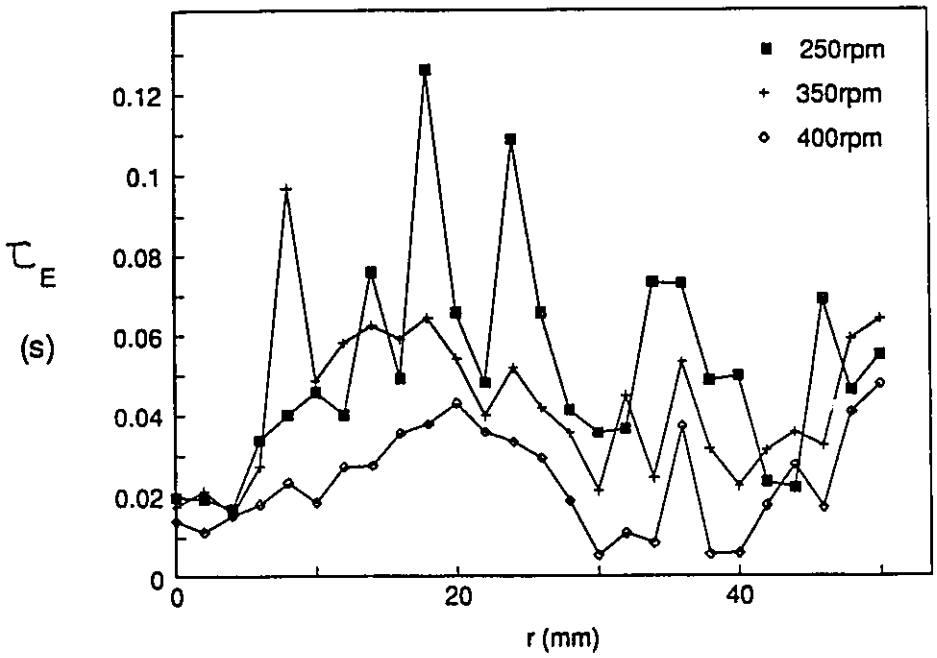

Figure 124. Effect of N on the dimensional time scale as calculated from the raw data.

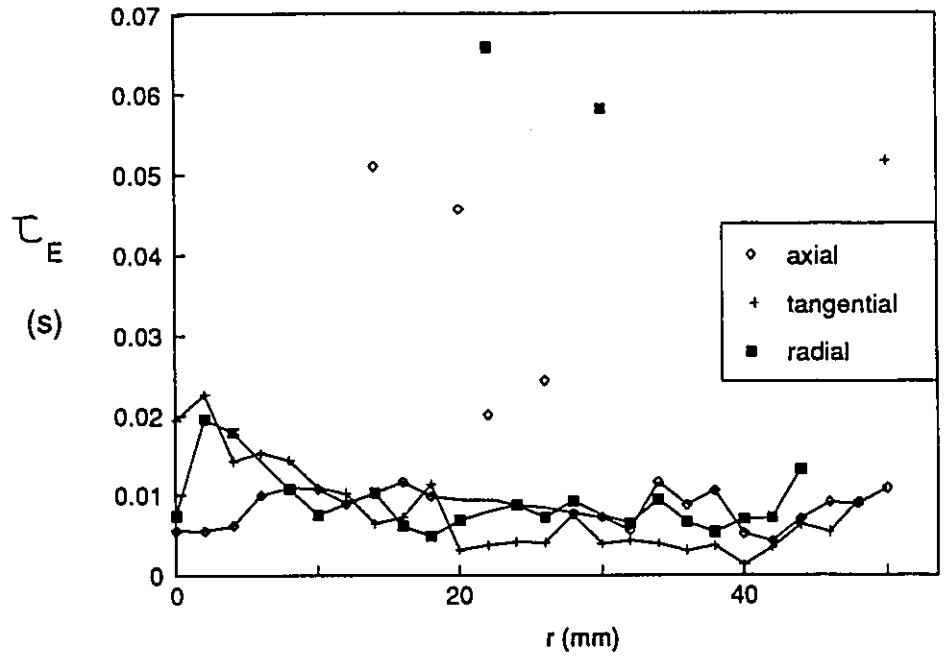

Figure 125. Comparison of time scales calculated from the three measured components of velocity.

The mean profiles of τ_E used in the ε calculations, and the data from which they were determined, are shown in figures 126 and 127.

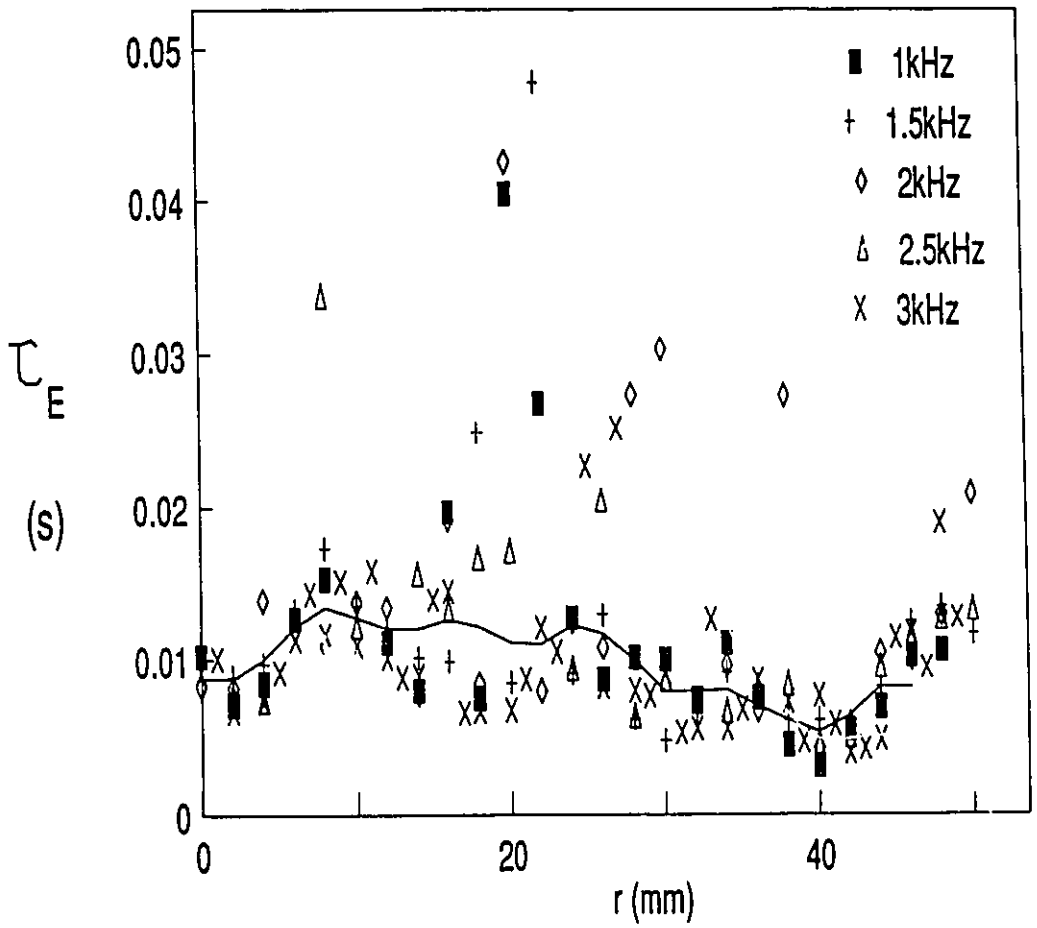

Figure 126. Mean profile of the filtered time scale at the lower edge of the impeller, shown with the data used to obtain it. Case T7; D=T/2, C=T/4, N=400rpm.

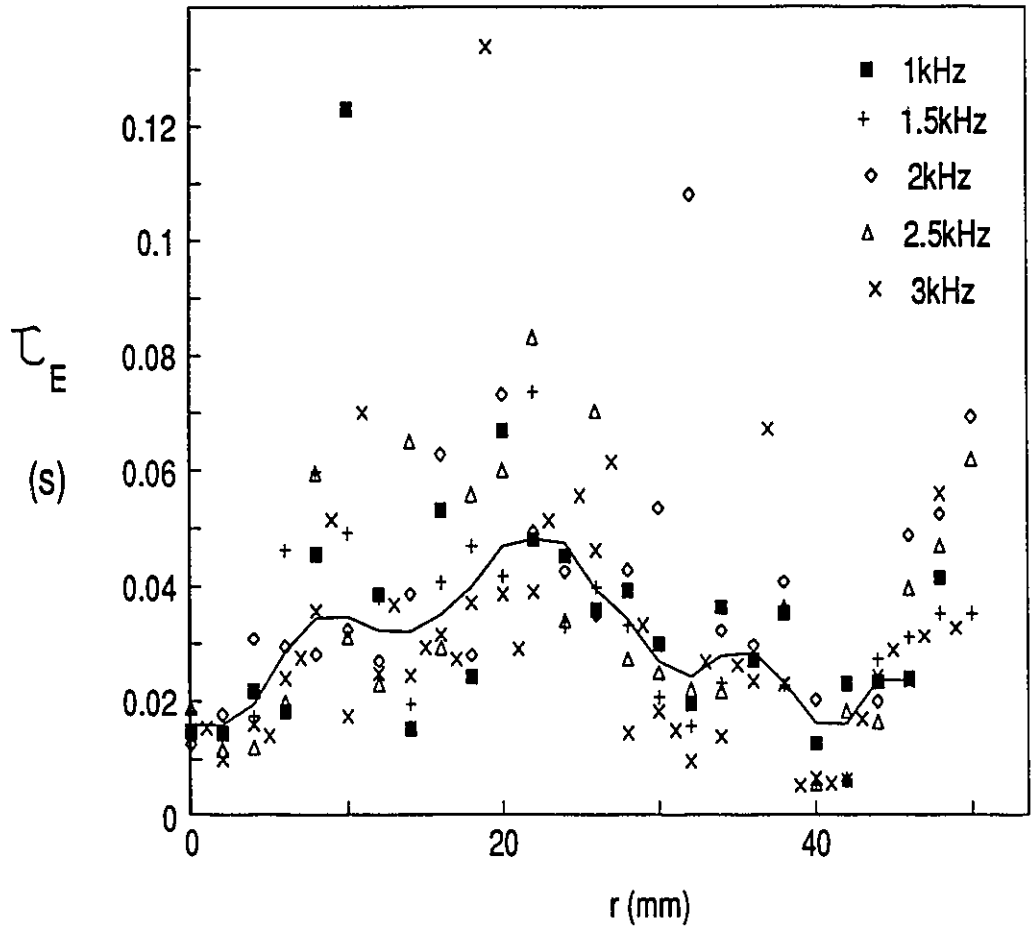

Figure 127. Mean profile of the raw time scale at the lower edge of the impeller, shown with the data used to obtain it. Case T7; D=T/2, C=T/4, N=400rpm.

7.3 Calculation of the dissipation rate at the impeller discharge

In chapter 5, four experimental methods for the determination of ε were presented. The dimensional argument and the autocorrelation method use characteristic time and velocity scales to estimate the dissipation rate. The gradient hypothesis assumes an analogy between the mean and turbulent flow fields, based

on a constitutive equation. Taylor's hypothesis relies on an assumed relation between the space and time derivatives. The four general equations are restated below, for convenience.

Dimensional argument:

$$\varepsilon = A\frac{u'^3}{L}$$

Autocorrelation coefficient:

$$\varepsilon = A\frac{u'^3}{\tau_E U_c}$$

Taylor's hypothesis:

$$\varepsilon = 30\nu\frac{u'^2}{2u_1'^2 U_c^2}\overline{\left(\frac{\partial u_1'}{\partial t}\right)^2}$$

Gradient hypothesis:

$$\varepsilon = -\frac{0.09k^2}{\overline{u_i'u_j'}}\frac{\partial \overline{U_i}}{\partial x_j}$$

In this section, only one traverse is considered; that at the lower edge of the impeller blades for the case T7 (D=T/2, C=T/4). All of the corrections previously proposed for the above equations are examined. Since this traverse encompasses both the simple discharge at the interior of the impeller, and the difficult trailing vortex at the impeller tip, it provides a good test of the robustness and applicability of the various methods and corrections. Each of the methods is examined in turn, and then aggregate comparisons of all of the methods conclude the section.

7.3.1 Gradient hypothesis

The gradient hypothesis is written

$$\varepsilon = -\frac{0.09k^2}{\overline{u_i'u_j'}}\frac{\partial \overline{U_i}}{\partial x_j}$$

This method requires measurement of the Reynolds stress and the mean velocity gradient, plus k: 4 high resolution traverses of one line for one ε traverse. The values obtained are then extremely sensitive to experimental error. No corrections are necessary.

For the apparatus used in this experiment, three seperate determinations of ε are possible. The first sets i=r and j=z (rz); the second sets i=z and j=r (zr), allowing a check on the validity of the isotropy assumption; the third sets i=θ and j=z (tz). Figure 128 shows the three results. It is clear from this figure that the rz results are highly susceptible to experimental error which originates in the spatial gradient term. Note the significant region around r=40mm where the estimate gives a negative result for both the rz and zr traverses. This occurs where the Reynolds stress and the spatial velocity gradient have the same sign; apparently transport of momentum occurs *up* the velocity gradient. Calabrese (1991) has asserted that this occurs due to the complexity of the flow field, and specifically due to the presence of the trailing vortex. While the mean velocity gradient (zr) is negative beyond the peak, the trailing vortex rotates in the counter clockwise direction (as observed from a position facing the blade). While the mean velocity gradient is negative, and momentum diffuses outward; the dominant convection mechanism is *inward* with the rotation of the trailing vortex. This produces the negative Reynolds stress term. Note that the "negative ε's" occur beyond the tip of the impeller, where the vortex has been convected down in the tank, so that the radial velocity is *inward.* The most dramatic evidence for the sharp flow reversal in V_r for case 1 in chapter 4, figure 47. Note that the real difficulty lies, not with an actual production of energy at the smallest scales, but with the difficulty of defining the streamwise direction in a complex flow

field. From another perspective, if the TKE equation is considered, the negative gradient and Reynolds stress will combine to give negative production. This unusual circumstance does not necessarily imply that the dissipation is negative. As has been noted before, it is expected that the pressure velocity correlations will be significant in this region as pressure differences are converted to velocity increases, and the flow field re-equilibrates with each successive blade passage.

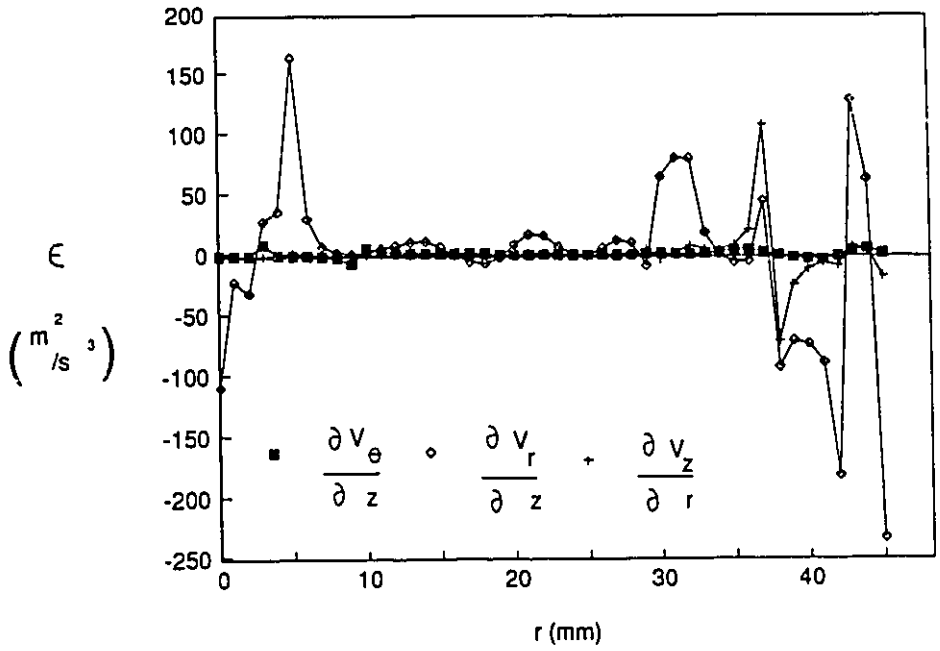

Figure 128. Dissipation rate results from three determinations of the gradient hypothesis method.

Figure 129 shows the two more reliable methods, tz and zr, on an expanded scale. With the exception of a few points, agreement is almost exact out to 30mm (where the trailing vortex is thought to begin). Beyond this point, similar trends are observed, but the magnitude of the zr result is much greater. Only the tz result will

be used for comparison with other methods, since both of the other determinations give values far greater than any other method. This is due more to the inherent instability of the experimental method than anything else.

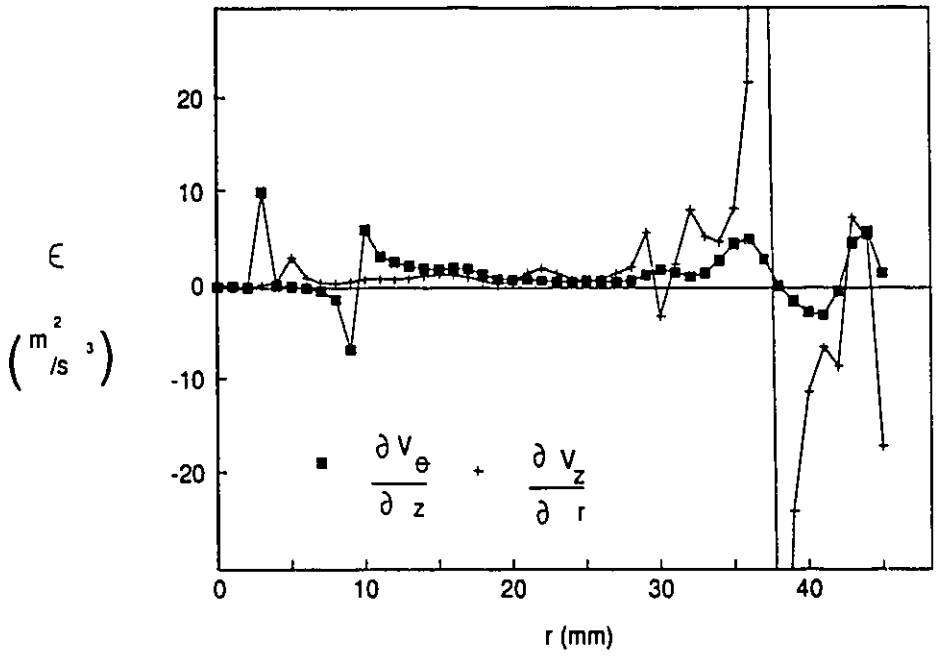

Figure 129. More useful dissipation rate results from the gradient hypothesis method.

7.3.2 Taylor's hypothesis

Taylor's frozen turbulence hypothesis leads to the equation

$$\varepsilon = 30\nu \frac{u'^2}{2u_1'^2 U_c^2} \overline{\left(\frac{\partial u_1'}{\partial t}\right)^2}$$

where the streamwise direction is taken to be z. Various interpretations have been applied to the terms u' and U_c. Considering first the u' term,

term	possible corrections
$\frac{u'^2}{u_1'^2}$	1) assume $u_1' = u'$
	2) take $u'^2 = k = \frac{v_z^2 + v_r^2 + v_\theta^2}{2}$
	3) use the average $u'^2 = \frac{v_z^2 + v_r^2 + v_\theta^2}{3}$

the resulting corrections are shown in figure 130. The k correction will always be exactly 1.5 times the average correction. Only the k correction will be compared with other methods. Both corrections are always greater than 1.

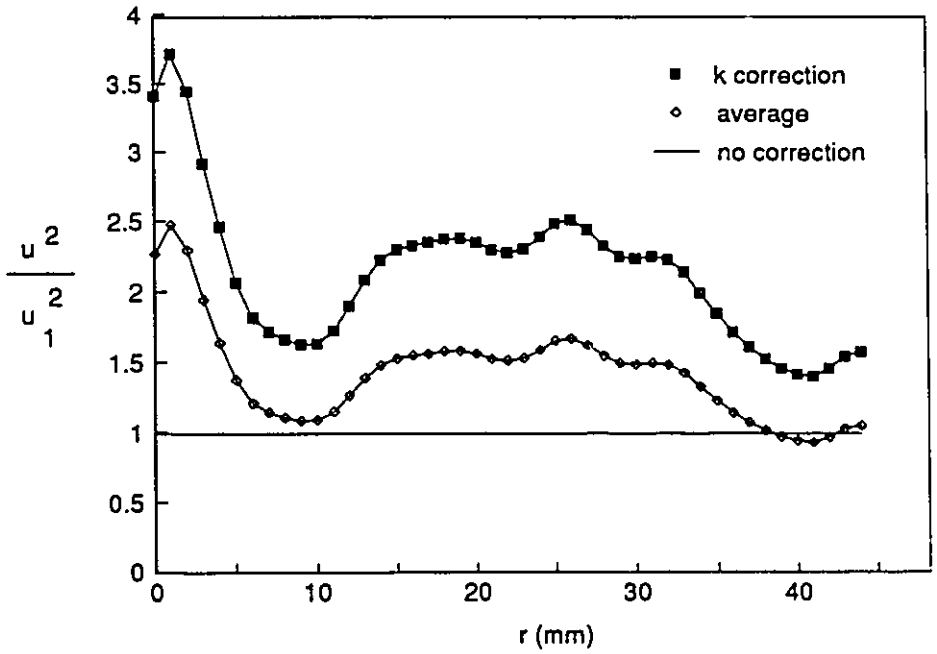

Figure 130. Comparison of corrections for the characteristic velocity of the turbulence.

The convection velocity (U_c) term is meant to correct a method developed for a one dimensional, low intensity flow for application to a three dimensional, or highly turbulent flow field. At least five different versions have been presented in the literature.

term	possible corrections
$\frac{1}{U_c^2}$	1) no correction, set $U_c = V_z$
	2) Wu et al. (1989) $U_c^2 = V_z^2 + v_z^2$
	3) for isotropic flow $U_c^2 = V_z^2 + 5v_z^2$
	4) Van Doorn (1981) $U_c^2 = V_z^2 + v_z^2 + 2v_r^2 + 2v_\theta^2$
	5) full correction $U_c^2 = V_z^2 + 2V_r^2 + 2V_\theta^2 + v_z^2 + 2v_r^2 + 2v_\theta^2$

The resulting profiles of $1/U_c^2$ are shown in figure 131. There is no difference between the Van Doorn and the total correction, and very little difference between the Wu result and no correction. The isotropic correction coincides with the full correction, except immediately below the hub, where the measured values of velocity can be questionable. For further comparisons, only the full correction and no correction are applied.

A final concern about this method is the effect of the sampling frequency on the value of the time derivative. This concern is valid, as was shown by Wu and Patterson (1989), and as previously shown in figure 112. The effect of variations in the time derivative on the final calculated values of ε is shown in figure 132. These traverses use both the k and the full U_c corrections. The k correction is very small relative to the U_c correction.

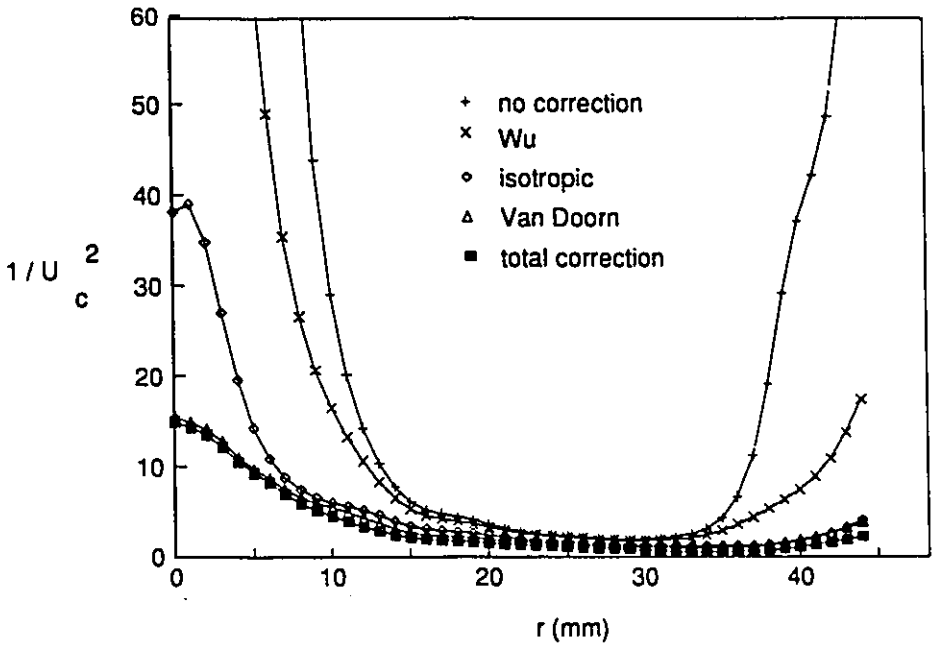

Figure 131. Comparison of various determinations of the convection velocity U_c as described in the text.

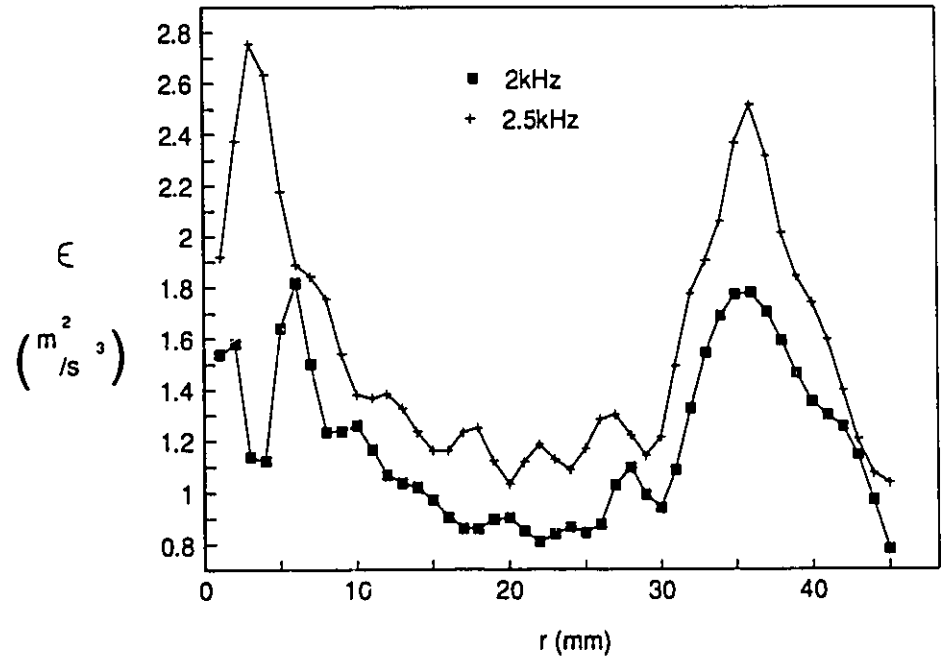

Figure 132. Effect of the sampling frequency on the final value of the dissipation rate for the fully corrected calculation.

7.3.3 Dimensional argument

Using a characteristic velocity scale to give the energy, and a characteristic length/velocity to give the time, results in the energy dissipated per unit time and mass as

$$\varepsilon = A\frac{u'^3}{L}$$

where A is a constant assumed equal to 1 and L is taken to be D/10. The arguments for these assumptions were given in chapter 5. For the characteristic velocity, either $k^{1/2}$ or $\left(\frac{3v_z^2}{2}\right)^{1/2}$ can be used. There is little difference between the two results, as shown in figure 133.

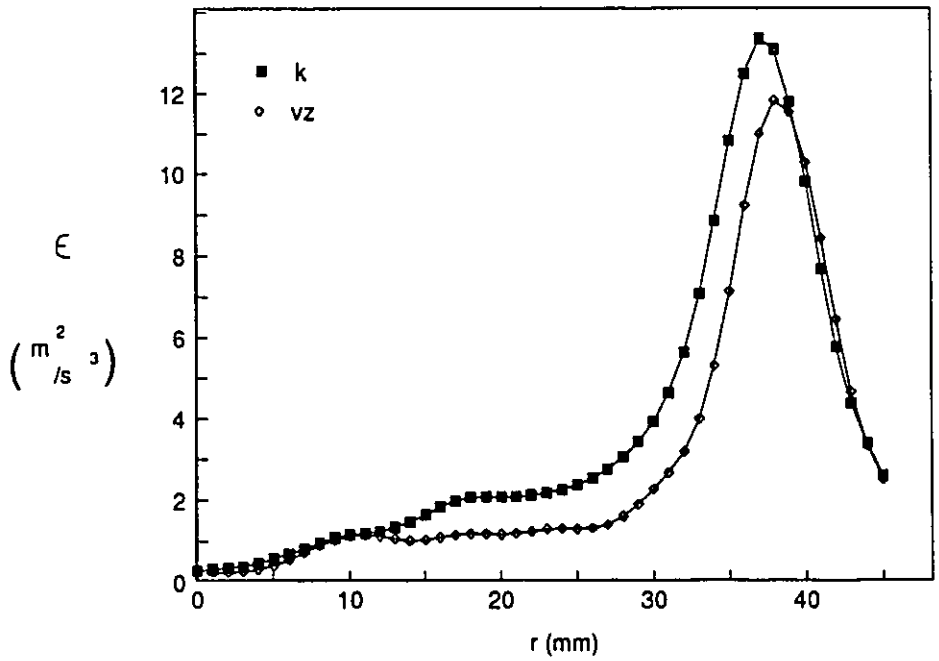

Figure 133. Dissipation rate results obtained from the dimensional method using two characteristic velocities.

7.3.4 Autocorrelation coefficient

Wu and Patterson (1989) discard the assumption of a constant length scale in favor of measurement of the integral time scale at the desired locations in the tank. The time scale is the converted to the length scale using the convection velocity, discussed in the section on Taylor's hypothesis.

$$\varepsilon = A \frac{u'^3}{\tau_E U_c}$$

As for the dimensional method, A is taken equal to one, and the characteristic velocity may be taken from either k or v_z. It is clear from the previous section that the only useful values of τ_E are those integrated to the first zero crossing for 1) filtered, and 2) raw data. The filtered data is likely to give more meaningful results for the turbulent quantities.

Wu and Patterson (1989) caution that the appropriate length scale is really the resultant length scale obtained from the vector sum of three components, and that the convection velocity, derived for time derivatives of velocity, may not be the appropriate velocity scale for this conversion. Recalling the origins of the dimensional equation, and considering the questionable applicability of U_c to this case, it is useful to consider

$$\varepsilon = A \frac{u'^2}{\tau_E} \qquad (106)$$

thus eliminating the conversion of the characteristic time scale to a length scale, and then back to a time scale using a different velocity. The same two choices are available for u. Initially, k is the obvious choice, since the quantity in question is

the dissipation of TKE per time; however, recalling Wu and Patterson's concern about a resultant length scale, and that both τ_E and k have been shown to have three approximately equal components, use of a single component of both the velocity and time scales may be a valid simplifying assumption (this would greatly reduce the experimental task for future determinations).

Five combinations of these alternatives have been considered for the filtered and the raw data as follows:

term	possible corrections
$A\frac{u'^3}{\tau_E U_c}$	1) full correction $u' = k^{1/2}, U_c = U_c$
	2) mixed $u' = k^{1/2}, U_c = V_z$
	3) no correction $u' = v_z, U_c = V_z$
$A\frac{u'^2}{\tau_E}$	4) $u' = v_z$
	5) $u' = k^{1/2}$

The resulting profiles of ε are shown in figure 134. Several things should be noted from this figure: 1) when two resultant scales, or two single component scales, are used, the traverses agree extremely well; the one component simplifying assumption is valid, 2) the conversion of the time scale to a length scale and back again can be eliminated if the single component velocity scale is used, and 3) when a single component scale is combined with a resultant scale, the calculated value of ε increases drastically. Recalling the dissipation results for the RT from chapter 6, the maximum dimensionless value of ε should be of the order 0.2. This corresponds to a dimensional value of 10 for this experiment, which lends further support to adoption of corrections leading to the lower peak values of ε.

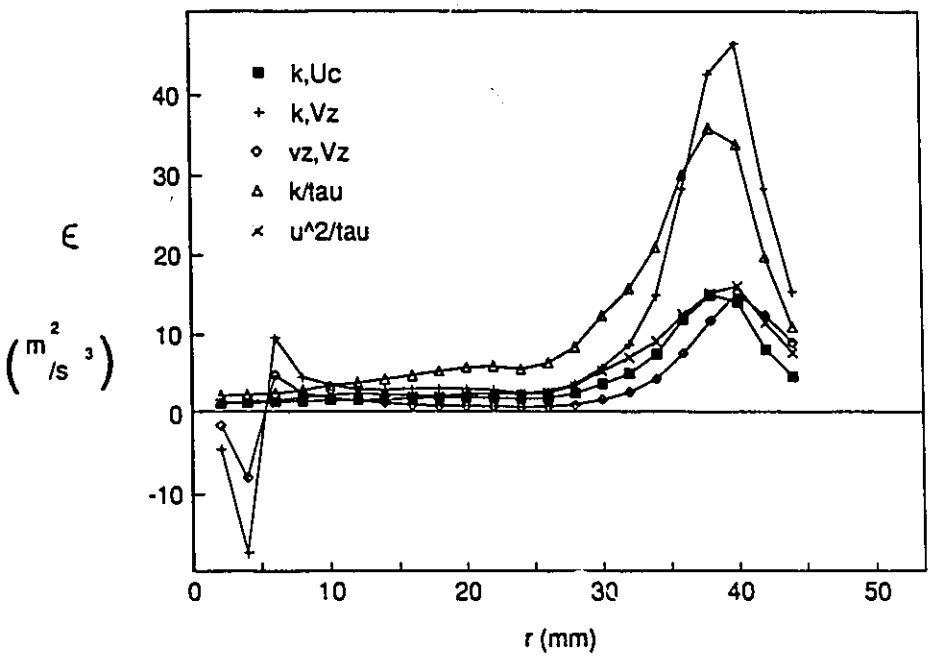

Figure 134. Dissipation rate results from the autocorrelation method, and the effect of suggested corrections.

The results shown in figure 134 are all for filtered values of τ_E. Figure 135 compares the filtered and raw results. The raw data returns a much lower ε, corresponding to the larger time scale (cf. figures 115 and 117).

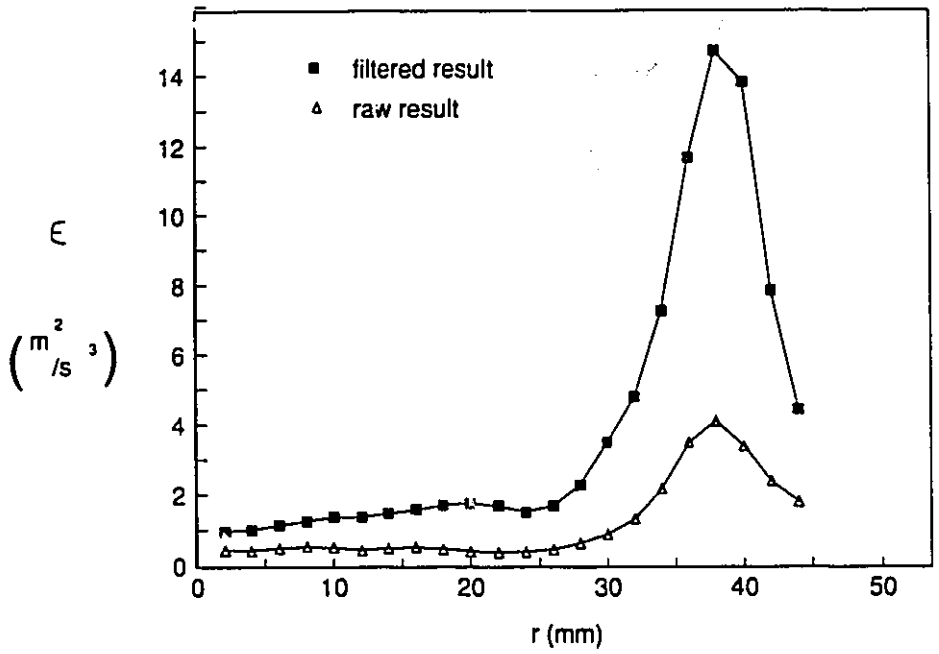

Figure 135. Effect of filtering on the final value of the dissipation rate.

7.3.5 Comparison of methods

The dissipation rate profiles for the different methods are divided into three groups to allow easier comparison. These groups are based on the maximum calculated value of ε in the traverse. High peak methods are defined as those where ε peaks around 40 m^2/s^3, medium around 12 m^2/s^3, and low around 4 m^2/s^3. It has already been established that a maximum value of the order of 10 m^2/s^3 is expected, so the most promising methods will be those that fall in the medium peak group. The high peak results are shown in figure 136, and include those from the auto-correlation method which mix single component and resultant scales, and the uncorrected Taylor results; methods over which some concern has already been extended. Note at this point that the lowest of the low peak results (see figure 137) is the fully corrected Taylor traverse. Taylor's hypothesis provides the bracketing

values for the results, but completely misses the middle range. Considering now the other low peak results, all four are from the autocorrelation method where no filtering has been applied. Note that this is exactly the opposite trend to that reported by Wu and Patterson (1989), whose ε values were higher for the unfiltered data. Figure 138 shows the medium peak results, which include three of the four methods used, and which are bracketed by the fourth method. It is interesting that both versions of the simple dimensional method agree so well with the various autocorrelation results, and that the three versions of the autocorrelation method using like scales agree so well with each other. Comparison with the gradient tz traverse is based on the positive slopes, rather than the negative peak value.

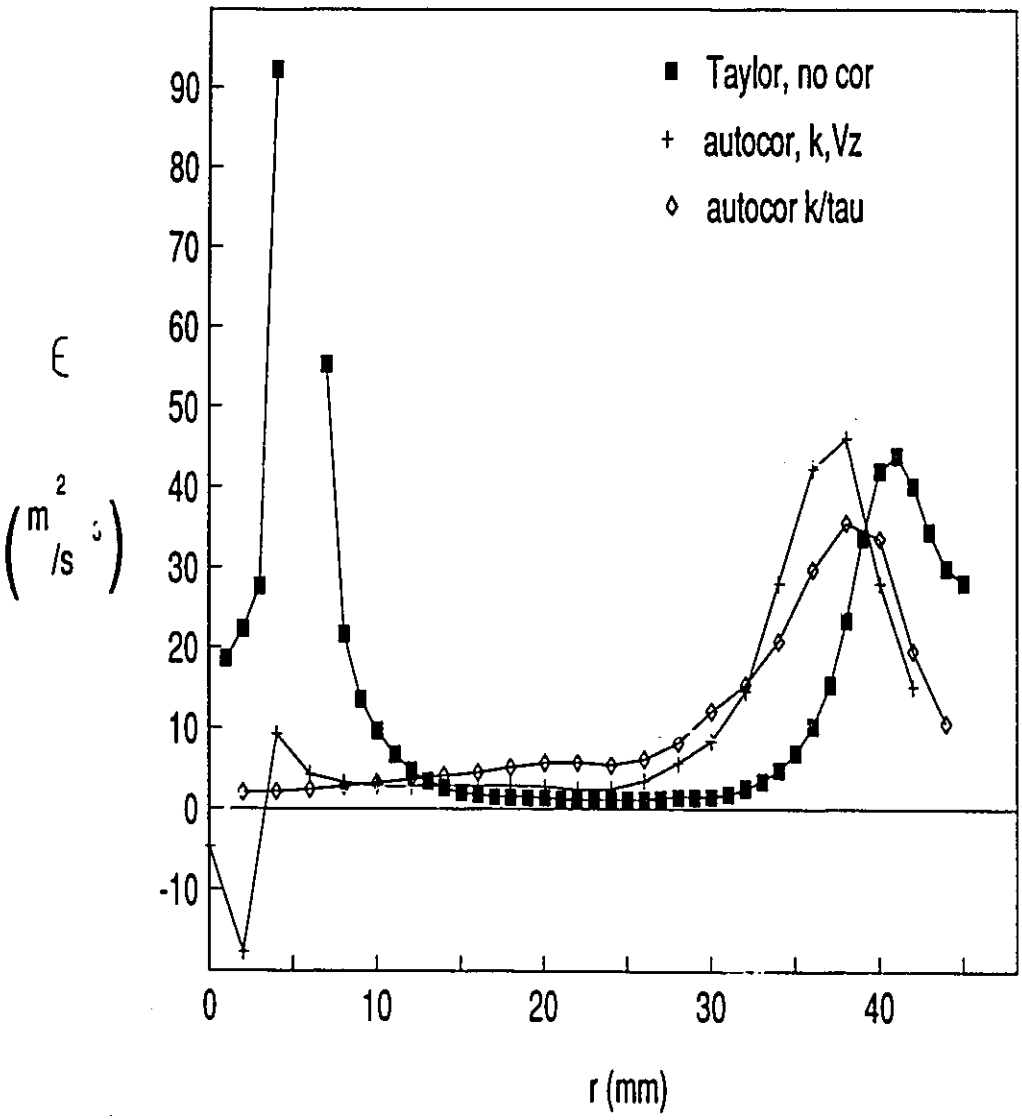

Figure 136. High peak methods

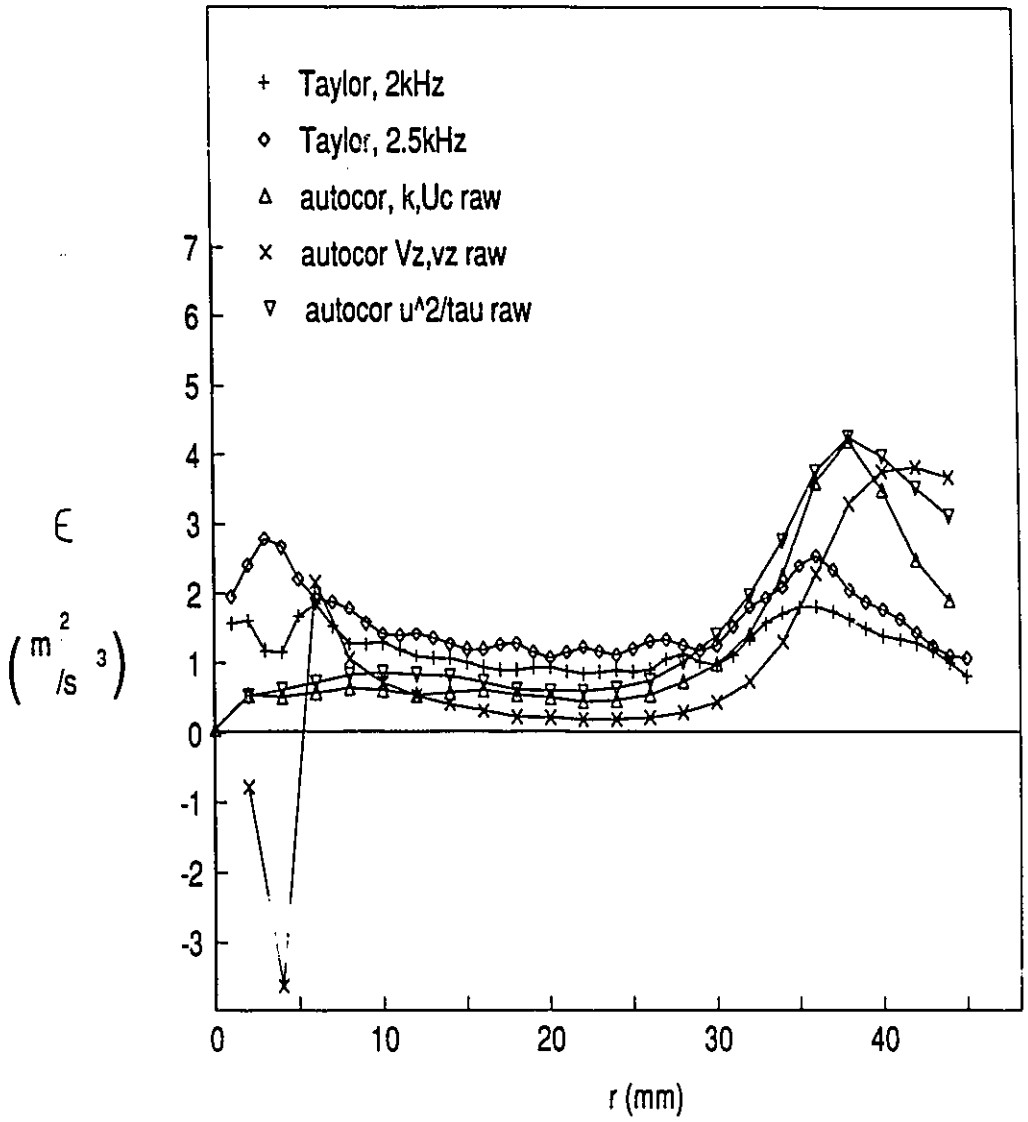

Figure 137. Low peak methods

From these three figures, it is concluded that the most reliable and practical methods at the impeller edge come from the medium peak group. The dimensional method and the autocorrelation methods using single component scales, one from each form of the equation, are extended out into the bulk of the tank for further verification, and further examination of ε and τ_ε. The resultant form of the auto-

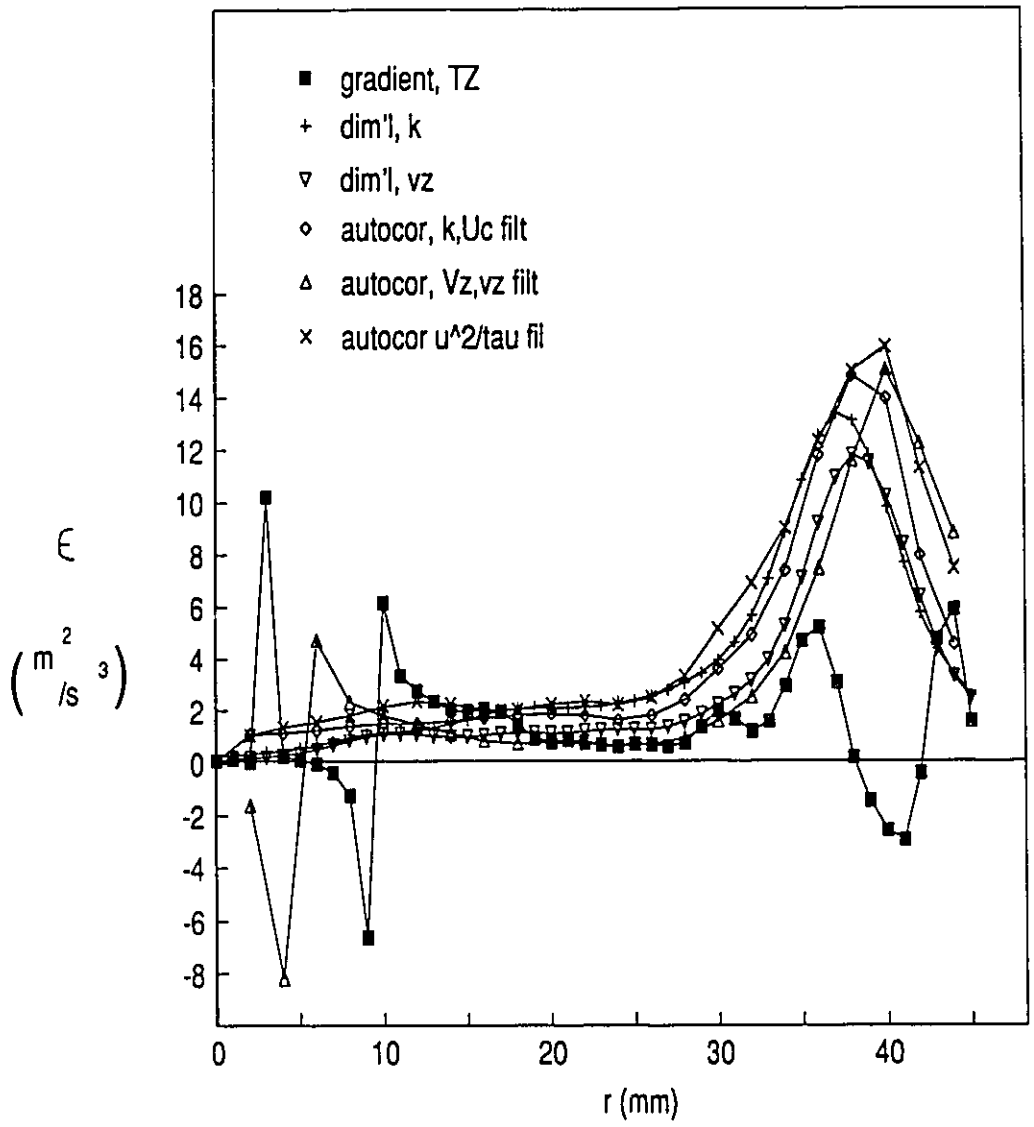

Figure 138. Medium peak methods

correlation method is equally valid, but is discarded because it is much more demanding from the point of view of experiment and analysis. The results from the methods selected for further analysis are repeated in figure 139 for reference and clarity.

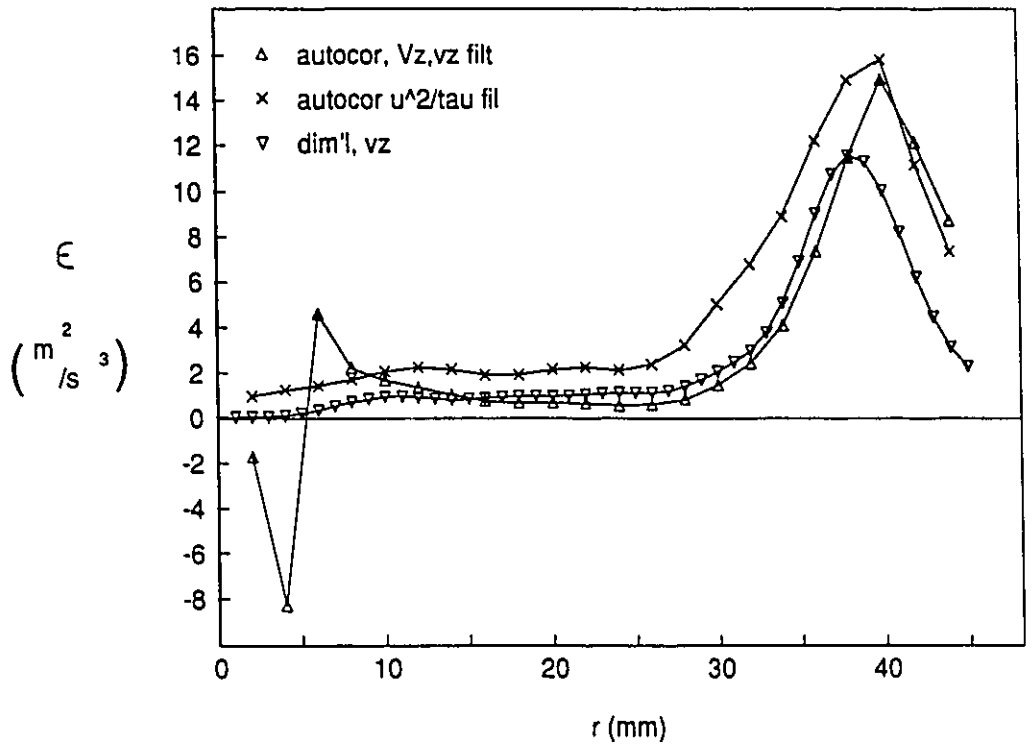

Figure 139. Methods selected for further verification and extension out into the tank.

7.4 Extension into the bulk of the tank

Extension of the examination of ε into the bulk of the tank, and to other geometric cases, has a three fold purpose:

1) further testing of ε methods,

2) to determine appropriate boundary conditions for other geometries,

3) to obtain results suitable for verification of simulation results.

With these objectives in mind, four sets of data have been analysed. The first is a traverse below the impeller at 2z/W = -3.5 for the case T7. This gives information about the decay of ε for the D=T/2 low clearance discharge condition. The second

set is the discharge condition and decay for case 1 (D=T/2, C=T/2); a T/2 high clearance discharge condition case. The third examines the T/3 high clearance discharge condition and decay using case 4 (D=T/3, C=T/3). Finally, the upper part of the tank is examined for case T7.

The three methods chosen as most promising from the results at the edge of the impeller are applied to all of the data above in order to test the consistency of their performance under the varying flow conditions found in a stirred tank. The equations applied, and the abbreviations used to refer to them, are

1) dimensional (dim'l k)

$$\varepsilon = A\frac{k^{3/2}}{D/10} \approx A\frac{(3v_z^2/2)^{3/2}}{D/10} \tag{107}$$

2) autocorrelation (autocor Vzvz)

$$\varepsilon = A\frac{v_z^3}{\tau_E V_z} \tag{108}$$

3) autocorrelation (autocor time)

$$\varepsilon = \frac{v_z^2}{\tau_E} \tag{109}$$

From this point on, keeping in mind the "streamwise" definition of direction, the absolute value of V_z is used for the autocor Vzvz method. This eliminates the occurence of "negative ε's." Even with this stipulation, the calculation will give unrealistically high values of ε wherever the mean velocity is small.

7.4.1 Decay of discharge flow below the impeller

Figure 140 shows the profile of τ_E at 2z/W=-2.5, with three repeats. Again, outliers show up as single points. The value of τ_E has approximately doubled from that at the impeller edge. Figure 141 shows the resulting values for ε. Agreement between the dim'l k method and the autocor time method is very good from the tank axis out to 30mm; then the autocor time method gives larger values. The autocor Vzvz method is the least stable of the three methods. The shape of the profile agrees well with the location of the most vigorous flow (see chapter 2). The peak value of ε has dropped from 16 to 9, the profile has flattened out, and the minimum value of 2 has been maintained.

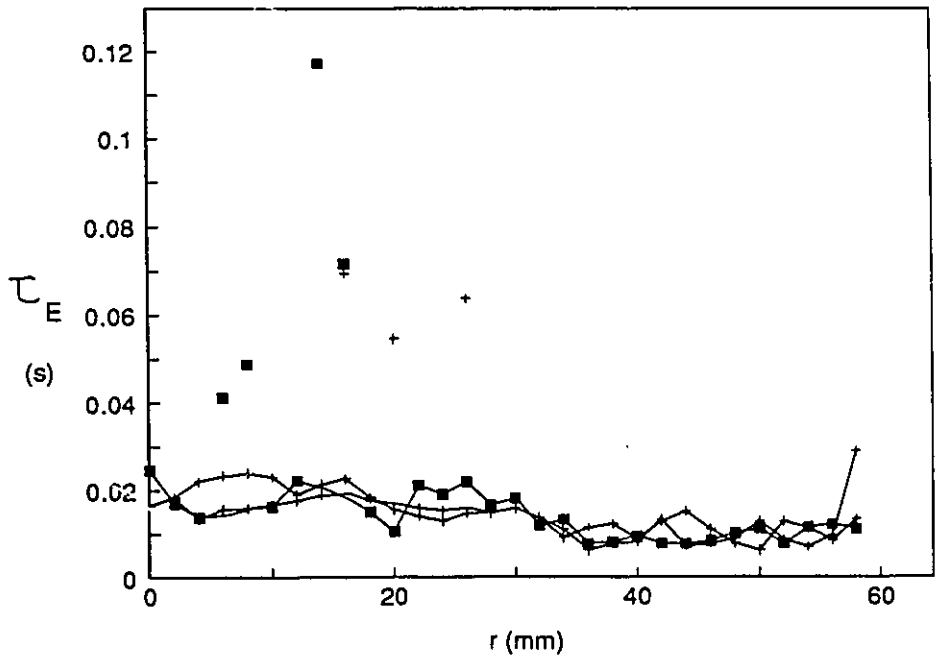

Figure 140. Integral time scale with several repeats at 2z/W= -2.5 for case T7.

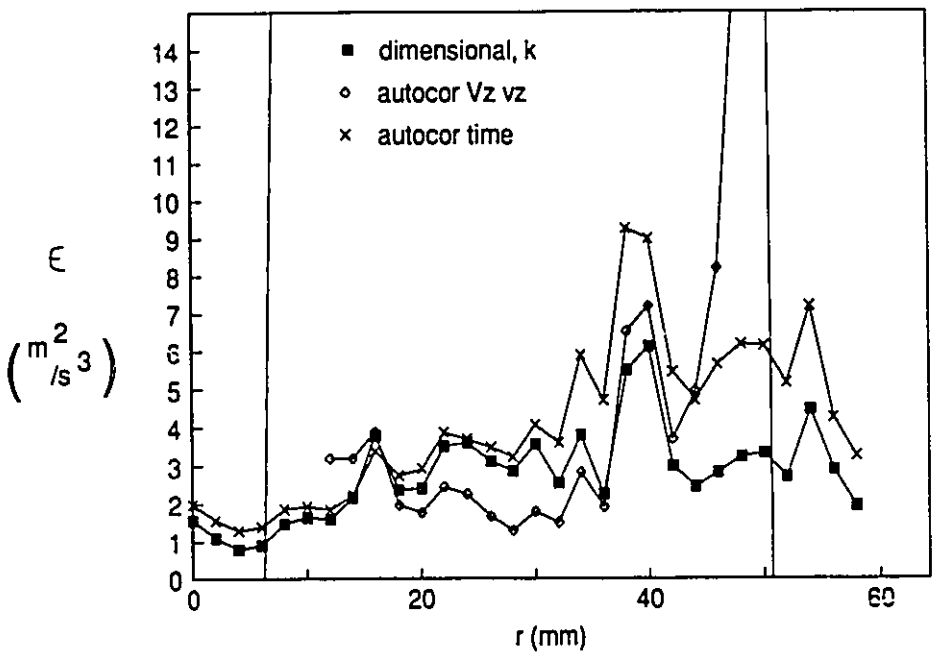

Figure 141. Results of dissipation rate calculations at 2z/W= -2.5. All calculations use forms which require the measurement of only one component of velocity.

Figure 142 shows the profiles of τ_E for traverses A, F, G, and H; case 1. Very small values of τ_E are recorded in the region of the impeller tip. The profile is flat by 2z/W = -2.5, and shows very little change beyond that point.

Figures 143, 144, 145 and 146 compare the three selected methods of calculating ε for the four traverses below the impeller as given above. The autocor Vzvz method consistently gives results much higher than the other methods, showing extreme sensitivity to the value of Vz. Agreement between the autocor time method and the dimensional method is generally very good, except at the edge of the impeller, where the very low values of τ_E recorded near the tip cause very large peak values of ε. Representative curves from each traverse are combined in figure 147 to show the decay of ε away from the impeller. By 2z/W=-4, most of the decay appears to

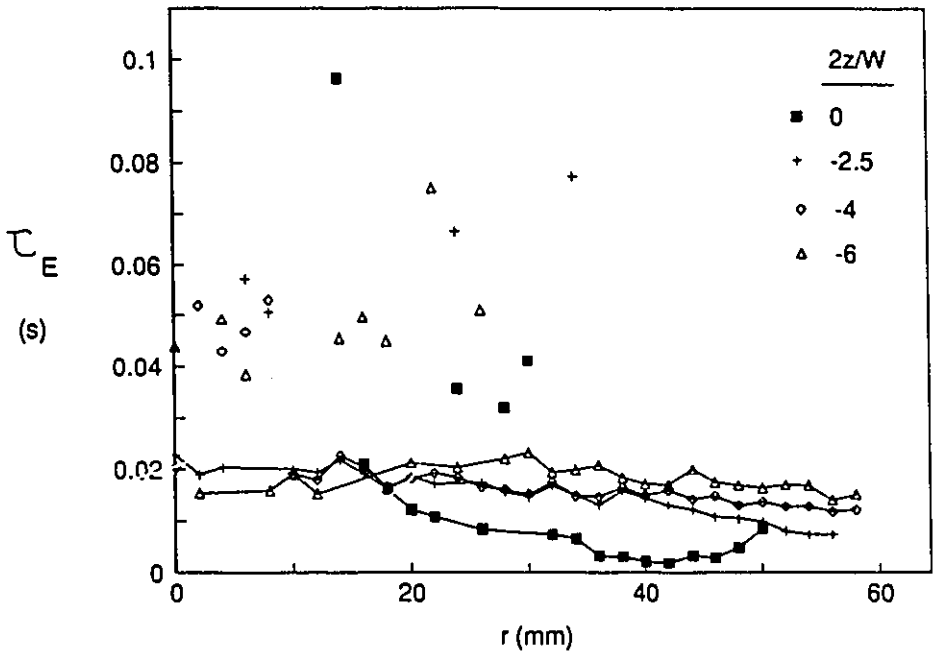

Figure 142. Integral time scale for case 1, T/2 upper boundary condition.

be complete. This is also the case for the T/3 impeller case, to be examined next.

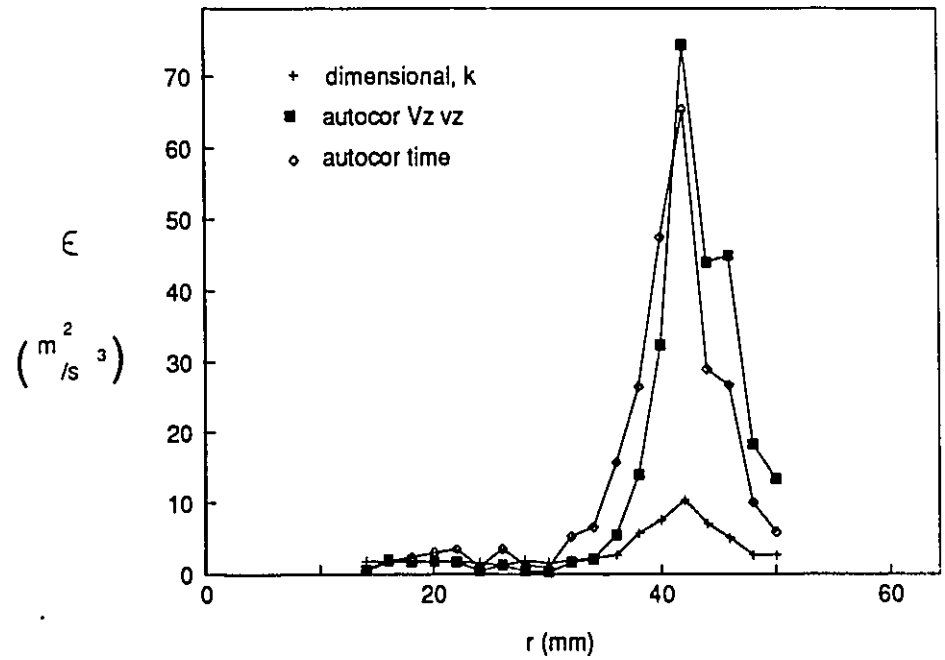

Figure 143. Results of dissipation rate calculations at the lower edge of the impeller for case 1: T/2 lower boundary condition.

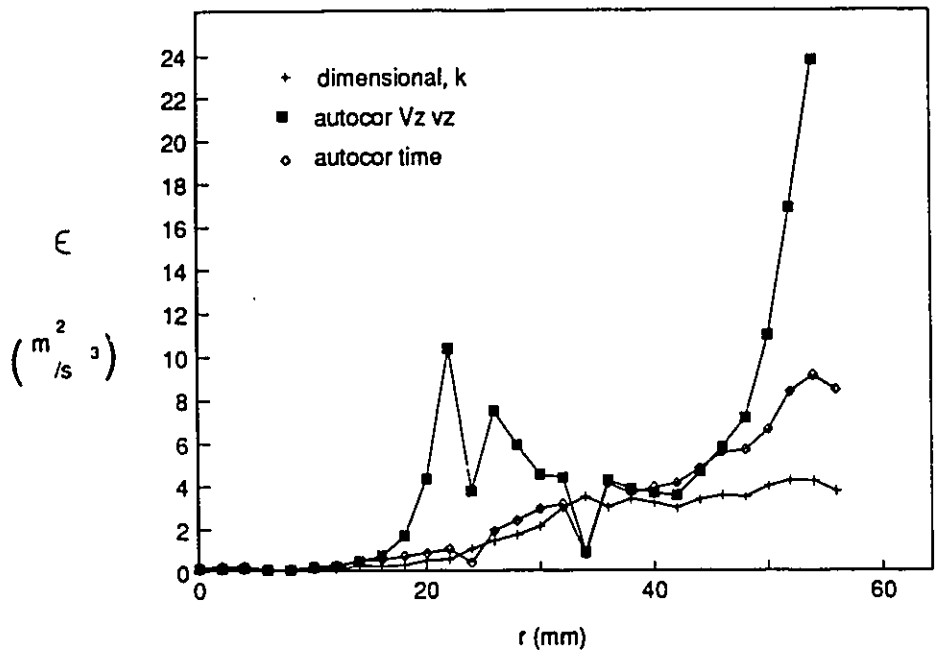

Figure 144. Results of dissipation rate calculations at 2z/W = -2.5 for case 1: T/2 lower boundary condition.

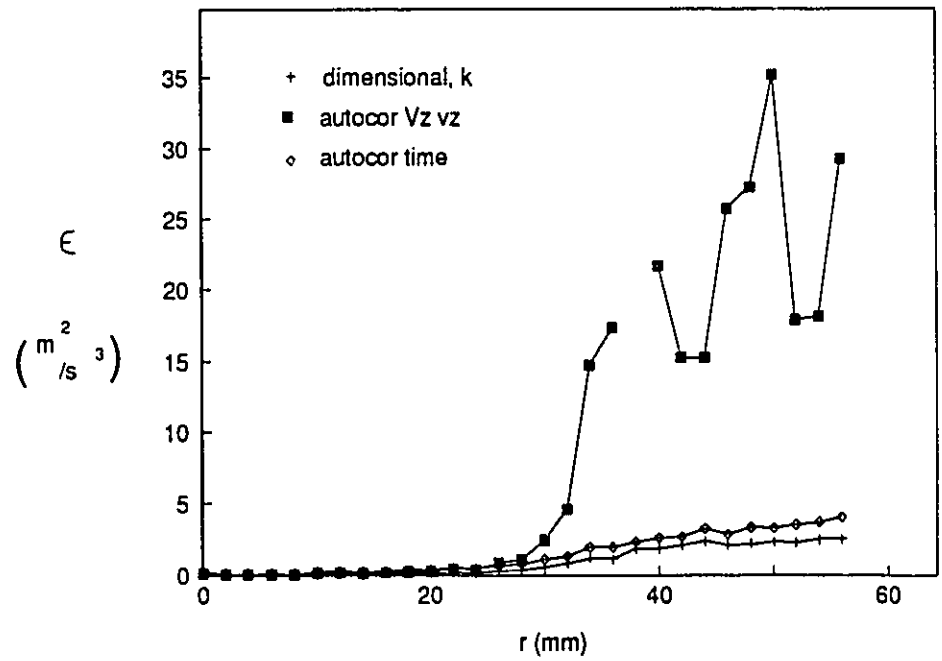

Figure 145. Results of dissipation rate calculations at 2z/W = -4 for case 1: T/2 lower boundary condition.

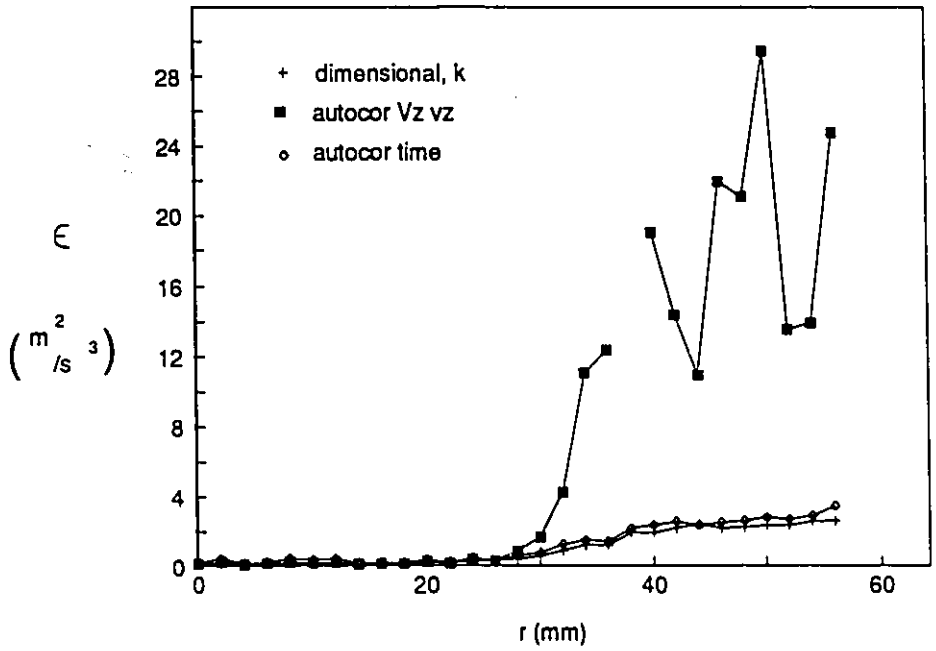

Figure 146. Results of dissipation rate calculations at 2z/W = -6 for case 1: T/2 lower boundary condition.

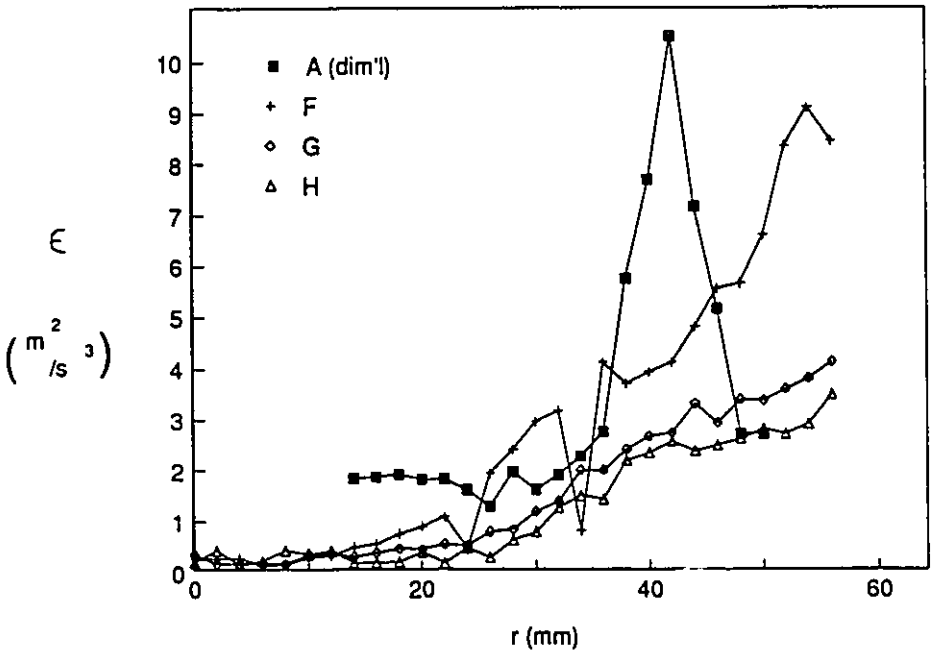

Figure 147. Decay of ε below the impeller for case 1: T/2 lower boundary condition. Traverses are the most stable methods from the previous four figures. With the exception of traverse A, the autocor time method is used.

A small (T/3) impeller is examined next from case 4 (C=T/3). The results for τ_ε are shown in figure 148; τ_ε increases with movement down in the tank for radial positions from 0 to 24mm, and shows the opposite trend for radii in the range of 24 to 50mm. The τ_ε's are up to 7 times larger than the time scales recorded for the T/2 impeller. This agrees well with the flow patterns observed in the flow visualization experiments. As with the last case, the methods for calculating ε show several regions of close agreement (see figures 149, 150 and 151). The traverse at the edge of the impeller is, again, the most prone to estimating extraordinarily large values of ε. The dimensional method peaks at 13, while the two autocorrelation methods peak at values much greater than 15. The T/3 impeller results in much lower dimensional values of ε away from the impeller (less than $1.5\,m^2/s^3$) compared

to the D=T/2 impeller (approximately 4 m^2/s^2). If ε is made dimensionless with $(\pi ND)^3/D$, the results from the two different impeller diameters agree. The decay of ε is not shown for this case, because agreement between the results was not good enough to make a clear recommendation of values for verification. The figures shown above give the overall trends, and the order of magnitude of ε for this case. Further experiments should use larger values of N, repeats of the traverses, and more exact removal of the low frequency variations in the mean in order to obtain more definitive values of ε.

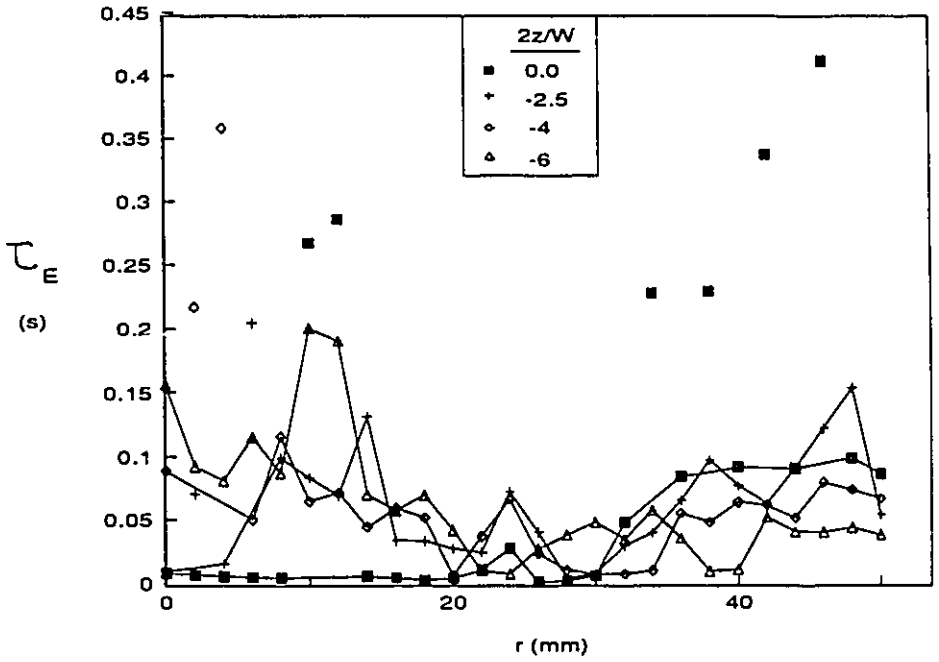

Figure 148. Integral time scale for case 4, T/3 upper boundary condition.

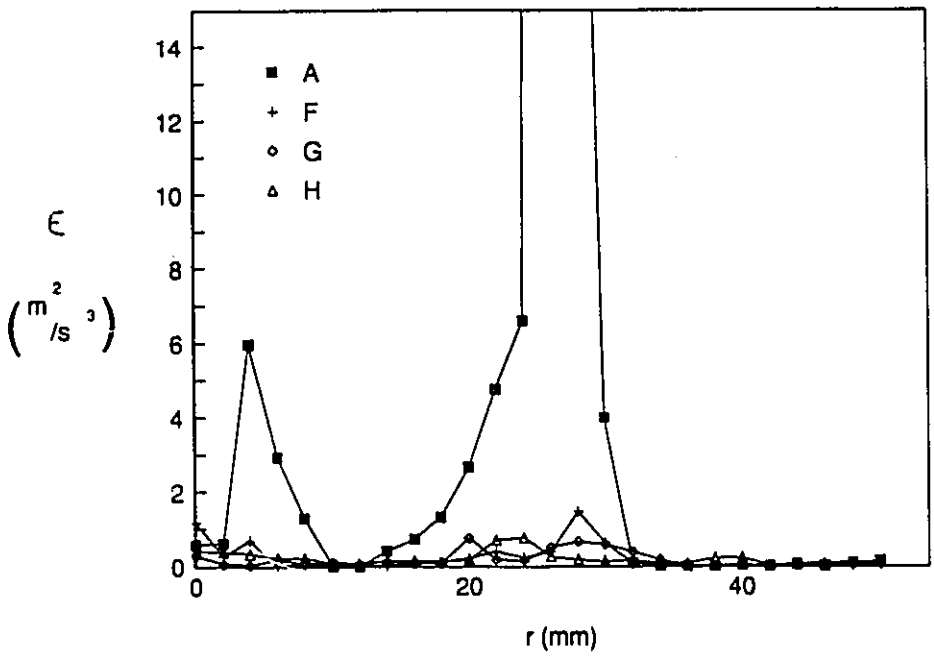

Figure 149. ε calculated from the autocorrelation, Vzvz method, case 4.

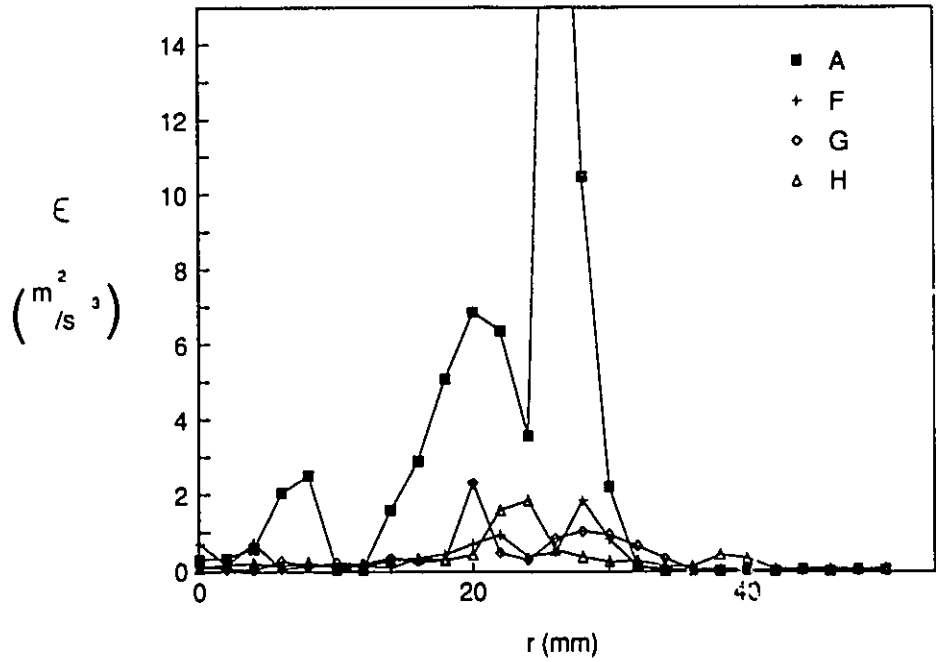

Figure 150. ε calculated from the autocorrelation, time method, case 4.

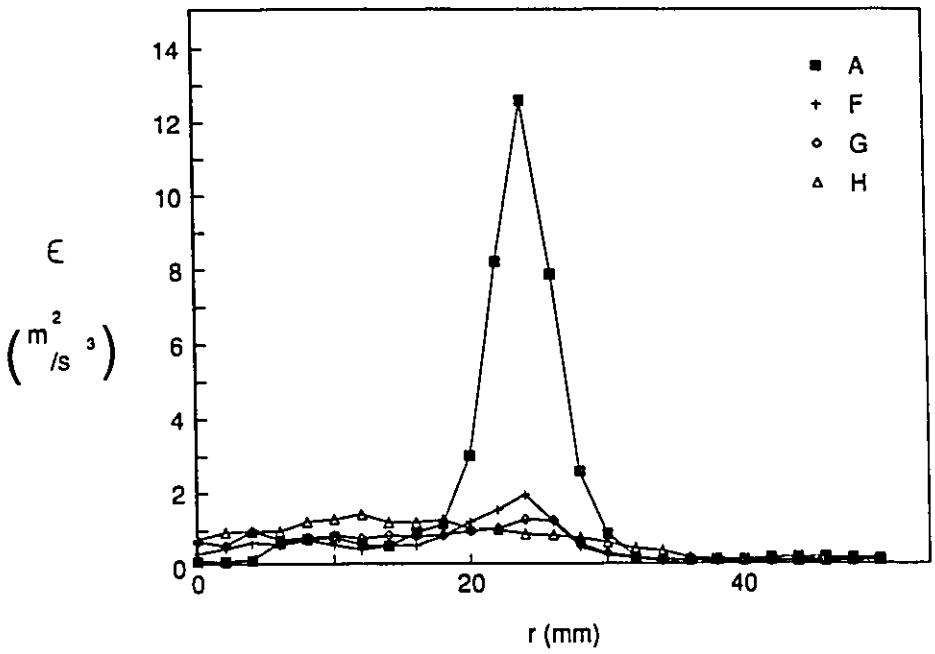

Figure 151. ε calculated from the dimensional k method, case 4.

7.4.2 Upper portion of the tank

The upper portion of the tank was examined for T7 (D=T/2, C=T/4) with 8 traverses at axial positions from 2z/W = 2.5 (just above the impeller) to 19, where the top of the tank is at 21. The low frequency oscillations are much less regular in this region, as is clear from the results for τ_E shown in figure 152. The trend becomes clearer if the mean value of τ_E is plotted for each traverse, as shown in figure 153. Both the raw and filtered time scales have been reported, to show that even though the pointwise results are less stable in the top of the tank, the filtering has approximately the same effect on the mean value of τ_E. The mean value of τ_E increases steadily as the probe is moved up in the tank.

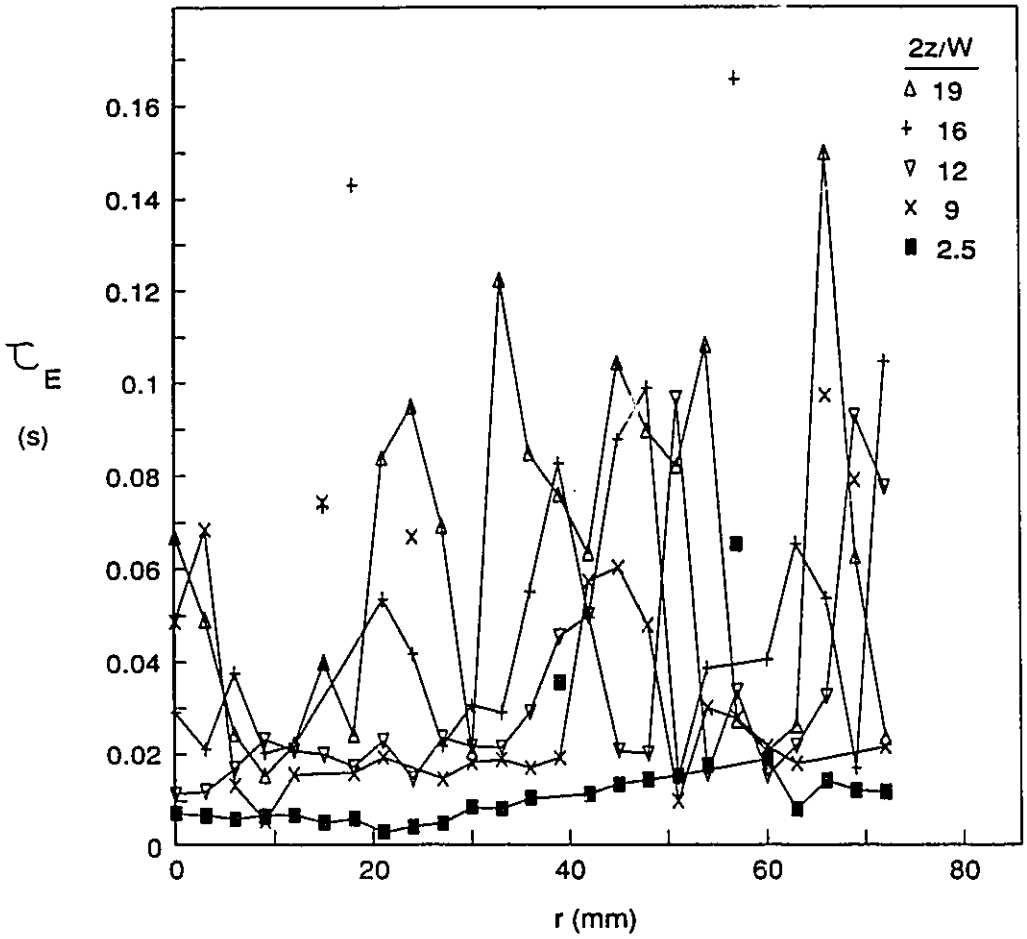

Figure 152. Integral time scale for case T7, upper portion of the tank.

Results from the three methods of ε calculation (figures 154, 155 and 156) all show decay to zero at the top of the tank. The autocor Vzvz is, again, the least stable of the three; and conclusions about the actual value of ε are best drawn from a comparison of the results from all methods, combined with examination of the intermediate values which lead to outlying points.

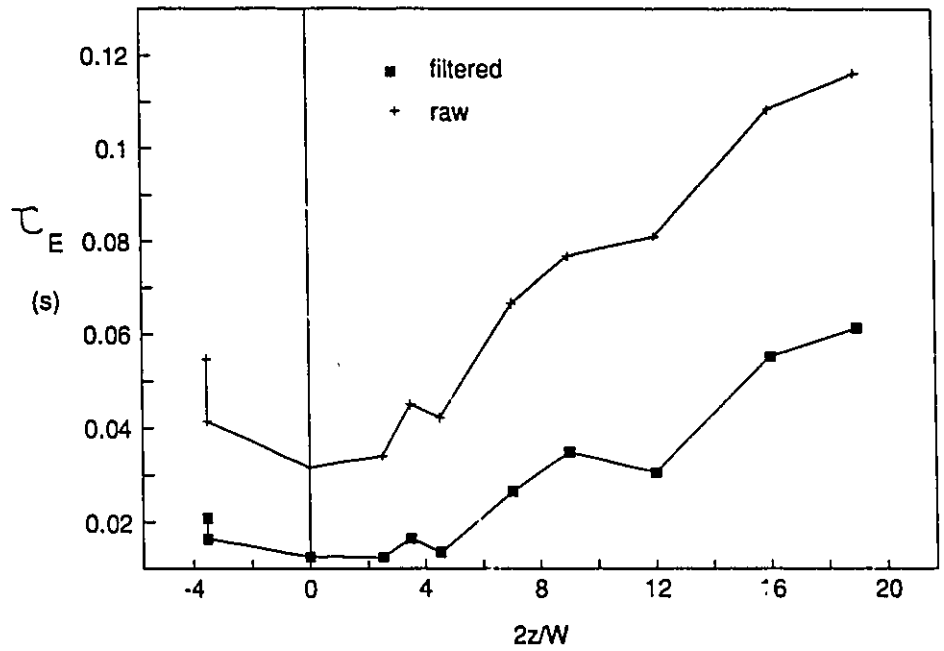

Figure 153. Mean integral time scale for case T7, upper portion of the tank.

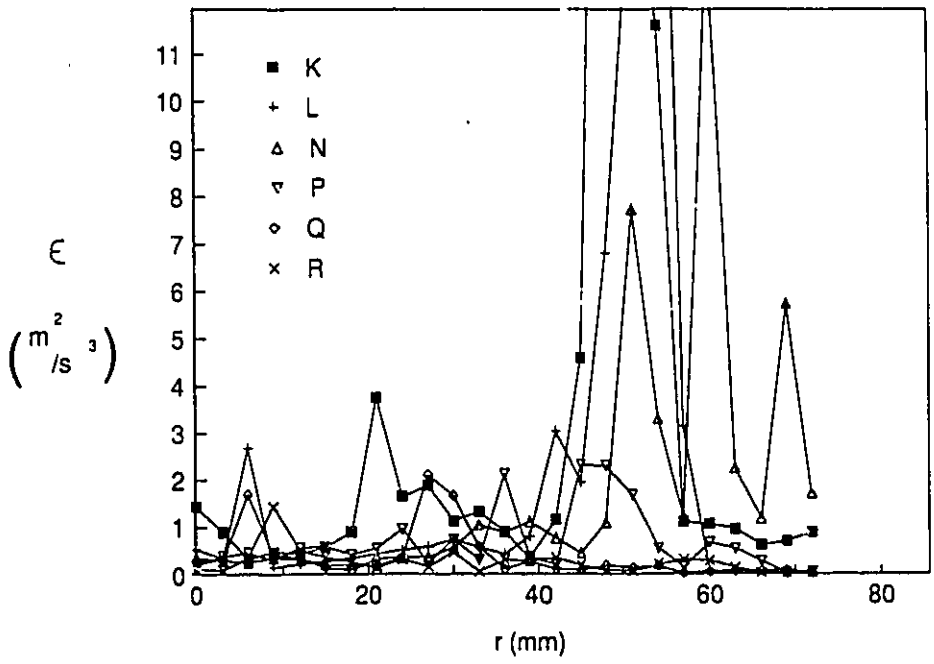

Figure 154. ε calculated from the autocorrelation, Vzvz method, upper tank, T7.

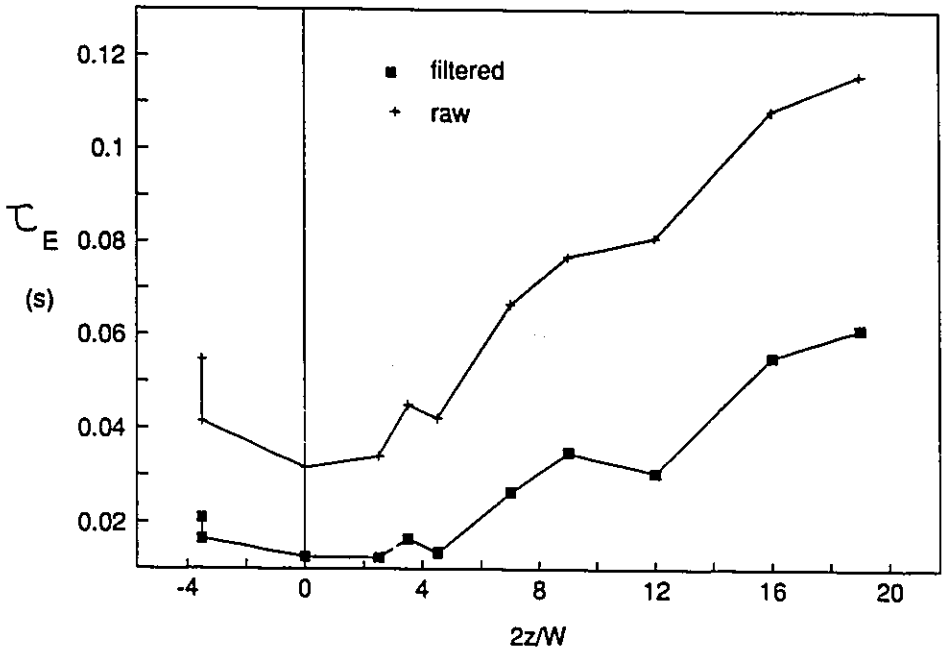

Figure 153. Mean integral time scale for case T7, upper portion of the tank.

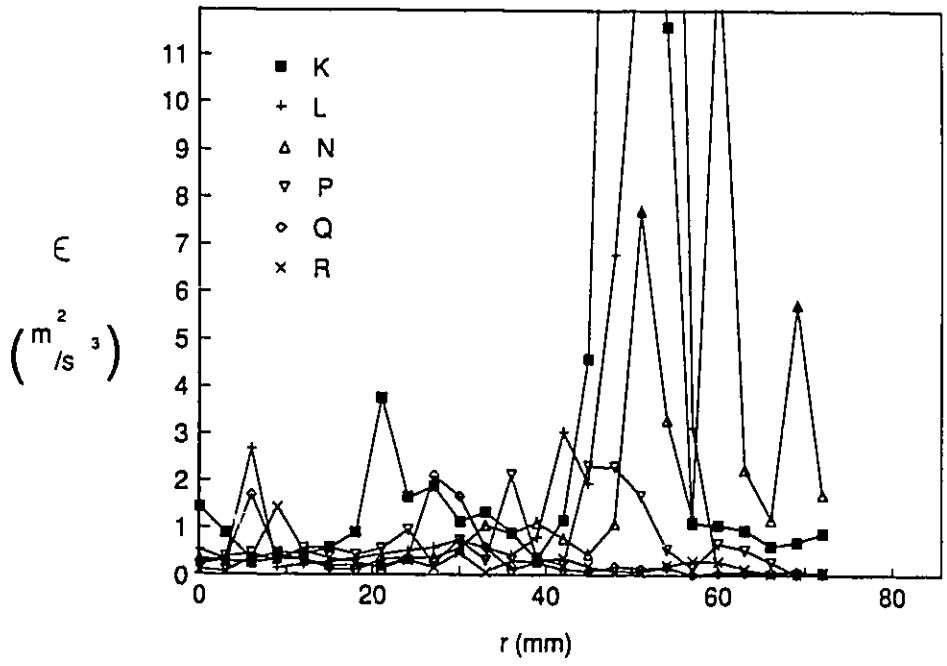

Figure 154. ε calculated from the autocorrelation, Vzvz method, upper tank, T7.

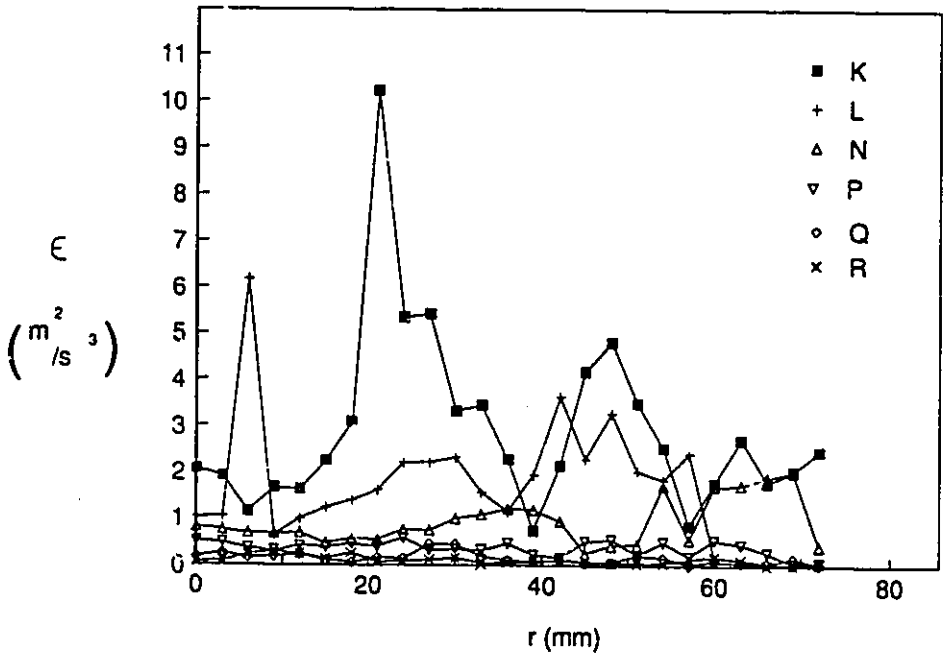

Figure 155. ε calculated from the autocorrelation, time method, upper tank, T7.

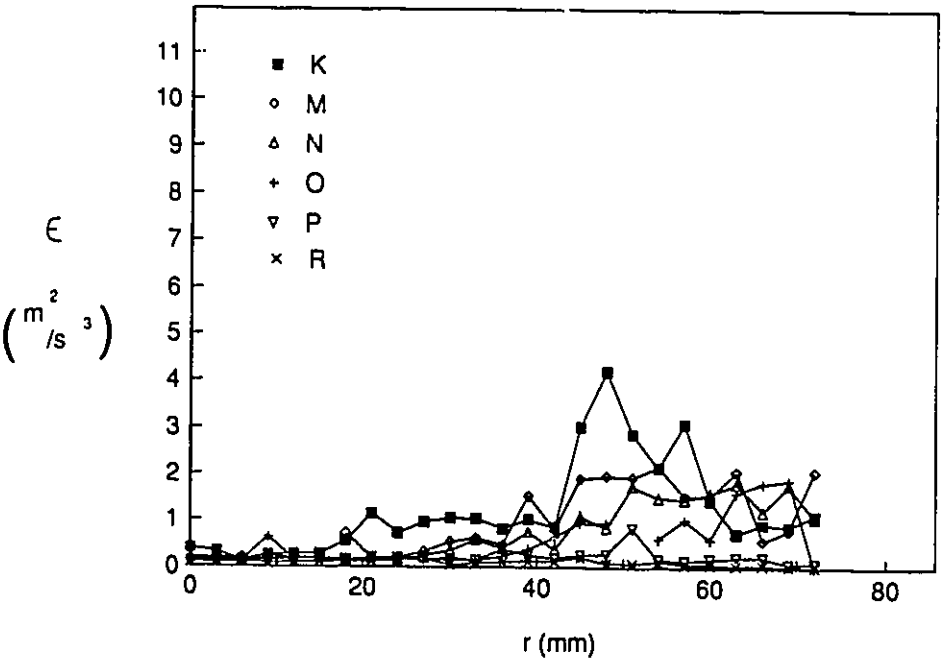

Figure 156. ε calculated from the dimensional k method, upper tank, T7.

The arithmetic mean value of ε for each traverse is shown in figure 157 for the three methods. This reflects the instability in the Vzvz method already observed in individual traverses. It shows surprisingly good agreement between the dimensional and autocorrelation methods in the upper region of the tank, where the worst agreement was expected. The autocor time method shows an exponential decay of ε moving away from the impeller, reminiscent of that obtained in the SRJ discharge.

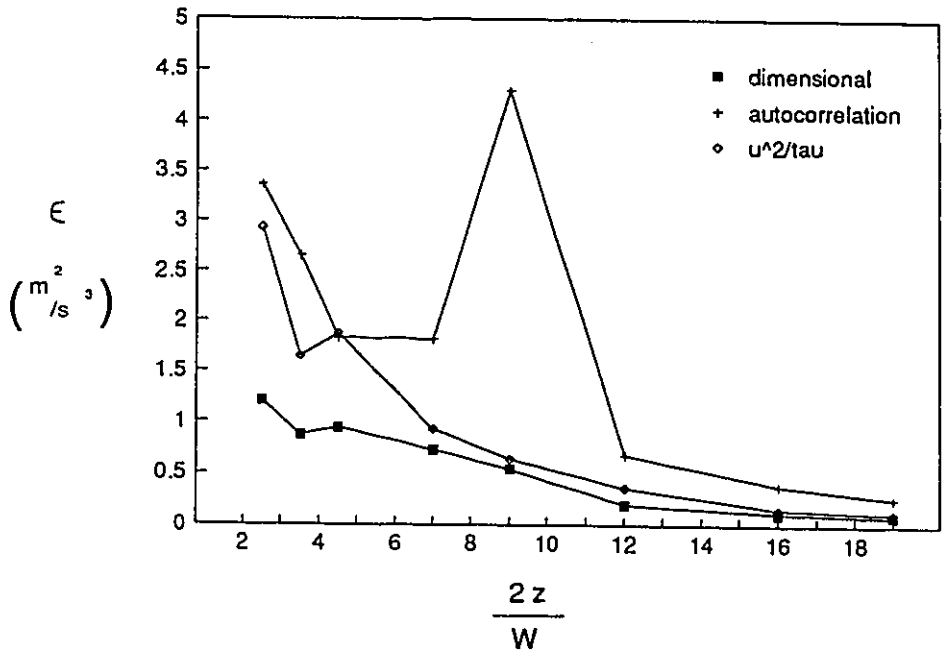

Figure 157. Mean values of ε calculated from the three recommended methods in the upper tank, T7.

7.5 Conclusions

Several conclusions about the calculation of τ_E and ε can be drawn from the work in this chapter:

For τ_E,

1) The low frequency fluctuations must be removed, and the integral evaluated to the first zero crossing. This gives a value of τ_E which is repeatable, and axisymmetric.

2) τ_E is independent of the sampling frequency, for the valid experimental range. A sampling frequency of five times the measuring volume limit will give erroneous values of both the RMS (see chapter 3), and τ_E.

3) τ_E scales correctly with N.

4) τ_E's calculated from the three components of velocity are approximately equal.

For ε,

1) All of the suggested methods for obtaining ε and their corrections were examined at the impeller discharge. Some degree of agreement among the methods is apparent. The three most stable methods were

1) dimensional (dim'l k)

$$\varepsilon = A\frac{k^{3/2}}{D/10} \approx A\frac{(3v_z^2/2)^{3/2}}{D/10}$$

2) autocorrelation (autocor time)

$$\varepsilon = \frac{v_z^2}{\tau_E}$$

3) autocorrelation (autocor Vzvz)

$$\varepsilon = A\frac{v_z^3}{\tau_E V_z}$$

2) One method of analysis is rarely sufficient to gain a reasonable picture of the behaviour of ε. Single point determinations should be avoided.

3) The Vzvz method often becomes unstable in the bulk of the tank, mainly due to the difficulty of defining "streamwise" in a complex flow field.

4) As was the case with the Rushton turbine, ε decays rapidly outside of the immediate vicinity of the impeller.

5) The simple dimensional method gives surprisingly good results, and is more stable than the autocorrelation methods.

6) Calculation and examination of the integral time scale, in conjunction with ε, leads to a much better physical understanding of the flow field.

7.6 Notation

A = constant in dimensional method

BPF = blade passage frequency

C = impeller off bottom clearance

D = impeller diameter

f = frequency

k = turbulence kinetic energy per unit mass

L = characteristic length scale

N = impeller rotational speed

N_q = flow number

PSD = power spectral density (see appendix 2)

Q = primary volumetric flow rate

R_E = autocorrelation coefficient function

sf = sampling frequency

t = time

T = tank diameter

u_i' = fluctuating component of the i'th component of velocity

U_c = convection velocity

$\overline{U_i}$ = time averaged component of velocity

V = tank volume

V_r, V_z, V_θ = mean radial, axial and tangential components of velocity; used in expressions for a specific flow.

v_r, v_z, v_θ = RMS radial, axial, and tangential components of velocity

W = blade width

ε = dissipation rate of the turbulence kinetic energy per unit mass

ν = kinematic viscosity

τ_E = Eulerian integral time scale, calculated from the autocorrelation function

7.7 References

Calabrese, Richard V., Pers. Comm., June 15, 1991.

Costin, M. H., P.A. Taylor, and J.D. Wright, "On the dynamics and control of a plasticating extruder," Polymer Eng. Sci., v. 22, pp. 1095-1106, 1982.

Melling, A. and J. H. Whitelaw, "Turbulent flow in a rectangular duct," J. Fluid Mech., v. 78, part 2, pp. 289-315, 1976.

Stoots, Carl M. and Richard V. Calabrese, "The Trailing vortex system behind a Rushton turbine blade," Mixing XII, Missouri, 1989.

Tatterson, G.B., H.S. Yuan, and R.S. Brodkey, "Stereoscopic visualization of the flows for pitched blade turbines," Chem. Eng. Sci., v. 35, pp. 1369-1375, 1980.

Winardi, S., S. Nakao, and Y. Nagase, "Pattern recognition in flow visualization around a paddle impeller," J. Chem. Eng. Japan, v. 21, pp. 503-508, 1988.

Winardi, S. and Y. Nagase, "Unstable phenomenon of flow in a mixing vessel with a marine propeller," J. Chem. Eng. Japan, v. 24, pp. 243-249, 1991.

Wu, H. and G. K. Patterson, "Laser Doppler measurements of turbulent flow parameters in a stirred mixer," Chem. Eng. Sci., v. 44, pp. 2207-2221, 1989.

Yianneskis, M., Z. Popiolek, and J. H. Whitelaw, "An experimental study of the steady and unsteady flow characteristics of stirred reactors," J. Fluid Mech., v. 175, pp. 537-555, 1987.

Appendix I. Refraction corrections for LDA in complex and three dimensional geometries

In laser Doppler anemometry, the intersection point of two (or three) beams of light defines the measurement volume. In confined systems, the laser beams are bent (refracted) as they cross material boundaries; so the point of intersection is not known a priori, but must be calculated using the principles of geometric optics. If the surfaces are planar, calculation of the intersection point is straightforward, but if the geometry of the system in question involves a curved interface, the solution for a desired point of intersection requires iteration. In some regions, the refraction effects will include differences in optical path length between the two beams, and/or a change in the orientation of the beam angle bisector (thus measurement of a different component of velocity than intended), as well as a change in the position of the measuring volume. Several authors have focussed on these problems [Broadway and Karahan (1981), Edwards and Dybbs (1984), Kehoe and Desai (1987), Gardavsky et al. (1989)] for two dimensional systems, but all have used trigonometric interpretations of the system geometry. This approach has several limitations. It leads to several sets of equations, where the choice of equation depends on where the beams cross the material boundary. It is also very difficult to formulate this interpretation in general terms for use in complex, or three dimensional, geometries. These difficulties have lead several authors (eg. Ranade and Joshi (1989)) to assume that the effects of refraction can be neglected. As Parry et al. (1990) have recently shown, this is not always a good assumption.

Any given experimental study may well involve several geometries for beam tracing. For example, a cylinder will assume a circular geometry for radial and tangential components of velocity (as discussed in example 1), a planar geometry for axial velocity, an elliptical geometry for measurement of Reynolds stresses, and will become a three dimensional problem if off-axis measurements of axial velocity are required (see example 2). For this reason, flexibility of the beam tracing equations becomes extremely important.

In this appendix, an alternative interpretation of refraction based on vector algebra is introduced. This approach allows development of one unambiguous set of equations, which are the same regardless of the point of interception[1] with the surface. In addition, the use of vectors allows an easier transition from the two dimensional to the three dimensional case, and has allowed definition of an algorithm virtually independent of the system geometry. This algorithm has been developed to deal with refraction at a general surface, with the beams expressed in parametric vector notation. Two examples of its application are considered, both for a cylindrical geometry. The first example deals with a specific two dimensional case and fully simplified equations. The second example involves three dimensional refraction, and relies more heavily on vector algebra. It is in the second example that the more general approach is given.

1 *intersection* is used for the intersection of the two beams, and *interception* is used for the interception of a beam with a surface.

Problem Definition

The problem of refraction, as applied to LDA, is as follows: two beams of light, labelled A and B, intersect at a focal length F_D and an angle ϕ in air. In the experiment, they cross several surfaces on their way to the probe position. At each surface, the beams are deflected due to changes in the refractive index of the medium.

The principle of refraction at a plane surface is shown in figure 158, and is described by Snell's law ($\mu_{in} \sin\theta_{in} = \mu_t \sin\theta_t$). The incident beam (B) is deflected at the surface in proportion to the ratio of the refractive indices of the two materials. The line perpendicular to the surface is used as a reference across the two materials. When this principle is extended to curved and three dimensional geometries, the reference to be used for Snell's law is the vector normal to the surface at the point of interception. The angle θ_{in} is measured from the normal vector to the incident beam, and θ_t from the normal vector to the transmitted beam. Both of these angles are measured in the plane of refraction, as defined by the beam B, the normal N, and the point of interception.

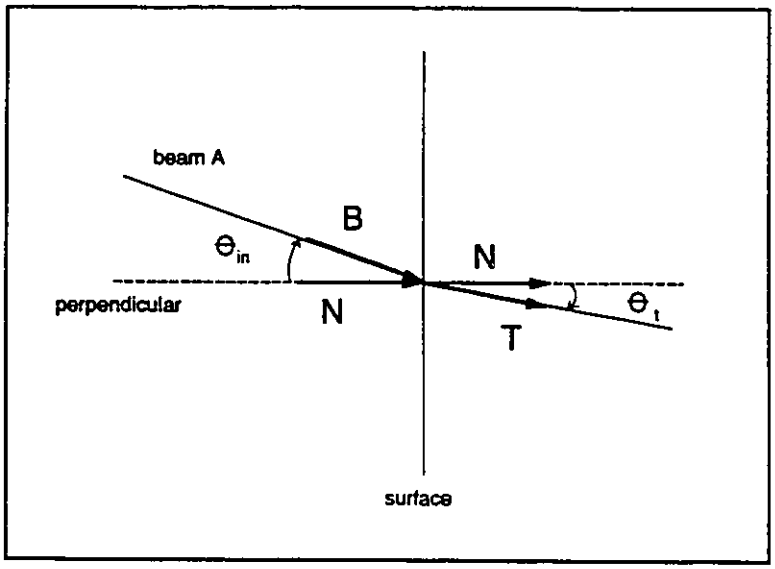

Figure 158. : Refraction at a planar surface

Beam tracing methods for LDA must:

1) determine the location of the intersection of beams A and B
2) check that the optical path lengths of beams A and B are equal
3) determine the effect of refraction on the orientation of the beam angle bisector (the deviation angle).

Once (1) is determined, (2) and (3) are simple calculations.

Two assumptions are implicit in the approach used here. First, it is assumed that surfaces, materials, and fluids are perfectly homogeneous. Given this condition, the beams will always follow equations of a straight line, but their slope and intercept will change at each surface. It is also assumed that the beams intersect at the beam waists when transmitted through air.

The system origin should be defined so that the equations describing the surface(s) assume their simplest form for the purpose of beam tracing. The origin used for beam tracing need not be the same one used for reporting of experimental results. For this work, the beams are defined as entering from the left (-x) direction, as shown in figure 159. The origin is placed on the axis of the cylinder for x and y, with z running perpendicular to the page.

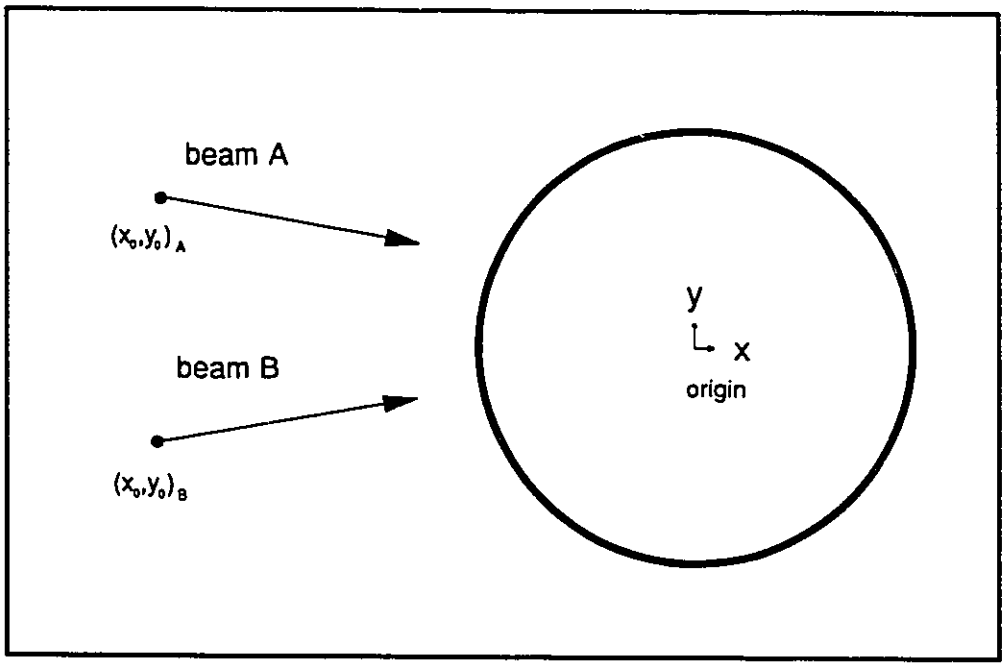

Figure 159. : System geometry

With each iteration to the desired point of intersection, it is the values for the beam origins ((x_o, y_o)) which are adjusted. This applies to systems where the traverses are installed on the laser and optics. For systems where the model is to be moved, consider this in terms of a displacement relative to the optics.

Algorithm

Assuming that the dimensions of the system, the refractive indices of the fluid(s) and the wall(s), and the equation(s) describing the surface(s) at which a change in refractive index occurs are known, and given the origin of the beam A $(x_o, y_o, z_o)_A$, and the slope of the line which follows its path, the following algorithm can be applied.

At each surface:

1. Express the equation describing the incident beam in its parametric vector representation $(x, y, z) = t(1, m_y, m_z) + (b_x, b_y, b_z)$, where $t = x - b_x$. This representation characterizes the beam using a vector $B = (1, m_y, m_z)$ which lies parallel to the beam at the origin, and a displacement, or offset vector (b_x, b_y, b_z) which points from the origin to any point on the beam. All possible multiples, t, of B then define all points on the beam (x, y, z).
2. From the equation describing the incident beam, and the equation describing the surface, calculate the point at which the beam intercepts the surface.
3. Construct a vector normal to the surface at the point of interception (N). This vector must point from the incident to the transmitting medium.
4. Compute the incident angle between the normal vector (3), and the beam (1). This follows from the cosine law ($\cos\theta_{in} = \frac{B \cdot N}{|B||N|}$). Use Snell's law to determine the angle between the normal vector and the transmitted beam ($\mu_{in} \sin\theta_{in} = \mu_t \sin\theta_t$).
5. Define the equation of the refracted beam. Move to the next surface.

Given the origin and slope of beam B, repeat steps 1 - 5 for each surface encountered by beam B. It is now possible to compute the point of intersection of the beams. If the desired position is not obtained, adjust the origin of the beams, and repeat from the beginning. Once the solution is converged, calculate the optical path length of each beam, and the deviation of the beam angle bisector.

Example 1: Cylinder in cross section - 2 dimensional problem

The cylinder is taken to be an intermediate surface, with the origin of the co-ordinate system defined to coincide with the axis of the cylinder. It is assumed that the beam diameter is small relative to the radius of curvature. The plane of refraction is exactly the cylinder cross section, with the point of interception appearing as in figure 160.

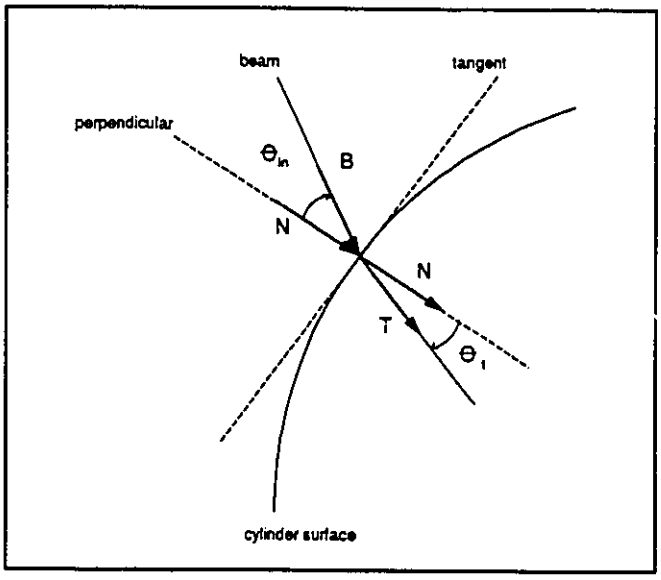

Figure 160. : Refraction at a cylinder surface.

Step 1: The equation of the beam is:

$$y = m_{in}x + b_{in} \tag{110}$$

or, in parametric vector form:

$$(x, y) = t(1, m_{in}) + (0, b_{in}) \tag{111}$$

$$t = x$$

so that $B = (1, m_{in})$.

Step 2: The equation of the surface is:

$$x^2 + y^2 = R^2 \tag{112}$$

To find the point of interception of the beam with the cylinder (x_s, y_s), substitute equation 110 into equation 111 and solve for x using the quadratic equation. The correct solution will always be the "-" one since the laser beams are defined as entering from the left (see figure 159).

Step 3: Take the derivative of the equation of the surface at the point of interception to determine the slope of the tangent line. The slope of the normal is exactly equal to $m_N = -\frac{1}{m_{tangent}}$. The normal vector is then $(1, m_N)$ [1].

Step 4: From the cosine law, the entering angle is:

$$\cos\theta_{in} = \frac{(1, m_{in}) \cdot (1, m_N)}{(1 + m_{in}^2)^{\frac{1}{2}} \times (1 + m_N^2)^{\frac{1}{2}}} \tag{113}$$

and its sign is defined by:

1 In the 3 dimensional example, a different approach to finding the normal vector is given, using the vector cross product. The result is equivalent to this 2 dimensional result.

$$sign = \frac{(m_{in} - m_N) \times ABS(m_{in} - m_N)}{(m_{in} - m_N)^2} \qquad (114)$$

Equations (113) and (114) (and more generally, equation (126)) eliminate the ambiguity inherent in previous approaches. Instead of two equations, the choice of which is dependent upon the position, one set of equations is defined for both beams, and all positions.

Using Snell's law, θ_t is determined.

$$\mu_{in} \sin\theta_{in} = \mu_t \sin\theta_t \qquad (115)$$

Step 5: The slope of the transmitted beam can be determined using:

$$m_t = \tan(\theta_t + \tan^{-1} m_N) \qquad (116)$$

The intercept of the transmitted beam is defined by:

$$b_t = y_s - m_t x_s \qquad (117)$$

Giving, finally, the equation of the transmitted beam:

$$y = m_t x + b_t \qquad (118)$$

Note that the vector refraction equation (126), given in the three dimensional example to follow, is equally applicable to two dimensional problems. The vector refraction equation is a more general result, but equation (116) is useful for this common geometry.

Example 2: Refraction in three dimensions: cylindrical geometry

Consider the geometry shown in figure 161. The entering beams are oriented in the x-z plane, for measurement of the axial velocity (figure 161a). The probe

volume is to be positioned away from the z-axis, so the vector normal to the surface lies out of the x-z plane, causing the plane of refraction to be tilted into the third, y dimension (figure 161b).

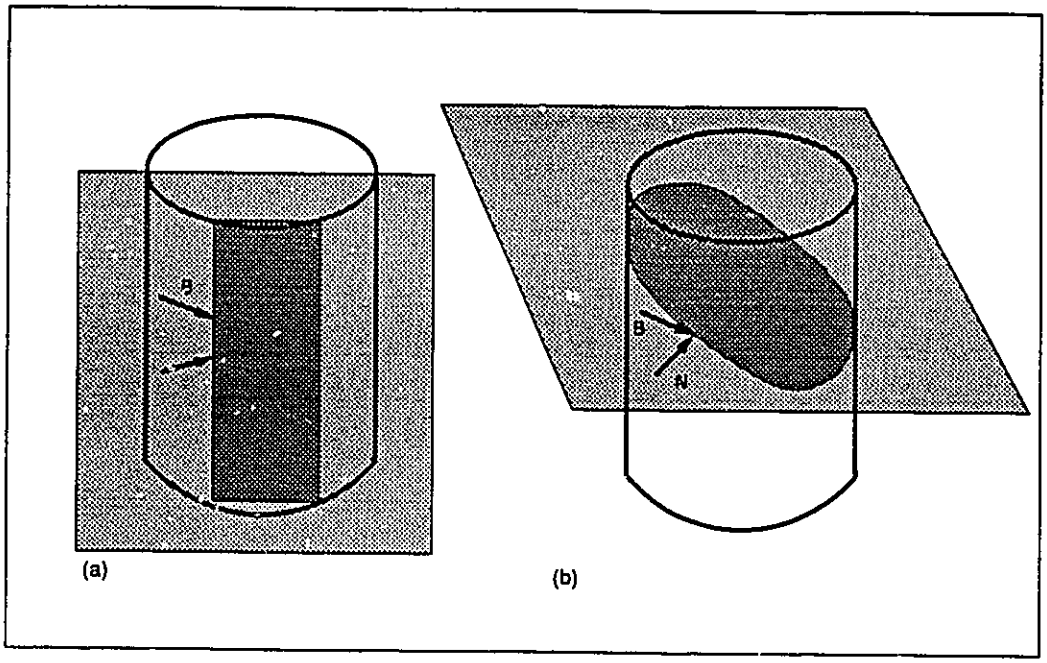

Figure 161. : Refraction in three dimensions for a cylindrical geometry: a) plane of the entering beams, b) plane of refraction for beam A, as defined by the vectors B and N.

Step 1: Given a beam fully contained in an x-z plane

$$(x,y,z) = t(1,0,m_z) + (b_x,b_y,b_z) \qquad (119)$$

$$= tB + (b_x,b_y,b_z)$$

$$t = x - b_x$$

and a cylinder, such that the beam intercepts the cylinder at an off-axis position as shown above.

Step 2: The equation of the surface is

$$x^2 + y^2 = R^2 \tag{120}$$

for all z, and the point of interception is given by:

$$y_s = constant = y_b \tag{121}$$

$$x_s = (R^2 - y_s^2)^{\frac{1}{2}}$$

$$z_s = m_s x_s + z_b$$

Step 3: The plane of refraction is defined by two vectors, one of which is B, and the other of which is the unit vector normal to the surface at the point of interception, N.

To obtain N, start from the tangent plane at the point of interception:

$$(x, y, z) = s(1, \frac{\partial y}{\partial x}]_s, 0) + t(0, \frac{\partial y}{\partial z}]_s, 1) + (x_s, y_s, z_s) \tag{122}$$

$$= sU + tV + W$$

$$s = x - x_s$$

$$t = z - z_s$$

From this, the normal vector pointing into the surface at the point of interception can be defined:

$$-(U \times V) = -\left(\left[\frac{\partial y}{\partial x}\right]_s, -1, \left[\frac{\partial y}{\partial z}\right]_s\right) = N \tag{123}$$

(see the discussion of cross products in Williamson and Trotter (1979)).

Step 4: The incident angle is computed from

$$\cos\theta_{in} = \frac{B \cdot N}{|B|\,|N|} \tag{124}$$

and the angle made by the transmitted beam from Snell's law.

$$\theta_t = \sin^{-1}\left(\frac{\mu_{in}}{\mu_t}\sin\theta_{in}\right) \tag{125}$$

Step 5: Given the plane of refraction, defined by the vectors B and N and the point of intersection, the vector describing the transmitted beam, T, can be defined from

$$\begin{aligned}\underline{T} &= \frac{\sin\theta_t}{\sin\theta_{in}}\underline{B} + \left(\cos\theta_t - \cos\theta_{in}\frac{\sin\theta_t}{\sin\theta_{in}}\right)\underline{N} \\ &= \left(\cos\theta_t - \frac{\mu_{in}}{\mu_t}\cos\theta_{in}\right)\underline{N} + \frac{\mu_{in}}{\mu_t}\underline{B}\end{aligned} \tag{126}$$

as given by Hecht (1987). This equation is obtained using the concept of direction cosines. Note that all of the vectors must be in unit vector form in order to apply this equation. Because of the form of this equation, it is no longer necessary to determine the sign of the incident and transmitted angles. The properties of the functions, and the nature of the information used and obtained, make it immaterial.

The transmitted beam vector T, and a point on the beam are now known, so the equation of the transmitted beam may be defined:

$$(x, y, z) = t\underline{T} + (x_s, y_s, z_s) \tag{127}$$

or

$$y = \frac{T_2}{T_1}x + \left(y_s - x_s\frac{T_2}{T_1}\right)$$

$$z = \frac{T_3}{T_1}x + \left(z_s - x_s\frac{T_3}{T_1}\right)$$

Point of intersection, path length, and deviation angle

The intersection of beams A and B is calculated by equating the elements of the transmitted beam equations at the last surface ($x_A = x_B$, $y_A = y_B$ and $z_A = z_B$). If the desired position is not obtained, the initial guess for the beam origins must be adjusted, and the values fed back into the initial equations.

The optical path lengths are computed using the usual vector length sum. Where the path lengths differ sufficiently, the beams will not cross at the beam waists, resulting in fringe distortion.

The deviation angle is discussed in detail in Broadway and Karahan (1981). It is calculated as follows:

slope of the bisector:

$$m_{bisector} = \frac{m_A + m_B}{2} \tag{128}$$

deviation angle:

$$\theta_{deviation} = \tan^{-1}(m_{bisector}) \tag{129}$$

If the deviation angle is non-zero, the velocity measured will be a combination of two components. Note that there may be up to three deviation angles for three dimensional calculations.

Verification

Three simple methods of code verification were used:

1) Set all refractive indices to one. At a beam origin corresponding to the given focal length of the lens, the point of intersection should be (0,0).

2) Check the values for beams A and B as the calculation proceeds through each of the surfaces (given interception at $y = 0$, any x). All values should be equal.
3) Check the symmetry of the results using positive and negative values of y for the same x.

Sensitivity to Experimental Measurements

Measured values for the dimensions of the system, the refractive indices of the fluid(s) and the wall(s), and the origin and slope of the laser beams (from the focal length and half angle, or beam separation) are used in these calculations. The absolute value of the point of intersection is very sensitive to small errors in the initial slope of the beam, but relative values (ie. the distance moved from one probe position to the next) are virtually unaffected. Small errors in any of the other values were found to have little or no effect.

Notation

b = offset

F_D = focal length

m = slope

R = radius of the cylinder

s, t = parameters

x, y, z = coordinate axes

ϕ = intersection angle of laser beams in air

μ = refractive index

θ_i = incident angle: angle from N to B with positive defined as counter-clockwise

θ_t = transmitted angle: angle from N to T with positive defined as counter-clockwise

vectors

B = vector lying parallel to the incident beam

N = vector normal to the surface at the point of interception; directed from the incident to the transmitting medium

T = vector lying parallel to the transmitted beam

$\underline{S}, \underline{T}, \underline{N}$ = unit vectors (vector divided by its own length)

U, V, W = vectors defining the tangent plane

$(x_o, y_o, z_o)_A$ = origin of beam A

subscripts

1,2,3 = vector components in the x,y,z directions respectively

A = beam A

B = beam B

in = incident (beam)

N = normal

o = beam origin

s = point of interception with the surface

t = transmitted (beam)

tangent = tangent line or plane

References

Broadway, John D. and Emin Karahan, "Correction of Laser Doppler Anemometer Readings for Refraction at Cylindrical Interfaces," Disa Information #26, February 1981.

Edwards, Robert V. and Alexander Dybbs, "Refractive index matching for velocity measurements in complex geometries," TSI Quarterly, v. 10, no. 4, 1984.

Gardavsky, J., J. Hrbek, Z. Chara, and M. Severa, "Refraction corrections for LDA measurements in circular tubes within rectangular optical boxes," Dantec Information, measurement and analysis, no. 8, 1989.

Hecht, Eugene, Optics, 2nd ed., pp. 85-87, Addison-Wesley, 1987.

Kehoe, Anthony B. and Prateen V. Desai, "Compensation for refractive index variations in laser Doppler anemometry," Applied Optics, v. 26, pp. 2582-2591, 1987.

Parry, A. J., M. J. Lalor, Y. D. Tridimas and H. H. Woolley, "Refraction corrections for laser-Doppler anemometry in a pipe bend," pp. 4-6, Dantec Information No. 09, September 1990.

Ranade, V. V., and J. B. Joshi, "Flow generated be pitched blade turbines I: measurements using laser Doppler anemometer," Chem. Eng. Comm., v. 81, pp. 197-224, 1989.

Williamson, Richard E., and Hale E. Trotter, Multivariable Mathematics, 2nd ed., pp. 30-31, Prentice Hall. 1979.

Appendix II. Calculations in the Fourier domain: NAP code

Overview of NAP

The instantaneous velocity signal from a turbulent flow can be interpreted as the sum of a wide spectrum of signals, each of which has a single frequency. The relative contributions of the individual signals to the sum are represented by the frequency spectrum. The characteristics of the frequency spectrum, and its close cousin, the autocorrelation function, provide powerful information for a physical interpretation of the dominant frequencies and time scales in the flow field. This is especially important in flows where a periodic component, such as the blade passage frequency (BPF), is present. NAP (Notch filter, Autocorrelation coefficient function, Power spectral density) was written to allow calculation of these properties, with the additional capability of notch filtering. Notch filtering removes a narrow frequency band from the signal (eg. BPF) so that its effects on the spectum and the autocorrelation can be examined.

Figure 162 and table 7 show the structure of the code and its subroutines. NAP is applied to a time series of discrete data obtained from LDA measurements. The filtering, autocorrelation, and spectral calculations can be performed in any order, so that intermediate results can be stored as required. There are two versions of the code, the first, NAP, runs interactively; the second, NAPBAT, runs in batch mode from a command file.

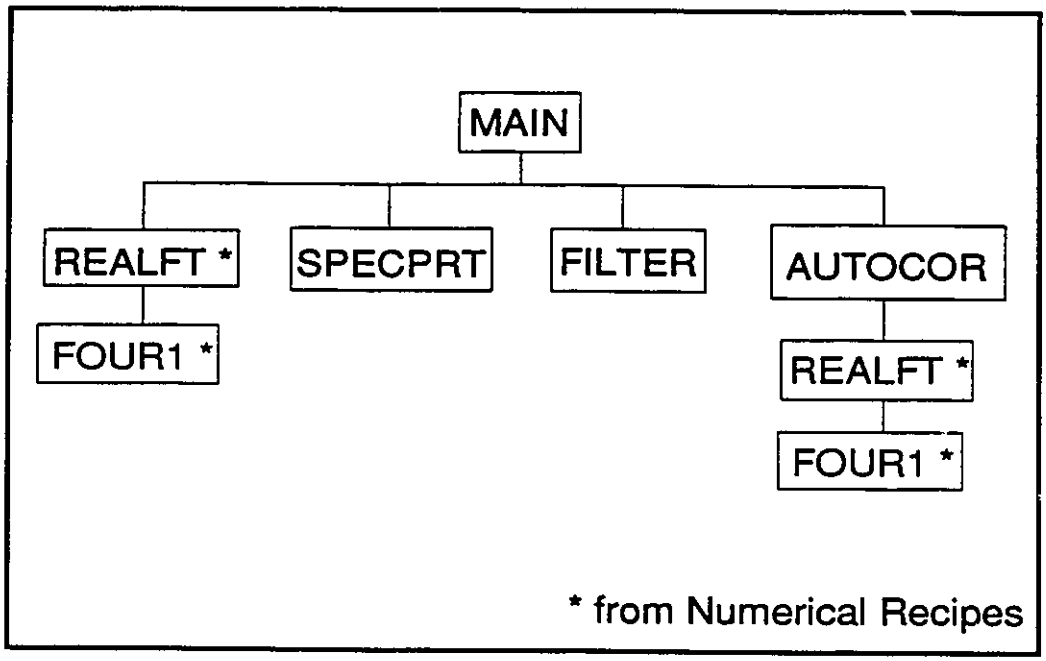

Figure 162. Flowchart of NAP code

All calculations are performed in the Fourier (frequency) domain. By using the Fourier domain, instead of the time domain, the computational speed is improved by several orders of magnitude. For example, calculation of the autocorrelation coefficients for 10000 data points required 3 hours in the time domain, but only 2 minutes in the Fourier domain. In addition to the time savings, the Fourier domain calculation returns substantially more information (16 384 points vs. 1750 points).

Table 7: Program and subroutine summary

Subroutine	Function
MAIN	- read data as time series - mean center - transform to Fourier domain - direct calculations
REALFT	- more efficient use of arrays for the case of real data
FOUR1	- FFT transform and inverse transform - reorder by bit reversal - apply Danielson - Lanczos lemma
SPECPRT	- scaling of power spectral density - print result at selected intervals
FILTER	- apply notch filter function
AUTOCOR	- calculate normalized autocorrelation in Fourier domain - apply inverse transform - print result at selected intervals

Fast Fourier transform (FFT)

The transformation from the time domain to the Fourier domain is defined as (Press et al., 1989, pg. 381)

$$H(f) = \int_{-\infty}^{\infty} h(t) e^{2\pi i f t} dt \tag{130}$$

$$h(t) = \int_{-\infty}^{\infty} H(f) e^{-2\pi i f t} df \qquad (131)$$

where t is in seconds, and f is in Hz. Note that the transformation will accept, and return, complex numbers. The combination of data reordering by bit reversal, and the Danielson-Lanczos lemma allows this transformation to be computed rapidly. This algorithm is known as a fast Fourier transform (FFT). The two FFT subroutines, REALFT and FOUR1, are taken directly from Press et al. (1989, pages 400 and 394 respectively). FOUR1 contains the actual FFT algorithm. Because the data is real, two things are true, first, the frequency spectrum is symmeteric about zero, so that only the positive half (zero to the Nyquist frequency) is required; second, the complex part of the time series is zero. REALFT takes advantage of these two properties to make the code more efficient. The array FFT(N) which is sent to REALFT contains the time series. The array FFT(N) which is returned from REALFT contains N/2 complex numbers ordered in the array as (real1, imaginary1, real2, imaginary2,...real N/2, imaginary N/2). For inverse transforms, the reverse is true. For more information on the details of the FFT calculation, Press et al. (1989, pp. 381-400) should be consulted.

Before further consideration of the subroutines, a careful distinction must be made between the variables DATPTS and N. DATPTS is the number of data points in the time series (for our data, this is typically either 7000 or 10000). N is the size of the array used for Fourier domain calculations. Because of the nature of the FFT algorithm, N must be an integer power of 2. The first power of two greater than 10000 is 16384, and it is this array size which is used in NAP. The array elements not occupied by data are set to zero (zero padding). The implications of

this will be examined for each function.

The frequency spectrum, power spectral density, or $E_1(f)$

The quantity calculated in the subroutine SPECPRT is, rigorously speaking, the power spectral density (PSD). It is related to the frequency spectrum by a constant factor. Some care will be taken here to define the normalization used, and the rationale behind it, since a great deal of confusion exists surrounding the exact procedure.

Hinze (1975, eqn. 1-91) defines the one dimensional energy spectrum, E_1:

$$\int_0^\infty E_1(f) = \frac{\sum_{k=0}^{DATPTS-1} u_{1,k}^2}{DATPTS} \tag{132}$$

Where 1 denotes the streamwise component, and $E_1(f)$ is a continuous function in the Fourier domain. Press et al. (1989, pg. 389) define the Fourier transform of a discrete set of points such that

$$H(f_k) \approx \frac{H_k}{sf} \tag{133}$$

Parseval's theorem (Press et al., 1989, pg. 390) states that

$$\sum_{k=0}^{N-1} |h_k|^2 = \frac{1}{N} \sum_{n=0}^{N-1} |H_n|^2 \tag{134}$$

Where h_k is the time domain data, sampled at regular intervals, and H_n is the discrete Fourier transform of the N points h_k.

Combining 130 and 132, the relation

$$\frac{\sum_{k=0}^{DATPTS-1} u_k^2}{DATPTS} = \frac{1}{DATPTS*N} \sum_{n=0}^{N-1} |H_n|^2 \qquad (135)$$

is obtained. This is the definition of the power spectral density used in NAP. Its sum (from zero to the Nyquist frequency) is equal to the RMS velocity, squared. Note that H_n has units of m/s, so the PSD will have units of m^2/s^2.

Continuing for now with the definition of the PSD, Press et al. (1989, pg. 384) give the basic definition of the power spectrum as

$$P_h(f) \equiv |H(f)|^2 + |H(-f)|^2 \qquad (136)$$

for a real valued function, $H(f) = H(-f)$, so that a factor of 2 is expected in equation 133. The spectrum as defined here, however, is a two sided spectrum where only the positive half is examined. Since the sum of interest is not the power, but the RMS velocity squared, the factor of 2 drops out.

How is the PSD defined in equation 133 related to $E_1(f)$? Comparing equations 130 and 133 gives

$$E_1(f) = \frac{|H_k|^2}{DATPTS*N} \frac{1}{\Delta f} \qquad (137)$$

If this is compared with the second definition as given by Hinze (1975, pg. 63),

$$E_1(f) = \frac{4\pi^2 a(f) a^*(f)}{DATPTS/sf} \tag{138}$$

$$= \frac{1}{sf^2} \frac{|H_k|^2}{DATPTS/sf}$$

$$= \frac{|H_k|^2}{DATPTS * N} \frac{1}{\Delta f}$$

the same result is obtained. The only difference between this and the PSD defined for NAP is the factor of $\frac{1}{\Delta f}$. Since Δf can be defined as either the FFT(N) step size (sf/N), or the final output step size (no set definition), it was considered more useful to present the PSD, allowing conversion to the desired $E_1(f)$ if necessary.

As a check on the calculation of the PSD, two functions were tested. First, equation 133 was verified for each; then the frequency spectra were examined. The first test function was a sine wave of frequency 0.1Hz having a mean value of zero, and an RMS of 0.5. The PSD calculation returned a sum of 0.5. The relative contributions of the real and imaginary parts of the Fourier transform to this spectrum are shown in figure 163. The effect of zero padding is shown in figure 164. As expected, the PSD returns one peak at a frequency of 0.1Hz. Zero padding does not change the results of the spectrum, but it does give finer frequency resolution.

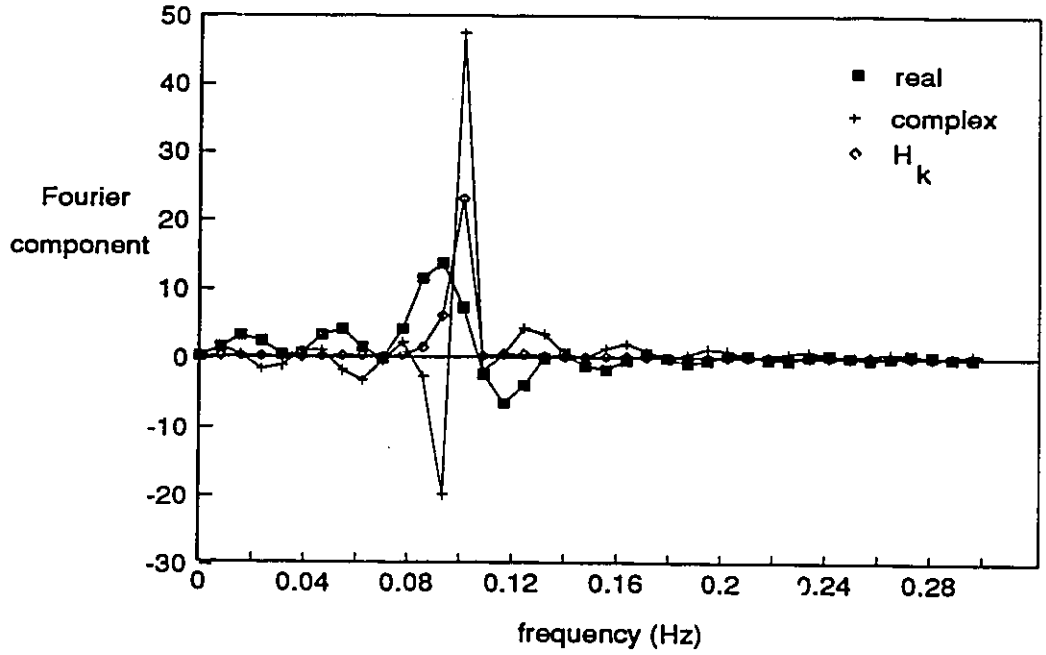

Figure 163. Contributions to the PSD from real and imaginary components for a sin wave of frequency 0.1Hz.

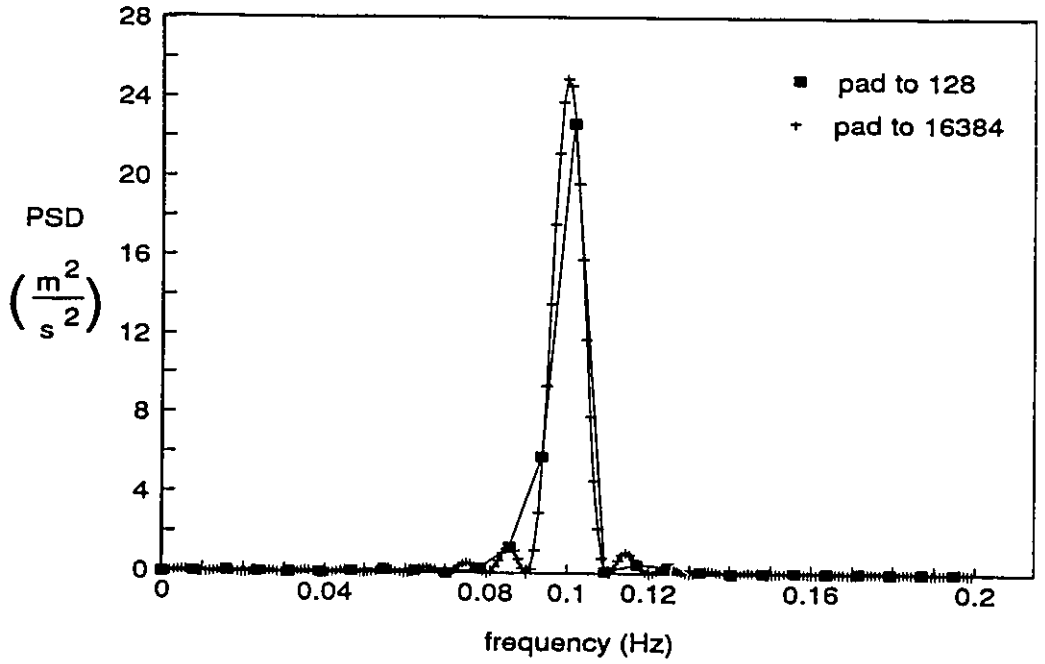

Figure 164. The effect of zero padding on the results of th PSD calculation.

The second test function used real data (point S1AZ020), and a comparison with the results obtained using LDS, an analysis program written by Cam Tropea (1987). The mean velocity at this point is -0.336 m/s, with an RMS velocity of 0.388 m/s. Application of equation 133 to the spectrum returned by LDS resulted in a sum of $(0.373 m/s)^2$, while for NAP the result was $(0.325 m/s)^2$. The real data does not return exact agreement with the true RMS. This is because the FFT gives a PSD estimation, whose standard deviation is exactly equal to the RMS velocity squared. The standard deviation cannot be decreased by changing the data collection settings. By increasing the number of data points at a set sampling frequency, the frequency resolution increases. By increasing the sampling frequency for the same collection time, the Nyquist frequency is increased. In neither case is the standard deviation decreased. The standard deviation for NAP, however, is not 100% of the RMS velocity squared. By summing the estimated PSD over several frequency intervals, the profile of the PSD is "smoothed", and the standard deviation is reduced by a factor of $1/\sqrt{K}$, where K is the number of intervals, in this case, 32. This factor (m/s) brings the results given by NAP and LDS into line with the data. This also reduces the data set to a manageable size (from 16384 to 512 points). Figure 165 shows the spectra calculated by the two codes. LDS gives a smoother profile, and is likely more accurate. It appears to be based on the same normalization as NAP.

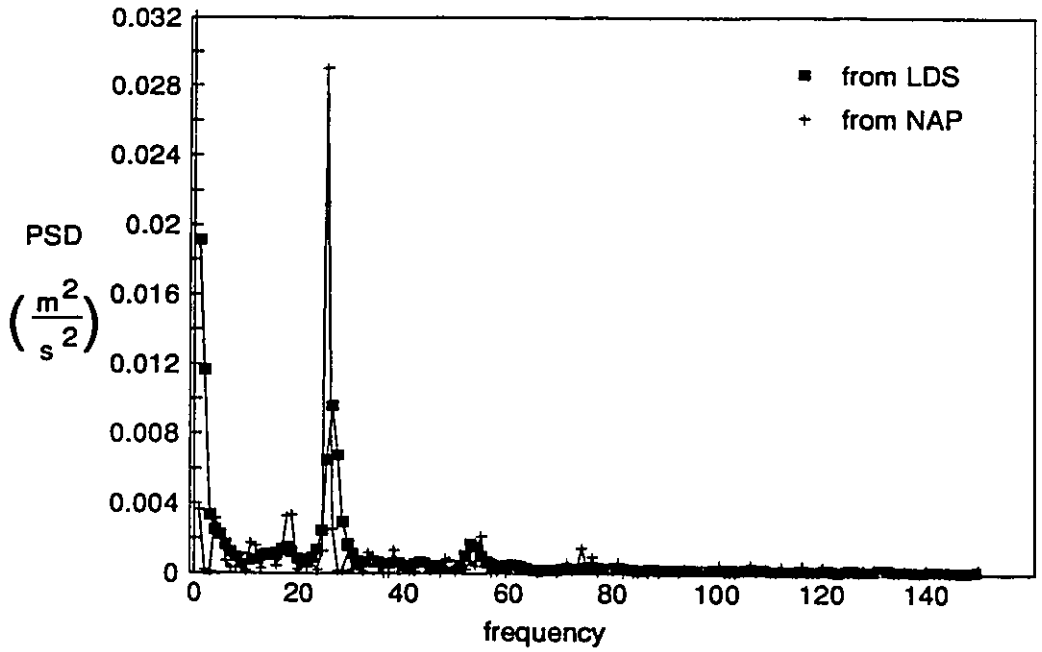

Figure 165. Comparison of spectra obtained by the two programs NAP and LDS.

In summary, the subroutine SPECPRT stores the power spectral density (PSD) as defined in equation 133. This spectrum is different from $E_1(f)$, the 1-dimensional energy spectrum, by a factor of $\frac{1}{\Delta f}$. Summing the spectrum values returns the RMS velocity squared, plus or minus a variance of $\frac{1}{K} * RMS^2$. The spectra calculated by NAP were verified using a sine wave of frequency 0.1Hz, a real data point, and some commercial data analysis software, LDS.

The autocorrelation coefficient function

Calculation of the autocorrelation coefficient function ("the autocorrelation") is straight forward. The autocorrelation is the left half of the Fourier pair

$$autocorrelation \Leftrightarrow H_k H_k^*$$

$$= |H_k|^2$$

Normalization by 1/N is required for the inverse transform.

Results of the autocorrelation calculation in the Fourier domain were compared with calculations performed in the time domain. Agreement is exact. Results are shown in figure 166.

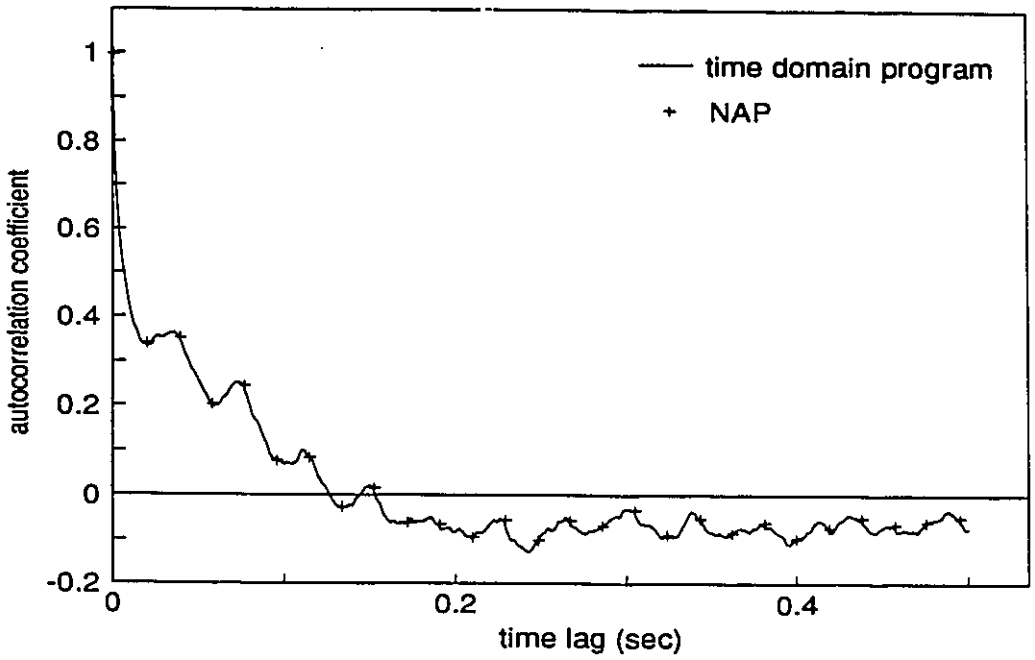

Figure 166. Verification of the autocorrelation subroutine AUTOCOR using results from a time domain calculation.

Zero padding is of significant interest for the autocorrelation calculation. Because of underlying assumptions in the algorithm, there is contamination of the result by data wraparound. The zero padding of z points removes this contamination from exactly z points. Zero padding should not be used to extend the lag time indefinitely, however, because the number of real data points used in the calculation decreases as the lag increases.

Notch filtering

The general filter equation is given by Press et al. (1989, pg. 438) as

$$\mathcal{H}(f) = \frac{\sum_{k=0}^{M} c_k e^{-2\pi i k(f\Delta)}}{1 - \sum_{j=1}^{N} d_j e^{-2\pi i j(f\Delta)}} \tag{139}$$

where $\Delta = 1/sf$. The filter is applied by multiplying the Fourier transform of the data H_k by the filter function. For a notch filter, the c's and d's to be used are given as (Press et al., 1989, pg. 442):

$$c_0 = \frac{1+\omega_0^2}{(1+\varepsilon\omega_0)^2+\omega_0^2} \tag{140}$$

$$c_1 = -2\frac{1-\omega_0^2}{(1+\varepsilon\omega_0)^2+\omega_0^2}$$

$$c_2 = c_0$$

$$d_1 = 2\frac{1-\varepsilon^2\omega_0^2-\omega_0^2}{(1+\varepsilon\omega_0)^2+\omega_0^2}$$

$$d_2 = -\frac{(1-\varepsilon\omega_0)^2+\omega_0^2}{(1+\varepsilon\omega_0)^2+\omega_0^2}$$

where

$$\omega = \tan(\pi f\Delta) \tag{141}$$

$\omega_0 =$ center of frequency notch

$\varepsilon =$ width of frequency notch as a fraction ofω_0

The filter function was tested on a sum of three sine waves having frequencies 0.5, 0.1 and 0.01Hz. The function is shown in figure 167, and its PSD in figure 168. First, the 0.01Hz frequency was removed with an ε of 0.5; the resulting PSD is shown in figure 169. Then, the 0.5Hz frequency was removed, at an ε of 0.2. Figure 170 shows the final PSD, with only the 0.1Hz signal remaining.

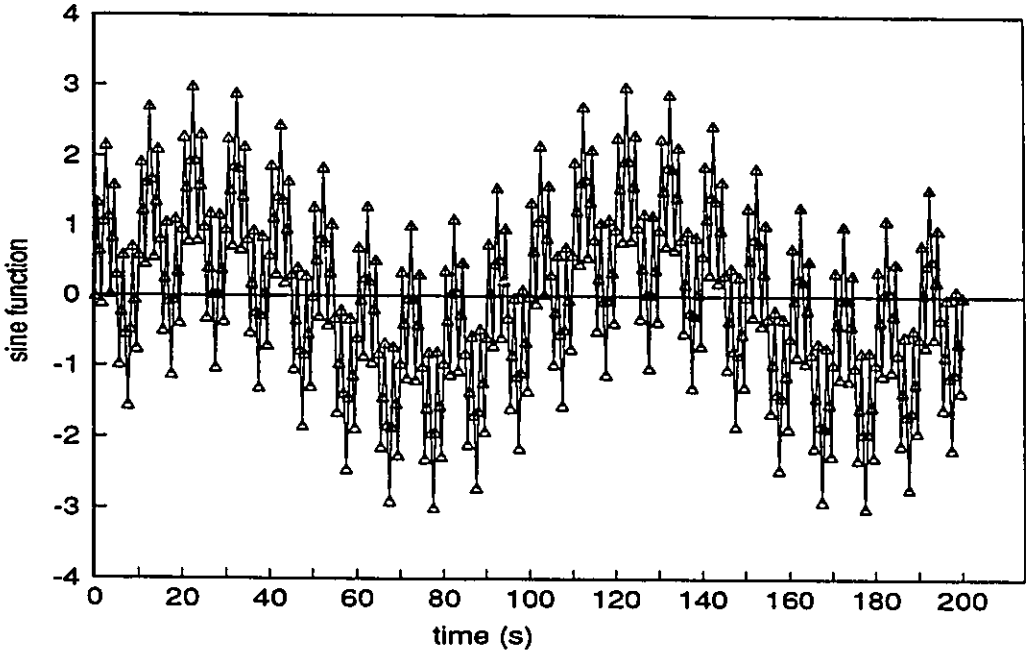

Figure 167. Test function for filter subroutine: sum of three sine waves at 0.5, 0.1, and 0.01Hz.

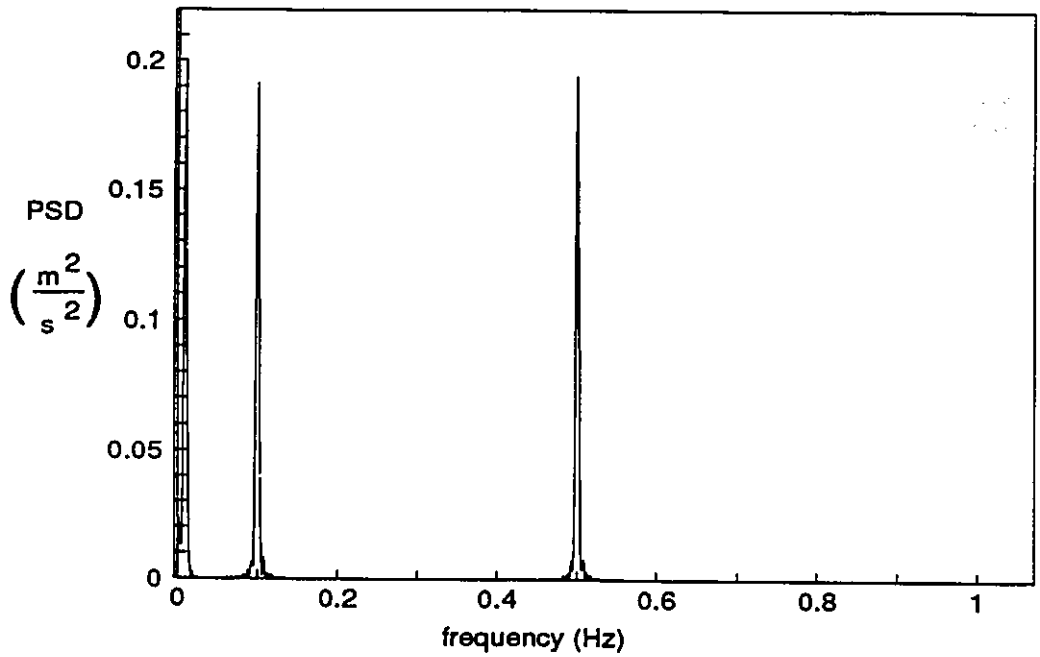

Figure 168. Intial PSD

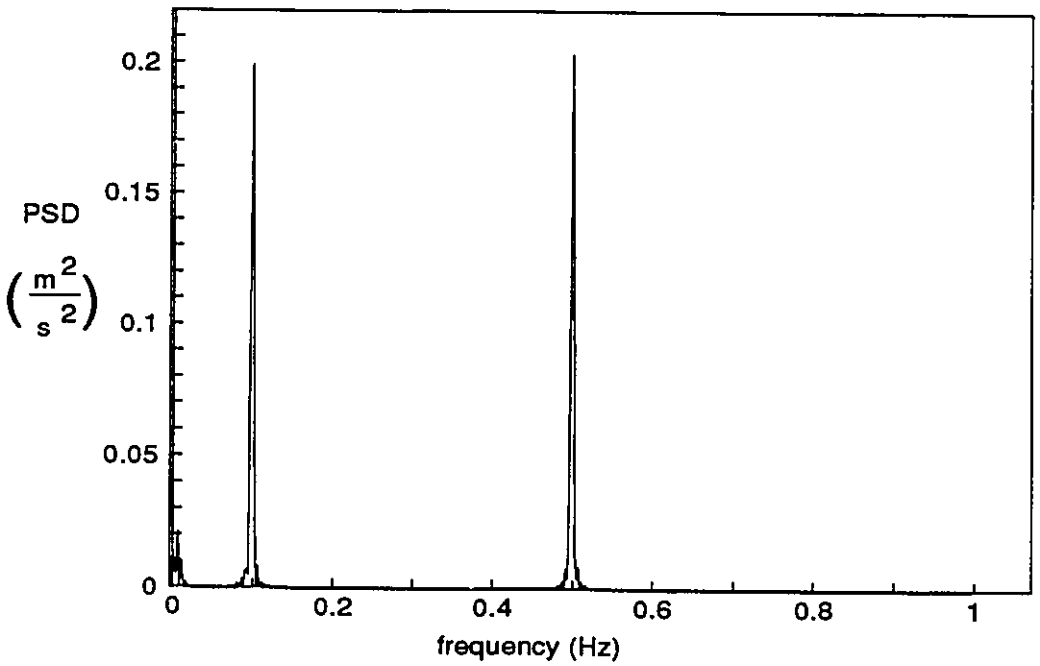

Figure 169. PSD with 0.01Hz filtered out at a level of 0.5.

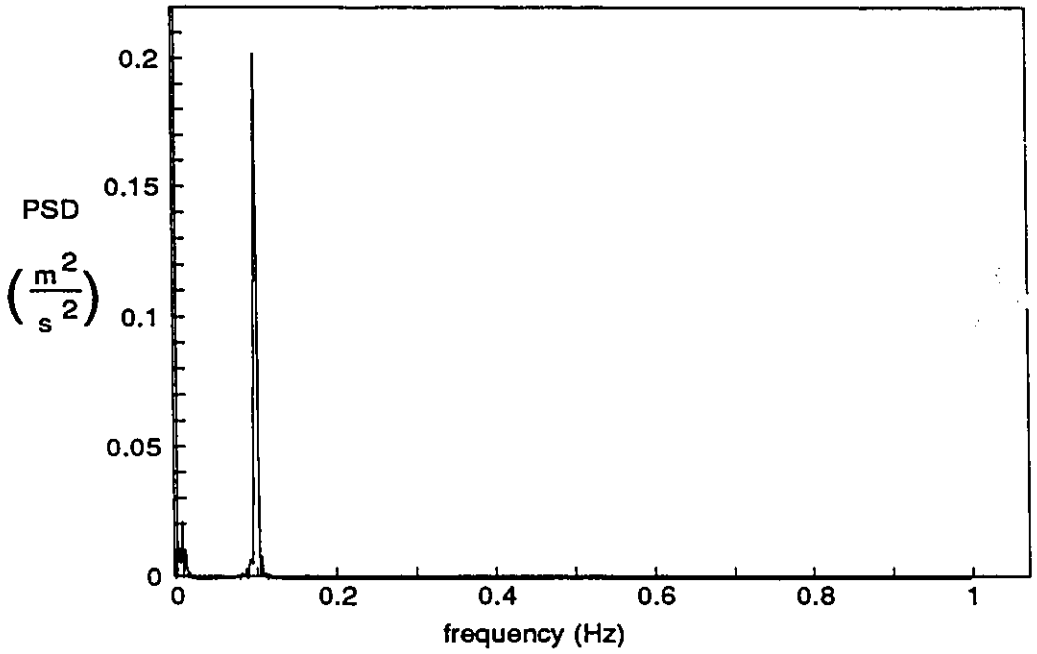

Figure 170. PSD with 0.01Hz and 0.5Hz (at 0.2) removed.

Finally, the FILTER subroutine was tested on the data point S1AZ020, removing first 26.667Hz at 0.2 (the BPF), then 1.28Hz at 0.5. The autocorrelations for the raw data and the succeeding filter steps are shown in figure 171.

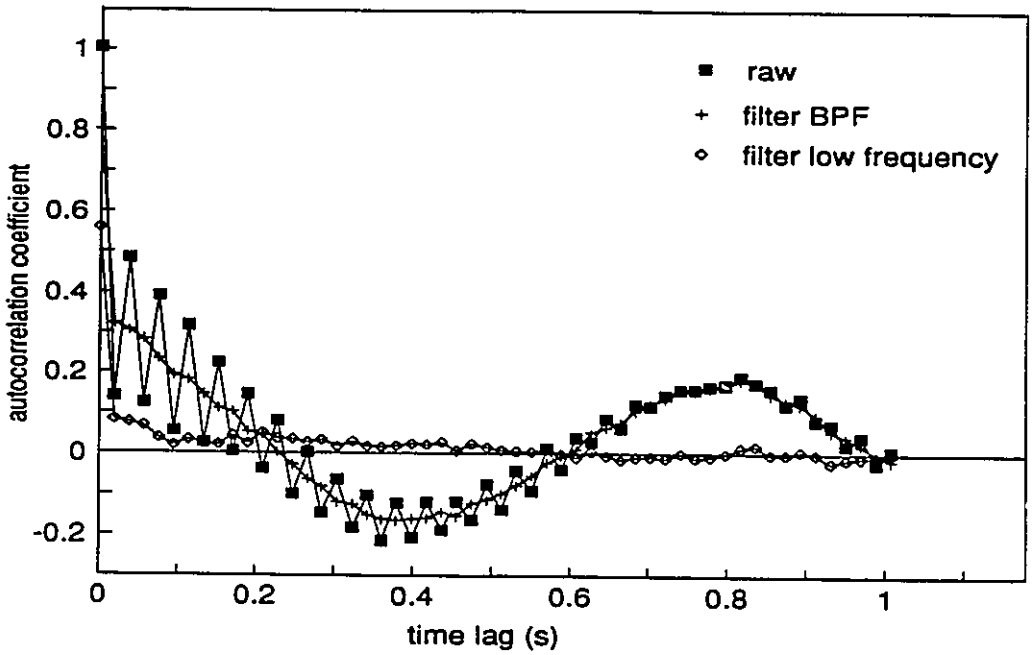

Figure 171. Test of filter on real data point S1AZ020.

Code listing

```
      PROGRAM NAP
c     Suzanne Kresta, June 5, 1991

C Calculates the autocorrelation of a time series of data
c using FFT (fast Fourier transforms) from Numerical Recipes
c       FOUR1  pg 394; REALFT  pg 400

c The energy spectrum (power spectral density) can be obtained at midway

C General algorithm:

c  DATA -> FFT -> FFT*complex conjugate -> inverse FFT -> autocorrelation
c                              -> E1 (power spectrum)
C           -> filter in Fourier domain

c Filtering is done using a notch filter as described on pg 442

      IMPLICIT NONE
      REAL TSR(16384), FFT(16384),ANS(16384),MEAN,SUM,RMS,SF
      INTEGER DATPTS,J,N,CHOICE,I,OLD
      CHARACTER*7 FILE
c Set N=16384 to accomodate 10000 data points.
```

```
c This allows a 6384 lag autocorrelation.
      N=16384
c Open data file
2     PRINT*,'Choose file type'
      PRINT*,'1) New time series input file'
      PRINT*,'2) Old FFT input file'
      READ*,OLD
      PRINT*,'Input data filename? (no .TSR)'
      READ(*,'(A)') FILE
      IF(OLD.EQ.1)THEN
        OPEN(UNIT=10,FILE='C:\SCRATCH\'//FILE//'.TSR',STATUS='OLD')
        PRINT*,'Sampling frequency? (kHz)'
        READ*,SF
        SF=SF*1000
C Read and mean center the data
        SUM=0.
        DO 30 J=1,N
          READ(10,*,END=10) TSR(J)
          SUM=SUM+TSR(J)
30      CONTINUE
10      DATPTS=J-1
        MEAN=SUM/DATPTS
        SUM=0
C Calculate RMS
        DO 40 J=1,DATPTS
          TSR(J)=TSR(J)-MEAN
          SUM=SUM+TSR(J)*TSR(J)
40      CONTINUE
        RMS=SQRT(SUM/DATPTS)
c Zero padding to obtain an array of size = power of 2 (16384)
        IF(DATPTS.LT.N)THEN
          DO 20 J=DATPTS+1,N
            TSR(J)=0.0
20        CONTINUE
        ENDIF

C Data processing in the Fourier domain

c Create working array
        DO 5 I=1,N
          FFT(I)=TSR(I)
5       CONTINUE
c Calculate FFT of data time series TSR and return the result in FFT.
c FFT contains the positive frequency half of the complex spectrum, with
c the first and last real results stored in array elements 1 and 2.
        CALL REALFT(FFT,N/2,1)
      ELSEIF(OLD.EQ.2)THEN
        OPEN(UNIT=10,FILE=FILE//'.FFT',STATUS='OLD')
        READ(10,*) SF,MEAN,RMS,DATPTS
```

```
      READ(10,*) (FFT(I),FFT(I+1),FFT(I+2),FFT(I+3),I=1,16384,4)
      CLOSE(UNIT=10)
    ELSE
      GOTO 2
    ENDIF

C Echo parameters
    PRINT*,'Sampling frequency',SF
    PRINT*,'data points',DATPTS
    PRINT*,'Mean is',MEAN
    PRINT*,'RMS',RMS

C Print menu for data treatment
1   PRINT*,'Choose next step'
    PRINT*,'1) Store spectrum as E1'
    PRINT*,'2) Apply filter'
    PRINT*,'3) Calculate autocorrelation'
    PRINT*,'4) Store FFT for later use'
    PRINT*,'5) Stop'
    READ*,CHOICE
    IF(CHOICE.EQ.1)THEN
      CALL SPECPRT(FFT,N,DATPTS,SF)
      GOTO 1
    ELSEIF(CHOICE.EQ.2)THEN
      CALL FILTER(FFT,N,SF)
      GOTO 1
    ELSEIF(CHOICE.EQ.3)THEN
      CALL AUTCOR(FFT,N,DATPTS,RMS,SF,ANS)
      GOTO 1
    ELSEIF(CHOICE.EQ.4)THEN
      OPEN(UNIT=15,FILE=FILE//'.FFT',STATUS='UNKNOWN')
      WRITE(15,*) SF,MEAN,RMS,DATPTS
      WRITE(15,*) (FFT(I),FFT(I+1),FFT(I+2),FFT(I+3),I=1,16384,4)
      CLOSE(UNIT=15)
      GOTO 1
    ELSEIF(CHOICE.EQ.5)THEN
      GOTO 999
    ELSE
      GOTO 1
    ENDIF
999 STOP
    END
```

```
      SUBROUTINE AUTCOR(FFT,N,DATPTS,RMS,SF,ANS)
c Calculate autocorrelation using real vectors only (store real and
c complex parts in adjacent elements)
C Modified from CORREL in Numerical Recipes (pg 416)
      REAL ANS(N),RMS,FFT(N),TIME
      CHARACTER*7 FILE
      INTEGER DATPTS
C Open file for printing of autocorrelation results
      PRINT*,'Filename for autocorrelation storage? (7 char, no ext)'
      READ(*,'(A)') FILE
      OPEN(UNIT=11,FILE=FILE//'.COR',STATUS='UNKNOWN')
c Normalize in advance for the inverse transform
      NO2=N/2
C Calculate the Fourier pair of the autocorrelation, which is F(f)F(f)*
c (the Fourier transform times its complex conjugate)
      ANS(1)=FFT(1)*FFT(1)/FLOAT(NO2)
      ANS(2)=FFT(2)*FFT(2)/FLOAT(NO2)
      DO 11 I=3,N-1,2
       TEMP=(FFT(I)*FFT(I)+FFT(I+1)*FFT(I+1))
       ANS(I)=TEMP/FLOAT(NO2)
       ANS(I+1)=0
11    CONTINUE
C ANS is a real array of length N/2 which contains the Fourier pair.
c REALFT calculates the inverse Fourier transform, returning it in ANS.
      CALL REALFT(ANS,NO2,-1)
c Step size for printing of result
C     JMAX=N-DATPTS
C Set for length of 1 second
C     J=SF+1
C     IF(J.GT.JMAX) J=JMAX
      J=N-DATPTS
      STEP=NINT(REAL(J)/500)
c Complete normalization of the autocorrelation coefficient, and write
      DO 50 K=1,J,STEP
       TIME=(K-1)/SF
       WRITE(11,*) K,TIME,ANS(K)/(RMS**2*DATPTS)
50    CONTINUE
      CLOSE(UNIT=11)
      RETURN
      END
```

```
      SUBROUTINE REALFT(DATA,N,ISIGN)
      REAL*8 WR,WI,WPR,WPI,WTEMP,THETA
      REAL DATA(2*N)
      THETA=3.141592653589793D0/DBLE(N)
      C1=0.5
      IF (ISIGN.EQ.1) THEN
       C2=-0.5
       CALL FOUR1(DATA,N,+1)
      ELSE
       C2=0.5
       THETA=-THETA
      ENDIF
      WPR=-2.0D0*DSIN(0.5D0*THETA)**2
      WPI=DSIN(THETA)
      WR=1.0D0+WPR
      WI=WPI
      N2P3=2*N+3
      DO 11 I=2,N/2
       I1=2*I-1
       I2=I1+1
       I3=N2P3-I2
       I4=I3+1
       WRS=SNGL(WR)
       WIS=SNGL(WI)
       H1R=C1*(DATA(I1)+DATA(I3))
       H1I=C1*(DATA(I2)-DATA(I4))
       H2R=-C2*(DATA(I2)+DATA(I4))
       H2I=C2*(DATA(I1)-DATA(I3))
       DATA(I1)=H1R+WRS*H2R-WIS*H2I
       DATA(I2)=H1I+WRS*H2I+WIS*H2R
       DATA(I3)=H1R-WRS*H2R+WIS*H2I
       DATA(I4)=-H1I+WRS*H2I+WIS*H2R
       WTEMP=WR
       WR=WR*WPR-WI*WPI+WR
       WI=WI*WPR+WTEMP*WPI+WI
11    CONTINUE
      IF (ISIGN.EQ.1) THEN
       H1R=DATA(1)
       DATA(1)=H1R+DATA(2)
       DATA(2)=H1R-DATA(2)
      ELSE
       H1R=DATA(1)
       DATA(1)=C1*(H1R+DATA(2))
       DATA(2)=C1*(H1R-DATA(2))
       CALL FOUR1(DATA,N,-1)
      ENDIF
      RETURN
      END
```

```
      SUBROUTINE FOUR1(DATA,NN,ISIGN)
      REAL*8 WR,WI,WPR,WPI,WTEMP,THETA
      REAL DATA(2*NN)
      N=2*NN
      J=1
      DO 11 I=1,N,2
       IF(J.GT.I)THEN
        TEMPR=DATA(J)
        TEMPI=DATA(J+1)
        DATA(J)=DATA(I)
        DATA(J+1)=DATA(I+1)
        DATA(I)=TEMPR
        DATA(I+1)=TEMPI
       ENDIF
       M=N/2
1      IF ((M.GE.2).AND.(J.GT.M)) THEN
        J=J-M
        M=M/2
       GO TO 1
       ENDIF
       J=J+M
11    CONTINUE
      MMAX=2
2     IF (N.GT.MMAX) THEN
       ISTEP=2*MMAX
       THETA=6.28318530717959D0/(ISIGN*MMAX)
       WPR=-2.D0*DSIN(0.5D0*THETA)**2
       WPI=DSIN(THETA)
       WR=1.D0
       WI=0.D0
       DO 13 M=1,MMAX,2
        DO 12 I=M,N,ISTEP
         J=I+MMAX
         TEMPR=SNGL(WR)*DATA(J)-SNGL(WI)*DATA(J+1)
         TEMPI=SNGL(WR)*DATA(J+1)+SNGL(WI)*DATA(J)
         DATA(J)=DATA(I)-TEMPR
         DATA(J+1)=DATA(I+1)-TEMPI
         DATA(I)=DATA(I)+TEMPR
         DATA(I+1)=DATA(I+1)+TEMPI
12       CONTINUE
        WTEMP=WR
        WR=WR*WPR-WI*WPI+WR
        WI=WI*WPR+WTEMP*WPI+WI
13     CONTINUE
       MMAX=ISTEP
      GO TO 2
      ENDIF
      RETURN
      END
```

```
      SUBROUTINE SPECPRT(SPEC,N,DATPTS,SF)
      REAL SPEC(N),SF,FREQ
      INTEGER STEP,I,J,K,DATPTS
      CHARACTER*7 FILE
C Open file for printing of energy spectrum results
      PRINT*,'Filename for energy spectrum storage? (7 char, no ext)'
      READ(*,'(A)') FILE
      OPEN(UNIT=12,FILE=FILE//'.SPC',STATUS='UNKNOWN')
c Calculate printing step size
      STEP=2
      J=N
1     IF(J.GT.1024)THEN
        J=J/2
        STEP=STEP*2
        GOTO 1
      ENDIF
      WRITE(12,*) 'STEP,FREQUENCY,E(f)'
c Calculate the power spectrum, which is the FFT divided by the
c number of actual data points and the total number of points (after
c zero padding) to give E1.
      LAST=SPEC(2)*SPEC(2)
      SPEC(2)=0
      SUM=0+LAST
      DO 10 I=1,N,STEP
        E1=0
        DO 100 K=I,I+STEP-1
          AACONG=(SPEC(I)*SPEC(I)+SPEC(I+1)*SPEC(I+1))
          E1=E1+AACONG/FLOAT(N*DATPTS)
100     CONTINUE
        FREQ=FLOAT((I-1)/2)/FLOAT(N)*SF
        WRITE(12,*) I,FREQ,E1
c Calculate integral
        SUM=SUM+E1
10    CONTINUE
      CLOSE(UNIT=12)
      RETURN
      END
```

```
      SUBROUTINE FILTER(FFT,N,SF)
      REAL FFT(N),W0,C0,C1,C2,D1,D2,EPS,F0,PI,BOTTOM
      REAL FDELTA,SIN1,SIN2,COS1,COS2,RENUM,REDEN,IMNUM,IMDEN
      REAL HRE,HIM,FFTRE,FFTIM
c Enter filtering parameters
      PRINT*,'Center of frequency notch?'
      READ*, F0
      PRINT*,'Width of frequency notch, as a fraction of the frequency?'
      READ*, EPS
      PI=ACOS(-1.0)
      W0=TAN(PI*F0/SF)
c Calculate filter constants
      BOTTOM=(1+EPS*W0)**2+W0**2
      C0=(1+W0*W0)/BOTTOM
      C1=-2*(1-W0*W0)/BOTTOM
      C2=(1+W0*W0)/BOTTOM
      D1=2*(1-EPS*EPS*W0*W0-W0*W0)/BOTTOM
      D2=-((1-EPS*W0)**2+W0*W0)/BOTTOM
C Loop to apply filter
      DO 10 I=1,N-1,2
c Calculate real and imaginary parts of numerator and denominator
         FDELTA=FLOAT((I-1)/2)/FLOAT(N)
         SIN1=SIN(2*PI*FDELTA)
         SIN2=SIN(4*PI*FDELTA)
         COS1=COS(2*PI*FDELTA)
         COS2=COS(4*PI*FDELTA)
         RENUM=C0+C1*COS1+C2*COS2
         REDEN=1-D1*COS1-D2*COS2
         IMNUM=-(C1*SIN1+C2*SIN2)
         IMDEN=D1*SIN1+D2*SIN2
c Calculate real and imaginary parts of filter
         HRE=(RENUM*REDEN+IMNUM*IMDEN)/(REDEN*REDEN+IMDEN*
IMDEN)
         HIM=(IMNUM*REDEN-RENUM*IMDEN)/(REDEN*REDEN+IMDEN*I
MDEN)
c Apply filter
         FFTRE=FFT(I)
         FFTIM=FFT(I+1)
         FFT(I)=FFTRE*HRE-FFTIM*HIM
         FFT(I+1)=FFTRE*HIM+FFTIM*HRE
10    CONTINUE
      RETURN
      END
```

Notation

$a(f)$ = continuous Fourier transform using Hinze's normalization

$a^*(f)$ = complex conjugate of $a(f)$

c, d = filter constants

$DATPTS$ = number of recorded data points in the time series

$E_1(f)$ = 1-dimensional energy spectrum m^2/s

f = frequency (Hz)

Δf = frequency step size in the discrete spectrum (Hz)

$H(f)$ = continuous Fourier transform

H_k = discrete Fourier transform (m/s)

H_k^* = complex conjugate of H_k

$\mathcal{H}(f)$ = filter function

$h(t)$ = continuous time series of data

K = number of original PSD points summed to obtain the output spectrum

N = NAP working array size, including zero padding

$P_h(f)$ = power spectral density, as defined by Press et al. (1989)

sf = sampling frequency (Hz)

t = time (s)

$u_{1,k}$ = discrete fluctuation velocity in the streamwise (1) direction (m/s), element k in the time series

References

Hinze, J.O., Turbulence, 2nd edition, McGraw Hill, Toronto, 1975.

Press, William H., Brian P. Flannery, Sual A. Teukolsky, and William T. Vetterling, Numerical Recipes, The Art of Scientific Computing, Cambridge University Press, New York, 1989.

Tropea, C. and D. Struthers, "Microprocessor based on-line measurement system for LDA," ISl proceedings on the use of computers in laser velocimetry, May 18-20, 1987.